Communauté
UNIVERSITÉ Grenoble Alpes

HABILITATION A DIRIGER DES RECHERCHES

Spécialité : **Astrophysique**

Présentée par

Benoît CERUTTI

Préparée au sein de l'**Institut de Planétologie et d'Astrophysique de Grenoble** dans l'**École Doctorale de Physique**

Accélération de particules dans les magnétosphères relativistes

Particle acceleration in relativistic magnetospheres

HDR soutenue publiquement le **8 janvier 2021 à 14h** dans la salle Manuel Forestini à l'IPAG devant le jury composé de :

Mme Elena AMATO
Chercheure INAF, Rapporteur
M Fabien CASSE
Professeur Université de Paris, Examinateur
M Laurent DEROME
Professeur Université Grenoble Alpes, Président
M Arache DJANNATI-ATAÏ
Directeur de recherche CNRS, Examinateur
M Serguei KOMISSAROV
Professeur University of Leeds, Rapporteur
M Martin LEMOINE
Directeur de recherche CNRS, Rapporteur

Contents

Prologue

In September 2010, as I just moved from Grenoble into Boulder, Colorado, for my first postdoc in the group of Prof. Dmitri Uzdensky, a cosmic phenomenon of prime significance was detected 550 km above our heads by the gamma-ray space telescopes *Fermi* and *Agile*. I am not yet aware of it then, but this event will have a huge impact on the focus of my research, leading me to unexpected and unexplored territories. This feeling is still alive today. This memoir traces this journey, from the first semi-analytical models of particle acceleration in reconnection layers to today's global general relativistic radiative particle-in-cell (PIC) simulations of Kerr black-hole magnetospheres.

Part I gives the context I was in back then during my first postdoc which lead me to the field of computational plasma astrophysics, culminating with the creation of the `Zeltron` PIC code in the Summer 2012 and its first applications to relativistic reconnection in the context of the Crab Nebula gamma-ray flares. These developments turned out to be crucial for the understanding of particle acceleration in relativistic magnetospheres. This part also explains how I naturally arrived into this field. Part II dives deep into the main focus of this memoir with the first type of relativistic magnetospheres discussed here, which forms around pulsars. This new Chapter of my scientific life began in Princeton when I joined Prof. Anatoly Spitkovsky's group back in 2013 as a Lyman Spitzer Junior Postdoctoral Fellow joint with the Max Planck Princeton Center. I describe the first global ab-initio PIC models of pulsar magnetospheres, and how those have contributed to a better understanding or perhaps even solve some of the most outstanding mysteries in high-energy astrophysics, such as the origin of the gamma-ray pulsed emission and magnetic dissipation in pulsar winds. Part III describes a new exciting chapter opened in 2017, born from the vow passed in 2015 between Sasha Philippov, Kyle Parfrey and myself just before we all left Princeton, to produce the first PIC model of a black hole magnetosphere. I describe the significant new numerical developments performed in `Zeltron` to reach this objective, and the first global models in both 1D and 2D. We are still at the dawn of a promising exploitation of this code in the context of horizon-scale observations of supermassive black holes. This is the purpose of the ERC Consolidator grant SPAWN that I have been awarded at the end of 2019. In Part IV, I describe some of the main lines of investigation proposed in the SPAWN project for the period 2020-2025, and I conclude this memoir with some thoughts about exciting new possibilities beyond

this horizon.

Before proceeding, I would like to warmly thank my closest collaborators Guillaume Dubus, Dmitri Uzdensky, Gregory Werner, Mitch Begelman, Sasha Philippov, Anatoly Spitkovsky, Kyle Parfrey, Amir Levinson, Benjamin Crinquand, Claire Guépin, Kumiko Kotera, and Gwenael Giacinti for making me grow as a scientist.

As a final historical note, this memoir was initiated and partly written during the Great Quarantine period of March-May 2020.

Part I

Context

Chapter 1

Gamma-ray flares from the Crab Nebula

This chapter is based on a review article I wrote with a few other colleagues on the recent progress in observations and theoretical models of pulsar wind nebulae. This work was performed in the context of the ISSI working group "The Strongest Magnetic Fields in the Universe" as a book chapter published in Space Science Reviews (Kargaltsev et al. 2015). This chapter is also inspired from a paper published in the annual special issue of Physics of Plasmas based on an invited talk at the 55$^{\text{th}}$ American Physical Society Division of Plamas Physics annual meeting held in Denver, Colorado (Cerutti et al. 2014a). One may refer to the excellent review on this topic by Bühler & Blandford (2014) for more details.

1.1 The discovery

Between September 19-21, 2010, the unthinkable had happened: the Crab Nebula, the steady high-energy astrophysical source *par excellence* used as a standard candle for calibrating X-ray and gamma-ray instruments for decades, is in fact a bright emitter of short gamma ray flares above 100MeV (Tavani et al. 2011; Abdo et al. 2011). This event was captured by both gamma-ray space telescopes operating at the time, *Fermi* and *Agile*, which immediately convinced both teams that they were dealing with a real astrophysical phenomenon rather than an instrumental fluke. After this event, both collaborations looked back in time and realized that their instruments have already made this discovery. Ironically, the *Agile* team observed a first flare back in 2007 during the calibration phase of the instrument. The information is kept secret and the most probable scenario envisioned at the time is an instrumental effect. The *Fermi* satellite is launched a year later, and another flare in February 2009 is discovered a posteriori.

Today, after more than 10 years of continuous monitoring of the gamma-ray sky, 17 flares have been clearly identified (see Huang et al. 2020 for a recent accounting). Figure 1.1 shows the complete data set of the *Fermi*-LAT lightcurve of the Crab

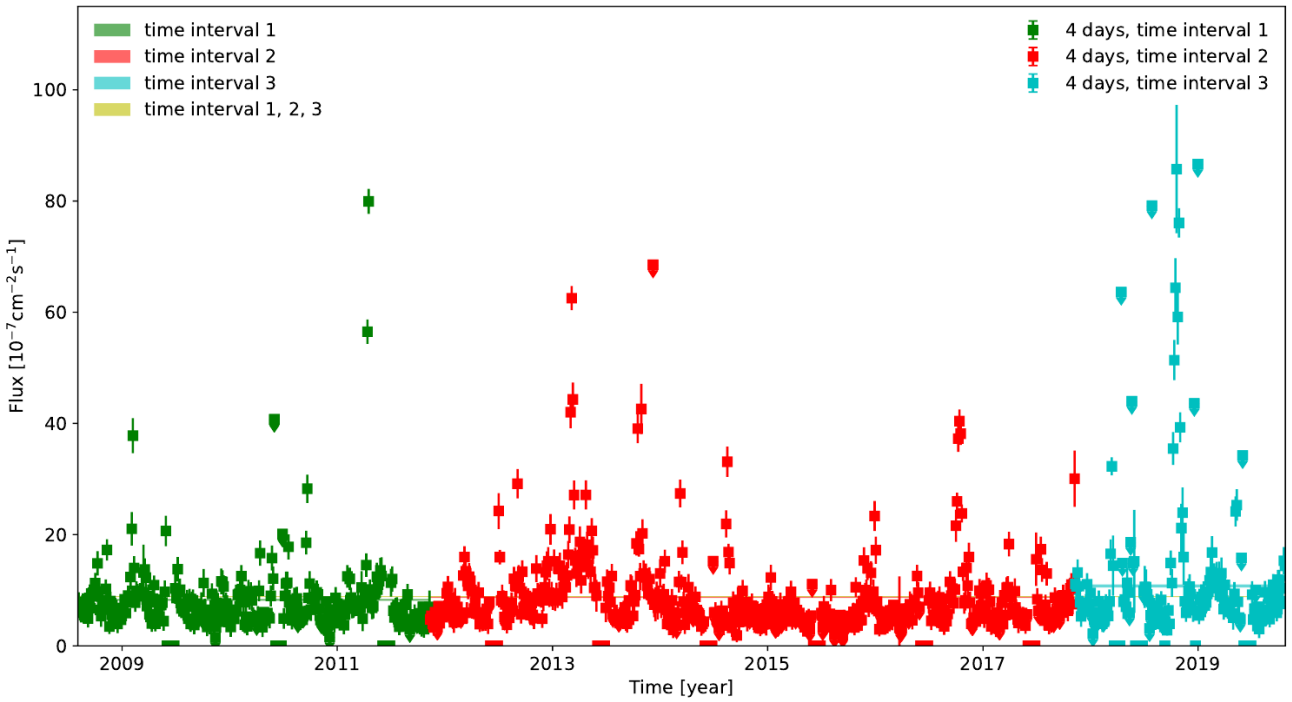

Figure 1.1: *Fermi*-LAT lightcurve above 100MeV of the Crab Nebula since the launch of the satellite in 2008. A 4-days binning is used in this figure taken from Huang et al. (2020).

Nebula. Outside of these spectacular events, identified as the "flares" where the flux goes well above the background, the gamma-ray lightcurve remains apparently restless with continuous small variations of the flux (Buehler et al. 2012; Striani et al. 2013), as if the engine never really switches off. One of the most extreme flare was detected in April 2011 during which the flux was multiplied by 30 over a period of about a week, representing nearly 1% of the total Crab pulsar spindown power (Buehler et al. 2012, Figure 1.2).

1.2 Implications

Now, why is this discovery so important? A closer look at the properties of the flares reveals a much richer and puzzling picture, showing that there is much more at stake here than the loss of a standard candle. First, the duration of the flare puts constraints on the size of the emitting region. For a typical 1-week long episode, and making the reasonable assumption that the emitting zone is causally connected, gives a source size $ct_{\rm flare} \sim 10^{16}$cm. This means that a volume equivalent to 10^6 times smaller than that of the Crab Nebula is outshining by 30 times the emission from the entire system. This constraints is even more stringent if one considers the intra-flare ultra-rapid variability (Balbo et al. 2011; Buehler et al. 2012; Mayer et al. 2013; Huang et al. 2020), which goes as short as $<$ 8-hours flux doubling time in the brightest events like the April 2011 superflare (Figure 1.2). Therefore, time-variability alone puts severe constraints on the energetic budget needed to power

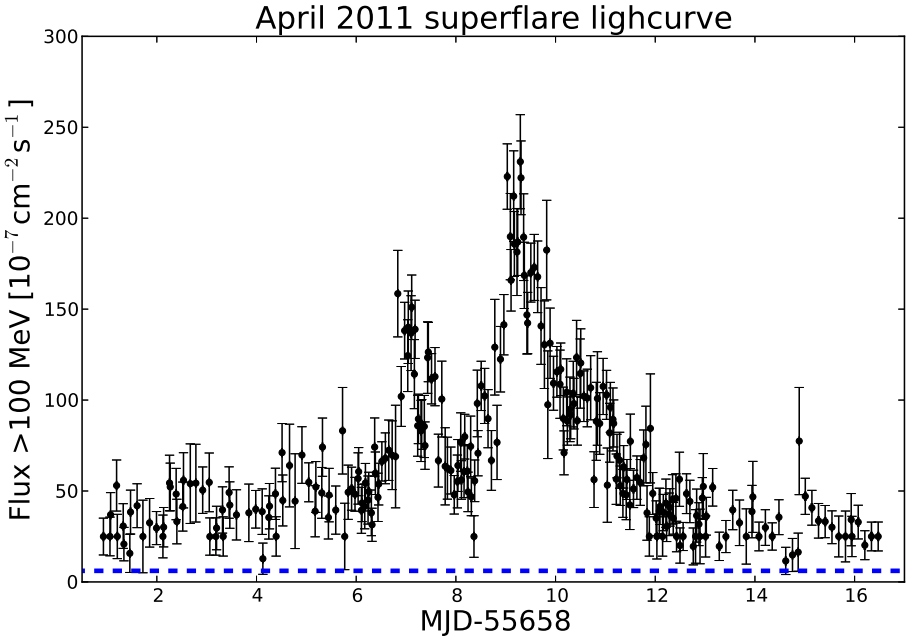

Figure 1.2: Zoomed-in view of the April 2011 superflare seen by the *Fermi*-LAT (Buehler et al. 2012). The horizontal blue dashed line shows the average, quiescent gamma-ray flux above 100 MeV.

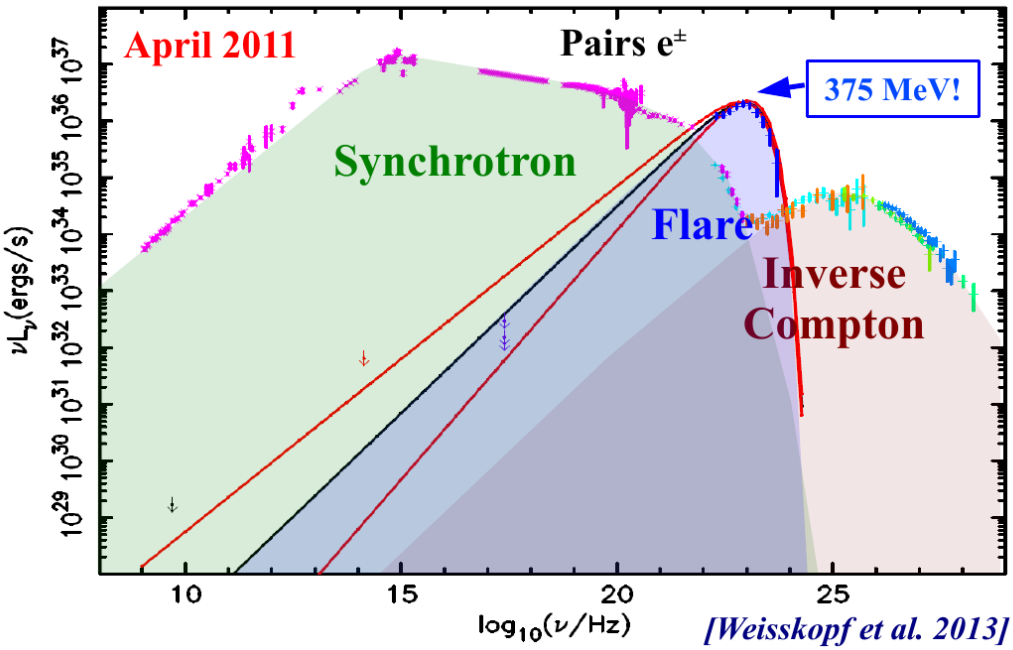

Figure 1.3: Broadband spectral energy distribution of the Crab Nebula. The quiescent emission is composed of a radio to gamma-ray synchrotron bump (green) along with an inverse Compton component in the TeV range (red). The April 2011 superflare spectrum (blue) sticks out above 100MeV without any other counterparts. Figure adapted from Weisskopf et al. (2013).

the flares. One may wonder, with good reason, whether such a compact region would not point towards the magnetosphere, but the flares do not seem connected with the pulsed emission produced there or with any other magnetospheric events like giant pulses or glitches.

Another very odd property of the flares is the lack of a counterpart at any other wavelength. Figure 1.3 shows the broadband spectral energy distribution averaged over the Crab Nebula. To a first order, it is usually interpreted in the context of a synchrotron-self Compton emission model (Atoyan & Aharonian 1996; Meyer et al. 2010). Electron-positrons pairs created within the pulsar magnetosphere escape in the form of a relativistic magnetic wind; they are randomized and re-accelerated at the wind termination shock radius. It follows a bright synchrotron emission in the nebula from radio to 100MeV. The inverse-Compton component takes over from 100MeV to about 100TeV. The flaring emission sticks out as an extra component at the end of the quiescent synchrotron component and peaking up to about 400MeV. It is consistent with a hard power-law with an exponential cut-off. The Crab Nebula cannot be resolved by *Fermi* or *Agile*, and therefore the hope quickly grew amongst observers that the location of the flare could be determined with a high precision at other wavelength, using radio, IR, optical and with X-rays observations where the nebula is well resolved. The morphology of the Crab Nebula is complex and rich of small scale features (e.g., knots, rings, anvil, etc...). In spite of a large coverage using the best telescopes, before, during and after the flares, nothing has been detected thus far. Figure 1.3 compiles the data of such an effort for the 2011 superflare (Weisskopf et al. 2013).

The particle spectrum emitting the flare must be very narrow in energy, perhaps even close to being monoenergetic. This is a strong argument against particle acceleration via diffusive-shock acceleration, which predicts steep and broad power-law distributions. Another strong argument against this scenario is again coming from the flare duration. The only viable radiative process which can possibly emit these photons in this band over this short period of time and in this environment is synchrotron radiation. Other processes such as bremsstrahlung or inverse Compton are far too inefficient and/or too slow in comparison. Incidentally, the inverse Compton component above 100GeV remained unchanged during the flare (H. E. S. S. Collaboration et al. 2014; Aliu et al. 2014). The synchrotron cooling time is given by

$$t_{\rm sync} = -\frac{\gamma m_{\rm e} c^2}{P_{\rm sync}} = \frac{9 m_{\rm e} c}{4 r_{\rm e}^2 B^2 \gamma} \approx 9\ B_{\rm mG}^{-2} \gamma_9^{-1}\ \text{days}, \tag{1.1}$$

where $m_{\rm e}$ is the electron rest mass, c is the speed of light, $r_{\rm e}$ is the classical radius of the electron, $B = B_{\rm mG}$ mG is the ambiant magnetic field strength and $\gamma = 10^9 \gamma_9$ is the electron Lorentz factor. Therefore, the flares can be emitted by PeV (10^{15}eV) electrons immersed in a milliGauss magnetic field, much stronger than the usual few 100 μG usually estimated from spectral fitting (e.g., Meyer et al. 2010). It was already known that the Crab Nebula accelerates particles up to PeV energies

(e.g., de Jager & Harding 1992). What is new, however, is the evidence that such particles are accelerated over such a short timescale. The gyration time of the PeV particles is

$$t_{\rm L} = \frac{\gamma m_{\rm e} c}{eB} \approx 16\ \gamma_9 B_{\rm mG}^{-1}\ \text{hours}, \tag{1.2}$$

i.e., of order the shortest variability timescale. Hence, the particles must be accelerated over a sub-Larmor timescale, i.e., the acceleration process must be extremely efficient. It also implies that when a flare is observed the acceleration mechanism is turned on. Diffuse shock-acceleration is not adequate because it operates over multiple gyrations of the particles moving back and forth through the shock front. Recent PIC simulations of relativistic collisionless shocks indicates that the particle energy increases as the square-root of time which is far too slow to explain the flare (Sironi et al. 2013; Plotnikov et al. 2018). In addition, diffusive shock acceleration do not operate in pulsar wind nebula because the plasma magnetization is most likely too high, but this is another story.

1.3 The synchrotron burnoff limit and the 160MeV barrier

The last, and arguably the most astonishing feature of the flare is the emission of synchrotron photons with energies above what is known as the synchrotron burnoff limit (Guilbert et al. 1983; de Jager et al. 1996). Consider a uniform medium where an electron is accelerated by a constant electric field such that the force applied to the electron is $F_{\rm E} = eE$. As the particle energy increases, the synchrotron energy losses grow as $\propto \gamma^2$. In reaction to the emission of synchrotron photons, a force opposite to the particle's velocity direction applies to the electron. In the context of classical electrodynamics, this force can be approximately expressed as (see next chapter for a more detailed discussion and derivation, Sect. 2.7)

$$F_{\rm rad} \approx -\frac{2}{3} r_{\rm e}^2 \gamma^2 B_\perp^2, \tag{1.3}$$

where $B_\perp$ is the magnetic field strength perpendicular to the particle's direction of motion. The radiation reaction force balances the electric force, $F_{\rm rad} = F_{\rm E}$, for $\gamma = \gamma_{\rm rad}$, where

$$\gamma_{\rm rad} = \sqrt{\frac{3eE}{2r_{\rm e}^2 B_\perp^2}}. \tag{1.4}$$

The corresponding synchrotron photon energy is

$$\epsilon_{\rm rad} = \frac{3\hbar e}{2m_{\rm e}c} B_\perp \gamma_{\rm rad}^2 = \frac{9}{4}\frac{m_{\rm e}c^2}{\alpha_{\rm F}}\left(\frac{E}{B_\perp}\right) \approx 160\left(\frac{E}{B_\perp}\right)\ \text{MeV}, \tag{1.5}$$

where $\alpha_{\rm F} = e^2/\hbar c \approx 1/137$ is the fine structure constant. Another way to interpret this limit is that a particle with such an energy would radiate away its energy over

a cyclotron turn. Therefore, under the usual astrophysical regime where ideal MHD applies, i.e., with $E < B_\perp$, we should not expect synchrotron radiation of energy above 100MeV and the quiescent emission spectrum of the Crab Nebula is indeed limited by the burnoff limit (de Jager et al. 1996; Abdo et al. 2010a). Yet, the spectral energy distribution systematically extends well above this limit and even peaks at about 400MeV in the most extreme flares (Figure 1.3). This implies either that the flaring region is moving relativistically towards the observer with a velocity $v > 0.9c$, or that the ideal MHD condition breaks down such that $E > 2 - 3B_\perp$.

To summarize, the discovery of the gamma-ray flares in the Crab Nebula calls for a revisit of the classical theory of particle acceleration in this environment, and perhaps also in other relativistic outflows as found in gamma-ray bursts and black hole jets. Diffusive-shock acceleration accumulates difficulties, a more impulsive acceleration mechanism seems preferable. The following section briefly discusses some of the scenario envisioned in the community, with an emphasis on my contribution.

1.4 Proposed models

We should first note that the estimates and constraints (e.g., energetic, size) derived above from observations are quite conservative, in a sense that the effect of beaming (geometrical or relativistic), spatial and/or temporal inhomogeneities were ignored. Models proposed so far are taking advantage of one or more of these effects to alleviate the tight constraints imposed by the flares. For instance, one feature commonly invoked in models is a strong inhomogeneity of the flaring region, in particular in the magnetic field structure. Bykov et al. (2012) proposed that the flares occur around the equatorial belt of the nebula where the abrupt dissipation of the striped pulsar wind at the shock may accelerate particles (Lyubarsky 2003; Pétri & Lyubarsky 2007; Sironi & Spitkovsky 2011) and generates strong magnetic turbulence. In this context, the fluctuating nature of the magnetic field can generate a strongly polarized, intermittent gamma-ray signal most pronounced at the high-energy synchrotron cut-off. To this end, however, the field must vary over a timescale shorter than the synchrotron cooling time of the particles, which is determined only by the mean value of the field. In their model, the observed gamma-ray variability would reflect the properties of the magnetic turbulence.

In the extreme turbulent regime where the coherence length-scale of the magnetic field, λ_B, is significantly smaller than the formation length of synchrotron photons, i.e., $l_{\rm sync} = m_{\rm e}c^2/eB \gg \lambda_B$, then the particles emit in the jitter regime rather than the classical synchrotron radiation regime (Medvedev 2000). While the cooling rate remains unchanged, the critical photon energy is boosted by a factor $\epsilon_{\rm jitter}/\epsilon_{\rm sync} \sim l_{\rm sync}/\lambda_B > 1$, and therefore the $>$ 100MeV flare emission could then be emitted by particles below the radiation reaction limit (Teraki & Takahara

2013). Another by-product is the hardening of the emission spectrum, changing from $F_\nu \propto \nu^{1/3}$ in the synchrotron regime to $F_\nu \propto \nu$ for a monoenergetic population of particles although the current upper limits in radio, IR anf X-rays are still compatible with the synchrotron spectrum (Weisskopf et al. 2013). Perhaps the most challenging issue with this scenario is how to generate magnetic turbulence to such small sub-Larmor scales. For instance, this regime cannot be achieved even within Weibel magnetic turbulence generated at the skindepth scale in relativistic shocks (Sironi & Spitkovsky 2009).

As mentioned earlier, an easy way out of this is to consider a relativistic bulk outflow within the flaring region, such that the radiation-reaction-limited synchrotron photons < 100MeV in the co-moving frame are Doppler boosted to higher energies in the observer's frame (Bednarek & Idec 2011; Yuan et al. 2011; Komissarov & Lyutikov 2011; Lyutikov et al. 2012; Clausen-Brown & Lyutikov 2012). A modest Lorentz factor would do, $\Gamma > 2$. Doppler beaming would also alleviate some of the energetic , size and duration constraints of the flares. The same argument is used in the context of rapid flares in blazars. This simple solution seems to solve many problems at once, but a direct evidence for such relativistic outflows in the Crab Nebula is still missing. At most, the flow velocity reaches above half the speed of light (Hester 2008). This being said, theoretically, a weak shock at the pulsar wind termination could easily result in a faster flow (Kennel & Coroniti 1984). It is reasonable to conceive this configuration at the polar regions of the nebula where the pulsar wind is more magnetized and the shock oblique (Lyubarsky 2012; Komissarov 2013). One region of particular interest is the so-called "inner knot", a bright compact feature near the pulsar (Hester et al. 1995) interpreted as the location where the downstream flow of the oblique shock points towards the observer, magnified by Doppler beaming (Komissarov & Lyubarsky 2003; Komissarov & Lyutikov 2011). Here again, in spite of a huge observational effort, no correlation was seen between the knot and the gamma-ray flares (Tavani et al. 2011; Lobanov et al. 2011; Weisskopf et al. 2013; Rudy et al. 2015), at odds with what the model predicts.

1.5 The magnetic reconnection scenario

The alternative scenario I have been working on shortly after my arrival in Boulder is that the flares are powered by a magnetic reconnection event. The idea was imagined by Dmitri Uzdensky, who made the simple observation that a reconnection site is a region where the non-ideal MHD approximation breaks down, and therefore where the electric field could locally exceed the magnetic field, $E > B$, leading to particle acceleration above the synchrotron burnoff limit (Uzdensky et al. 2011). We realized afterwards that this argument was already proposed by Kirk (2004) and Contopoulos (2007), well before the discovery of the flares.

In the classical Sweet-Parker reconnection site (Sweet 1958; Parker 1957), the

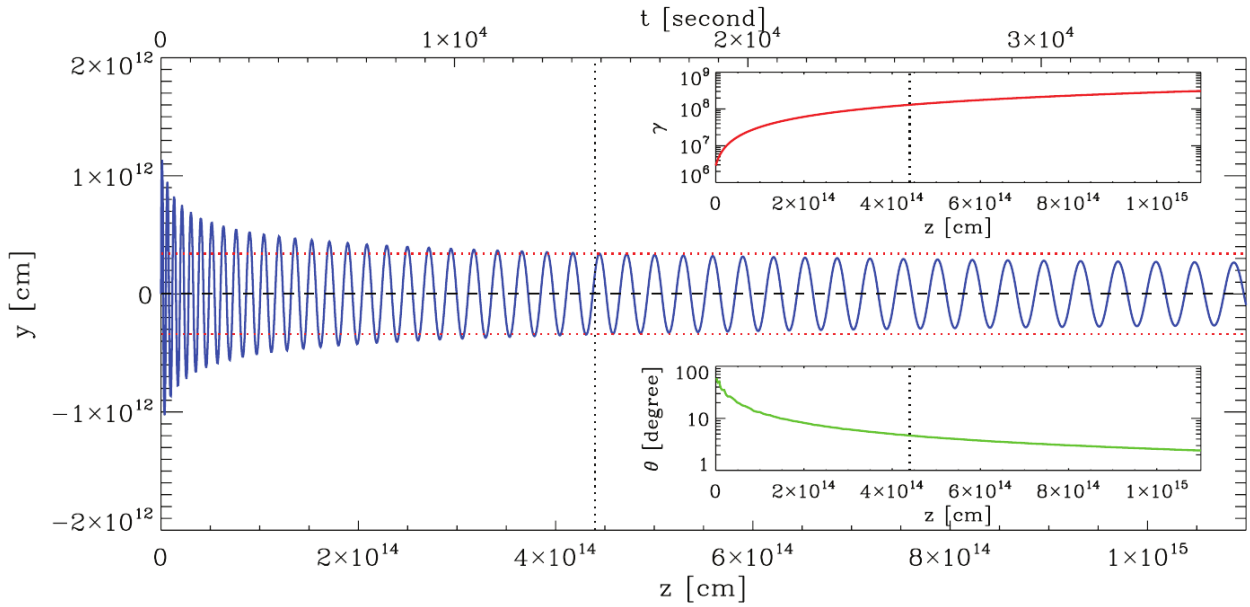

Figure 1.4: Example of a test particle trajectory (blue line) numerically integrated in the vicinity of a symmetric plane-parallel reconnection current sheet whose thickness is shown by the red dotted lines. The inset plots shows the evolution of the particle Lorentz factor and velocity pitch angle with respect to the y-axis. Figure taken from Uzdensky et al. (2011).

magnetic field reverses sign over a small diffusion layer of thickness δ, or simply referred to as the reconnection layer or the current sheet in the following. By symmetry, the field must decrease within the layer and even vanish at its center. An electric field and current localized in the layer must also flow to sustain the sharp gradient of the magnetic field. In principle, a particle trapped deep inside a reconnection layer could be linearly accelerated to arbitrary large energies with virtually no synchrotron losses. At best, a particle is trapped over the full length of the layer, L, limiting the particle energy to $E_{\max} = eEL$.

The first question I have been investigating was whether particles could be trapped long enough in the sheet to overcome the burnoff limit. Using a test-particle approach with static prescribed magnetic and electric fields, and the radiation-reaction force turned on, I showed that particles were naturally trapped by the layer (Uzdensky et al. 2011; Cerutti et al. 2012a). Their trajectories have the peculiar property to be composed of a succession of a fraction of a Larmor circular motion which flips direction each time the particle crosses the midplane due to the change of sign of the magnetic field, leading to a sine-like trajectory instead of the usual Larmor gyromotion (see Figure 1.4). These trajectories are the relativistic analog of the well-known Speiser orbits in space physics (Speiser 1965).

Another odd, but important property of these trajectories is that the amplitude of the particle motion transverse to the sheet decreases as the particle energy grows. In other words, the particle becomes more confined within the sheet as it accelerates, and as a consequence of this the particle probes an ever smaller

effective magnetic field reducing even more synchrotron losses. This behavior can be understood as the effect of a $\mathbf{E} \times \mathbf{B}$ drift motion, which pushes the particles towards the midplane. The model therefore predicts a strong anisotropy of the particle and photon distributions, the higher the energy the higher the anisotropy.

At this point, we were aware that these conclusions were drawn upon a very naive model of a reconnection site. Current sheets are known to be bursty and prone to several plasma instabilities, and thus it was unclear whether this scenario would still hold under more realistic physical conditions. Therefore, the only way to make progress and develop further our model for the Crab flares in this extreme, yet unexplored regime of particle acceleration was to use more sophisticated and ab-initio numerical methods, which naturally lead me to PIC simulations.

Chapter 2

Birth of the Zeltron PIC code

Being in a laboratory filled with plasma physicists (the Center for Integrated Plasma Studies, CIPS) gave me the opportunity to meet specialists of plasma simulations. My encounter with Greg Werner was particularly fortunate and crucial for what follows. At the time, I had no experience as a developer or not even as a user in plasma simulations. Being a specialist of electromagnetic and PIC simulations for his own research, Greg taught me the basics of the numerical methods and algorithms and a collaboration naturally began between us. A PIC code was even available at CIPS, the VSim code[1], a commercial product under license co-developed between the University of Colorado and Tech-X corporation, but it became quickly clear for various reasons that its use would not be well adapted for my needs. One important reason is that I needed to implement new capabilities that regular PIC codes did not have at the time: radiation and the radiation-reaction force. Having no access to the source code was therefore not an option. I ended up writing my own PIC code from scratch during the academic summer break in 2012, which later became the `Zeltron` code. Since I was not (and still not!) a computer scientist nor a HPC specialist, the spirit was to create a simple and robust code that could be easily handled by other users, but also a code that I could adapt rapidly to my research needs and interests. This spirit is still alive today.

In this chapter, I give a brief overview of the main numerical methods used in explicit, relativistic electromagnetic PIC code as in `Zeltron` , with an emphasis on the implementation of the radiation reaction force. Here, I focus on the publicly available Cartesian grid version, more recent developments involving spherical and more generally curvilinear grids will be described later in this memoir. This chapter is partially based on a review paper published in the book "Modelling Nebulae" edited by Diego Torres, that I wrote with my colleague from Columbia University Lorenzo Sironi (Sironi & Cerutti 2017), but also on my lectures notes and hands-on sessions prepared for the Astrosim doctoral school held in Lyon (2017) and in Montpellier (2020). Many of the material presented here is also described in a more comprehensive way in Birdsall & Langdon (1991), the "holy book" for the

[1] https://www.txcorp.com/vsim

PIC addicts like me.

2.1 Relativistic plasmas under the PICoscope

The particle-in-cell method was first developed by plasma physicists back in the sixties, but it is only in the last two decades or so and with the rise of supercomputers that it became an increasingly essential tool for theoretical high-energy astrophysics. PIC simulations led to ground-breaking discoveries in the field, such as first evidence of particle acceleration in collisionless shocks (Spitkovsky 2008), relativistic reconnection (Zenitani & Hoshino 2001, next chapter), kinetic turbulence (Zhdankin et al. 2017), pulsar magnetospheres (Part II) and spinning black hole magnetospheres (Part III). The PIC approach consists of describing a plasma ab-initio, i.e., from its most fundamental components: discrete charged particles (e.g., electrons, ions) evolving in time-dependent electromagnetic fields. The main purpose of the PIC method is to capture microscopic plasma processes, i.e., at the plasma skindepth and sub-Larmor radius scales, or simply referred below to as the "kinetic" scale. As we will see in the next chapter, these microscopic scales are involved in particle acceleration processes and, thus, they must be well resolved by simulations. In constrast, the MHD approach, more widely used in the astrophysical community, is valid on the large plasma scales and assumes the Larmor radius scale to be infinitely small and therefore ignores the microphysics. In this sense, the PIC and the MHD approaches are complementary and cannot address the same questions. This being said, PIC simulations must also capture large scale features, i.e., system size and long integration time to obtain meaningful astrophysical results, which makes PIC simulations particularly challenging to carry out and computationally expansive.

2.2 Collisionless plasmas

A necessary condition for non-thermal particle acceleration is the absence of Coulomb collision in the plasma of interest. This is the case for most high-energy astrophysical systems, and in particular pulsar wind nebulae, where plasmas are very diluted. Roughly speaking, a plasma can be considered as "collisionless" if the frequency of Coulomb collision (ν) is much smaller than the plasma frequency, $\omega_{\rm pe} \gg \nu$. This condition implies that the number of particles per Debye sphere must be large, i.e., $N_{\rm D} \gg 1$. The dynamics of individual particle is driven by collective plasma phenomena rather than binary collisions at the sub-Debye length and plasma frequency scales.

The evolution of a collisionless plasma is governed by the Vlasov equation

$$\frac{\partial f}{\partial t} + \frac{\mathbf{p}}{\gamma m} \cdot \frac{\partial f}{\partial \mathbf{r}} + q\left(\mathbf{E} + \frac{\mathbf{v}\times\mathbf{B}}{c}\right) \cdot \frac{\partial f}{\partial \mathbf{p}} = 0, \tag{2.1}$$

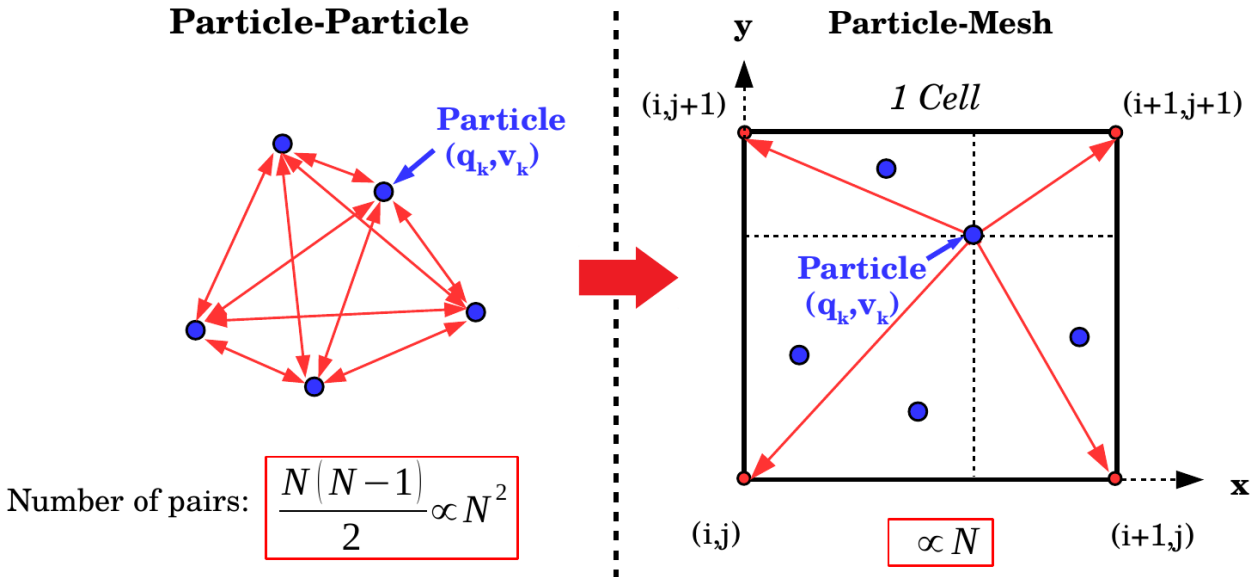

Figure 2.1: Particle-particle versus particle-mesh interaction.

where $f \equiv d\mathrm{N}/d\mathbf{r}d\mathbf{p}$ is the particle distribution function defined in the 6D phase space $(\mathbf{r}, \mathbf{p})$ and 1D in time, where $\mathbf{r}$ is the position and $\mathbf{p} = \gamma m\mathbf{v}$ is the momentum, and q is the electric charge. Along with Maxwell's equations for the fields ($\mathbf{E}$ and $\mathbf{B}$), this is a closed set of equations to model a collisionless plasma from first principles.

2.3 The particle approach

Analytical solutions to the Vlasov equation are known for a few idealized situations only. In most cases, it must be solved numerically. They are at least two ways to solve this equation. In the first approach, phase space is treated as a continuous fluid and Vlasov equation is solved directly using semi-Lagrangian or Eulerian methods (Cheng & Knorr 1976; Elkina & Büchner 2006). This approach has the advantage to be insensitive to particle noise, and hence can capture well weak plasma phenomena and broad particle distribution functions. In theory, this is the most appropriate approach to follow, but in practice the use of Vlasov codes is currently limited due to prohibitive numerical costs for multidimensional problems (6D phase space +1D for time).

In PIC, Vlasov equation is solved indirectly by integrating discrete particle trajectories. This approach is equivalent to the direct method. An easy way to see this is to rewrite Vlasov equation as a usual advection equation: $\partial f/\partial t + \boldsymbol{\nabla}_{\mathbf{r},\mathbf{p}} \cdot (f\mathbf{U}) = \mathbf{0}$, where $\boldsymbol{\nabla}_{\mathbf{r},\mathbf{p}} = (\partial/\partial\mathbf{r}, \partial/\partial\mathbf{p})$ and $\mathbf{U} = (\mathbf{p}/\gamma m, q\,(\mathbf{E} + \mathbf{v} \times \mathbf{B}/c))$. Thus, using the methods of characteristics, this first-order partial differential equation can be rewritten as a sets of ordinary differential equations (Newton's law) along characteristic curves which corresponds here to particle trajectories. For point-like

particles, the particle distribution function is then approximated as

$$f(\mathbf{r}, \mathbf{p}, t) \approx \sum_{k=1}^{N} \delta(\mathbf{r} - \mathbf{r}_k(t)) \, \delta(\mathbf{p} - \mathbf{p}_k(t)), \tag{2.2}$$

where δ is the Dirac delta function, and N is the total number of particles. The number of particles must be very high for a good sampling of phase space and to be close to the exact solution of Vlasov equation. In practice, however, this number will be limited by computing resources and is always much smaller than the number of particles contained in real plasmas. To overcome this difficulty, a PIC particle represents a large number of physical particles that would follow the same trajectory in phase space (with the same q/m ratio). For this reason, the simulation particles are usually called "macroparticles" or "superparticles". The number of physical particles the macroparticle k represents is given by a weight, w_k.

Even though the plasma is collisionless, particles feels each other via long-range interactions. Summing over all particle-particle binary interactions, i.e. $N(N-1)/2 \approx N^2$, is numerically expansive and hard to implement (e.g., propagation effects, global communications in the parallelization of the code). Instead, in PIC, particles do not feel each other directly but via the electromagnetic fields known on the grid which result from the plasma evolution. In this case, the number of operations scales as the number of particles N instead of N^2, which is numerically much more manageable (Figure 2.1). PIC codes are much cheaper in comparison to Vlasov codes, and they are also conceptually simple, robust and easy to implement and parallelize efficiently to a large number of cores. This simplicity comes at the cost of significant particle noise which can lead to poor sampling of the particle distribution (e.g., steep power-law tails), difficulty in capturing subtle or weak phenomena, artificial collisions, and load-balancing issues in parallel computing.

2.4 Main computing procedures in PIC

Figure 2.2 describes the three main operations performed per timestep Δt of an explicit PIC code like `Zeltron` : (i) Solve Newton's equation for each particle to evolve velocities and positions (ii) Collect charge and current densities from all particles and deposit them on the grid, and (iii) Solve Maxwell's equations to update the fields on the grid. In this way, particle motion and electromagnetic fields evolve in a self-consistent manner. Below is a brief technical description of each step:

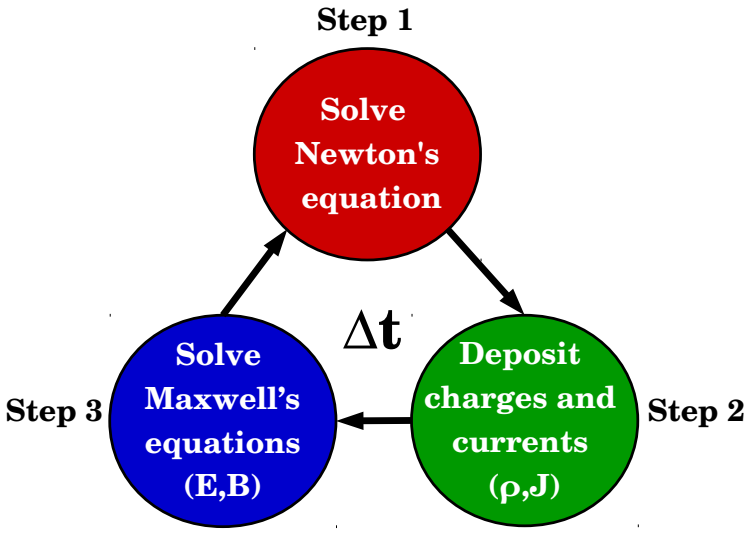

Figure 2.2: Computation procedure per time step Δt in PIC.

Step 1: Particle push

For a pure electromagnetic model, the set of equations to solve are

$$\frac{d\mathbf{u}}{dt} = \frac{q}{m_e c}\left(\mathbf{E} + \frac{\mathbf{u}\times\mathbf{B}}{\gamma}\right) \tag{2.3}$$

$$\frac{d\mathbf{r}}{dt} = \frac{c\mathbf{u}}{\gamma}, \tag{2.4}$$

where $\mathbf{u} = \gamma\mathbf{v}/c$ is the particle 4-velocity vector divided by the speed of light and $\gamma = 1/\sqrt{1-(v/c)^2}$ is the Lorentz factor. One of the most successful and most common method used in PIC to solve Newton's equation is the Boris push (Birdsall & Langdon 1991). It has all the desirable numerical features one might think of: it is fast, stable and second order accurate, conserves well the particle energy and phase space volume (Qin et al. 2013). The algorithm is based on the usual leapfrog integration scheme, i.e., 4-velocities $\mathbf{u}$ and positions $\mathbf{r}$ are staggered in time by half a timestep (Figure 2.3). If particle positions and fields are known at time t^n ($\mathbf{r}^n$, $\mathbf{E}^n$, $\mathbf{B}^n$) and velocities at time $t^{n-1/2}$ ($\mathbf{u}^{n+1/2}$), the finite-difference time-centered expression of Eq. (2.3) is

$$\frac{\mathbf{u}^{n+1/2} - \mathbf{u}^{n-1/2}}{\Delta t} = \frac{q\mathbf{E}^n}{m_e c} + \frac{q}{m_e c}\left(\frac{\mathbf{u}^n \times \mathbf{B}^n}{\gamma^n}\right). \tag{2.5}$$

Now, the trick is to rewrite $\mathbf{u}^n$ appearing on the right-hand side of the equation as $\mathbf{u}^n = \left(\mathbf{u}^{n-1/2} + \mathbf{u}^{n+1/2}\right)/2$. Assuming that $\mathbf{E}^n$ and $\mathbf{B}^n$ are known, $\mathbf{u}^{n+1/2}$ can be extracted. To this end, it is convenient to define the following intermediate

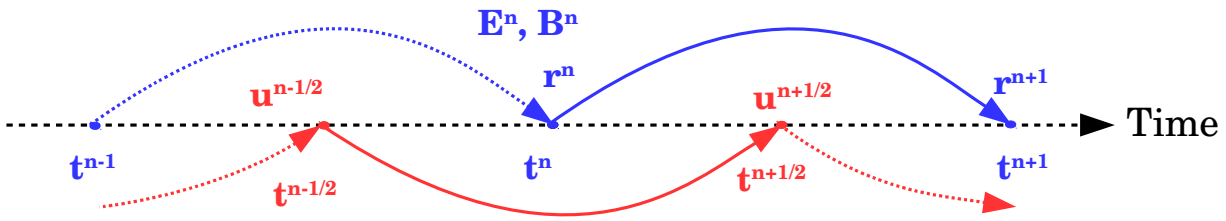

Figure 2.3: The leapfrog scheme of the Boris method to solve Newton's equation.

variables

$$\mathbf{u}^- = \mathbf{u}^{n-1/2} + \frac{q\Delta t \mathbf{E}^n}{2m_e c} \tag{2.6}$$

$$\mathbf{u}^+ = \mathbf{u}^{n+1/2} - \frac{q\Delta t \mathbf{E}^n}{2m_e c}. \tag{2.7}$$

Then, using Eqs. (2.6)-(2.7) and after a few algebraic manipulations, one finds

$$\mathbf{u}^+ = \mathbf{u}^- + \mathbf{u}^- \times \mathbf{s} + \left(\mathbf{u}^- \times \mathbf{w}\right) \times \mathbf{s}, \tag{2.8}$$

where

$$\mathbf{w} = \frac{q\Delta t \mathbf{B}^n}{2m_e c\gamma^n}, \quad \mathbf{s} = \frac{2\mathbf{w}}{1+\mathbf{w}^2}, \quad \gamma^n = \sqrt{1+(\mathbf{u}^-)^2}. \tag{2.9}$$

Physically, the Boris push can be seen as a decomposition of the Lorentz force in three separate steps, (1) half-acceleration by the electric field (Eq. 2.6), (2) a pure rotation by the magnetic force (Eq. 2.8), and (3) another half-acceleration by the electric force (Eq. 2.7). It is important to notice that the fields appearing in these equations are those felt at the particle position, not at the grid point where the fields are known. The fields must be interpolated to the particle positions. A linear interpolation scheme is usually sufficient and this is what is done in `Zeltron` . The final step is to update the particle positions

$$\mathbf{r}^{n+1} = \mathbf{r}^n + c\Delta t \frac{\mathbf{u}^{n+1/2}}{\gamma^{n+1/2}}, \tag{2.10}$$

where $\gamma^{n+1/2} = \sqrt{1+\left(\mathbf{u}^{n+1/2}\right)^2}$.

For completeness, other efficient methods exist in the literature like the Vay (2008) or the Higuera & Cary (2017) pushers or even fully implicit schemes (Ripperda et al. 2018). These particle pushers can sometimes be more accurate than the Boris push depending on the physical problem (e.g., whether there is a strong drift, gradients). For a comprehensive comparison between different schemes, see Ripperda et al. (2018). The Boris and the Vay pushers have been implemented in `Zeltron` .

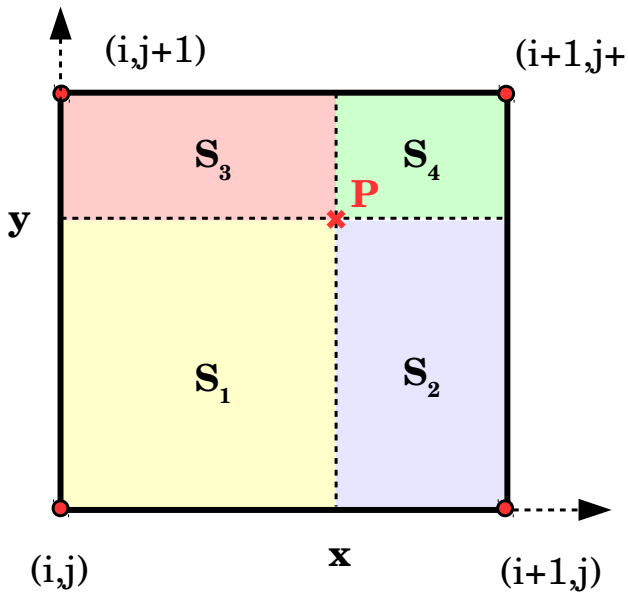

Figure 2.4: The area-weighting technique to interpolate fields or deposit charges and currents onto a 2D Cartesian cell (x_i, y_i) for a particle located in $P(x, y)$. The contribution to node (i, j) is given by S_4/S_{tot}, to $(i+1, j)$ is S_3/S_{tot}, to $(i, j+1)$ is S_2/S_{tot} and to $(i+1, j+1)$ is S_1/S_{tot}.

Step 2: Charge and current deposition

To evolve the fields, we need the source terms in Maxwell's equations ρ and $\mathbf{J}$ that are given by the particles. In a continuous space, these macroscopic quantities can be recovered by summing over the contribution from all particles

$$\rho(\mathbf{r}) = \sum_{k=1}^{N} q_k w_k \delta(\mathbf{r} - \mathbf{r}_k), \quad \mathbf{J}(\mathbf{r}) = \sum_{k=1}^{N} q_k w_k \mathbf{v}_k \delta(\mathbf{r} - \mathbf{r}_k), \tag{2.11}$$

where q_k, $\mathbf{v}_k$ are respectively the electric charge and the 3-velocity of the particle k. In PIC, charges and currents from the particles must be collected and dispatched among the nearest grid points. Charge and current densities at the grid point $\mathbf{r}_i$ can be written as

$$\rho(\mathbf{r}_i) = \sum_{k=1}^{N} q_k w_k S(\mathbf{r}_i - \mathbf{r}_k), \quad \mathbf{J}(\mathbf{r}_i) = \sum_{k=1}^{N} q_k w_k \mathbf{v}_k S(\mathbf{r}_i - \mathbf{r}_k), \tag{2.12}$$

where S is a shape function which depends on the desired deposition scheme. Even though the particles are point-like, they have a virtual size that is effective through the deposition of currents on the grid.

In the spirit of keeping things simple and robust in `Zeltron`, we use a first order deposition scheme identical to the interpolation procedure used for computing the fields felt by the particles. It is important to keep the same scheme for deposition and interpolation to avoid numerical effects like self-force, which could lead for instance to spurious particle acceleration (Birdsall & Langdon 1991). Figure 2.4

shows the example of a first order linear deposition scheme in a 2D Cartesian grid cell (or area-weighting method). The contributions from all the particles contained in the cell (x_i, y_j) to the current $\mathbf{J}$ are given by

$$\mathbf{J}_{i,j} = \sum_{k=1}^{N_{\text{cell}}} q_k w_k \mathbf{v}_k \left(1 - a_k\right)\left(1 - b_k\right) \tag{2.13}$$

$$\mathbf{J}_{i+1,j} = \sum_{k=1}^{N_{\text{cell}}} q_k w_k \mathbf{v}_k a_k \left(1 - b_k\right) \tag{2.14}$$

$$\mathbf{J}_{i,j+1} = \sum_{k=1}^{N_{\text{cell}}} q_k w_k \mathbf{v}_k \left(1 - a_k\right) b_k \tag{2.15}$$

$$\mathbf{J}_{i+1,j+1} = \sum_{k=1}^{N_{\text{cell}}} q_k w_k \mathbf{v}_k a_k b_k, \tag{2.16}$$

where

$$a_k = \frac{x_k - x_i}{x_{i+1} - x_i}, \quad b_k = \frac{y_k - y_j}{y_{j+1} - y_j} \tag{2.17}$$

are the usual bilinear interpolation coefficients.

Step 3: Fields evolution

The last step is to update the fields on the grid. Knowing the current density as well as the fields at the previous time step, we just need to solve Maxwell-Faraday and Maxwell-Ampère equations,

$$\frac{\partial \mathbf{E}}{\partial t} = c\boldsymbol{\nabla} \times \mathbf{B} - 4\pi\mathbf{J} \tag{2.18}$$

$$\frac{\partial \mathbf{B}}{\partial t} = -c\boldsymbol{\nabla} \times \mathbf{E}. \tag{2.19}$$

In `Zeltron` , we use what is by far the most successful explicit numerical scheme to solve the time-dependent Maxwell's equations known as the finite difference time domain (FDTD) method proposed by Yee (1966). Like the Boris push, the FDTD method combines stability, efficiency and second-order accuracy (here in both space and time). To achieve this, fields must be staggered in time and in space. Figure 2.5 shows the order in time (top panel), as well as the spatial configuration of the fields within a Cartesian cell in 2D (bottom-left panel) and in 3D (bottom-right panel). For illustrative purposes, within this framework the z-component of Eq. (2.19) is

$$\frac{(B_{\text{z}})^{n+1/2}_{i+1/2,j+1/2,k} - (B_{\text{z}})^{n-1/2}_{i+1/2,j+1/2,k}}{\Delta t} = -c\frac{(E_{\text{y}})^{n}_{i+1,j+1/2,k} - (E_{\text{y}})^{n}_{i,j+1/2,k}}{\Delta x} + c\frac{(E_{\text{x}})^{n}_{i+1/2,j+1,k} - (E_{\text{x}})^{n}_{i+1/2,j,k}}{\Delta y}, \tag{2.20}$$

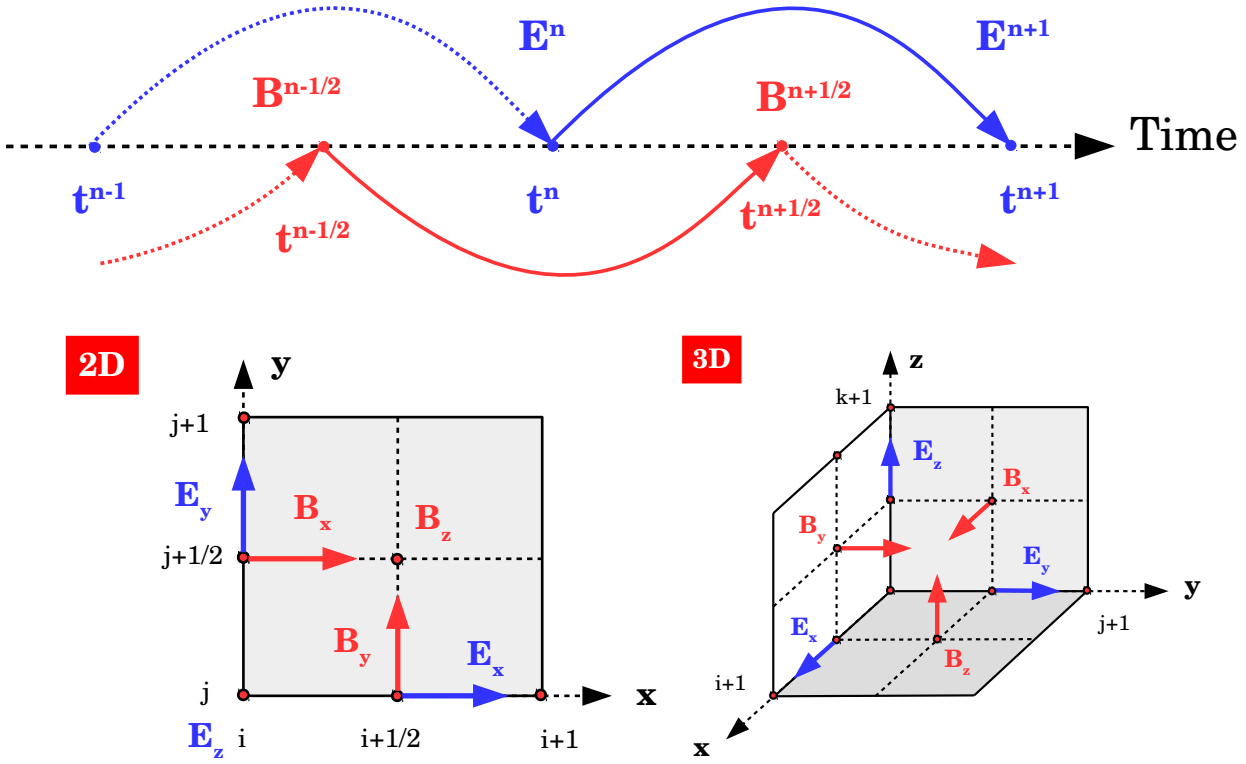

Figure 2.5: Top: Leapfrog scheme for the fields in time. Bottom: Staggered mesh proposed by Yee (1966) in 2D (left) and in 3D (right).

where Δx, Δy are the spatial step size along x and y, Δt is the time step, and where the integer indices (i, j, k) give the coordinates of the cell in the x- y- and z- directions respectively. In essence, the Yee algorithm solves the integral form of Maxwell's equations at the scale of a cell

$$\frac{\partial}{\partial t} \iint \mathbf{B} \cdot \mathbf{dS}_{\text{cell}} = -c \oint \mathbf{E} \cdot \mathbf{dl}_{\text{cell}}. \tag{2.21}$$

For instance, the way to interpret Eq. (2.20) is the flux of B_z centered on the cell face, which is equal to the contour line integral of the electric field whose components are centered on the edges of the cell face. As we will see in Part II and Part III, it is important to keep this in mind for generalizing the scheme to non-Cartesian lattices. The FDTD method is stable under the usual Courant-Friedrichs-Lewy (CFL) condition, i.e.,

$$\begin{aligned} \left(\frac{c\Delta t}{\Delta x}\right)^2 &< 1 \text{ (1D)}, \\ (c\Delta t)^2 \left(\frac{1}{\Delta x^2} + \frac{1}{\Delta y^2}\right) &< 1 \text{ (2D)}, \\ (c\Delta t)^2 \left(\frac{1}{\Delta x^2} + \frac{1}{\Delta y^2} + \frac{1}{\Delta z^2}\right) &< 1 \text{ (3D)}. \end{aligned} \tag{2.22}$$

This is a purely numerical requirement for the electromagnetic fields alone, but plasma physics imposes other constraints on the size of the steps, namely that the Debye length and the plasma frequency are well resolved by the code ($\Delta x/\Lambda_{\mathrm{D}} \ll 1$ and $\omega_{\mathrm{pe}}\Delta t \ll 1$), the latter condition being more stringent.

2.5 Numerical Cherenkov radiation

For a plane wave in vacuum of the form

$$A^n_{i,j,k} = A_0 \exp I\,(n\omega t - ik_x x - jk_y y - kk_z z), \tag{2.23}$$

where I is the imaginary number unit, and using the FDTD discretization of Maxwell's equations, the dispersion relation is given by

$$\frac{1}{c^2\Delta t^2}\sin^2\frac{\omega\Delta t}{2} = \frac{1}{\Delta x^2}\sin^2\frac{k_x\Delta x}{2} + \frac{1}{\Delta y^2}\sin^2\frac{k_y\Delta y}{2} + \frac{1}{\Delta z^2}\sin^2\frac{k_z\Delta z}{2}, \tag{2.24}$$

instead of the exact dispersion relation for light waves

$$\frac{\omega^2}{c^2} = k_x^2 + k_y^2 + k_z^2. \tag{2.25}$$

We can recover the good relation for small wave numbers, while we observe significant deviations at high wave numbers where the speed of electromagnetic waves becomes smaller than the speed of light in vacuum (see Figure 2.6). As a side note, it is interesting to notice that the form of the numerical dispersion relation resembles those derived in condensed matter, in this sense the Yee lattice behaves like a crystalline medium. Therefore, an ultrarelativistic particle can travel faster than the electromagnetic waves it generates thus leading to a Cherenkov effect, very much like cosmic rays travelling through ice in the Icecube detector, except that in PIC simulations this phenomenon is spurious. This effect is a real plague in simulations involving a ultrarelativistic beam of particles moving coherently through the grid, such as shock simulations. It leads to numerical heating and eventually to the disruption of the beam. This is the reason why relativistic shock simulations are usually limited to moderate bulk Lorentz factors (see Greenwood et al. 2004 for ways to mitigate this effect). Fortunately, in other situations this effect is generally harmless and we will not need to worry about it.

2.6 Conservation of charge and magnetic flux

In principle, by solving the time-dependent Maxwell equations the other two should be automatically satisfied but this is not necessarily true due to truncation errors in the discretization of space and time derivatives. The other beauty of the FDTD scheme is that it conserves $\boldsymbol{\nabla} \times \mathbf{B} = 0$ to machine roundoff precision (similarly

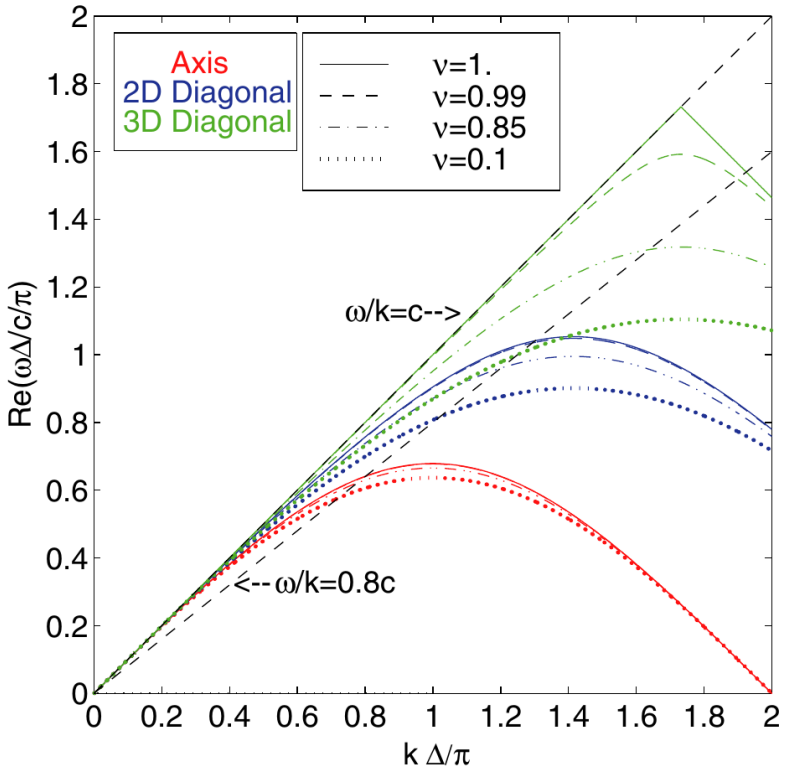

Figure 2.6: Dispersion relation of electromagnetic plane waves solved on the Yee mesh, where $\Delta x = \Delta y = \Delta z = \Delta$ and ν is the CFL number. Figure taken from Greenwood et al. (2004).

to the constraint transport method often used in MHD simulations). It is unfortunately not so straightforward for Gauss law. The simple current deposition scheme presented in Section 2.4 does not guarantee charge conservation to machine precision, meaning that

$$\boldsymbol{\nabla} \cdot \mathbf{J} = -\partial\rho/\partial t \tag{2.26}$$

is not exactly satisfied. Today, the standard procedure is to use a different current deposition scheme and particle shape function than the simple linear method presented above to enforce Eq. (2.26) to machine precision, as proposed by Villasenor & Buneman (1992) and Esirkepov (2001).

In `Zeltron` , I made the choice to keep the simple linear interpolation/deposition scheme for more flexibility when dealing with non-Cartesian or non-uniformly spaced grids as we will see later in this memoir. This comes at the expense of solving Poisson equation to correct the electric field so that $\boldsymbol{\nabla} \cdot \mathbf{E} = 4\pi\rho$. Fortunately, this procedure does not need to be done at every time step, every once for a while is usually sufficient (by default, this is done every 25 time steps in `Zeltron`). If $\mathbf{E}$ is the electric field evolved on the Yee mesh, and if $\delta\mathbf{E} = -\boldsymbol{\nabla}\delta\phi$ is the small correction to the electric field to ensure charge conservation, we must solve

$$\nabla^2 (\delta\phi) = -\left(4\pi\rho - \boldsymbol{\nabla} \cdot \mathbf{E}\right). \tag{2.27}$$

We use a standard iterative Gauss-Seidel method with 3 points in 1D, 5 points in 2D and a 7-points stencil in 3D. We are interested in local variations so that the

global scale and boundary conditions are usually irrelevant for the correction. By default, the code performs 500 iterations per divergence cleaning cycle. As for the time-dependent equations, we use the integral form of Poisson equation at the cell scale on the Yee lattice,

$$\oiint (\mathbf{E} + \delta\mathbf{E}) \cdot \mathbf{dS}_{\text{cell}} = 4\pi \iiint \rho dV_{\text{cell}}. \tag{2.28}$$

So far, this method has been working well but it has a non-negligible numerical cost. This is why I am currently considering to use more efficient numerical methods such as parabolic and hyperbolic divergence cleaning (Marder 1987; Munz et al. 2000).

2.7 The radiation-reaction force

While all of the above is standard in explicit PIC codes, the main novelty of the `Zeltron` code at its creation was the ability to take into account the radiation-reaction force, in addition to the Lorentz force. The equation of motion is then changed into the Lorentz-Abraham-Dirac equation Landau & Lifshitz (1971)

$$m_{\text{e}} c \frac{\mathrm{d}u^\mu}{\mathrm{d}s} = -\frac{e}{c} F^{\mu\nu} u_\nu + g^\mu, \tag{2.29}$$

where $F^{\mu\nu}$ is the electromagnetic tensor, and

$$g^\mu = \frac{2e^2}{3c} \frac{\mathrm{d}^2 u^\mu}{\mathrm{d}s^2} - \frac{\mathcal{P}_{\text{rad}}}{c^2} u^\mu, \tag{2.30}$$

is the radiation-reaction force, where $s = cdt/\gamma$ and $\mathcal{P}_{\text{rad}}$ is the radiative energy loss rate given by the Larmor formula

$$\mathcal{P}_{\text{rad}} = \frac{2}{3} e^2 c \left(\frac{\mathrm{d}u^\mu}{\mathrm{d}s}\right) \left(\frac{\mathrm{d}u_\mu}{\mathrm{d}s}\right). \tag{2.31}$$

The strength of the radiation-reaction force depends on the acceleration of the particle, which itself depends on the Lorentz force and the radiation-reaction force. The second derivative of the particle momemtum appearing in g^μ is particularly problematic, and finding a general solution to this equation is delicate. Fortunately, there is a solution valid in the framework of classical electrodynamics proposed by Landau & Lifshitz (1971), whose two main terms are given by in the 3-vector formulation

$$\begin{aligned}\mathbf{g} = \frac{2}{3} r_{\text{e}}^2 \left[(\mathbf{E} + \boldsymbol{\beta} \times \mathbf{B}) \times \mathbf{B} + (\boldsymbol{\beta} \cdot \mathbf{E})\, \mathbf{E}\right] \\ -\frac{2}{3} r_{\text{e}}^2 \gamma^2 \left[(\mathbf{E} + \boldsymbol{\beta} \times \mathbf{B})^2 - (\boldsymbol{\beta} \cdot \mathbf{E})^2\right] \boldsymbol{\beta},\end{aligned} \tag{2.32}$$

where $r_\mathrm{e} = e^2/m_\mathrm{e}c^2$ is the classical radius of the electron. In the ultrarelativistic limit $\gamma \gg 1$, the second term dominates such that

$$\mathbf{g} \approx -\frac{P_\mathrm{rad}}{c^2}\mathbf{v}, \tag{2.33}$$

the radiation-reaction force acts as a classical friction force opposite to the direction of the particle motion. However, we will see in Part II that the non-relativistic term can play a surprisingly important role in some cases, and therefore both terms are included in `Zeltron` .

We follow the numerical scheme proposed by Tamburini et al. (2010) to include the radiation-reaction force into the particle pusher (see, e.g., Sokolov et al. 2009 and Capdessus et al. 2012 for alternative implementations). The idea is to split the equation of motion into two, where the contribution from each force is solved separately, such that

$$\frac{\mathbf{u}_L^{n+1/2} - \mathbf{u}_L^{n-1/2}}{\Delta t} = \frac{\mathbf{F}_L^n}{m_\mathrm{e}c}, \tag{2.34}$$

where $\mathbf{F}_L^n$ is the Lorentz force, and

$$\frac{\mathbf{u}_R^{n+1/2} - \mathbf{u}_R^{n-1/2}}{\Delta t} = \frac{\mathbf{g}^n}{m_\mathrm{e}c}. \tag{2.35}$$

Adding these two equations up, and assuming that $\mathbf{u}_L^{n-1/2} = \mathbf{u}_R^{n-1/2} = \mathbf{u}^{n-1/2}$ yields

$$\mathbf{u}^{n+1/2} = \mathbf{u}_L^{n+1/2} + \mathbf{u}_R^{n+1/2} - \mathbf{u}^{n-1/2}, \tag{2.36}$$

so that we obtain the final result

$$\mathbf{u}^{n+1/2} = \mathbf{u}_L^{n+1/2} + \frac{\mathbf{g}^n \Delta t}{m_\mathrm{e}c}. \tag{2.37}$$

Thus, the first step is to solve Eq. (2.34) using the standard Boris push to calculate $\mathbf{u}_L^{n+1/2}$. This is not yet over because we need an estimate of the particle momentum at time t^n, $\mathbf{u}^n$, to compute $\mathbf{g}^n$. This is done in a similar way as in the Boris push, i.e., we evaluate the midpoint value by doing the following average

$$\mathbf{u}^n = \frac{\mathbf{u}_L^{n+1/2} + \mathbf{u}^{n-1/2}}{2}, \quad \gamma^n = \sqrt{1 + (u^n)^2}, \quad \boldsymbol{\beta}^n = \frac{\mathbf{u}^n}{\gamma^n}. \tag{2.38}$$

This method preserves the fantastic features of the Boris push (stability and accuracy) while adding a small computing overhead due to the few extra steps required to include the radiation-reaction force. Its implementation is therefore rather straightforward in an explicit PIC code.

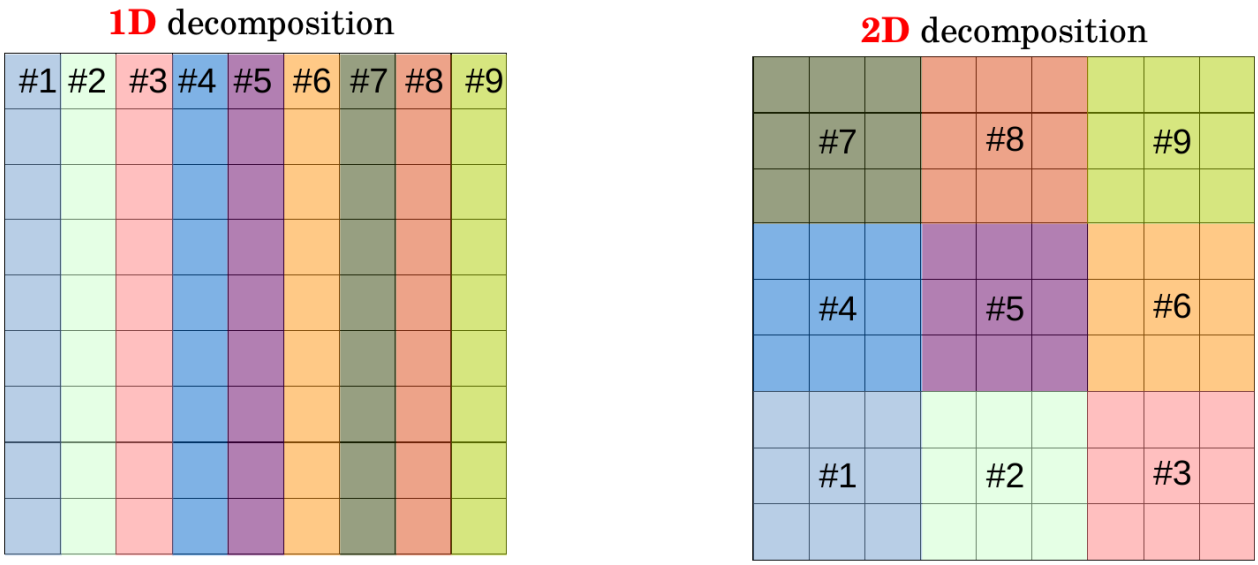

Figure 2.7: Spatial arrangements of 9 processors using a domain decomposition technique in 1D (left) and in 2D (right) for a full domain size composed of 9×9 cells.

2.8 Parallelization strategies

PIC codes must be efficiently parallelized to model large system size and long integration time to have meaningful astrophysical applications. A common practice is to use the domain decomposition technique. It consists in dividing the computational box into smaller domains where one or more cores are assigned along with the particles they contain. In `Zeltron` , the cores are arranged in space according to a Cartesian topology in 1D, 2D or 3D. For instance, consider a full 2D domain of 9×9 cells and 9 processors. Using a 1D topology means slicing the full domain into 9 subdomains of 1 cells, while using a simple 2D topology would mean slicing into 9 3×3 cells subdomains (Figure 2.7). Each CPU goes through the main steps described in Sect. 2.4 independently of the other processors. At the end of each time step all CPU must communicate with their nearest neighbours to exchange information about particle leaving/entering their subdomain and the electromagnetic fields at their interface stored in ghost cells. The number of communications depends on the number of nearest neighbours, 2 in 1D (left-right), 8 in 2D, and 26 in 3D.

Communications between an arbitrary number of processes are done thanks to the Message Passing Interface (MPI) library. While the number of operations to evolve electromagnetic fields is fixed, the number of particles can vary significantly both in time and in space over the duration of a simulation. Given that pushing particles and depositing currents onto the grid typically take about 90% of the commuting time, a common issue in PIC simulations is load balancing. A situation where the number of particles per core is of the same order will be perfectly balanced and parallelization will be optimal. In contrast, a poor load balancing severely slows down a simulation. If, for some reason, there is a concentration of

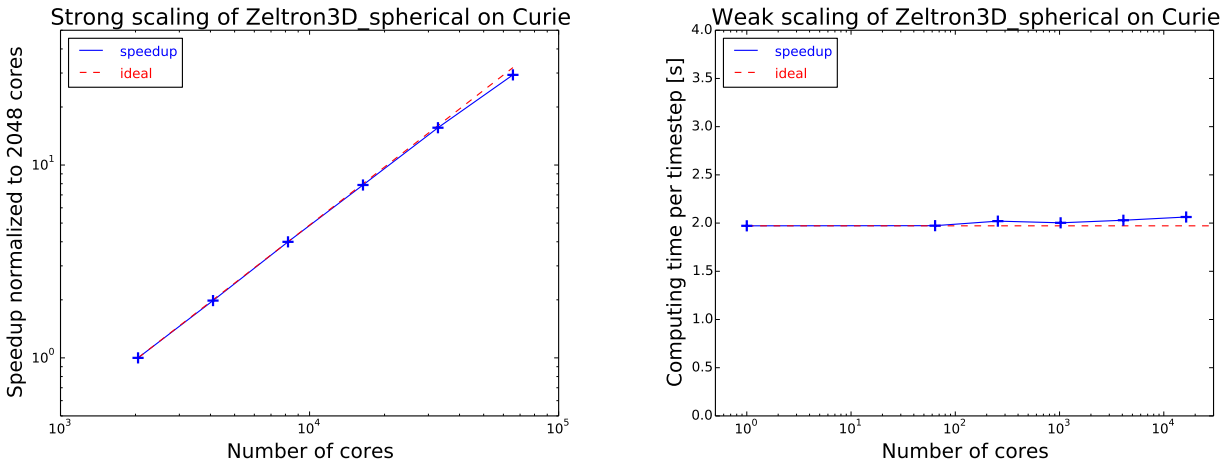

Figure 2.8: Strong (fixed total domain size, left panel) and weak (fixed domain size per processor, right panel) scaling of `Zeltron` in its 3D spherical version on the TGCC-Curie machine, tested up to 80% of the full machine (65,536 cores).

particles in a few subdomains (e.g., a current sheet), only a few processors will have to push a lot of particles while the others will remain idle. The way how the domain is decomposed for a given setup can usually make a big difference. Hybrid codes combining MPI and OpenMP, variable particle weighting, or dynamical changes of the domain decomposition are other solutions to have better performances.

PIC codes scale well to a large number of CPUs, today at least up to $\sim 10^6$ processes. These scaling plots are usually done under ideal conditions with perfect load balancing, and do not necessarily reflect problem-dependent loss of performance. Over the past 8 years, Zeltron ran on many different supercomputer types and architectures (e.g., Blue Gene, Skylake, KNL) and has shown excellent performances over a very large number of cores on several different machines such as Kraken (Oak Ridge National Lab, USA), Stampede (TACC, USA), Janus (Univ. of Colorado, USA), Curie and Irene (TGCC, France), Mira (Argonne National Laboratory, USA), and Occigen (CINES, France). The code has been tested successfully up to 2^{19} (524288) cores or up to 2.1 million MPI ranks (4 ranks per core) on Mira with nearly perfect scaling. Figure 2.8 shows an example of scaling plots performed on the TGCC-Curie machine in the context of the FROMTON PRACE Project Access (Part II).

2.9 Brief overview of `Zeltron` architecture

Zeltron is written in Fortran 90. It is divided into several modules which deal with the different steps of the PIC loop, for instance, there is one module dedicated to the particle motion, one for the field evolution, one for the currents, etc... This division allows for a better readability and an easier management of the code. The code has the ability to write/read simulation data efficiently in parallel. A module exists to perform data writing/reading with parallel HDF5. The code has

also checkpointing abilities which is essential for performing large production runs. Except for MPI and HDF5, Zeltron does not need any other external libraries which makes the code easily deployable into a new system. Zeltron contains a series of diagnostic tools embedded into the code which can analyse efficiently the data on the fly (e.g., particle spectra, density map, fields, pressure, radiation distribution). This ability turns out to be extremely useful to check that simulations are running correctly well before the wall time has ended. It also allows to reduce significantly the amount of useful data dumped to disk, the raw data is not necessarily needed if the user already knows what to look for. In the last resort, checkpoint data contain the full raw information so that there is no risk to lose information. I usually perform more advanced data analysis and visualization of the data with a library of Python scripts and Paraview for 3D rendering.

2.10 Publications and impact on the community

The basic Cartesian version of the code has been released in 2015 and is publicly available under the terms of the GNU General Public License on the Git repository: `https://github.com/bcerutti/Zeltron-code`. So far, the code was successfully used in 30 refereed journal articles. This number includes the 20 publications where I am a co-author. Research topics includes the study of relativistic magnetic reconnection, pulsar and double pulsar magnetospheres and winds, Kerr black hole magnetospheres and jets, kinetic plasma turbulence, and more recently collisionless shocks.

Below is a list of important milestones reached over the last 8 years, in chronological order:

- Summer 2012: Creation a 2D and 3D Cartesian serial version.
- Fall 2012: Parallelization with MPI.
- 2013: First publication using simulations performed with Zeltron (Cerutti et al. 2013).
- Summer 2013: Special and successful production 3D run on the entire Kraken supercomputer (97,200 cores) (Cerutti et al. 2014b).
- 2014: Development of the 2D axisymmetric and full 3D spherical versions.
- 2015: Publication of the aligned pulsar magnetospheric model (Cerutti et al. 2015).
- 2016: INCITE allocation awards, 93 millions CPU hours on the Mira supercomputer, PI: D. Uzdensky.
- 2017: Development of the full general relativistic 1D and 2D versions.

- 2018: FROMTON PRACE Project Access, 26.7 millions Intel Skylake CPU hours on the Irene supercomputer, PI: B. Cerutti.
- 2019: INCITE allocation awards, 108 millions CPU hours on the Mira supercomputer, PI: D. Uzdensky.
- 2019: First 2D GRPIC model of a Kerr black hole magnetosphere (Parfrey et al. 2019), main cover of PRL.
- 2020: First 2D black hole magnetospheric model with radiative transfer (GRRPIC, Crinquand et al. 2020).

Today, the main developers of `Zeltron` are: my current PhD student Benjamin Crinquand (IPAG, Grenoble), Krzysztof Nalewajko (CAMK, Warsaw), Kyle Parfrey (PPPL, Princeton), Alexander Philippov (CCA, New York City), Gregory Werner (CU Boulder) and myself.

Chapter 3

First applications: Particle acceleration in relativistic reconnection sites

My first incentive to develop `Zeltron` was to perform a more realistic model of particle acceleration in a magnetic reconnection site, with the hope it could bring a viable explanation of the Crab gamma-ray flares. Little was known on this topic at the time, in particular in the relativistic regime and even less on the strong synchrotron cooling regime (Jaroschek & Hoshino 2009). There is no real theory of magnetic reconnection, thus, the only way to make progress is through simulations. Early studies of particle acceleration in reconnection sites focused on the test particle approximation using a static prescribed magnetic field configuration (Romanova & Lovelace 1992; Schopper et al. 1998, 1999; Larrabee et al. 2003; Nodes et al. 2003), very much like what I have presented in the first chapter. While this approach bring valuable insights on particle trajectories and trapping phenomena, it cannot capture the intermittent nature of magnetic reconnection and the feedback of the particles on the dynamics. PIC simulation is the natural next step to have a more self-consistent model of reconnection. While this numerical exercise has already been performed rather extensively in space physics (Solar corona, Earth magnetosphere), only a few studies were done in the relativistic regime starting from the seminal paper by Zenitani & Hoshino (2001). My goal was to reproduce a similar numerical setup, and extend it to a larger box size taking into account the radiation reaction force.

This chapter gives an overview of my research activity from 2012 to 2015 which was mostly focused on the study of particle acceleration in magnetic reconnection sites using PIC simulations. It begins with a short introduction on relativistic reconnection partly based on an ISSI working group review paper that I wrote with 3 other colleagues on the topic (Kagan et al. 2015) and an invited review talk I gave at the HEPRO VII meeting (Cerutti 2019). I will then proceed with a description of the classical numerical setup used in the community to study reconnection.

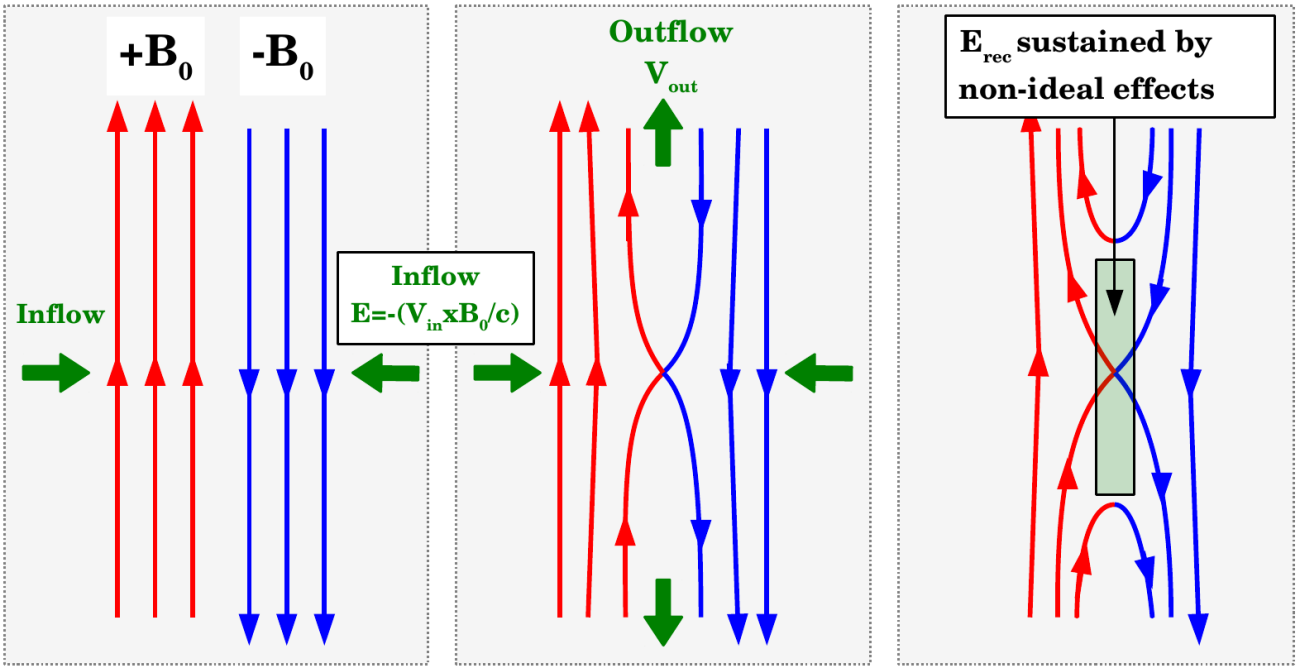

Figure 3.1: Schematic anti-parallel magnetic reconnection configuration.

I will summarize some of the highlights of reconnection dynamics and particle acceleration as a generic mechanism, with an emphasis on my contribution to the field. I will close the loop and this first part by discussing the application to the Crab flares.

3.1 Relativistic magnetic reconnection

Magnetic reconnection is by definition a sudden rearrangement of the magnetic field line topology (Zweibel & Yamada 2009; Yamada et al. 2010). If one considers the simplest configuration of anti-parallel field lines brought together, Ampère law implies that a current sheet must form where both polarities meet. Field lines diffuse and reconnect within the current layer whose thickness is governed by the scale at which non-ideal MHD effects dominate. In astrophysical plasmas, the resistivity is usually very low meaning that the diffusion layer will be very small in comparison to the system size. In the absence of collisions, there is no explicit resistive scale such that the layer thickness drops to the smallest plasma scale there is, where finite-Larmor radius effects play the role of effective resistivity. Field lines entering the reconnection region bring plasma from the upstream into the layer. Plasma is then expelled close to the Alfvén speed sideways in the plane of the layer in the form of outflows as field lines snap and reconnect (Figure 3.1). The ratio of the inflow to the outflow velocity is the reconnection rate, $\beta_{\rm rec}$, which defines how fast reconnection proceeds,

$$\beta_{\rm rec} = \frac{V_{\rm in}}{V_{\rm A}}. \tag{3.1}$$

Away from the layer, ideal MHD applies such that

$$\mathbf{E} + \frac{\mathbf{V}_{\rm in} \times \mathbf{B}}{c} = \mathbf{0}, \tag{3.2}$$

meaning that the reconnection rate is also a measure of the ratio between the electric and the magnetic field. In the steady state, the electric field within the layer matches the ideal MHD field upstream except that it is sustained by non-ideal effects rather than by the motion of field lines. There is probably no clear answer to which electric field comes first, but perhaps part of the answer may be whether reconnection is "spontaneous", i.e., driven by microphysics in the sheet, or whether it is "forced" or "driven" from the outside by large-scale plasma motion.

Using mass-conservation between the inflow and reconnection ouflow and assuming incompressibility imply that the reconnection rate is directly related to the aspect ratio of the layer,

$$\beta_{\rm rec} = \frac{V_{\rm in}}{V_{\rm A}} = \frac{\delta}{L}, \tag{3.3}$$

where δ is the layer thickness and L its length. In the classical Sweet-Parker model of reconnection (Sweet 1958; Parker 1957), the length scale is macroscopic of order the system size, while, as we have argued earlier, the layer thickness is microscopic such that the expected reconnection rate should be tiny, $\delta/L \ll 1$. This is clearly at odds with observations of the Solar Corona, the Earth magnetosphere, or measurements in laboratory experiments which show must faster reconnection rates of order 0.01 to 0.1. As an alternative, Petschek (1964) proposed a much smaller aspect ratio reconnection region to allow for a higher rate. To do so, he proposed that this configuration is maintained by standing oblique shock waves on both sides of the sheet. Unfortunately, this configuration requires special physical conditions to exist and remain stable (Uzdensky & Kulsrud 2000). This being said, the basic idea of shortening the reconnection layer is the key to achieve fast reconnection as we will report in the following, although its cause has a fundamentally different origin than what Petschek envisioned: plasma instabilities (Sect. 3.3).

Magnetic reconnection proceeds in the relativistic regime when the Alfén speed approaches the speed of light (Blackman & Field 1994; Lyutikov & Uzdensky 2003; Lyubarsky 2005),

$$V_{\rm A} = \sqrt{\frac{\sigma}{1+\sigma}}c \approx c, \tag{3.4}$$

or in other words when the plasma magnetization parameter, defined as the ratio of the magnetic enthalpy density to the particle enthalpy density in the upstream medium (outside the layer), is

$$\sigma = \frac{B_0^2}{4\pi\left(nmc^2 + P\right)} \gtrsim 1, \tag{3.5}$$

where B_0 is the upstream magnetic field strength, nmc^2 is the mean plasma internal energy density, and P is the plasma pressure (we will neglect this term in the

following for simplicity since it will be at best of the same order as the internal energy density). Another way to interpret this definition is that if a significant fraction of the magnetic energy density B_0^2 is dissipated and channelled to the particles, and $B_0^2/4\pi \gtrsim nmc^2$ ($\sigma \gtrsim 1$) the plasma energy density will become larger than its rest mass energy density, i.e., it necessarily becomes relativistic. This regime is achieved in very peculiar astrophysical environments, most certainly in pulsar magnetospheres and pulsar winds (Cerutti & Beloborodov 2017; Kirk et al. 2009, Part II) and black hole magnetospheres (Blandford & Znajek 1977, Part III), most likely in relativistic jets (Romanova & Lovelace 1992; Giannios et al. 2009), black-hole accretion-disk coronae (Galeev et al. 1979; Goodman & Uzdensky 2008), pulsar wind nebulae (Porth et al. 2014, this chapter), and possibly gamma-ray bursts (Drenkhahn & Spruit 2002). It will therefore be the main regime of interest throughout this memoir.

Some of the key questions we want to address are: What are the basic features of relativistic reconnection dynamics? How fast is it? How efficient reconnection is at producing non-thermal particle acceleration? What are the acceleration mechanisms and where do they take place? How does reconnection proceed in the strong synchrotron cooling regime and can this explain the Crab flares?

3.2 Numerical setup

3.2.1 The relativistic Harris equilibrium

It is often desirable to initialize a numerical simulation from an equilibrium. For reconnection studies, the most commonly used configuration is given by the Harris solution[1], an exact 1D kinetic equilibrium generalized to the relativistic regime by Kirk & Skjæraasen (2003). In a (x,y,z) Cartesian coordinate system, this solution is characterized by the magnetic profile

$$B_{\mathrm{x}}(y) = B_0 \tanh\left(\frac{y}{\delta}\right), \tag{3.6}$$

where δ is the layer thickness (Figure 3.2). A current density must flow within the layer along the z-direction so that

$$J_{\mathrm{z}}(y) = \frac{c}{4\pi}\boldsymbol{\nabla}\times\mathbf{B} = -\frac{cB_0}{4\pi\delta}\cosh^{-2}\left(\frac{y}{\delta}\right). \tag{3.7}$$

The current is carried by two counter-streaming beams of opposite electric charges moving along the $\pm z$-direction at the constant speed

$$\beta_{\mathrm{d}} = \pm\frac{\lambda_{\mathrm{D}}}{\delta}, \tag{3.8}$$

[1] see however, e.g., Guo et al. (2014) for an initially force-free configuration, Lyutikov et al. (2017b); Nalewajko (2018) for an initially ABC equilibrium, and Lyutikov et al. (2017a) for an X-point collapse configuration.

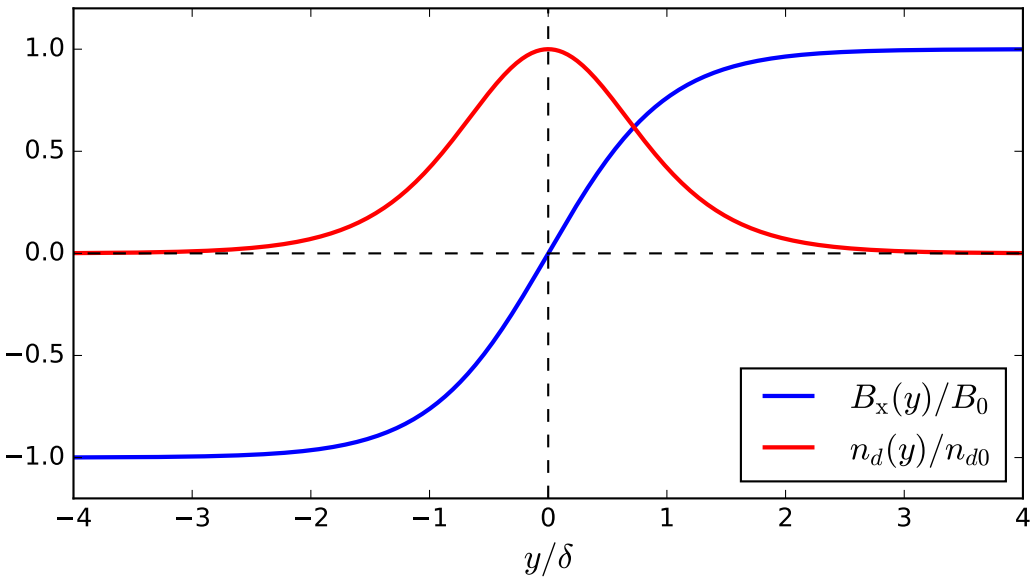

Figure 3.2: Magnetic field and plasma density profiles in the Harris equilibrium.

where λ_D is the Debye length defined in the layer,

$$\lambda_D = \sqrt{\frac{kT_d^\star}{4\pi n_{d0} e^2 \Gamma_d}}, \tag{3.9}$$

$T_d^\star$ is the co-moving temperature and n_{d0} is the density of the drifting particles, and $\Gamma_d = 1/(1-\beta_d^2)^{1/2}$. The plasma density profile must thus follow

$$n_d(y) = n_{d0} \cosh^{-2}\left(\frac{y}{\delta}\right), \tag{3.10}$$

which is maximum inside the layer and quickly vanishes outside (Figure 3.2). Pressure balance across the sheet, connects the upstream magnetic field strength to the plasma parameters of the sheet via

$$B_0 = \sqrt{16\pi n_{d0} k T_d}. \tag{3.11}$$

3.2.2 Numerical implementation

The problem with the above solution is that there is virtually vacuum outside of the sheet, meaning an infinite magnetization. If the reconnection process begins, there will be no plasma inflow to maintain the process active. In practice, we always add a uniform plasma at rest of density n_0 all over the box, including inside the sheet. In this way, this plasma does not change the pressure balance of the Harris equilibrium. The relevant magnetization is defined with the upstream plasma parameters,

$$\sigma = \frac{B_0^2}{4\pi n_0 m c^2}. \tag{3.12}$$

Using Eq. (3.11) yields

$$\sigma = \frac{4kT_\mathrm{d}}{mc^2}\left(\frac{n_{d0}}{n_0}\right), \tag{3.13}$$

meaning that in the relativistic regime where $\sigma \gg 1$, and with $kT_\mathrm{d}/mc^2 \lesssim 1$, the background density must be much smaller than the initial plasma density in the sheet, $n_0 \ll n_{d0}$. This high density contrast can be problematic in PIC and lead to a poor statistical sampling of the particle distribution function of the upstream plasma, which will be the plasma of interest in the following. To circumvent this problem, we split the plasma into two separate populations: (i) a high-density "drifting" component concentrated inside the sheet carrying the initial current, and (ii) a low-density "background" component for the uniform plasma at rest. Both distributions are sampled with the same number of particle per cell, but the trick is to assign them a different numerical weight to model the desired density contrast. This technique also allows to model the exact initial density profile of the drifting particles (Eq. 3.10).

The background plasma is initialized with an isotropic relativistic Maxwellian distribution in the simulation frame of temperature $\Theta_\mathrm{b} = kT_\mathrm{b}/mc^2$, such that

$$f_\mathrm{b}(\mathbf{u}) \propto \exp\left(-\frac{\gamma-1}{\Theta_\mathrm{b}}\right), \tag{3.14}$$

where $\mathbf{u} = \gamma\boldsymbol{\beta}$. Integrated over a spherical shell in phase space yields the distribution function of the total particle momentum, $||\mathbf{u}|| = u$,

$$f_\mathrm{b}(u) \propto u^2 \exp\left(-\frac{\gamma-1}{\Theta_\mathrm{b}}\right). \tag{3.15}$$

In `Zeltron` , we generate this distribution in two steps:

- Step 1: Generate the total particle momentum u. A particularly elegant and general way to do so is to use the cumulative distribution function,

$$F(u) = \int_{-\infty}^{u} f(u')du'. \tag{3.16}$$

  We can invert it numerically by sampling F with a random number R uniformly distributed between 0 and 1, and then infer u given that $F(u) = R$.

- Step 2: Generate an isotropic distribution by drawing the two spherical angles θ and ϕ such that ϕ is uniformly distributed between 0 and 2π and $\cos\theta$ is uniformly distributed between -1 and 1. The three components of the particle momentum are then given by

$$u_\mathrm{x} = u\sin\theta\cos\phi \tag{3.17}$$
$$u_\mathrm{y} = u\sin\theta\sin\phi \tag{3.18}$$
$$u_\mathrm{z} = u\cos\theta. \tag{3.19}$$

Generating the drifting particle population is more involved because of frame transformation. We follow below the derivation proposed by Swisdak (2013). In the co-moving frame, particles are distributed according to an isotropic relativistic Maxwellian of temperature $\Theta_\mathrm{d} = kT_\mathrm{d}/mc^2$. In the lab frame, the distribution of momentum is

$$f_\mathrm{d}\left(\mathbf{u}\right) \propto \exp\left(-\frac{\gamma^\star - 1}{\Theta_\mathrm{d}}\right), \tag{3.20}$$

where $\gamma^\star = \Gamma_\mathrm{d}\left(\gamma - \boldsymbol{\beta_\mathrm{d}}\cdot\mathbf{u}\right)$. Because of the Lorentz boost, the distribution function in the lab frame is anisotropic and it is therefore more practical to decompose the momentum into a parallel and perpendicular component to the direction of the drift motion. Eq. (3.20) can be rewritten as

$$f_\mathrm{d}\left(\mathbf{u}\right) \propto \exp\left(-\frac{\Gamma_d\sqrt{1+u_\parallel^2+u_\perp^2} - \Gamma_\mathrm{d}\beta_\mathrm{d}u_\parallel - 1}{\Theta_\mathrm{d}}\right). \tag{3.21}$$

Integrating over the perpendicular component in phase space and taking a cylindrical integration elementary volume $u_\perp du_\perp d\theta$ gives the following distribution function for the parallel component (and dropping constant multiplicative factors which do not matter here because we only need normalized distributions)

$$\begin{aligned} f_\mathrm{d}(u_\parallel) &= \int_0^{2\pi}\int_0^{+\infty} u_\perp f_\mathrm{d}\left(\mathbf{u}\right) du_\perp d\theta \\ &\propto \left(1+\frac{\Gamma_d\gamma_\parallel}{\Theta_\mathrm{d}}\right)\exp\left(-\frac{\left(u_\parallel - u_\mathrm{d}\right)^2}{\Theta_\mathrm{d}\left(\gamma_\parallel\Gamma_\mathrm{d} + u_\parallel u_\mathrm{d} + 1\right)}\right), \end{aligned} \tag{3.22}$$

where $u_\mathrm{d} = \Gamma_\mathrm{d}\beta_\mathrm{d}$ and $\gamma_\parallel = \sqrt{1+u_\parallel^2}$. The parallel component is obtained from the corresponding cumulative distribution. Once $u_\parallel$ chosen, $u_\perp$ cannot be taken independently. Defining $u_\mathrm{s} = u_\perp/\sqrt{1+u_\parallel^2}$, its distribution function knowing $u_\parallel$ is (Swisdak 2013)

$$f_\mathrm{d}(u_\mathrm{s}|u_\parallel) \propto u_\mathrm{s}\exp\left(-\frac{\left(u_\parallel - u_\mathrm{d}\right)^2 + \gamma_\parallel^2\Gamma_\mathrm{d}^2u_\mathrm{s}^2}{\Theta_\mathrm{d}\left(\gamma_\parallel\Gamma_\mathrm{d}\gamma_\mathrm{s} + u_\parallel u_\mathrm{d} + 1\right)}\right), \tag{3.23}$$

where $\gamma_\mathrm{s} = \sqrt{1+u_\mathrm{s}^2}$. Once again u_s (and therefore $u_\perp$) is obtained from the cumulative distribution. As a final check, one can compute the total particle momentum distribution function of a relativistic drifting Maxwellian,

$$\begin{aligned} f_\mathrm{d}\left(u\right) &= 2\pi\int_{-1}^{+1} u^2 f_\mathrm{d}\left(\mathbf{u}\right) d\cos\theta \\ f_\mathrm{d}\left(u\right) &\propto u\frac{\sinh\left(u_\mathrm{d}u/\Theta_\mathrm{d}\right)}{u_\mathrm{d}/\Theta_\mathrm{d}}\exp\left(-\frac{\Gamma_\mathrm{d}\gamma - 1}{\Theta_\mathrm{d}}\right). \end{aligned} \tag{3.24}$$

In the limit $u_\mathrm{d} \to 0$, we recover the more familiar isotropic Maxwellian distribution (Eq. 3.15).

Although these considerations may appear as rather technical, it turns out to be important to begin with the correct distribution function, otherwise an equilibrium cannot be reached initially and a transient forms which can disturb the system. For this reason, I found it useful to report this non-trivial solution here. We now have all the elements for the initial configuration. All of the results described below, whether this is my work or from other groups, were obtained with this setup.

3.3 Tearing and kink instabilities

The Harris solution is not a stable equilibrium, it is prone to two main plasma instabilities which have a major role in the reconnection dynamics, namely the tearing and the kink. The tearing mode fragments a long thin current layer into a succession of magnetic loops, or O-point, and magnetic X-points. In the relativistic regime, the fastest growing mode is (Zelenyi & Krasnoselskikh 1979; Zenitani & Hoshino 2007; Pétri & Kirk 2007)

$$k_\mathrm{x}\delta = \frac{1}{\sqrt{3}}, \tag{3.25}$$

where k_x is the wave number along the x-direction, meaning that the layer will break apart if the aspect ratio of the layer is greater than

$$\frac{L_\mathrm{x}}{\delta} \gtrsim 2\pi\sqrt{3} \approx 10. \tag{3.26}$$

As a result, the classical Sweet-Parker sheet which assumes $L/\delta \gg 1$ is unstable, and instead breaks up into a chain of shorter secondary current layers of aspect ratio or order 10, analog to a Petschek configuration. For this reason, the tearing instability mediates fast reconnection. In the ultrarelativistic regime, the growth rate of the tearing modes, γ_TI, is (Zenitani & Hoshino 2007)

$$\gamma_\mathrm{TI}\omega_0^{-1} = \frac{2\sqrt{2}}{\pi} k_\mathrm{x}\delta \left(1 - k_\mathrm{x}^2\delta^2\right) \beta_\mathrm{d}^{3/2}, \tag{3.27}$$

where ω_0 is the fiducial upstream plasma Larmor gyrofrequency. For $\beta_\mathrm{d} = 0.6$, the growth rate peaks at $\gamma_\mathrm{TI}\omega_0^{-1} \approx 0.16$, i.e., the sheet in unstable after less than 10 Larmor cycles, which is very fast.

In this context, the kink instability has similar fastest growing modes and rates than the tearing instability. Following Zenitani & Hoshino (2007), the fastest growing mode in the ultrarelativistic limit is

$$k_\mathrm{z}\delta = \frac{1}{8\Gamma_\mathrm{d}\beta_\mathrm{d}^2}, \tag{3.28}$$

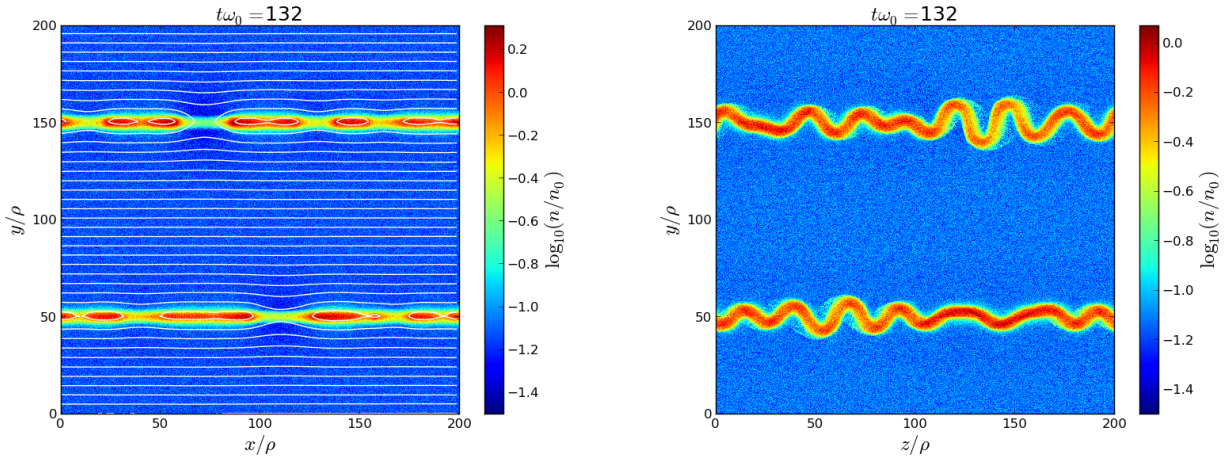

Figure 3.3: Effect of the tearing (left panel) and kink (right panel) instabilities on two anti-parallel Harris sheets using 2D PIC simulations. Figure taken from Cerutti et al. (2014b).

with a growth rate

$$\gamma_{\rm KI}\omega_0^{-1} = \frac{1}{16\Gamma_{\rm d}\beta_{\rm d}}. \tag{3.29}$$

Thus, both instabilities compete in the linear phase, although they operate in directions perpendicular to each other. The kink modes grow along the direction of the current (z-direction), while the tearing modes grow along the reconnecting magnetic field (x-direction). Figure 3.3 shows PIC simulations of two parallel Harris sheets simulated in the plane perpendicular to the current (xy-plane, left panel) where the tearing modes alone operate, and in the plane perpendicular to the field (zy-plane, right panel) where the kink modes operate. These snapshots are taken in the early evolution of the simulations to show the linear phase of each instabilities. The measured growth rates are compatible with the predicted rates from the linear analysis given above. The kink instability eventually leads to the disruption of the sheet, or at least to an effective broadening of the layer. However, it can be effectively quenched by adding some stiffness to the field lines along the current direction, known as the guide field (Zenitani & Hoshino 2008; Cerutti et al. 2014b). The latter represents the non-reconnecting component of field lines crossing at an arbitrary angles, as opposed to the perfectly antiparallel case we have considered so far where there is no guide field. Although the kink does indeed play an important role at the early stages, large-box size 3D PIC simulations have shown that it becomes subdominant over the tearing mode in the non-linear phase (Sironi & Spitkovsky 2014; Werner & Uzdensky 2017), and for this reason we will not discuss any further the role of the kink in what follows (although we will briefly encounter it again later in the context of relativistic magnetospheres).

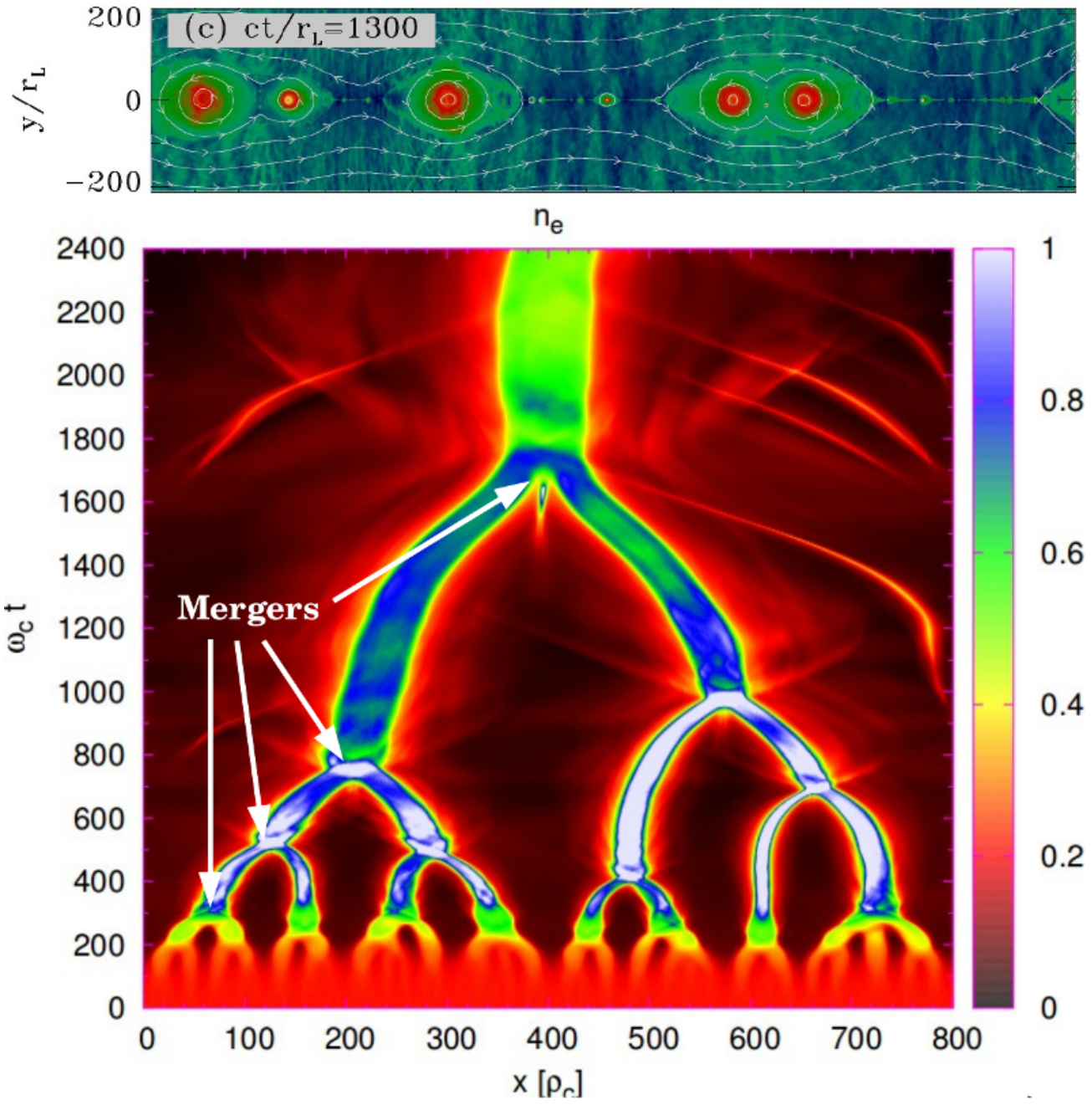

Figure 3.4: Top: Plasma density snapshot of a 2D PIC simulation in the non-linear phase of the plasmoid evolution from Sironi & Spitkovsky (2014). Bottom: Space-time diagram showing the merging tree of plasmoids as the simulation evolves leading to bigger and bigger structures, until there is just one island left filling the simulation box. Figure adapted from Nalewajko et al. (2015).

3.4 Reconnection dynamics

Fast magnetic reconnection is triggered when the tearing instability fragments the current layer into a series of shorter secondary current layers separated by magnetic O-points filled with plasma, called "plasmoids" or "magnetic islands". This structure is highly dynamical in the non-linear phase. Plasmoids move away from secondary layers leading to the mergers of plasmoids pushed towards each other by the reconnection outflows. Mergers result to bigger and bigger structures over time as more plasmoids are accreted until a single giant plasmoid fills the entire simulation box in the saturated state. The space-time diagram in Figure 3.4 (bottom panel) shows this inverse-cascade process as observed in a PIC simulation. In parallel to this process, the motion of plasmoids leads to the stretching of secondary layers which in turn becomes tearing unstable and new plasmoids form. This phenomenon is often called the plasmoid instability as discussed in Uzdensky et al. (2010). In a well-evolved but not saturated state, the reconnection layer is composed of a hierarchical chain of magnetic islands of different sizes (Figure 3.4, top panel). Plasmoids can also be produced at the interface between two large merging islands where a short-lived current sheet forms perpendicular to the main reconnection plane.

Field lines reconnect within secondary current sheets. The tension of freshly reconnected field lines drives powerful plasma ouflows into plasmoids. The reconnection process is maintained by the advection of new field lines and plasma from the upstream. Figure 3.5 shows the bulk fluid velocity structure reconstructed from a 2D PIC simulation. It clearly shows this inflow-outflow structure within each layer. The inflow velocity is of order $V_{\rm in} \approx 0.1\text{-}0.2c$, while the outflow velocity approaches the speed of light, $V_{\rm out} \sim c$, as anticipated by Lyubarsky (2005) (see also Sironi et al. 2016). Using the definition in Eq. (3.1), the reconnection rate is of order 0.1-0.2, which is also consistent with the aspect ratio of the secondary layers. A measure of the electric field strength gives a similar rate. This rate is also nearly independent of the plasma magnetization as long as $\sigma \gtrsim 1$, meaning that relativistic reconnection is very fast because it operates over a few light-crossing time of the reconnection site.

3.5 Particle acceleration

There is also a consensus today in the community that relativistic reconnection is efficient at channeling the dissipated magnetic energy into energetic particles. Different groups over the last two decades, including myself, came to the same conclusion that reconnection naturally produces hard particle spectra at high magnetization (Zenitani & Hoshino 2001; Cerutti et al. 2012b; Sironi & Spitkovsky 2014; Werner et al. 2016). The spectrum hardens with increasing σ and seems to saturate to nearly $\gamma^{-1.2}$. A physical origin of such power-law indices is still debated and poorly understood. But the simple fact that reconnection produces

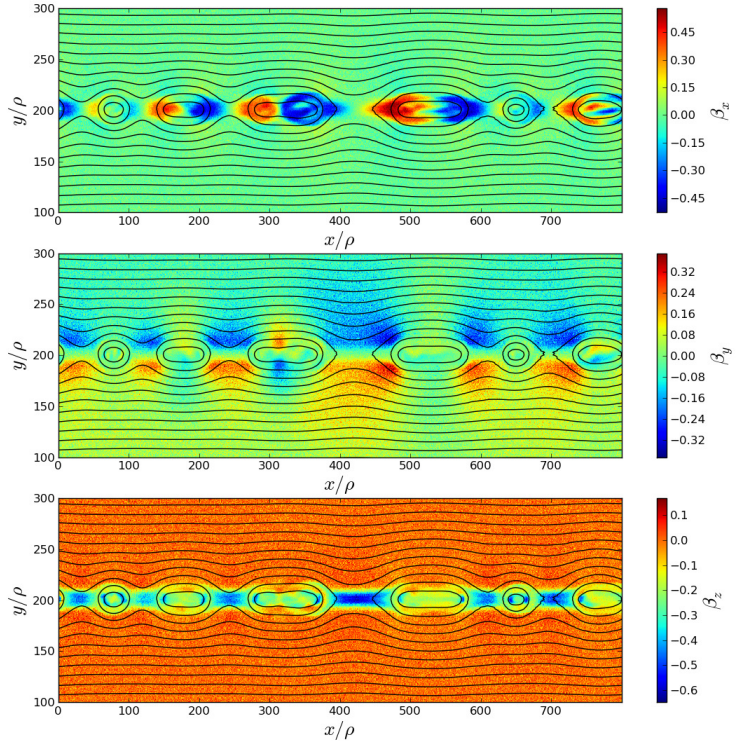

Figure 3.5: Plasma bulk velocity structure in the vicinity of a reconnecting current sheet in the plasmoid-dominated regime. Taken from Kagan et al. 2015.

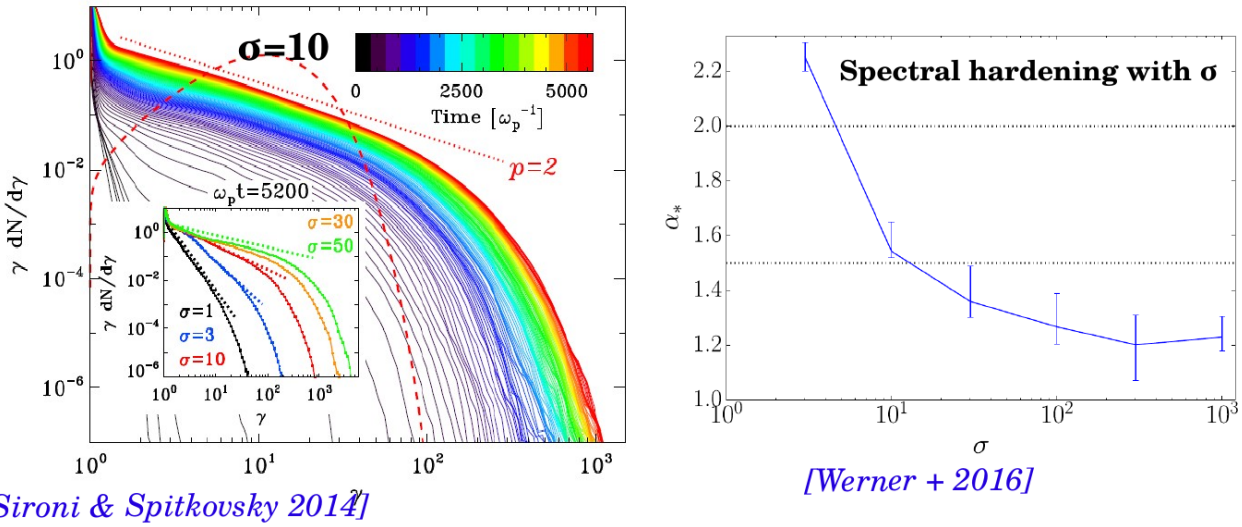

Figure 3.6: Left: Time evolution of the particle energy spectrum in a 2D PIC relativistic reconnection simulation with $\sigma = 10$ (other values are shown in the inset plot). Right: Power-law index of the particle spectrum as function of σ. Figure adapted from Sironi & Spitkovsky (2014) and Werner et al. (2016).

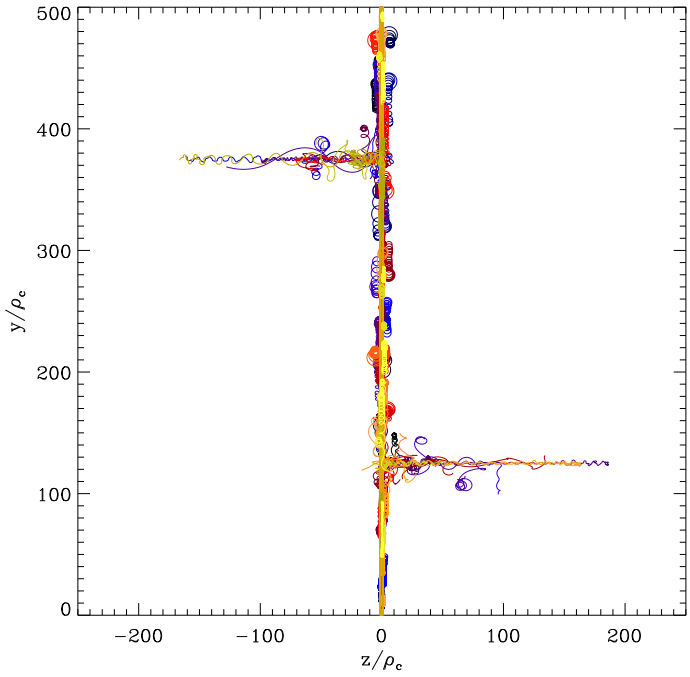

Figure 3.7: PIC electron trajectories from a 2D PIC simulation of two anti-parallel Harris sheet located at $y/\rho_c = 125$ and 375 projected into the plane perpendicular to the simulation plane. Energetic particle are running away along the $\pm z$-direction within the sheet along the reconnection electric field E_z. Taken from Kagan et al. 2015.

power laws harder than -2 already have strong implications on the maximum particle energy. Indeed, this means that the energy distribution $\gamma^2 dN/d\gamma$ peaks at the high end of the spectrum, $\gamma_{\rm max}$. Conservation of energy tells us that $\gamma_{\rm max}$ cannot be arbitrarily large and should depend on how much magnetic energy there is available per particle, i.e., σ. In Werner et al. (2016), we indeed found that the maximum particle energy is limited by $\gamma_{\rm max} \approx 4\sigma$.

To gain physical insights into the acceleration process itself, it is usually instructive to use the full power of PIC simulations by looking at individual particle trajectories. This analysis shows that particle acceleration usually begins with an impulsive episode by the reconnection electric field inside the current layer. Particles undergo a quasi-linear acceleration and follow relativistic Speiser orbits as expected from test-particle simulations. Figure 3.7 shows a randomly selected sample of particle trajectories from a 2D PIC simulation similar to Figure 3.3 (left panel) projected into the plane perpendicular to the magnetic field, where the high-energy particles run away along the direction of the electric field (along the z-direction here). The further away they go, the higher their energy is. The particle lifetime in the accelerating region, and therefore its final energy, is limited by the deflections of the reconnected magnetic field line which pushes the particle into the islands (Cerutti et al. 2012a; Sironi & Spitkovsky 2014). It already results from this a broad particle energy distribution. The energy gain is proportional to

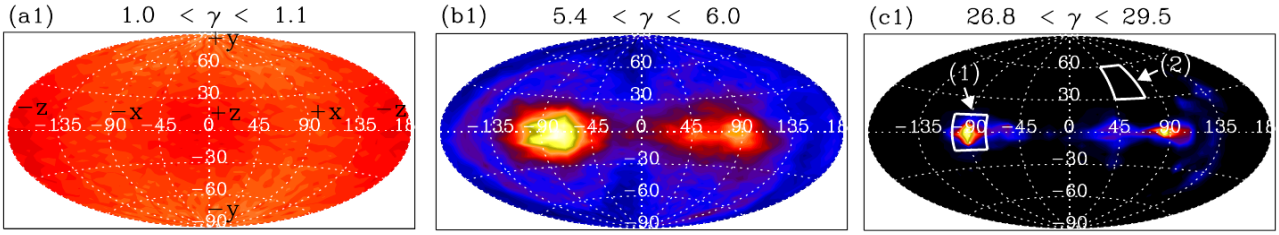

Figure 3.8: Energy-dependent angular distribution of the particle velocity distribution reconstructed from 2D PIC simulations of relativistic reconnection. Figure adapted from Cerutti et al. (2012b).

time, consistent with a linear-like acceleration.

We also found that the particle distribution within the layer is highly anisotropic due to the preferential direction of the reconnection electric field, the most energetic particles being the most beamed (see Figure 3.8), as we anticipated from test particle simulations (Cerutti et al. 2012a). This beaming mechanism differs from the usual achromatic relativistic Doppler beaming effect, and for this reason we called this effect the "kinetic beaming" (Cerutti et al. 2012b; Mehlhaff et al. 2020). This beaming is lost as soon as the particles enter the magnetic islands where they are confined by the magnetic field, and where their directions are randomized. Nonetheless, this anisotropy could be observed in the form of short bright flares in the strong radiative cooling regime which can apply near the high-energy cutoff, the best example being the Crab Nebula (see next section).

Mergers of large plasmoids can lead to an extra particle energy boost within the short-lived, perpendicular current sheets. The acceleration process is of similar nature as for the initial acceleration within secondary current layers. A recent study by Petropoulou & Sironi (2018) suggests that another regime of particle acceleration has been missed by previous studies at even larger system sizes. They found that while the early evolution of reconnection is consistent with linear-like acceleration episodes leading to $\gamma_{\rm max} \propto t$ and hard spectra, the late evolution is dominated by a slower, diffusive-like acceleration within large magnetic islands such that $\gamma_{\rm max} \propto \sqrt{t}$. This is accompanied by a spectral steepening allowing the maximum energy to grow significantly above the 4σ limit without any clear sign of saturation. This extra acceleration is attributed to the slow compression of magnetic islands. It is a promising way to accelerate particles to very high energies in astrophysical environments where σ may not be very high (of order unity), except of course in pulsar and black hole magnetospheres where $\sigma \gg 1$ is most likely guaranteed. If island compression is indeed the dominant acceleration process in reconnection, this also implies that the role of the kinetic scale physics at X-points becomes secondary. What happens at X-points could be seen as an injection mechanism which promotes a low-energy particle from the background plasma into a high-energy particle which will further be accelerated to even higher energies inside islands. Ironically, we can speculate that the full PIC simulation artillery may not be needed in the future, and resistive MHD simulations with

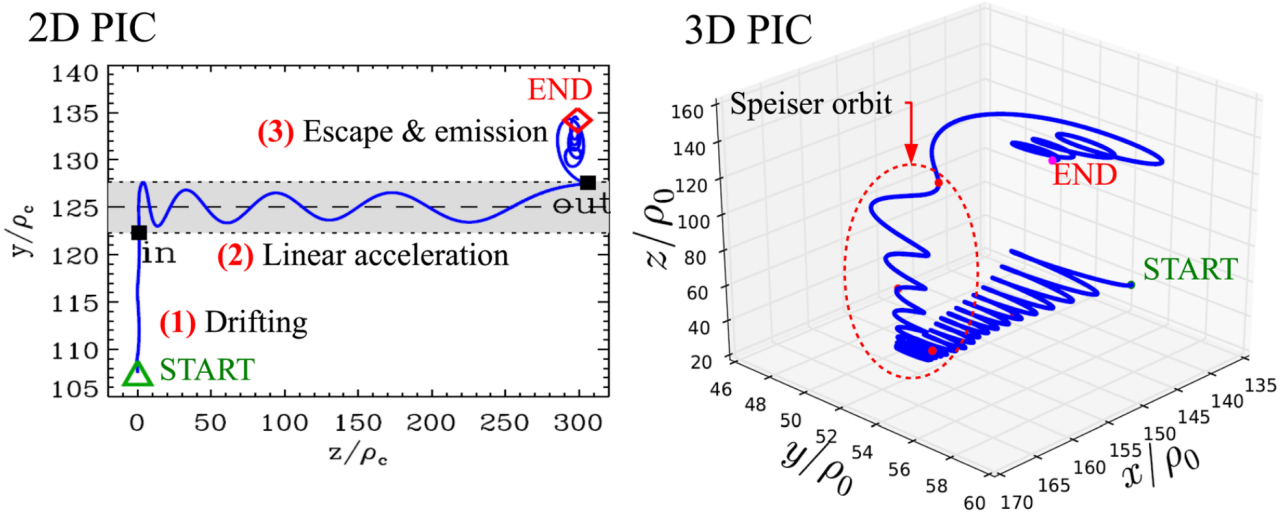

Figure 3.9: Typical PIC particle trajectory accelerated above the radiation-reaction limit in 2D (left panel) and 3D (right panel) PIC simulations. Figure adapted from Cerutti et al. (2014a).

test particles could come handy to explore larger, more realistic system sizes at a smaller numerical cost without missing much of the dominant particle acceleration physics.

3.6 Application to the Crab flares

To come back to what has initiated and motivated all this work, at least as far as I am concerned, we now consider a regime of special interest for the Crab gamma-ray flares. This regime is characterized by particle acceleration above the radiation reaction limit, i.e., the radiation reaction force is now turned on and can be as large as the Lorentz force. As we have shown in test-particle simulations, this can be achieved deep within the reconnection layer, where $E > B_\perp$, but does this happen in PIC simulations? The answer is a clear yes. Figure 3.9 shows the typical trajectory of a particle accelerated above the radiation reaction limit, both in 2D (top panel) and 3D simulations (bottom panel). The particle first drifts from the upstream into the current layer where it is linearly accelerated by the reconnection electric field above the radiative limit. Not only the trajectory follows a Speiser orbit, but the amplitude of the oscillatory motion perpendicular to the layer also shrinks at the rate we have predicted (Cerutti et al. 2012a). The particle is then pushed away towards an island where the perpendicular magnetic field suddenly increases and the particle loses its energy catastrophically over a sub-Larmor radius, i.e., it radiates synchrotron photon above the classical 160MeV limit. Figure 3.10 shows the total particle and synchrotron radiation energy spectra measured towards the end of the simulation, where we can see a clear excess above the radiation reaction limit.

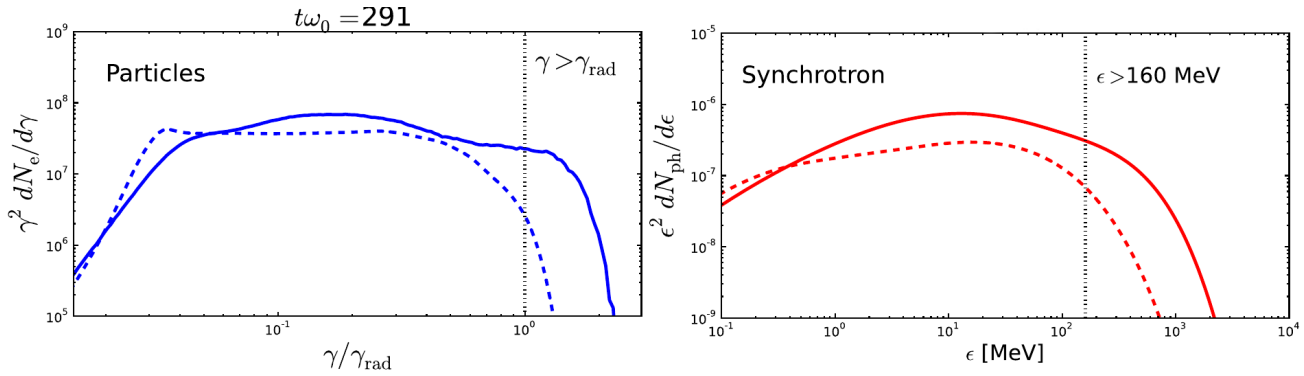

Figure 3.10: Total particle (left panel) and synchrotron radiation (right panel) spectra in 2D (solid lines) and 3D (dashed lines) PIC simulations with radiation reaction force turned on. The particle Lorentz factor is normalized to the classical radiation-reaction limit value defined in Eq. (1.4). Figure adapted from Cerutti et al. (2014a).

As mentioned in the previous section, this impulsive acceleration mechanism naturally produces a strong particle anisotropy, the higher the particle energy is, the higher the degree of anisotropy is (kinetic beaming). Under usual circumstances where radiative cooling is small, the radiative cooling time is larger than the acceleration time such that particles radiate while moving inside magnetic islands giving a nearly isotropic emission. In the strong cooling regime, particles radiate at the end point of their acceleration in the layer and therefore their emission is strongly beamed in a preferential direction. The beam direction changes rapidly and reflects the dynamics of the reconnection process (island formation, mergers). A static observer looking in the plane of the reconnection layer would see short, bright and symmetric in time flares as the reconnection beam sweeps by its line of sight (Figure 3.11, left panel), with a variability timescale as short as 6 hours. We proposed that particle acceleration deep inside the reconnection layer combined with the effect of the kinetic beaming could provide a viable explanation for the origin of the fast Crab Nebula gamma-ray flares. Figure 3.11 (right panel) shows the final 3D PIC synchrotron spectrum model compared with the Crab flare data. Our model can at least reproduce weak flares like the February 2009 one, stronger flare may be produced with a larger simulation box size but this issue has not been investigated due to limited numerical ressources at this time.

While this model addresses successfully some of the most puzzling features of the flares, such as the synchrotron photon energy above 160 MeV and the fast variability and energetic requirements, we are still left with an important open question: Where are the flares emitted in the Nebula? A fundamental consequence of the reconnection scenario is that the zone of interest must be highly magnetized, with $\sigma \gg 1$. However, the classical 1D MHD model of Kennel & Coroniti (1984) predicts a very low magnetization on average in the nebula, $\sigma = 3\times10^{-3}$. A higher magnetization would lead to a strong magnetic hoop stress that would squeeze and collimate the nebula along the pulsar rotation axis which would be at odds with

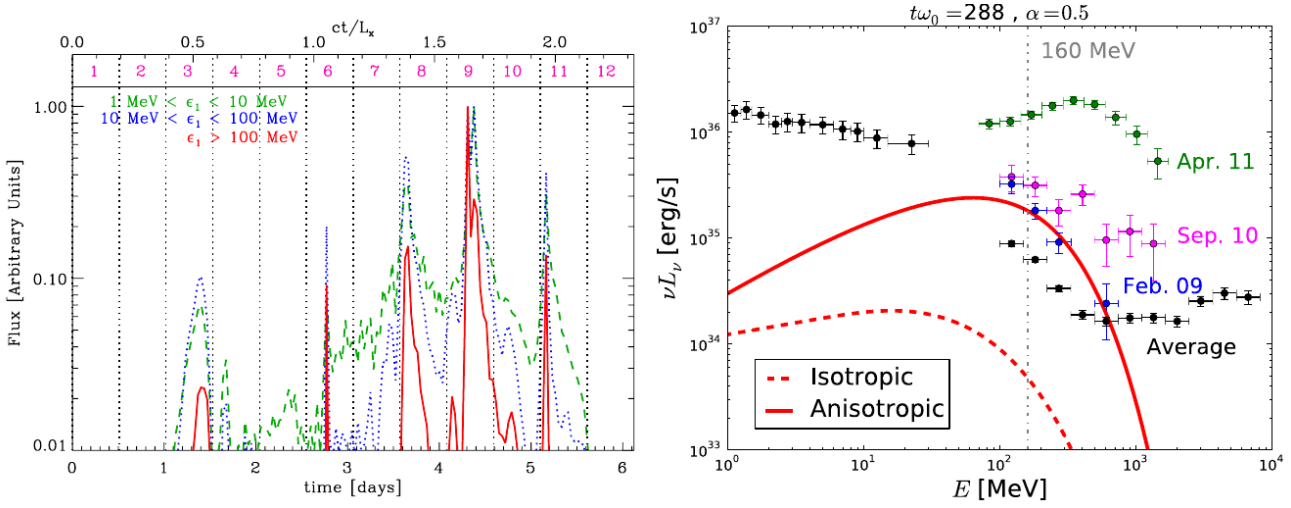

Figure 3.11: Energy-dependent synchrotron emission lightcurve produced within the reconnection layer seen by a distant observer. Total synchrotron spectrum produced by the reconnection event and comparison with the observed gamma-ray flare data. The quiescent emission are the black data points, as opposed to flaring emission given by the colored points. Figure adapted from Cerutti et al. (2013) and Cerutti et al. (2014b).

observations. 2D MHD simulations later confirmed this conclusion and showed that this limit could be pushed to $\sigma \sim 10^{-2}$.

This obvious discrepancy was partly lifted shortly after the publication of our model thanks to the first 3D MHD model of the Crab Nebula by Porth et al. (2013, 2014). This important study shows that 3D effects lead to a significant decrease of the magnetic hoop stress due to kink instabilities and magnetic dissipation in the nebula, as predicted by Begelman (1998). As a result, the mean magnetization in the nebula must be as large as $\sigma \sim 1$, and may be even higher, in order to explain all the details of the Crab Nebula morphology. Because of the anisotropic nature of the pulsar wind (see next part), the magnetization varies significantly with latitude, from nearly zero within the equatorial plane to high values, close to $\sigma \sim 10$ at high latitudes. The formation of current sheets in the magnetized environment of the polar and jet regions is seen as the most promising location of the flares (Cerutti et al. 2012a; Lyubarsky 2012; Komissarov 2013; Mignone et al. 2013). Kink-like motion of the Crab jet as notoriously known in the Vela pulsar wind nebula (Pavlov et al. 2003; Durant et al. 2013), and perhaps already seen in the Crab Nebula (Weisskopf 2011), could be a clear manifestation of dissipation in the nebula.

There is still one last, yet critical, unsolved issue. As discussed in the previous section, the high-energy cut-off of the particle spectrum is limited to about 4σ. Particle acceleration within islands at later times is not an option here because (1) this process is too slow, and (2) ideal MHD applies within islands so the the maximum energy will be limited by the radiation reaction force. If the bulk of the pairs is injected at TeV energies in the Nebula as usually assumed, $\gamma_0 \sim 10^6$, and

taking $\sigma = B_0^2/4\pi\gamma_0 n_0 mc^2 \sim 10$ would give $\gamma_{\rm max} \sim 4\gamma_0\sigma_0 \sim 4\times10^7$, which is too small in comparison with the $\gamma_{\rm max} \sim 10^9$ required to power the flares.

In a recent study in collaboration with Gwenael Giacinti, postdoctoral fellow in Heidelberg, we showed that a complete revisit of particle acceleration in highly magnetized, anisotropic shocks may bring new insights into this issue (Cerutti & Giacinti 2020). This is a promising new approach to this problem that we are intending to pursue in the near future.

Part II

Pulsar magnetospheres

This new chapter in my scientific life began when I moved to Princeton at the end of the summer 2013. Like in Boulder, this research activity has been strongly influenced by a particularly fortunate encounter, the one with Sasha Philippov, a protégé of Vasily Beskin and PhD student of Anatoly Spitkovsky. I knew little about how pulsar worked in details when I arrived, but I knew this would be the best environment to study particle acceleration in relativistic reconnection under strong radiative cooling. `Zeltron` was all ready for it. This is what convinced me to come to Princeton. Shortly after my arrival, Sasha and Anatoly published the very first global PIC model of an aligned pulsar magnetosphere (Philippov & Spitkovsky 2014), which showed everyone that such an ambitious enterprise, as impossible as it may sound (in particular at this time), was in fact possible. Perhaps more importantly, it also demonstrated that PIC simulations were very promising to make further progress in the field and the next logical step following the breakthroughs of MHD simulations in the late nineties and early 2000 (Contopoulos et al. 1999; Spitkovsky 2006). The discovery of a few hundred gamma-ray pulsars by the *Fermi*-LAT (Abdo et al. 2010b, 2013) has also revived a strong interest of the commmunity onto the old problem of pulsar electrodynamics.

To this end and as a first step, I developed a global high-resolution 2D axisymmetric PIC model to investigate the role of plasma supply in structuring pulsar magnetospheres, and I performed a detailed analysis of particle acceleration via particle tracking to establish the role of reconnection. This work required significant code development to adapt `Zeltron` to a spherical grid as well as non-standard boundary conditions for both the fields and the particles (e.g., plasma injection, open boundaries). These new technical developments are reported in Chapter 5. This first axisymmetric model marked another important milestone in my research because it became the elementary building block of all the models and studies that followed, including black hole magnetospheres. I then report on the main results obtained with this 2D axisymmetric setup in the context of an isolated aligned pulsar. Next, I describe new extensions done to this setup to include ions and the study of their acceleration in millisecond pulsars, and interacting magnetospheres in the context of binary pulsar systems.

My next objective was to combine this new setup with the radiative capabilities of `Zeltron` to focus on the origin of the incoherent (i.e., high-energy as opposed to the coherent radio emission) pulsed emission. Observed pulsars are most likely inclined rotators, meaning that the rotation and the magnetic axes are not aligned, and therefore full 3D effects must be taken into account to capture the pulsar phenomenon. After extending the code to a full 3D spherical domain, I performed the first ab-initio modeling of high-energy pulsar lightcurves which establishes its origin to the base of the equatorial current sheet, at odds with the classical models where the loci of emission lie within the light-cylinder radius, but consistent with Lyubarskii (1996) remarkable prediction. This work is described in Chapter 6. I show that the model reproduces well some of the basic features of the gamma-ray pulsed profiles observed by the *Fermi*-LAT. I argue that phase-resolved polarization

is probably the best diagnostic to disentangle between models in the future. Last, I report on a more recent project which focuses on the pulsar wind region and magnetic dissipation and particle acceleration within the equatorial current sheet at large scales. To probe these distant regions, simulations on an unprecedented large scale have been carried out in 2D and more recently in full 3D. The later required to move to the next level of computing power available in Europe, i.e., Tier-0 via a PRACE allocation successfully granted to us in the fall 2018 (17^{th} call).

We begin this new part with a brief introduction to pulsar electrodynamics.

Chapter 4

Pulsar electrodynamics

This chapter is based on an ISSI working group review paper that I wrote in 2016 in collaboration with Andrei Beloborodov, professor at Columbia University (Cerutti & Beloborodov 2017). It aims at briefly introducing the basic concepts of pulsar electrodynamics from a theoretical perspectives that will be important to interpret the simulations results presented in the following chapters. Other relevant reviews in the field are by Arons (1979, 2009, 2012); Michel & Li (1999); Michel (2004); Grenier & Harding (2015); Beskin et al. (2015); Pétri (2016).

4.1 Introduction

Pulsars are compact ($r_\star \sim 10$km, $M_\star \sim 1$–$2\mathrm{M}_\odot$), strongly magnetized ($B_\star \sim 10^9$–10^{15}G), and rapidly rotating ($P_\star \sim 1$–1000ms) neutron stars. They represent great laboratories to probe extreme physical conditions, e.g., super-strong electromagnetic fields, strong gravitational field, super-nuclear densities, particle acceleration and relativistic outflows. Shortly after the discovery of neutrons, Baade & Zwicky (1934) hypothesized that neutron stars would form after the collapse of massive stars and the forthcoming supernovae explosions. Pulsars were also invoked to explain the additional source of energy needed to explain the late activity at the center of supernova remnants like in the Crab Nebula (Pacini 1967). They were then serendipitously discovered as pulsating radio sources in 1967 (Hewish et al. 1968) and quickly associated to spinning neutron stars, especially thanks to the remarkable stability of the pulsations (Pacini 1968; Gold 1968). The precise measurements of both the rotation period and the spinning down of the star provide an extremely accurate knowledge of both the total energy reservoir, and the total power (seen and unseen) released by the star. This is a real advantage in comparison with other astrophysical compact objects.

Thanks to multi-wavelength observations, we know that pulsars radiate throughout the electromagnetic spectrum, from radio waves up to very-high energy gamma rays. *Fermi*-LAT observations revealed that young rotation-powered pulsars radiate away a significant fraction of their spindown power (typically 1-10%) in the high-energy gamma-ray band (0.1-10 GeV, Abdo et al. 2010b, 2013). This result

suggests that pulsars are efficient particle accelerators. The origin of particle acceleration and radiation are still largely unsolved problems today, but it appears clear that these processes must happen in the magnetosphere of an oblique rotator, i.e., where the magnetic axis is misaligned with the rotation axis. Hence, one needs to understand really well what is happening in the magnetosphere. At first sight, this looks like a fairly well-posed problem, but behind this apparent simplicity there is a complex interplay between electrodynamics, plasma physics, particle acceleration and creation, and non-thermal radiation.

I summarize some of the theoretical efforts developed over the last 50 years to model pulsar magnetospheres. I will focus on the close environment of the star, delimited by the stellar surface up to a few light-cylinder radius, $R_{\rm LC}$, the latter being defined where the co-rotation velocity with the star equals the speed of light. This introduction is relevant to rotation-powered pulsars ; accreting (X-ray pulsars) or highly magnetized pulsars (magnetars) follow a different dynamics and phenomenology that I do not address here. I adopt a simple heuristic approach to the development of pulsar magnetosphere theory which approximatively follows the chronological order, from the early models of vacuum (Sect. 4.2) and charge-separated magnetospheres (or "electrospheres", Sect. 4.3) to the plasma-filled force-free magnetosphere solutions (Sect. 4.4).

4.2 Vacuum magnetospheres: The Deutsch fields

In the early models of pulsar magnetosphere, the star is surrounded by near vacuum (Pacini 1967, 1968; Ostriker & Gunn 1969). The argument behind this assumption is that the gravitational field at the surface of the star is too strong to allow for a dense plasma to fill the magnetosphere (Hoyle et al. 1964). This assumption is most likely incorrect as we will see in the next section. Nevertheless, it is useful to have this model in mind to understand how particles are injected into the magnetosphere (Sect. 4.3). For illustrative purposes and for simplicity, we consider only the case where the magnetic dipole moment of the star, $\boldsymbol{\mu}$, is aligned with the rotation axis. The aligned rotator will guide us through the main features of the magnetosphere. This simplier configuration also played an important role in the development of the theory of pulsar magnetospheres.

It is commonly accepted that neutron stars are very good electric conductors. If the star is at rest and neglecting the effect of gravity, the electric field inside the star would vanish for an infinite conductivity, i.e., $\mathbf{E}_{\rm int} = \mathbf{0}$. Now, if the star is rapidly rotating, this condition is replaced by

$$\mathbf{E}_{\rm int} + \frac{\mathbf{V} \times \mathbf{B}_{\rm int}}{c} = \mathbf{0}, \tag{4.1}$$

where $\mathbf{V} = \boldsymbol{\Omega} \times \mathbf{r}$, and $\Omega = c/R_{\rm LC}$ is the stellar angular velocity. This condition implies that the star is polarized by the rotation, very much like in a Faraday disk ("unipolar induction"). Charges would quickly rearrange inside the star to

compensate the Lorentz force exactly, with an excess of negative charges at the poles and positive charges at the equator (for $\mathbf{\Omega}\cdot\boldsymbol{\mu} > 0$ and vice-versa if $\mathbf{\Omega}\cdot\boldsymbol{\mu} < 0$). Charges would also be in rigid co-rotation with the star, such that

$$\mathbf{V} = c\frac{\mathbf{E}_{\rm int}\times\mathbf{B}_{\rm int}}{B_{\rm int}^2} = r\sin\theta\Omega\mathbf{e}_\phi, \tag{4.2}$$

where we use the usual spherical coordinate system (r,θ,ϕ). With these properties in mind, and using the boundary conditions for the electromagnetic fields at the surface of the star, Davis (1947); Deutsch (1955); Hones & Bergeson (1965) derived the structure of the external fields (i.e., for $r > r_\star$). For a dipolar magnetic field in vacuum[1], and assuming that the star has no net charge, the fields near the star are given by (for $r \ll R_{\rm LC}$, Michel & Li 1999)

$$B_{\rm r} = 2B_\star\left(\frac{r_\star}{r}\right)^3\cos\theta \tag{4.3}$$

$$B_\theta = B_\star\left(\frac{r_\star}{r}\right)^3\sin\theta \tag{4.4}$$

$$B_\phi = 0 \tag{4.5}$$

$$E_{\rm r} = \frac{\Omega r_\star B_\star}{c}\left(\frac{r_\star}{r}\right)^4\left(1-3\cos^2\theta\right) \tag{4.6}$$

$$E_\theta = -\frac{\Omega r_\star B_\star}{c}\left(\frac{r_\star}{r}\right)^4\sin 2\theta \tag{4.7}$$

$$E_\phi = 0, \tag{4.8}$$

where $B_\star = \mu/r_\star^3$ is the magnetic field strength at the equator. The external electric field has a pure quadrupolar structure (see Figure 4.1). If the star has a net electric charge Q, the radial electric field would admit an additional monopolar component.

The net Poynting flux from the aligned rotator (integrated over a sphere of radius $r > r_\star$) vanishes, $L_{\rm vac} = 0$. Therefore, the rotating star does not lose energy and hence does not spin down. The vacuum solution can be generalized to the case of an oblique rotator, where the magnetic moment is inclined at an angle χ relative to the rotation axis. In this case, the net Poynting flux becomes (Pacini 1968; Ostriker & Gunn 1969)

$$L_{\rm vac} = \frac{2}{3}\frac{\mu^2\Omega^4}{c^3}\sin^2\chi. \tag{4.9}$$

4.3 Electrosphere: The Goldreich-Julian solution

From the vacuum solution (Eqs. 4.3-4.8), one immediately realizes that there is a strong unscreened component of the electric field parallel to the magnetic field,

[1] The Deutsch solution was generalized to arbitrary multipolar order by Bonazzola et al. (2015); Pétri (2015).

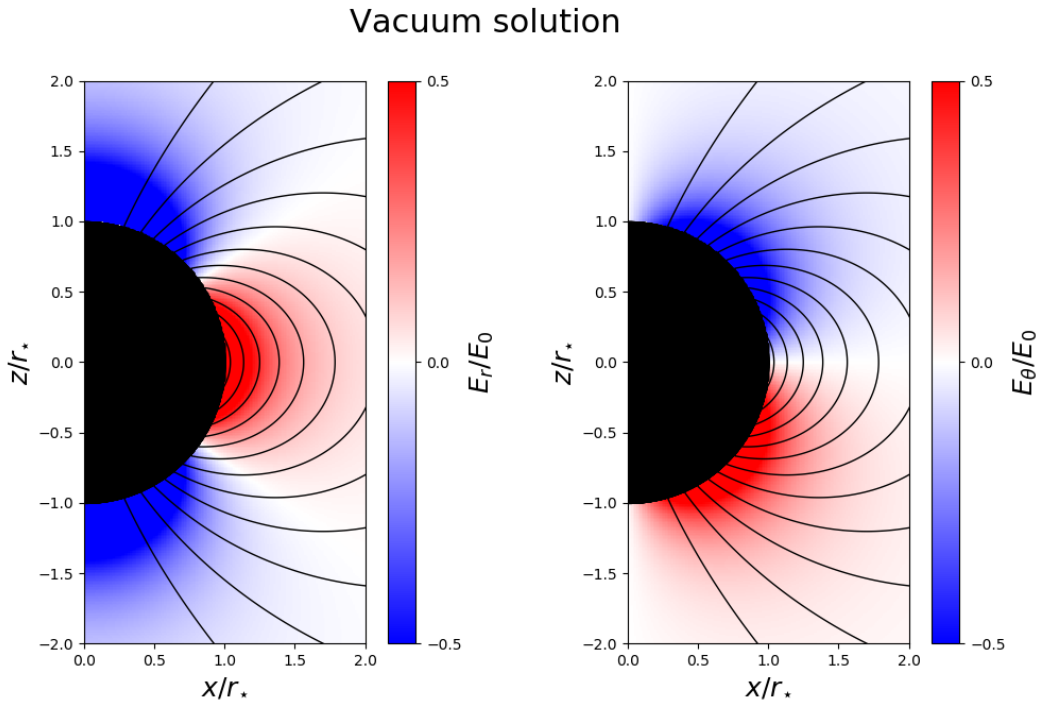

Figure 4.1: External electric field (left: $E_{\rm r}$, right: E_θ) induced by the rotation of an aligned perfectly conducting neutron star in vacuum (Michel & Li 1999). Electric fields are normalized to $E_0 = \Omega r_\star B_\star / c$. Black solid contours represent magnetic field lines.

i.e., $\mathbf{E}_\parallel = \mathbf{E}\cdot\mathbf{B}/\mathbf{B}^2 \neq 0$. This is in contrast with the interior of the star where $\mathbf{E}\cdot\mathbf{B} = 0$ everywhere. Goldreich & Julian (1969) pointed out that the potential difference at the surface of the star would largely overcome any work function and the gravitational potential. Hence, charges would be extracted and accelerated from the surface of the star and fill the magnetosphere until the charge density is dense enough to screen the parallel electric field. The minimum charge density needed to achieve this is

$$\rho_{\rm GJ} = \frac{1}{4\pi}\boldsymbol{\nabla}\cdot\mathbf{E}_{\rm co} = -\frac{1}{4\pi c}\boldsymbol{\nabla}\cdot((\boldsymbol{\Omega}\times\mathbf{r})\times\mathbf{B}) \tag{4.10}$$

$$= -\frac{1}{4\pi c}\left[-(\boldsymbol{\Omega}\times\mathbf{r})\cdot(\boldsymbol{\nabla}\times\mathbf{B}) + \mathbf{B}\cdot\boldsymbol{\nabla}\times(\boldsymbol{\Omega}\times\mathbf{r})\right] \tag{4.11}$$

$$= \frac{1}{4\pi c}(\boldsymbol{\Omega}\times\mathbf{r})\cdot(\boldsymbol{\nabla}\times\mathbf{B}) - \frac{\boldsymbol{\Omega}\cdot\mathbf{B}}{2\pi c}. \tag{4.12}$$

Since these charges are in co-rotation with the star, they generate an electric current such that

$$\boldsymbol{\nabla}\times\mathbf{B} = \frac{4\pi}{c}\mathbf{J} = \frac{4\pi}{c}\rho_{\rm GJ}(\boldsymbol{\Omega}\times\mathbf{r}), \tag{4.13}$$

which gives the final result (Goldreich & Julian 1969)

$$\rho_{\rm GJ} = -\frac{\boldsymbol{\Omega}\cdot\mathbf{B}}{2\pi c}\frac{1}{1-(\boldsymbol{\Omega}\times\mathbf{r})^2/c^2}. \tag{4.14}$$

In practice, we will always neglect the relativistic corrections which appear in the denominator, i.e., $\Omega r/c \ll 1$, which is a good approximation near the stellar surface, so that

$$\rho_{\rm GJ} \approx -\frac{\mathbf{\Omega}\cdot\mathbf{B}}{2\pi c} = -\frac{\Omega B_\star}{2\pi c}\left(\frac{r_\star}{r}\right)^3\left(3\cos^2\theta - 1\right), \tag{4.15}$$

for a dipolar field. Goldreich & Julian (1969) envisioned a fully charged-separated magnetosphere (or "electrosphere") instead of pure vacuum, with negative charges at the poles and positive charges at the equator (for $\mathbf{\Omega}\cdot\boldsymbol{\mu} > 0$) separated by a null surface, i.e., $\rho_{\rm GJ}\left(\theta_{\rm null}\right) = 0$, located at $\theta_{\rm null} = \cos^{-1}\left(1/\sqrt{3}\right) \approx 55^{\rm o}$ at the surface of the star for a dipole (see Figure 4.2).

Some of the main features of this scenario were confirmed by several groups using iterative or PIC numerical simulations (Krause-Polstorff & Michel 1985a,b; Shibata 1989; Neukirch 1993; Thielheim & Wolfsteller 1994; Smith et al. 2001; Pétri et al. 2002b; Spitkovsky & Arons 2002; McDonald & Shearer 2009; Wada & Shibata 2011; Philippov & Spitkovsky 2014; Cerutti et al. 2015). In almost all cases, simulations are initiated with the vacuum solution and zero work function at the surface of the star. Then, as expected, the surface electric field extracts charges from the star, which fill out the magnetosphere to form a perfectly charge-separated structure. The equilibrium configuration looks like a dome of electrons on top of both poles, and an equatorial torus of positive charges at about the Goldreich-Julian charge density (Eq. 4.15). Both species are separated by a large vacuum gap along the null surface. Figure 4.2 presents the charge spatial distribution obtained from a 2D axisymmetric PIC simulation of the aligned electrosphere similar to what is presented in Cerutti et al. (2015).

In contrast to the original Goldreich & Julian (1969) scenario, numerical simulations show no particle outflow through the light-cylinder, but instead, charges are electrostatically trapped very close to the star. There are no currents so no spindown, in other words the pulsar is "dead". However, Pétri et al. (2002a); Spitkovsky & Arons (2002) realized that the disk of charges in the equator is not in rigid co-rotation. A velocity shear causes the disk to be unstable to the diocotron instability, the analog of the Kelvin-Helmholtz instability in neutral fluids, which can be captured by 3D simulations (the unstable modes are not axisymmetric). This instability induces a drift of the disk outward and even result in an outflow through the light cylinder. Unfortunately, the densities are too low to drive strong currents and a powerful wind, and explain the pulsar spindown. Pétri (2007) showed that the situation is even more desperate because the diocotron instability is suppressed when relativistic effects become important near the light cylinder.

The bottom line is that the electrosphere model might not a good description either of active pulsars. However, it could be appropriate to model old inactive pulsars.

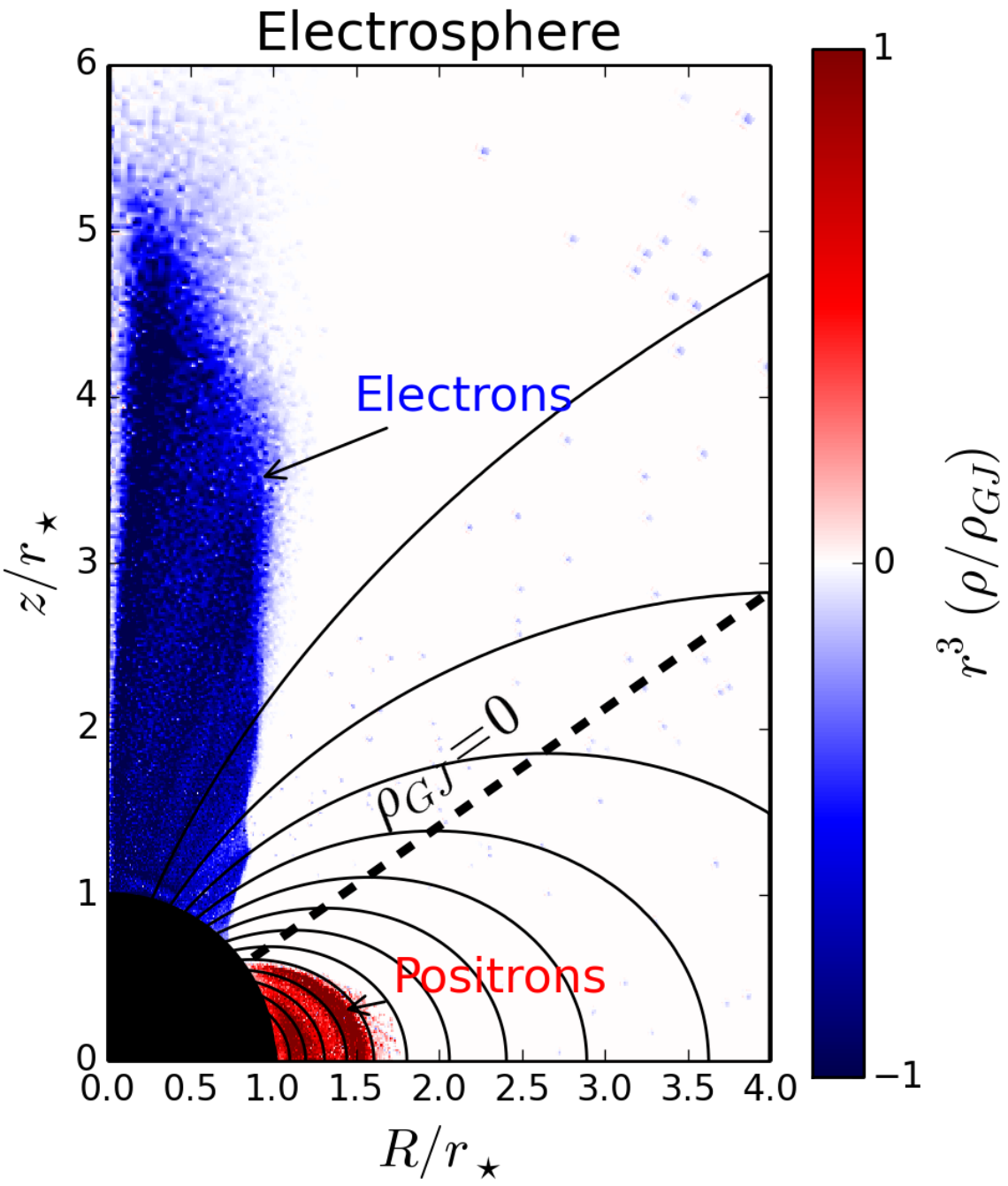

Figure 4.2: Fully charge-separated solution (electrosphere) of the aligned rotator ($\boldsymbol{\Omega} \cdot \boldsymbol{\mu} > 0$) obtained with a 2D axisymmetric PIC simulation after one rotation period (Cerutti et al. 2015). Electrons form a dome on top of each pole (in blue), while positive charges (here positrons, in red) form the equatorial torus. Both species are contained well within the light-cylinder radius, here set at $R_{\rm LC} = 6r_\star$. Charge densities are normalized by the surface Goldreich-Julian density. Solid contours are magnetic field lines and the oblique dashed line shows the null surface (where $\rho_{\rm GJ} = 0$).

4.4 Force-free magnetosphere: The plasma-filled solution

Observations and models of pulsar wind nebulae suggest that pulsars provide a large supply of electron-positrons pairs, well above the fiducial Goldreich-Julian density $n = \kappa n_{\rm GJ} = \kappa \rho_{\rm GJ}/e$, where $\kappa \gg 1$ is the multiplicity (Hibschman & Arons 2001a,b). This dense plasma cannot be created by pulling off charges from the star only, there must be copious pair creation in the magnetosphere (Sturrock 1971; Ruderman & Sutherland 1975; Daugherty & Harding 1982). The basic picture is that as the primary particles are accelerated by $\mathbf{E}_{\parallel}$ along the curved field lines, they emit gamma-ray curvature radiation that is quickly absorbed by the intense magnetic field to form a pair (Erber 1966; Harding & Lai 2006). This process ignites an electromagnetic cascade of gamma rays and pairs until the density of the plasma is high enough to short out the accelerating electric field, so that the ideal magnetohydrodynamic condition $\mathbf{E} \cdot \mathbf{B} = 0$ applies.

4.4.1 Analytical solution: the monopole

In the limit where the electromagnetic force dominates over the plasma inertia and other external forces such as gravity and pressure gradient, the plasma dynamics is solely governed by the force-free condition

$$\rho \mathbf{E} + \frac{\mathbf{J} \times \mathbf{B}}{c} = \mathbf{0}, \tag{4.16}$$

where ρ and $\mathbf{J}$ are the charge and current densities. In steady state axisymmetric MHD, it is possible to translate the force-free condition into the so-called "pulsar equation" (Scharlemann & Wagoner 1973; Michel 1973b). Unfortunately, there is no known analytical solution to this equation for a dipolar field. Instead, Michel (1973b) found an exact solution for a monopolar magnetic field. Although not physically sound, this result is very instructive because it captures a number of important features also found in the dipole case. In particular, this configuration turns out to be relevant for describing the pulsar wind zone, beyond the light-cylinder. Michel's solution is given by (in spherical coordinates)

$$B_{\rm r} = B_\star \left(\frac{r_\star}{r}\right)^2 \tag{4.17}$$

$$B_\theta = 0 \tag{4.18}$$

$$B_\phi = -B_\star \left(\frac{r_\star}{R_{\rm LC}}\right)\left(\frac{r_\star}{r}\right)\sin\theta \tag{4.19}$$

$$E_{\rm r} = 0 \tag{4.20}$$

$$E_\theta = B_\phi \tag{4.21}$$

$$E_\phi = 0. \tag{4.22}$$

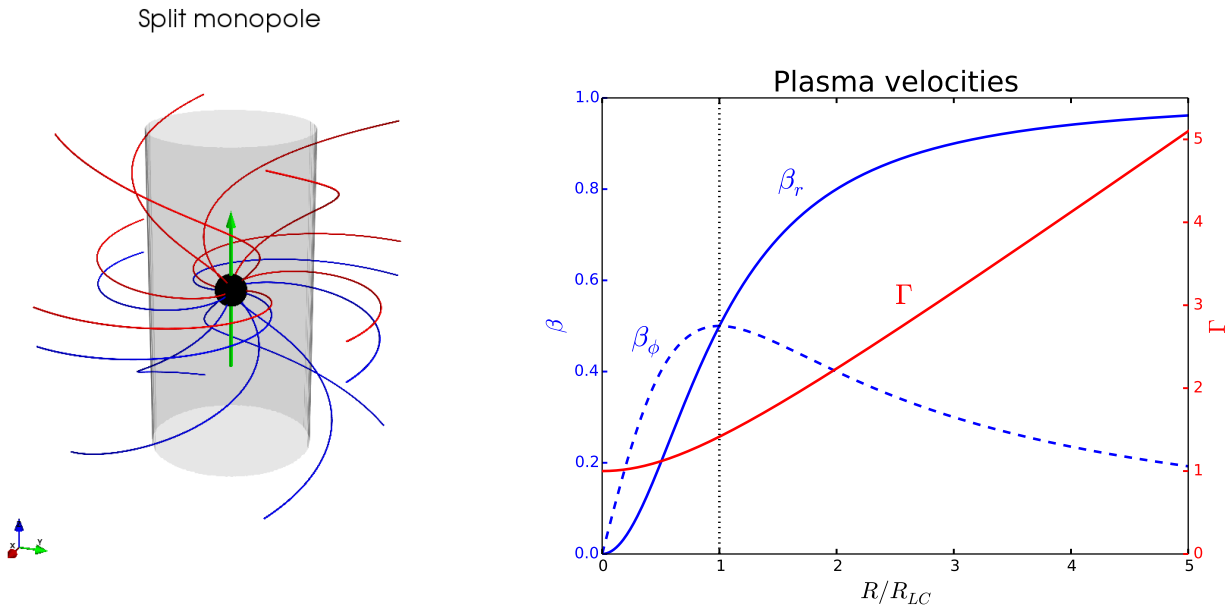

Figure 4.3: Analytical solution of the aligned split monopole (Michel 1973b). Left: Magnetic field line structure winding up around the star (black sphere) due to the stellar rotation. The green arrow is the rotation axis of the star. Red lines represent outgoing field lines while blue lines show the incoming field lines. The field changes its polarity in the equator. The magnetosphere contained within the light-cylinder radius is shown in grey. Right: $\mathbf{E} \times \mathbf{B}$ drift velocity (solid line: $\beta_\mathrm{r} = V_\mathrm{r}/c$, dashed line: $\beta_\phi = V_\phi/c$) and Lorentz factor ($\Gamma = 1/\sqrt{1-\beta^2}$) as a function of the cylindrical radius to the star.

The associated current density is purely radial,

$$\mathbf{J} = \frac{c}{4\pi}\left(\nabla \times \mathbf{B}\right) = -\frac{\mathbf{\Omega}\cdot\mathbf{B}}{2\pi}\mathbf{e}_\mathrm{r} = c\rho_\mathrm{GJ}\mathbf{e}_\mathrm{r}, \tag{4.23}$$

meaning that the current can be carried away by one sign of charge pulled out from the star and moving at close to the speed of light. To ensure that we have $\nabla \cdot \mathbf{B} = 0$, this solution can be applied to one hemisphere only. In the opposite hemisphere, we must change $\mathbf{B} \to -\mathbf{B}$, $\mathbf{E} \to -\mathbf{E}$, and $\mathbf{J} \to -\mathbf{J}$, i.e., we must form a "split monopole". The reversal of the magnetic field along the equator implies that a current sheet must form there (missing in Eq. 4.23) that carries the necessary return current back to the star and ensures that the net charge of the star does not grow indefinitely. We will come back to the essential role of the return current layer later.

Field lines are purely radial close to the star ($r \sin\theta \ll R_\mathrm{LC}$), and starts winding up around the pulsar with increasing distance (see Figure 4.3, left panel). At the light-cylinder radius, the poloidal and toroidal magnetic components are equal near the equator, i.e., the field line makes a 45° angle with the radial direction. Far from the light cylinder, the field is almost purely toroidal. Contrary to the vacuum solution, the split-monopole solution predicts that the aligned rotator is spinning

down at a rate given by the outflowing Poynting flux, i.e.,

$$L_{\rm mono} = \iint \mathbf{\Pi} \cdot \mathbf{e}_{\rm r} dS = \frac{2cB_\star^2 r_\star^4}{3R_{\rm LC}^2}, \tag{4.24}$$

where $\mathbf{\Pi} = (c/4\pi)\,\mathbf{E}\times\mathbf{B}$ is the Poynting vector. This result applies also to oblique split monopole, i.e., it does not depend on the inclination angle χ (Bogovalov 1999).

In the large pair supply limit, the plasma motion is set by the $\mathbf{E}\times\mathbf{B}$ drift velocity given by,

$$\mathbf{V} = c\frac{\mathbf{E}\times\mathbf{B}}{\mathbf{B}^2} = \frac{c\,\mathbf{e}_{\rm r}}{1+\left(\frac{R_{\rm LC}}{R}\right)^2} + \frac{R\Omega\,\mathbf{e}_\phi}{1+\left(\frac{R}{R_{\rm LC}}\right)^2}, \tag{4.25}$$

where $R = r\sin\theta$ is the cylindrical radius[2]. Close to the star ($R/R_{\rm LC} \ll 1$), the plasma is in solid rotation, i.e., $\mathbf{V} \approx R\Omega\,\mathbf{e}_\phi$. Far from the light cylinder, the plasma flies away radially at the speed of light, $\mathbf{V} \approx c\,\mathbf{e}_{\rm r}$, and form a relativistic wind (Figure 4.3, right panel). It follows from Eq. (4.25) that the bulk Lorentz factor of the flow is given by

$$\Gamma = \sqrt{1+\left(\frac{R}{R_{\rm LC}}\right)^2}, \tag{4.26}$$

so the pulsar wind accelerates linearly with cylindrical radius beyond the light cylinder (Buckley 1977; Contopoulos & Kazanas 2002).

4.4.2 Numerical solutions: the dipole

Contopoulos et al. (1999) obtained the structure of the aligned dipole in rotation by direct numerical integration of the pulsar equation (see also, Goodwin et al. 2004; Gruzinov 2005; Timokhin 2006). The solution of the force-free magnetosphere presents the following essential features, depicted schematically in Figure 4.4: (i) a closed zone, (ii) an open zone, and (iii) current sheets. In contrast to the split-monopole configuration, the solution presents closed magnetic field lines co-rotating with the star, which correspond approximatively to the vacuum dipolar field lines that are closing within the light-cylinder. The plasma contained within this region is trapped and does not participate to the pulsar activity. The field lines near the rotation axis cross the light cylinder. They open to infinity due to the effective inertia of the magnetic field lines (Michel 1973a) and not due to the plasma inertia since it is negligible by construction (i.e., the force-free condition). Considering a pure dipolar field, the bundle of open field lines at the polar cap of the star has an angular size given by

$$\sin^2\theta_{\rm pc} = \frac{r_\star}{R_{\rm LC}}. \tag{4.27}$$

[2]This would not be valid if the magnetosphere was perfectly charge-separated. In this case, charges must travel close to the speed of light to carry the necessary current, see Eq. (4.23).

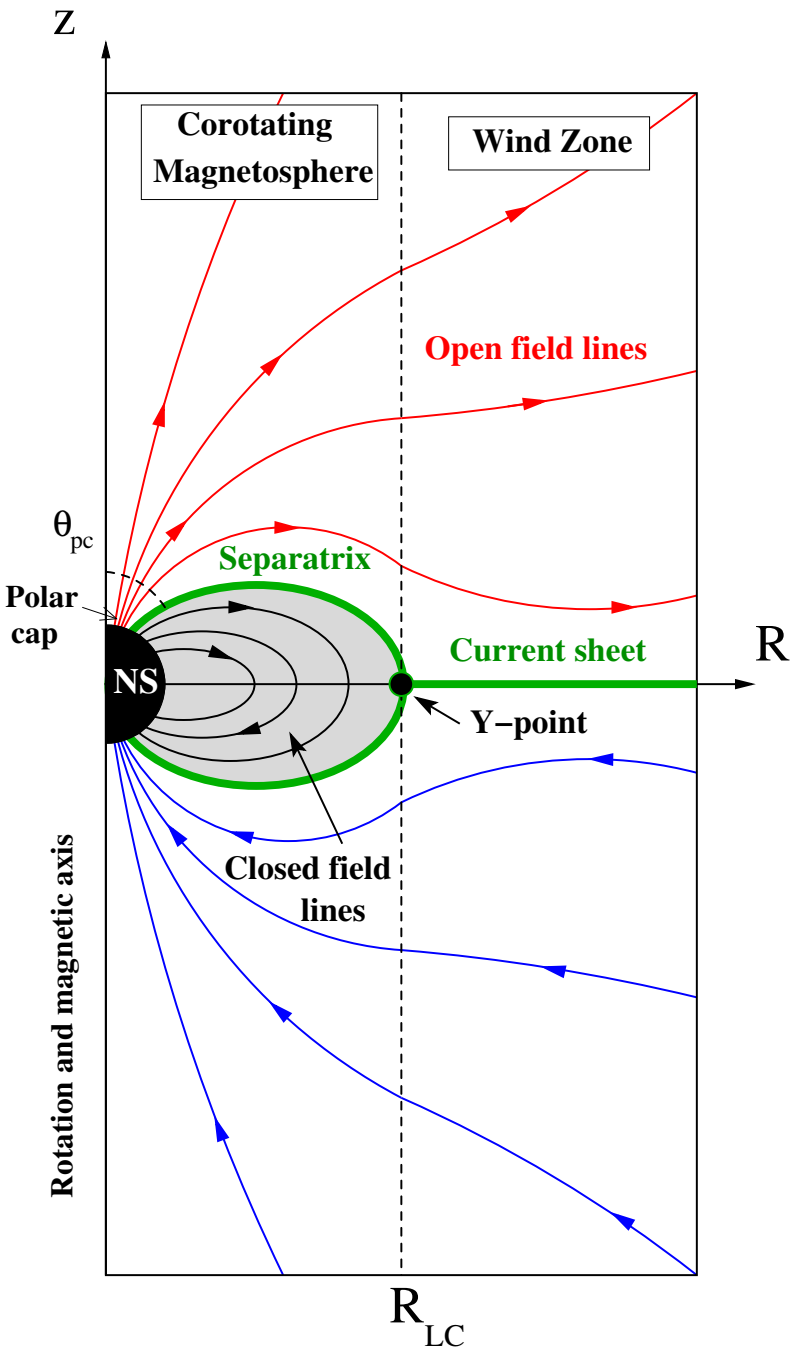

Figure 4.4: Sketch of the ideal force-free magnetosphere of the aligned dipole pulsar. The main elements are: (i) The closed field line region (grey, and black field lines) lying between the star surface and the light-cylinder radius. This zone is dead as it does not participate to the pulsar activity. (ii) The open field line region (red and blue field lines) extend beyond the light cylinder, carries the polar cap current, the outflowing Poynting flux and the relativistic pulsar wind. (iii) The equatorial current sheet separating both magnetic polarities in the wind zone, and the separatrix current sheets flowing in between the last open and the first closed field lines (shown in green), and the Y-point connecting both sheets. These sheets enable the polar-cap currents to close back to the star.

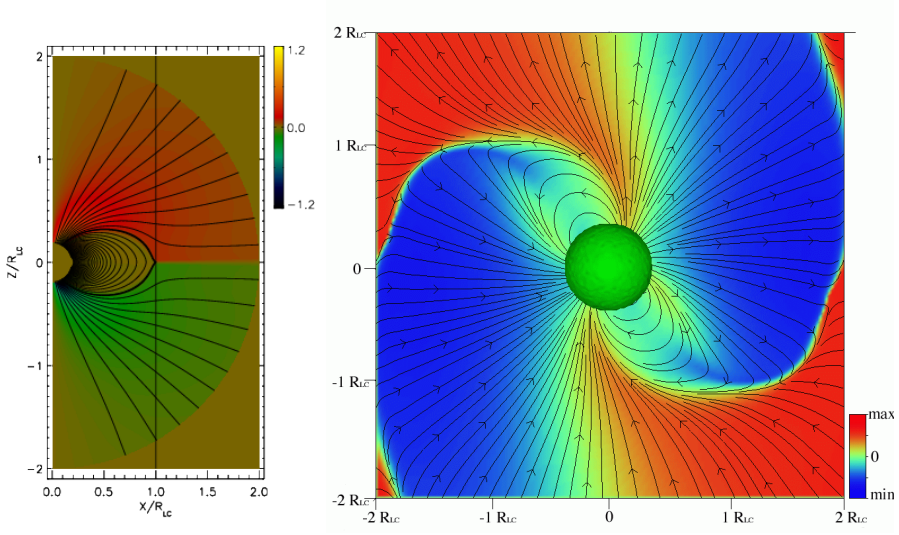

Figure 4.5: Time-dependent force-free simulations of the aligned (left) and oblique (right, $\chi = 60^{\rm o}$ in the $\boldsymbol{\Omega} - \boldsymbol{\mu}$ plane) rotators from Spitkovsky (2006). Solid lines represent magnetic field lines while the colors give the amplitude of the magnetic field perpendicular to the plane (i.e., the toroidal field in the left panel).

In real pulsars, $r_\star/R_{\rm LC} \ll 1$ so that only a small fraction of the field lines are open. Yet, this region carries the polar-cap current and the outflowing Poynting flux in the wind zone. This is the active part of the magnetosphere which can slow down the star. To quantify the amount of open field lines, it is convenient to work with the magnetic flux function, Ψ, defined as (in axisymmetric MHD)

$$\mathbf{B}_{\rm P} = \frac{\nabla\Psi \times \mathbf{e}_\phi}{r\sin\theta}, \tag{4.28}$$

with $\mathbf{B}_{\rm P} = \mathbf{B}_{\rm r} + \mathbf{B}_\theta$ is the poloidal magnetic field. Then, the magnetic flux across the polar cap is

$$\Psi_{\rm pc} = \int_0^{\theta_{\rm pc}} B_{\rm r} r^2 \sin\theta d\theta = \frac{\mu}{R_{\rm LC}}. \tag{4.29}$$

In fact, numerical simulations show that the amount of flux is slightly larger than $\Psi_{\rm pc}$ (by about 30%) because the polar cap is wider in the force-free magnetosphere than in the vacuum dipole case (e.g., Bai & Spitkovsky 2010a,b). The pulsar spindown power can be obtained with order of magnitude estimates (e.g., see Arons 2009). At the light cylinder, the poloidal and the toroidal magnetic components are comparable (in the split monopole they are exactly equal), then $B_\phi(R_{\rm LC}) \sim \mu/R_{\rm LC}^3$. With $E_\theta \approx B_\phi$, we have $L \sim 4\pi R_{\rm LC}^2 \times (c/4\pi) B_\phi^2$ which gives

$$L_0 \approx \frac{\mu^2\Omega^4}{c^3}. \tag{4.30}$$

We implicitly assumed above that the last closed field line touches the light-cylinder radius, which is not necessary the case as pointed out by Timokhin (2006).

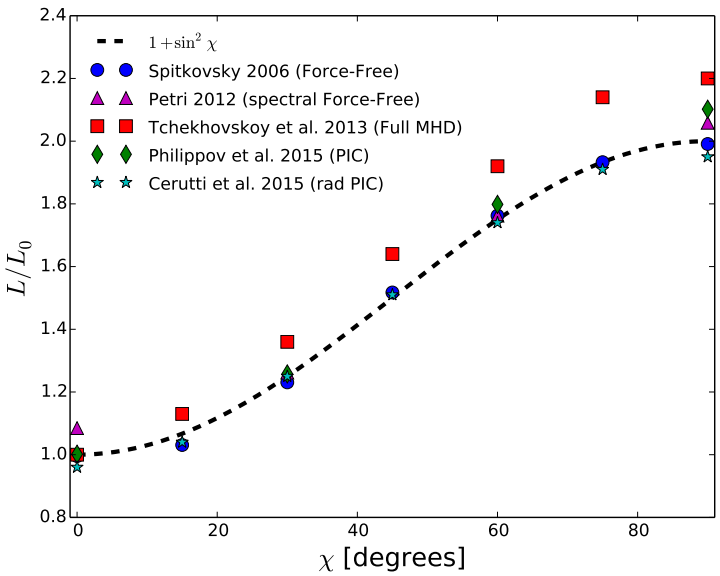

Figure 4.6: Compilation of the spindown power for the oblique plasma-filled magnetosphere reported in the literature using the following numerical approach: force-free (Spitkovsky 2006), spectral force-free (Pétri 2012), full MHD (Tchekhovskoy et al. 2013), PIC (Philippov et al. 2015b; Cerutti et al. 2016b). The spindown power is normalized to the force-free aligned spindown power $L_0 = \mu^2\Omega^4/c^3$.

However, time-dependent simulations show that the system naturally relaxes to the configuration depicted in Figure 4.4 once the steady state is established, i.e., where the Y-point is at the light cylinder (left panel in Figure 4.5, Spitkovsky 2006; McKinney 2006b; Parfrey et al. 2012). In such simulations, the time-dependent Maxwell equations are solved numerically. In ideal force-free MHD, the current density is fully determined by a combination of the $\mathbf{E}$ and $\mathbf{B}$ fields. Combining Eq. (4.16) with $\partial\left(\mathbf{E}\cdot\mathbf{B}\right)/\partial t = 0$, we have (Blandford 2002; Spitkovsky 2006)

$$\mathbf{J} = \frac{c}{4\pi}\nabla\cdot\mathbf{E}\left(\frac{\mathbf{E}\times\mathbf{B}}{\mathbf{B}^2}\right) + \frac{c}{4\pi}\left(\mathbf{B}\cdot\nabla\times\mathbf{B} - \mathbf{E}\cdot\nabla\times\mathbf{E}\right)\frac{\mathbf{B}}{\mathbf{B}^2}. \tag{4.31}$$

These two terms correspond to the current densities perpendicular (first) and parallel (second) to the magnetic field lines. Three-dimensional time dependent simulations were then obtained for the oblique rotator (right panel in Figure 4.5, Spitkovsky 2006; Kalapotharakos & Contopoulos 2009; Kalapotharakos et al. 2012b; Pétri 2012). One of the main result is the variation of the pulsar spindown power with the inclination (Figure 4.6, Spitkovsky 2006)

$$L \approx L_0\left(1+\sin^2\chi\right), \tag{4.32}$$

which is almost identical to the vacuum solution (Eq. 4.9), with the notable difference that the aligned force-free rotator does spin down. This important result is in contradiction with the oblique split-monopole solution which does not depends

on the inclination angle (Bogovalov 1999). The origin of the variations of the spin-down with the inclination was clarified only recently. Tchekhovskoy et al. (2016) found that this difference is partly due to a variation of the open magnetic flux (explains 40%) with the inclination. In their analysis, the rest is attributed to the concentration of open magnetic flux in the equatorial regions. Other than this, the split monopole solution roughly captures the structure of the magnetosphere in the wind region.

Force-free simulations have also clearly established the existence of current sheets in the magnetosphere. Their presence in the system is essential because they carry the return current which enables the closure of the poloidal current streaming through the polar caps of the star. In the wind zone, a current sheet separates the two magnetic polarities in the equatorial regions. In the aligned rotator, the current sheet is flat and is located at $\theta = 90^{\rm o}$. For an oblique rotator, the sheet has the shape of a ballerina skirt ("striped wind", the relativistic analog to the heliospheric current sheet) which oscillates between $\pi/2 - \chi < \theta < \pi/2 + \chi$ with a wavelength $2\pi R_{\rm LC}$. At the light cylinder (the "Y-point"), the current splits and flows along the magnetic separatrices, i.e., in the region that separates the closed and the open field line regions. They extend all the way to the star along the outer edge of the polar caps (Figure 4.4).

The force-free MHD approach has proven to be very useful for better understanding the structure of the magnetosphere of pulsars, but it has also severe limitations which obliges us to seek for more physical realism. First of all, the equatorial current sheet is a non-ideal MHD region where the magnetic field vanishes so that $E > B$, and where the force-free approximation breaks down (the plasma pressure and inertia become important). Artificial resistivity can be applied there to stabilize the layer (Li et al. 2012; Parfrey et al. 2012; Kalapotharakos et al. 2012b), or the full MHD approach can be employed to have a better description of the plasma heating and inertia in the sheet (Komissarov 2006; Tchekhovskoy et al. 2013). This fluid approach cannot also capture near vacuum regions, or "gaps" where pairs may be created in the magnetosphere (e.g., the polar-cap gap). More importantly, the ideal force-free approach cannot put constraint on particle acceleration and radiation since $\mathbf{E} \cdot \mathbf{B} = 0$ everywhere by construction. This is where global PIC simulations become relevant and what motivated my work presented in the next chapters.

Chapter 5

2D axisymmetric model

Before turning into the main PIC simulation results, I will review some of the major transformations that I had to implement into the `Zeltron` code in order to be capable of simulating pulsar magnetospheres (Sect. 5.1). To my knowledge, there was not PIC code capable of handling spherical coordinates at the time, so I had to figure out the way to do this. What I did not know then was that two other researchers were doing the exact same thing independently and at the same time, Alexander Chen at Columbia University and Mikhail Belyaev at UC Berkeley, which lead to stimulating discussions between us afterwards. My guideline was to keep the architecture of the code and algorithms as much as possible to preserve their nice features (accuracy, stability and efficiency, see Chapter 2). We will then turn to the fundamental question of plasma supply in the simulation (Sect. 5.2), a delicate issue that must be explicitly addressed in PIC simulations, in constrast to MHD simulations where the plasma is present by construction. The main results obtained with the 2D model are then presented for a variety applications: the dipole (Sect. 5.3) and the role of plasma supply on the magnetospheric features and on particle acceleration (Sects. 5.4-5.5.1), and interacting binary pulsar magnetospheres in the context of merging neutron star binaries (Sect. 5.5.2).

This chapter is based on the following papers: Cerutti et al. (2015); Crinquand et al. (2019); Guépin et al. (2020).

5.1 Numerical developments in Zeltron: Spherical geometry

Throughout this memoir, we refer to the usual spherical coordinates systems: the spherical radius r, the angle to the polar axis θ, and the azimuthal angle ϕ.

5.1.1 Maxwell's solver and spherical Yee mesh

The second-order accuracy is preserved by keeping the field components offset in space and in time. The electric field is defined in full time steps, $\mathbf{E}^n$, whereas

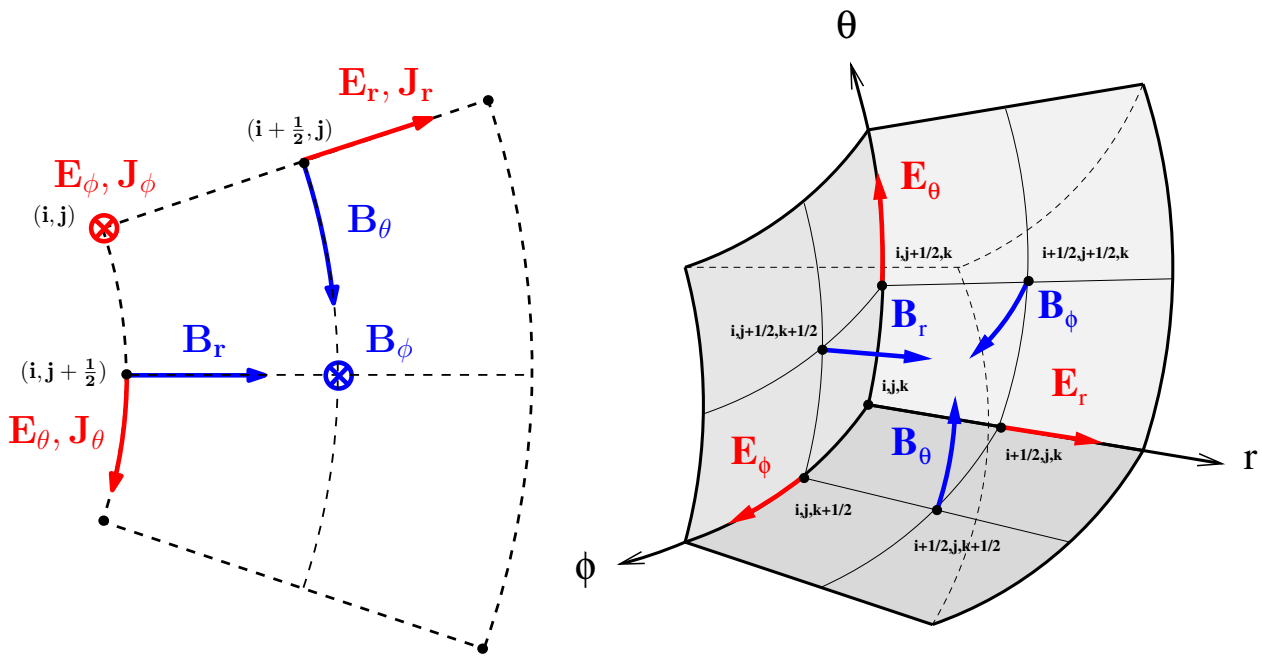

Figure 5.1: Yee lattice for a 2D axisymmetric spherical grid (2D) and full 3D spherical grid (right).

the magnetic field is in half-time steps, $\mathbf{B}^{n+1/2}$ (same as in Cartesian coordinates). The field components are mapped on the spherical Yee lattice shown in Figure 5.1.

To derive the second-order finite-difference scheme, we use the integral form of Maxwell equations integrated over the volume of a cell. For conciseness and for illustrative purposes, I give the derivation for the 2D axisymmetric grid only. It can easily be generalized to full 3D as shown in Cerutti et al. (2016b). Using the usual relation

$$\iint (\boldsymbol{\nabla} \times \mathbf{E}) \cdot \mathbf{dS}_{\rm cell} = \oint \mathbf{E} \cdot \mathbf{dl}_{\rm cell}, \tag{5.1}$$

we find the components of $(\boldsymbol{\nabla} \times \mathbf{E})$ as

- $(\boldsymbol{\nabla} \times \mathbf{E})_{{\rm r}i,j+1/2}$: The flux is computed through the a belt of radius $r_{\rm i}$ contained between the angle $\theta_{\rm j}$ and $\theta_{\rm j+1}$, $\Delta S = 2\pi r_{\rm i}^2 (\mu_{\rm j} - \mu_{\rm j+1})$, where $\mu \equiv \cos\theta$. The integration gives

$$(\boldsymbol{\nabla} \times \mathbf{E})_{{\rm r}i,j+1/2} = \frac{E_{\phi_{\rm i,j+1}} \sin\theta_{\rm j+1} - E_{\phi_{\rm i,j}} \sin\theta_{\rm j}}{r_{\rm i} (\mu_{\rm j} - \mu_{\rm j+1})}. \tag{5.2}$$

- $(\boldsymbol{\nabla} \times \mathbf{E})_{\theta i+1/2,j}$: The flux is computed through an annulus of inner radius $r_{\rm i}$ and outer radius $r_{\rm i+1}$ inclined at an angle $\theta_{\rm j}$, of total surface $\Delta S = \pi \left(r_{\rm i+1}^2 - r_{\rm i}^2\right) \sin\theta_{\rm j}$. The integration gives

$$(\boldsymbol{\nabla} \times \mathbf{E})_{\theta i+1/2,j} = -2 \frac{E_{\phi_{\rm i+1,j}} r_{\rm i+1} - E_{\phi_{\rm i,j}} r_{\rm i}}{r_{\rm i+1}^2 - r_{\rm i}^2}. \tag{5.3}$$

- $(\boldsymbol{\nabla} \times \mathbf{E})_{\phi_{i+1/2,j+1/2}}$: The flux is computed through the area of the cell in the poloidal plane of area $\Delta S = \left(r_{\mathrm{i+1}}^2 - r_{\mathrm{i}}^2\right) \Delta\theta/2$. The integration yields

$$(\boldsymbol{\nabla} \times \mathbf{E})_{\phi_{i+1/2,j+1/2}} = -2\frac{r_{\mathrm{i+1}} - r_{\mathrm{i}}}{\left(r_{\mathrm{i+1}}^2 - r_{\mathrm{i}}^2\right)\Delta\theta}\left(E_{\mathrm{ri+1/2,j+1}} - E_{\mathrm{ri+1/2,j}}\right) + \tag{5.4}$$

$$\frac{2}{r_{\mathrm{i+1}}^2 - r_{\mathrm{i}}^2}\left(E_{\theta \mathrm{i+1,j+1+1/2}} r_{\mathrm{i+1}} - E_{\theta \mathrm{i,j+1/2}} r_{\mathrm{i}}\right). \tag{5.5}$$

The curl of $\mathbf{B}$ can be derived in the same way, which we do not report here. Perhaps the most important feature to remember in these expressions is to have the correct indices, and make sure that the time and spatial indices on the right hand side correspond to, or are centered around the indices on the left hand side of the above expressions. These local integral expressions also have the advantageous property to show no divergence at the polar axis ($\theta = 0,\ \pi$), in contrast with the differential expressions (division by $\sin\theta$). With these expressions at hand, Maxwell's equations can be evolved in time using the same scheme in time as used in the Cartesian version, i.e.,

$$\mathbf{E}^{n+1} = \mathbf{E}^n + \Delta t\left[c\left(\boldsymbol{\nabla} \times \mathbf{B}\right)^{n+\frac{1}{2}} - 4\pi\mathbf{J}^{n+\frac{1}{2}}\right], \tag{5.6}$$

$$\mathbf{B}^{n+\frac{1}{2}} = \mathbf{B}^{n-\frac{1}{2}} - c\Delta t\left(\boldsymbol{\nabla} \times \mathbf{E}\right)^n. \tag{5.7}$$

Similarly, the Poisson solver can be adapted using the integral expressions of the divergence and gradient operators on a spherical grid cell. The stability criterion is again fixed by the CFL condition. For a 2D axisymmetric grid with a constant spacing in r and θ, this condition translates into

$$c\Delta t \leq \frac{1}{\sqrt{1/\Delta r^2 + 1/(r_{\min}\Delta\theta)^2}}, \tag{5.8}$$

where $r_{\min}$ is the inner radius of the domain.

5.1.2 Particle pusher, spherical remapping and shape

The code keeps in memory the particle position and normalized four-velocity components in spherical coordinates,

$$\mathbf{r} = \begin{pmatrix} r \\ \theta \\ \phi \end{pmatrix}, \qquad \mathbf{u} = \begin{pmatrix} u_{\mathrm{r}} \\ u_\theta \\ u_\phi \end{pmatrix}. \tag{5.9}$$

In order to preserve the fantastic numerical properties of the Boris pusher, a complete remapping of particle positions and velocities into Cartesian coordinates is necessary,

$$x = r\sin\theta\cos\phi,\ y = r\sin\theta\sin\phi,\ z = r\cos\theta, \tag{5.10}$$

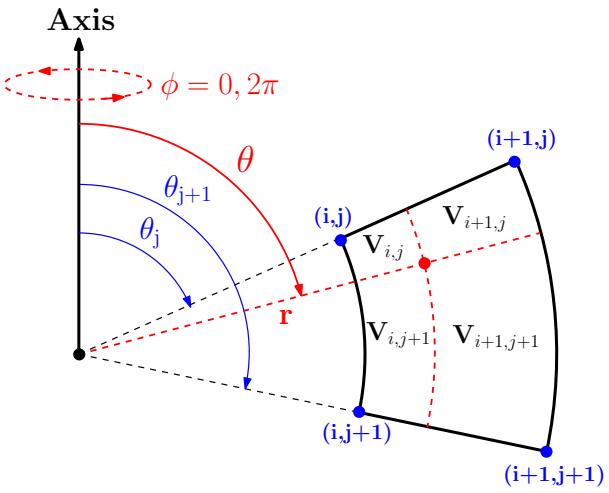

Figure 5.2: Geometry of a single cell in a 2D axisymmetric spherical mesh, as well as the volumes involved in the linear interpolation and current deposition scheme used in `Zeltron` .

$$u_x = u_r \sin\theta\cos\phi + u_\theta \cos\theta\cos\phi - u_\phi \sin\phi \tag{5.11}$$
$$u_y = u_r \sin\theta\sin\phi + u_\theta \cos\theta\sin\phi + u_\phi \cos\phi \tag{5.12}$$
$$u_z = u_r \cos\theta - u_\theta \sin\theta \tag{5.13}$$

and its reverse operation (from Cartesian to spherical) once the push has been completed, i.e.,

$$r = \sqrt{x^2+y^2+z^2},\ \theta = \arccos\left(\frac{z}{r}\right), \tag{5.14}$$

$$\phi = \left\{ \begin{array}{ll} \arccos\left(\frac{x}{\sqrt{x^2+y^2}}\right) & \text{if } y \geq 0 \\ 2\pi - \arccos\left(\frac{x}{\sqrt{x^2+y^2}}\right) & \text{if } y < 0 \end{array} \right\}, \tag{5.15}$$

$$u_r = u_x \sin\theta\cos\phi + u_y \sin\theta\sin\phi + u_z \cos\theta \tag{5.16}$$
$$u_\theta = u_x \cos\theta\cos\phi + u_y \cos\theta\sin\phi - u_z \sin\theta \tag{5.17}$$
$$u_\phi = -u_x \sin\phi + u_y \cos\phi. \tag{5.18}$$

Charge and current depositions use the same linear interpolation scheme and volume weighting technique as introduced in Chapter 2 (Sect. 2.4). The contribution to the current of a single particle located in the cell (i, j) of position (r, θ),

velocity $\mathbf{v}$, electric charge q and numerical weight w is

$$\mathbf{J}_{\mathrm{i,j}} = \frac{V_{\mathrm{i+1,j+1}}}{V_{\mathrm{tot}}} qw\mathbf{v} = (1-f_{\mathrm{r}})(1-f_{\theta})\, qw\mathbf{v} \tag{5.19}$$

$$\mathbf{J}_{\mathrm{i+1,j}} = \frac{V_{\mathrm{i,j+1}}}{V_{\mathrm{tot}}} qw\mathbf{v} = f_{\mathrm{r}}(1-f_{\theta})\, qw\mathbf{v} \tag{5.20}$$

$$\mathbf{J}_{\mathrm{i,j+1}} = \frac{V_{\mathrm{i+1,j}}}{V_{\mathrm{tot}}} qw\mathbf{v} = (1-f_{\mathrm{r}})\, f_{\theta} qw\mathbf{v} \tag{5.21}$$

$$\mathbf{J}_{\mathrm{i+1,j+1}} = \frac{V_{\mathrm{i,j}}}{V_{\mathrm{tot}}} qw\mathbf{v} = f_{\mathrm{r}} f_{\theta} qw\mathbf{v}, \tag{5.22}$$

where $V_{\mathrm{tot}} = \frac{2\pi}{3}\left(r_{\mathrm{i+1}}^3 - r_{\mathrm{i}}^3\right)(\mu_{\mathrm{j}} - \mu_{\mathrm{j+1}})$ is the total volume of the cell, $V_{\mathrm{i(+1),j(+1)}}$ are the partial volumes shown in Figure 5.2, and the interpolation parameters

$$f_{\mathrm{r}} = \frac{r^3 - r_{\mathrm{i}}^3}{r_{\mathrm{i+1}}^3 - r_{\mathrm{i}}^3} \tag{5.23}$$

$$f_{\theta} = \frac{\mu_{\mathrm{j}} - \cos\theta}{\mu_{\mathrm{j}} - \mu_{\mathrm{j+1}}}. \tag{5.24}$$

5.1.3 Boundary conditions

We consider here the specific configuration where the inner boundary coincides with the neutron star surface, the outer boundary is located outside the light cylinder radius. The θ-boundary extends all the way to the polar axis which is aligned with the rotation axis of the star.

Fields

- **θ-boundaries:** We apply the axial symmetry to all Yee field components sitting on the boundary $\theta = 0$, $\theta = \pi$, i.e., $\partial E_{\mathrm{r}}/\partial r = 0$, $E_{\phi} = 0$ and $B_{\theta} = 0$.

- **Radial inner boundary:** The initial magnetic field is frozen into the surface of the star and fixed throughout the simulation. The star is assumed to be a conducting sphere of infinite conductivity spinning at the angular velocity Ω. The solid rotation of the magnetic field lines is enforced through the co-rotation electric field applied on the stellar surface,

$$\mathbf{E}_{\star} = -\frac{(\mathbf{\Omega} \times \mathbf{r}_{\star}) \times \mathbf{B}_{\star}}{c}. \tag{5.25}$$

  In fact, $E_{\theta,\star}$ alone must be enforced for an axisymmetric configuration ($E_{\phi,\star} = 0$), E_{r} is free to evolve because it is defined above the surface on the Yee lattice.

- **Radial outer boundary:** In the particular problems we are interested in the following, a natural choice for the outer edges of the box is an open

boundary. What we mean by "open" here is a perfectly absorbing boundary with no reflection of waves and particles, which isolates the system from the external environment. A simple and robust way to achieve this is to add an unphysical dissipative term to Maxwell's equations to damp exponentially the fields in a spherical shell located in the outer regions of the box, such that (Birdsall & Langdon 1991)

$$\frac{\partial \mathbf{E}}{\partial t} = -\lambda(r)\mathbf{E} + c\,(\boldsymbol{\nabla} \times \mathbf{B}) - 4\pi\mathbf{J}, \tag{5.26}$$

$$\frac{\partial \mathbf{B}}{\partial t} = -\lambda(r)\mathbf{B} - c\,(\boldsymbol{\nabla} \times \mathbf{E})\,, \tag{5.27}$$

where $\lambda(r)$ is the conductivity of the absorbing region. This approach is a simplified 1D version of the more general perfectly-matched-layer technique valid for multidimensional open boundaries (Berenger 1994, 1996). The radial profile of the conductivity term must be chosen with care. A simple step function or any abrupt profile would lead to a partial reflection of waves back into the physical domain, and therefore fail the purpose of the layer. The profile cannot be too shallow either otherwise the absorbing layer must be very thick to full absorb the incoming waves, reducing the size of the physical domain of interest, and therefore it would increase the cost of the simulation. Empirically, I found that the following polynomial is a good compromise between gradual absorption and compactness of the damping layer,

$$\lambda(r) = \frac{K_{\rm abs}}{\Delta t}\left(\frac{r - r_{\rm abs}}{r_{\rm max} - r_{\rm abs}}\right)^3 \tag{5.28}$$

where $K_{\rm abs} > 1$ is a numerical prefactor that controls the damping strength, and $r_{\rm abs}$ ($r_{\rm max}$) is the inner (outer) radius of the absorbing layer. Typically, I chose the thickness of this layer to be 10% of the total box size, i.e., $(r_{\rm max} - r_{\rm abs})/r_{\rm max} = 0.1$. On top of this, we apply the regular zero-gradient boundary conditions to all field components at $r = r_{\rm max}$, i.e., $\partial(B_{\rm r}, E_\theta, E_\phi)/\partial r = 0$.

- **ϕ-boundary (3D runs):** Regular periodic boundary conditions apply to all components.

Particles

- **θ-boundaries:** Particles are reflected with no loss of energy.
- **Radial-boundaries:** Whether a particle hits the inner or outer (inner radius of the absorbing layer) boundaries, it is deleted from the simulation.
- **ϕ-boundary (3D runs):** Regular periodic boundary conditions apply.

5.2 The plasma supply problem

Before turning into the main results, we must address the delicate issue of the plasma supply in the simulation. The simple fact that the simulation box is open means that whatever plasma is injected in the first place, it must be continuously replenished throughout the simulation. Particle injection is of paramount importance for the problem of pulsar magnetospheres, and it is still an unsolved issue as of today.

The first source of particles for which there is no controversy is the stellar surface itself, where a primary beam of charges is extracted from the surface electric field. The surface charge density, Σ, is given by the jump conditions of the electric field at the surface of a conducting medium, i.e., by the difference between the radial electric field right above the neutron star surface and the co-rotation solution (Eq. 5.25, Cerutti et al. 2015),

$$4\pi\Sigma = E_{\mathrm{r},\star} - E^{\mathrm{co}}_{\mathrm{r},\star}. \tag{5.29}$$

This numerical recipe combined with a plasma limiter at the surface to avoid over-injection is well-suited to model electrosphere-like configurations (see Chapter 4). However, it is insufficient to establish a force-free-like configuration.

As discussed in Chapter 4, the main source of plasma supply is most likely provided by copious pair creation within the magnetosphere, but the loci and the efficiency of this process are still uncertain. PIC simulations coupled with a Monte-Carlo description for the treatment of the radiative transfer is an adequate tool to tackle this difficult problem (Timokhin & Arons 2013, and see Chapter 9), but published multidimensional PIC studies have proposed simplified formulations of the problem, which all slightly differ from one another. The main reason for this simplification is the lack of a realistic separation of scales in multidimensional simulations, separation between the macroscopic (stellar radius, light cylinder) and microscopic (skindepth, Larmor radius, cooling and pair production lengths) scales. In the first model by Philippov & Spitkovsky (2014), pair creation is assumed to be so vigorous that new particles are injected in every cell and at every timestep to reach a configuration as close to force-free as possible (see also Kalapotharakos et al. 2018). In the same spirit, Belyaev (2015) proposed an injection criterion based on a the local magnitude of the parallel electric field, which traces potential zones of intense particle acceleration, such that the number of created pairs per time step is

$$\frac{dN}{dt} \propto f_{\mathrm{inj}} \frac{|\mathbf{E}\cdot\mathbf{B}|}{B}, \tag{5.30}$$

where f_{inj} is a numerical prefactor that controls the strength of pair creation.

In Cerutti et al. (2015), I proposed another efficient way to fill the magnetosphere, which consists in injecting cold pairs at the stellar surface with an initial mildly relativistic speed along the field lines, v_{kick}, in addition to the corotation velocity. The motivation behind this choice is to assume that the cascade took

place near the stellar surface on scales unresolved by the global model. The initial net momentum along field lines is also a natural outcome of the development of the cascade near the star. The flux of new pairs, $F_{\rm inj}$, in then parametrized as

$$F_{\rm inj} = v_{\rm kick} f_{\rm inj} n^{\star}_{\rm GJ}, \tag{5.31}$$

where $f_{\rm inj}$ is a dimensionless parameter which controls how much of the fiducial Goldreich-Julian density is delivered per timestep. In the following, the initial kick velocity will be set at $v_{\rm kick} = 0.5c$. The last prescription discussed here and that we make use of in the applications discussed in Sects. 5.5.1-5.5.2 is based on the particle energy. A particle produces a new pair if its energy exceeds a fixed fraction of the full vacuum potential drop, $f_{\rm pp} < 1$. In return, the created pair takes away a fixed fraction of the parent particle energy, $\gamma_{\rm p}$, such that $\gamma_{\rm new} = f_{\gamma}\gamma_{\rm p}$. The parent particle is cooled accordingly. This prescription allows to produce pairs wherever particle acceleration takes place in the magnetosphere (Philippov et al. 2015b), which is physically sound and well-motivated. An analogous prescription was also used by Chen & Beloborodov (2014) and Chen et al. (2020).

5.3 From the electrosphere to the force-free magnetosphere

The first numerical experiment I carried out was the aligned dipole. My objective was to investigate the impact of the plasma supply on the magnetosphere, from a nearly vacuum solution to a quasi force-free magnetosphere. Initially, the box is filled with a static magnetic dipole in vacuum. At $t > 0$, the star is set into a solid rotation by applying the co-rotation electric field (Eq. 5.25) at the inner boundary. Plasma is injected from the stellar surface at a constant rate controlled by the parameter $f_{\rm inj} = 0.1,\ 0.2,\ 0.5,\ 1$. Shortly after the onset of the simulation, a torsional Alfvén wave is launched from the surface which gradually sets the magnetosphere into rotation. A quasi-steady state is quickly established after a few rotation periods.

Figure 5.3 shows the final state for a high plasma injection rate ($f_{\rm inj} = 1$, left panels) and a low plasma injection rate ($f_{\rm inj} = 0.2$, right panels). The high-supply solution exhibits all of the expected features of a force-free magnetosphere: (i) a bundle of open magnetic field lines at the polar caps passing smoothly through the light cylinder, (ii) closed field lines within the light cylinder (top panel), and (iii) a set of current layers flowing along the magnetic separatrices inside the light cylinder, merging at the Y-point to form a single current layer in the equatorial plane beyond the light-cylinder (middle panel). There are also important differences with respect to the ideal force-free solution, even if the plasma supply is high, which are the features of interest here. While numerical tricks are needed to model the equatorial current sheet in force-free simulations where ideal MHD breaks down,

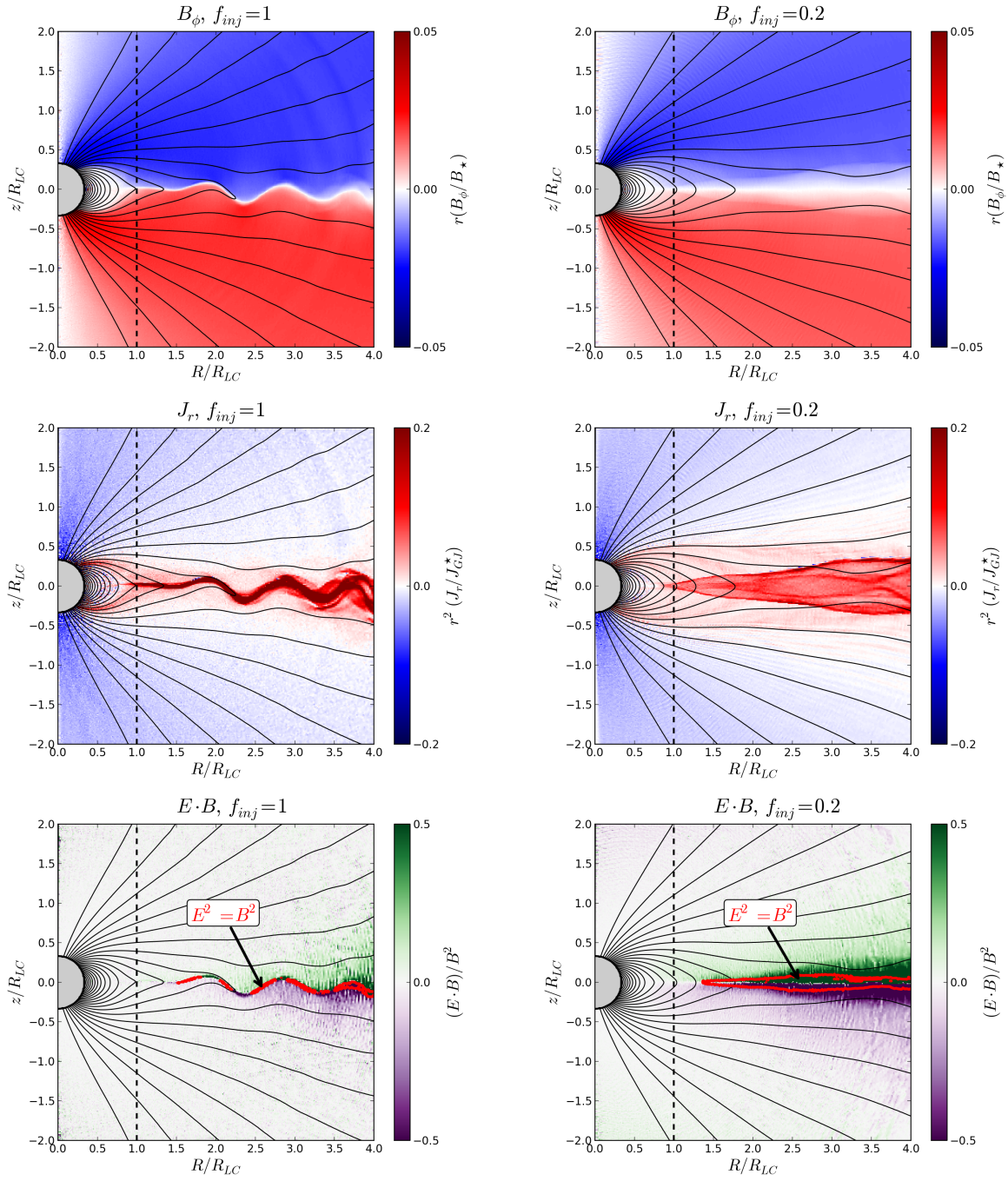

Figure 5.3: 2D axisymmetric PIC model of an aligned pulsar magnetosphere with $R_{\rm LC}/r_\star = 3$. Top: toroidal field $rB_\phi/B_\star$, middle: Radial current density normalized to the fiducial Goldreich-Julian value, $r^2 J_{\rm r}/J^\star_{\rm GJ}$, bottom: Electric field component parallel to the magnetic field, $\mathbf{E}\cdot\mathbf{B}/B^2$. Left: high-plasma supply solution leading to a quasi-force-free magnetosphere, right: low-plasma supply solution. Figure taken from Cerutti et al. (2015).

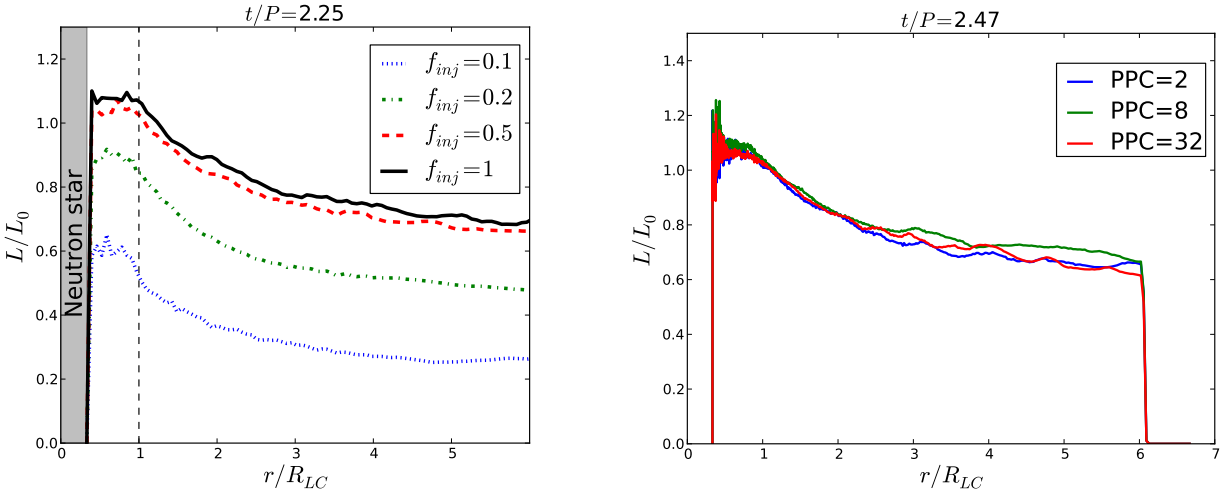

Figure 5.4: Radial profile of the outgoing Poynting flux integrated over a sphere of radius r. Left: Effect of the plasma injection rate $f_{\rm inj}$. Right: Effect of the number of particle-per-cell for $f_{\rm inj} = 1$.

PIC simulations capture the physics of magnetic reconnection leading to dissipation and particle acceleration. These zones of interest are well-visible as $\mathbf{E}\cdot\mathbf{B} \neq 0$ regions localized within the layer (bottom panel). Kinks in the equatorial current sheet are also the signature of kinetic effects driven by the beams of particles carrying the current, reminiscent of kink modes in Harris layers (Sect. 3.3).

These departures from the ideal solution are necessarily more pronounced if the plasma supply is insufficient to sustain the force-free current. In this case, some field lines remain closed even outside the light cylinder, and large gap forms in the magnetosphere. The low-plasma supply solution shown in the right panels in Figure 5.3 is intermediate between an electrosphere-like solution (no pair production, no current and therefore no spindown, see Sect. 4.3) and a force-free magnetosphere. The plasma structure is highly (but not perfectly) charge separated, $n \sim q\rho$, with almost exclusively electrons at the poles and positrons at the equator. Plasma supply has a direct influence on the pulsar spindown and dissipation. Figure 5.4 (left panel) shows the outgoing Poynting flux integrated over a sphere of radius r as a function of $f_{\rm inj}$. For the high-supply solutions $f_{\rm inj} = 0.5,\ 1$, $L \approx 1.1 L_0$ inside the light cylinder followed by a gradual dissipation reaching about 30% at $6R_{\rm LC}$. The spindown power decreases with decreasing plasma supply as expected, reaching $L \approx 0.6 L_0$ for $f_{\rm inj} = 0.1$ and a dissipation rate of about 50% at $r = 6R_{\rm lC}$.

It is important to emphasize at this point that the dissipation reported here is by no means of numerical origin, it is physical. The lost electromagnetic power is self-consistently channeled to particle kinetic energy via the reconnection electric field in the sheet or via vacuum gap electrostatic fields, if any. We checked that the dissipation rate is robust against numerical effects such as resolution and the number of particle-per-cell as shown in Figure 5.4 (right panel). These numbers

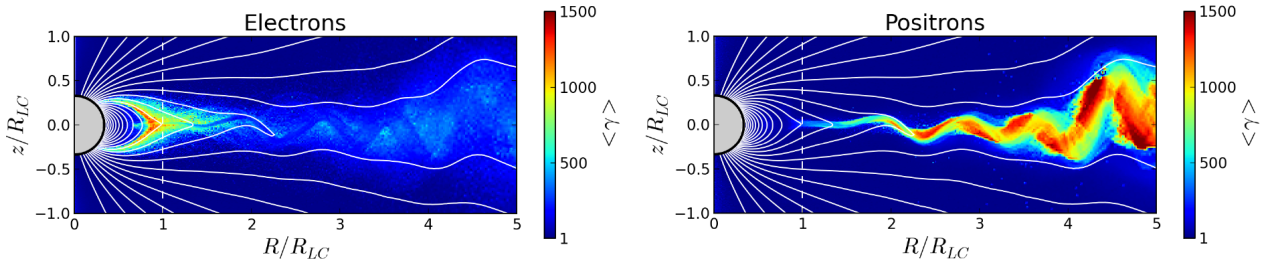

Figure 5.5: Electron (top) and positron (bottom) mean particle Lorentz factor, $\langle\gamma\rangle$.

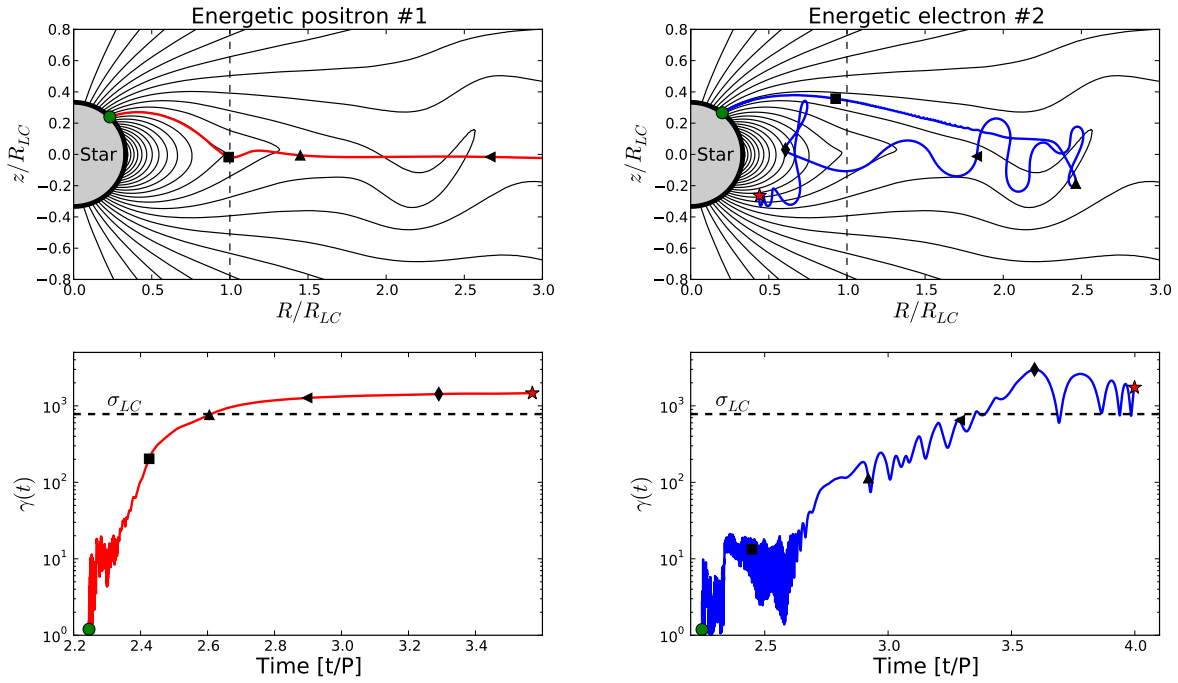

Figure 5.6: Representative high-energy positron (left) and high-energy electron (right) trajectories.

are also consistent with other PIC studies, in particular with Belyaev (2015) who performed a similar analysis of the plasma supply on the magnetosphere using the prescription based on Eq. (5.30). What is important to notice is that dissipation reaches a saturation at a high plasma supply ($f_{\rm inj} = 0.5,\ 1$), meaning that simulations are capturing an irreducible amount of dissipation. No matter how close to force-free the magnetosphere is and how high the numerical resolution is, there will always be a finite amount of dissipation due to reconnection occuring at kinetic scales, in contrast to MHD simulations (Tchekhovskoy et al. 2013). We will come back to the delicate issue of dissipation in the following chapter.

5.4 Particle acceleration

The connection between dissipation in the current sheet and particle acceleration has been well established thanks to this study. Figure 5.5 shows the mean particle Lorentz factor computed in each cell and for both species. There is a clear spatial correlation between the location of the high-energy particles and the sheets. High-energy positrons are exclusively found in the equatorial current sheet, while energetic electrons are concentrated near the Y-point and the separatrix current layers. To understand this asymmetry, it is more instructive to look at individual particle trajectories. Figure 5.6 shows a representative trajectory of an accelerated particle for each species. High-energy positrons are injected at the footpoints of the last open field lines. They flow out along the separatrices and equatorial current layers. Most of their energy gain occurs near the Y-point and proceeds at a slower rate further out. In contrast, high-energy electrons originate from higher latitudes. They propagate in the wind without much acceleration until they are captured by the equatorial current sheet. At this point, they experience an abrupt acceleration by the reconnection electric field, which pushes them back towards the star. Their acceleration stops when they reach Y-point. Electrons then head back to the star along the separatrices. These major differences between electronic and positronic trajectories lead to a strong excess of positrons at high energies leaving the system (and vice-versa if $\mathbf{\Omega} \cdot \mathbf{B} < 0$). This result may give new clues as to a possible astrophysical origin of the high-energy positron excess as reported by the PAMELA collaboration Adriani et al. (2009).

As discussed in Chapter 3, relativistic reconnection accelerates particles are an energy scale given by the upstream plasma magnetization. In this global configuration where σ varies significantly, it is most relevant to use the magnetization measured at the light-cylinder,

$$\sigma_{\rm LC} \equiv \frac{B_{\rm LC}^2}{4\pi\Gamma_{\rm LC}\kappa_{\rm LC} n_{\rm GJ}^{\rm LC} m_{\rm e} c^2}, \tag{5.32}$$

as also shown in Figure 5.6 (bottom panels) where $\gamma \sim \sigma_{\rm LC}$. Compared with the vacuum potential drop across the polar cap, defined as

$$\Phi_{\rm pc} = \int_0^{\theta_{\rm pc}} E_\theta(r_\star) r_\star d\theta = \frac{\mu\Omega^2}{c^2}, \tag{5.33}$$

the particle Lorentz factor accelerated in the sheet can be recast as

$$\gamma \sim \frac{\phi_{\rm pc}}{\Gamma_{\rm LC}\kappa_{\rm LC}}. \tag{5.34}$$

where $\phi_{\rm pc} = e\Phi_{\rm pc}/m_{\rm e}c^2$. It is interesting to notice that this expression depends on both the global properties of the star (μ and Ω) and the microphysics of pair production via the multiplicity parameter. This result does not depend significantly on synchrotron cooling (not modeled in this work, but see next chapter)

because particles are accelerated within the current layer where synchrotron losses are small (chapter 3). In the high-supply solution, this energy scale represents a substantial fraction of the polar-cap potential drop, 20% on average and up to 50% for the most energetic particles.

To summarize, this work has clearly established a link between reconnection, dissipation and particle acceleration in the current sheet. Major results are: (i) An irreducible amount of dissipation in the high-supply regime (ii) A very efficient particle acceleration close to the maximum polar-cap potential drop, and (iii) The magnetospheric features and spindown are strongly sensitive to the plasma supply. In particular, we discovered charge-separated pulsar magnetosphere states, intermediate between an electrosphere and a force-free solution, which may be appropriate for describing pulsars near the death line, i.e. pulsars where pair production is weak, but not absent.

5.5 Other applications

This first 2D PIC magnetospheric model inspired other studies. I briefly describe below two of those applications:

- The study of ion acceleration in millisecond pulsar magnetospheres carried out by Claire Guépin when she was a PhD student at IAP with Kumiko Kotera (Guépin et al. 2020). This work has been performed in the context of the ANR JCJC APACHE project led by Kumiko, for which I was a collaborator.

- The study of binary pulsar magnetospheres and the emission of a high-energy radiation precursor during the inspiral phase prior to their merger. This work has been carried out by Benjamin Crinquand during his Master 2 thesis under my supervision (Crinquand et al. 2019).

Another application was dedicated to the study of the Lense-Thirring effect on pair production at the polar caps (Philippov et al. 2015a), but this work will not be presented here for conciseness.

5.5.1 Acceleration of ions

The extraction of ions from the crust via the surface electric field is a natural outcome of pulsar electrodynamics. For instance, if $\mathbf{\Omega} \cdot \mathbf{B} > 0$, ions are extracted within the equatorial regions and are injected into the magnetosphere. In contrast to pairs, their number density can be at most of the order of the Goldreich-Julian density, and therefore ions should be highly subdominant in number for a force-free-like magnetosphere. In this work, Claire studied how and how much protons are accelerated in the magnetosphere as a function of the pair cascade efficiency,

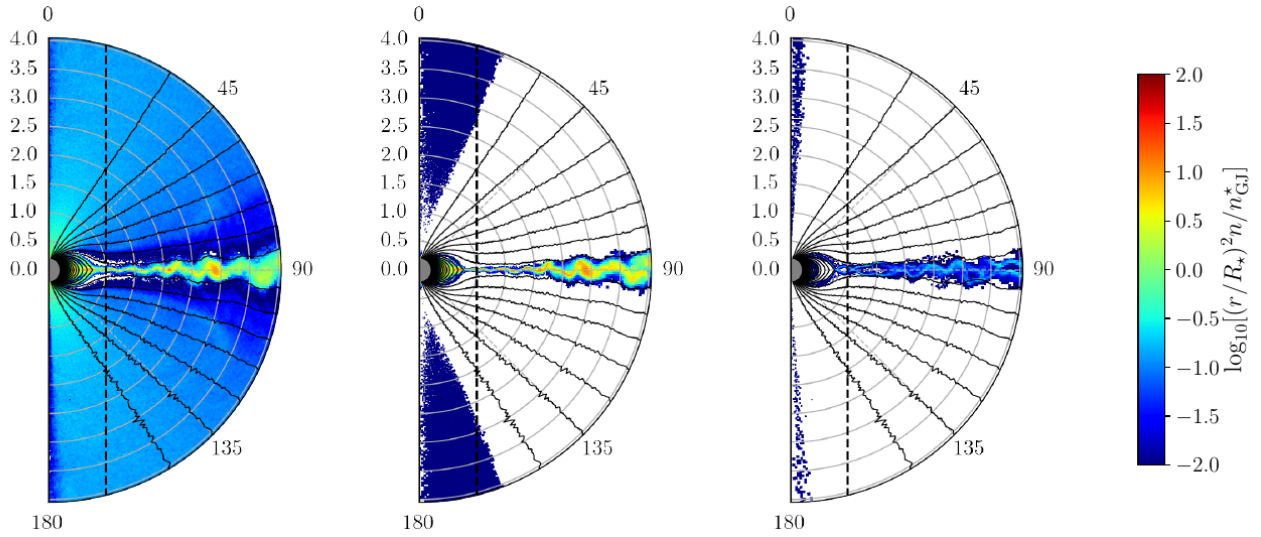

Figure 5.7: Electron (left), positron (middle) and ion (right) densities for a high pair production rate.

using the particle threshold energy recipe for pair production. Ions are injected as a third species, with a reduced mass ratio $m_{\rm p} = 18.36 m_{\rm e}$ for numerical convenience. Figure 5.7 shows the plasma density of all species for a high rate of pair production. A static disk of ions forms very close to the stellar surface, reminiscent of the electrosphere solution. These protons are trapped and are not significantly accelerated. Ions extracted along the last open field lines freely stream along the separatrices current layers and in the equatorial plane outside the light cylinder.

Claire showed that protons are significantly accelerated along the separatrices inside the light cylinder rather than in the equatorial current layer, in contrast to pairs. Ions being highly subdominant, the layer thickness is determined by the electronic scale. Although captured by the layer, the meandering width of ion Speiser trajectories is too wide so that ions spend most of their time outside the layer, and thus they do not feel the reconnection electric field. Nonetheless, in this regime ions are accelerated close to the polar-cap potential drop (Figure 5.8, left panel, see also Philippov & Spitkovsky 2018). If pair production decreases, large vacuum gaps open up as described in the previous section, and the ion maximum energy increases until it reaches nearly 80% of the full vacuum potential drop. The total power carried away by ions represents a few percent of L_0 (right panel in Figure 5.8).

This work confirms that pulsars are very efficient particle accelerators, also for hadrons. Although few in number, ions carry a substantial fraction of the pulsar spindown. Scaled up to the typical millisecond pulsars properties with $B_\star = 10^9$G, $P = 1$ ms, our results suggest that protons can be accelerated to a few PeV in a force-free state and up to a few tens of PeV in low-plasma supply solutions, and contribute to the flux of galactic cosmics ray. For new-born millisecond pulsars with $B_\star = 10^{13}$G, pulsars could even accelerate ultra-high energy cosmic rays (Fang et al. 2012). This exciting perspective should be confirmed in future studies

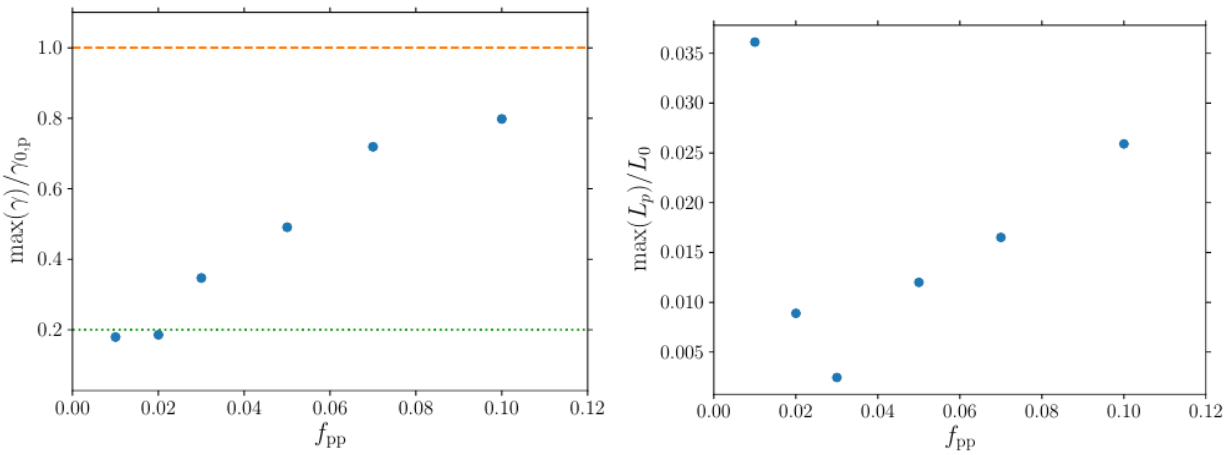

Figure 5.8: Left: Maximum proton energy normalized to the full vacuum potential drop ($\gamma_{0,\mathrm{p}}$, orange dashed line) as a function of the energy threshold for pair production (γ_{th}, in terms of the fraction of the $f_{\mathrm{pp}} = \gamma_{\mathrm{th}}/\gamma_{0,\mathrm{p}}$). The green dashed line represents the polar-cap potential drop. Right: Power carried away by ions in terms of L_0 as a function of f_{pp}. Figure taken from Guépin et al. (2020).

with a larger separation of scales than what we can afford numerically today.

5.5.2 Binary pulsars

The discovery of the first gravitational wave event associated with a binary neutron star merger has revived a strong interest in the study of interacting pulsar magnetospheres (Abbott et al. 2017a). The magnetic coupling between both stars, combined with different stellar spins and the relative orbital motion can significantly change the magnetospheric features observed in an isolated pulsar, in particular in the last orbits prior the merger. The goal of this work, led by my student Benjamin Crinquand, was to revisit the theory of binary pulsar magnetospheres (Vietri 1996; Hansen & Lyutikov 2001; Lai 2012; Piro 2012), with the help of PIC simulations. As thoroughly discussed in the next chapter, particle acceleration in isolated pulsar magnetospheres leads to bright high-energy synchrotron emission. My hope with this work was to estimate how much energy could be channeled in the form of a high-energy percursor electromagnetic emission from the interacting magnetospheres, prior the merger, the short gamma-ray burst and the kilonova emission (Abbott et al. 2017b).

As a proof of principle and for practical reasons, I proposed to Benjamin to perform this study using 2D axisymmetric simulations, meaning that the spin axis of both stars must be aligned. The orbital motion must also be neglected, but we consider that the orbital separation, a, decreases due to the energy losses carried away by gravitational waves emitted by the system, such that

$$a(t) = a_0 \left(1 - \frac{t}{\tau}\right)^{1/4}, \tag{5.35}$$

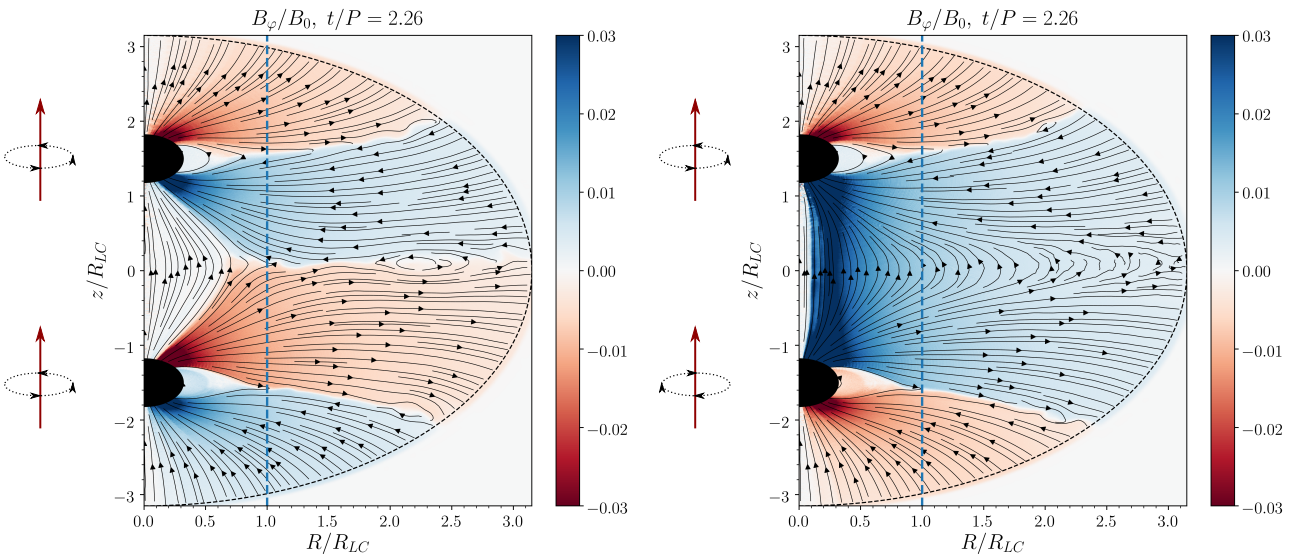

Figure 5.9: Magnetospheric structure for a parallel (left) and anti-parallel (right) configurations. The dashed vertical line shows the light cylinder of both stars. Figure taken from Crinquand et al. (2019).

where τ is the inspiral time, and a_0 the initial orbital separation between both stars. Although unphysical, this setup is ideally suited to study some of the basic features of interacting magnetospheres, with a particular emphasis on the role played by the pulsar spins and the orbital separation. This work is the first step towards future, more realistic 3D PIC simulations of merging pulsar-pulsar and pulsar-black-hole binaries, which will include the orbital motion (see research project, Chapter IV).

For this study, it was most convenient to work with a cylindrical version of `Zeltron` in the Rz-plane. The injection of pairs in based on the particle energy threshold as in the previous section, but without ions. Benjamin considered two main classes of initial setup: (i) the parallel configuration where both pulsars are identical (spin and magnetic polarity), and (ii) the anti-parallel configuration where the magnetic axes are aligned but the spin axes are anti-aligned. We assumed that pair production is efficient so that both magnetospheres are close to the force-free regime.

Figure 5.9 shows the magnetic structure once a quasi-steady state has been established and assuming a constant orbital separation. In both configurations, we can easily recognize the familiar structures of an isolated pulsar: a set of open field lines at the poles pointing away from the binary and an equatorial current sheet for each star. In contrast, the inter-binary region presents new structures, where both stars interact. In the parallel configuration, another current sheet forms in between both stars to sustain the jump in the magnetic field topology. Apart from a narrow bundle of field lines directly connecting both stars at the poles, the magnetic interaction is mainly felt through reconnection. In the anti-parallel configuration, there is a direct magnetic linkage between both stars and no inter-pulsar current sheet. The differential rotation between both stars leads

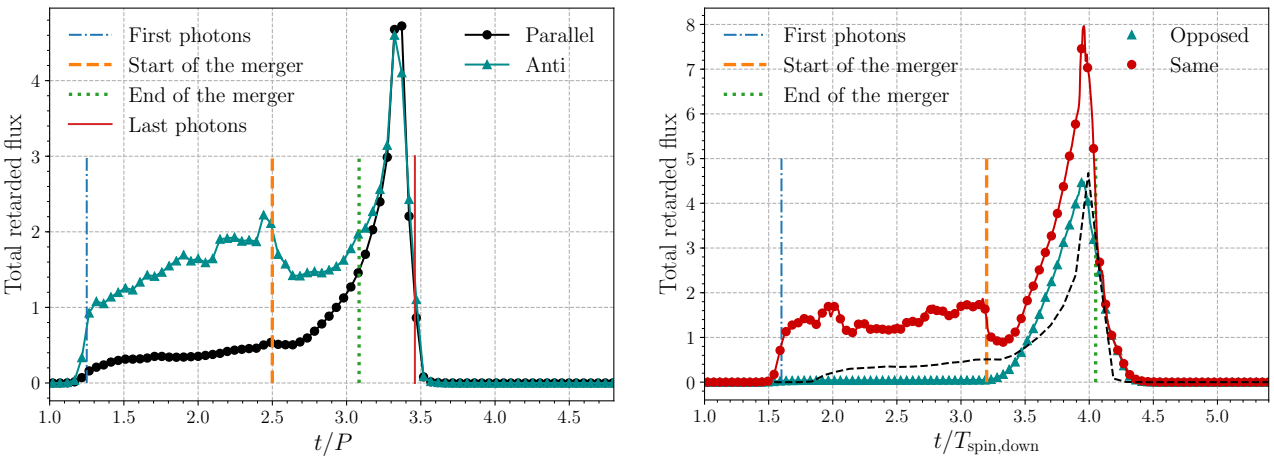

Figure 5.10: High-energy synchrotron lightcurve as received by a distant observer for a symmetric (left) and asymmetric (right, $\Omega_{\mathrm{down}}/\Omega_{\mathrm{up}} = 4$, $B_{\mathrm{up}}/B_{\mathrm{down}} = 4$) binary pulsar system. Fluxes are normalized by L_0. Figure taken from Crinquand et al. (2019).

to a strong winding of magnetic fields at the poles, and therefore a strong electric current must flow. In 3D, this configuration is highly unstable to kink modes when the toroidal field becomes greater than the poloidal component, $B_\phi/B_{\mathrm{z}} \gtrsim 1$, which momentarily disrupts the magnetic linkage in the form of powerful flares driven by reconnection (Lai 2012; Most & Philippov 2020).

The magnetic coupling becomes stronger with decreasing orbital separation. Efficient dissipation and particle acceleration occur within the current sheets and intense synchrotron radiation is emitted. Figure 5.10 shows that a bright precursor emission is indeed expected prior the merger. Regardless of the initial magnetic/spin configuration, the radiative power represents up to $5L_0$ in the form of high-energy synchrotron radiation, i.e., it is a two orders of magnitude increase with respect to an isolated pulsar (see next chapter). Benjamin also explored asymmetric, arguably more realistic binary systems: a high-spin low-field pulsar (millisecond pulsar) in orbit with a lower-spin higher-field pulsar (young pulsar). The same scenario as the one described above qualitatively holds in this asymmetric configuration (right panel in Figure 5.10).

In spite of this large magnification, the expected flux is way too weak to be detected at cosmological distances, even in the nearby Universe. Assuming a powerful Crab-like pulsar would give a 10^{38}erg/s luminosity. For comparison, the luminosity of the gamma-ray burst that followed the gravitational wave event GRB 170817A detected by the *Fermi*-GBM is 10^{45}erg/s for a source located at 40 Mpc, and was just above the noise level. A more promising way to observe a precursor emission from these systems could be in the radio band. We noticed that a strong enhancement of pair production at the polar caps that accompanies the increase in the synchrotron emission during the inspiral phase. The quasi-periodic discharge of the polar caps is an efficient mechanism to produce coherent radio waves (Philip-

pov et al. 2020). If a small fraction of the total spindown power is channeled into these waves, it could be detectable as a fast, non-repeating radio transient. Last, the orbital motion could also play an important role at magnifying even more the expected radiative output. This issue is left to future 3D simulations.

Chapter 6

3D model: pulsed emission and dissipation of the striped wind

The simple fact that pulsars are pulsating sources by definition means that the emission most likely originates from an oblique magnetosphere, i.e., where the magnetic axis is misaligned at an arbitrary angle with respect to the spin axis. In practical terms, breaking the axisymmetry implies that full 3D simulations must be employed to model realistic pulsar magnetospheres, in the hope of elucidating one of the most outstanding mystery of high-energy astrophysics: the origin of the high-energy (incoherent) pulsed emission from pulsars. I begin this chapter with a brief summary of some of the most important observational features discovered by the *Fermi*-LAT in the > 100MeV gamma-ray band. I then turn into the numerical strategies that I developed to model the radiative output, and I present the main PIC results. I will close this part of the memoir with the most recent study of dissipation and particle acceleration in the wind region based on a large 3D PIC model of pulsar magnetosphere and striped wind.

This chapter is based on the following articles: Cerutti et al. (2016b), Cerutti et al. (2016a), Cerutti & Philippov (2017), Cerutti et al. (2020), and Cerutti (2018) based on an invited review talk at at the *Agile* gamma-ray symposium held in Rome in 2017.

6.1 Gamma-ray pulsars: Salient observational features

The gamma-ray space telescopes *Agile* and *Fermi* have greatly contributed to the discovery of new pulsars shinning in the gamma-ray band, and therefore they have clearly established that pulsars are efficient particle accelerators. Their number detected in the high-energy gamma-ray band increased from the 6 EGRET pulsars

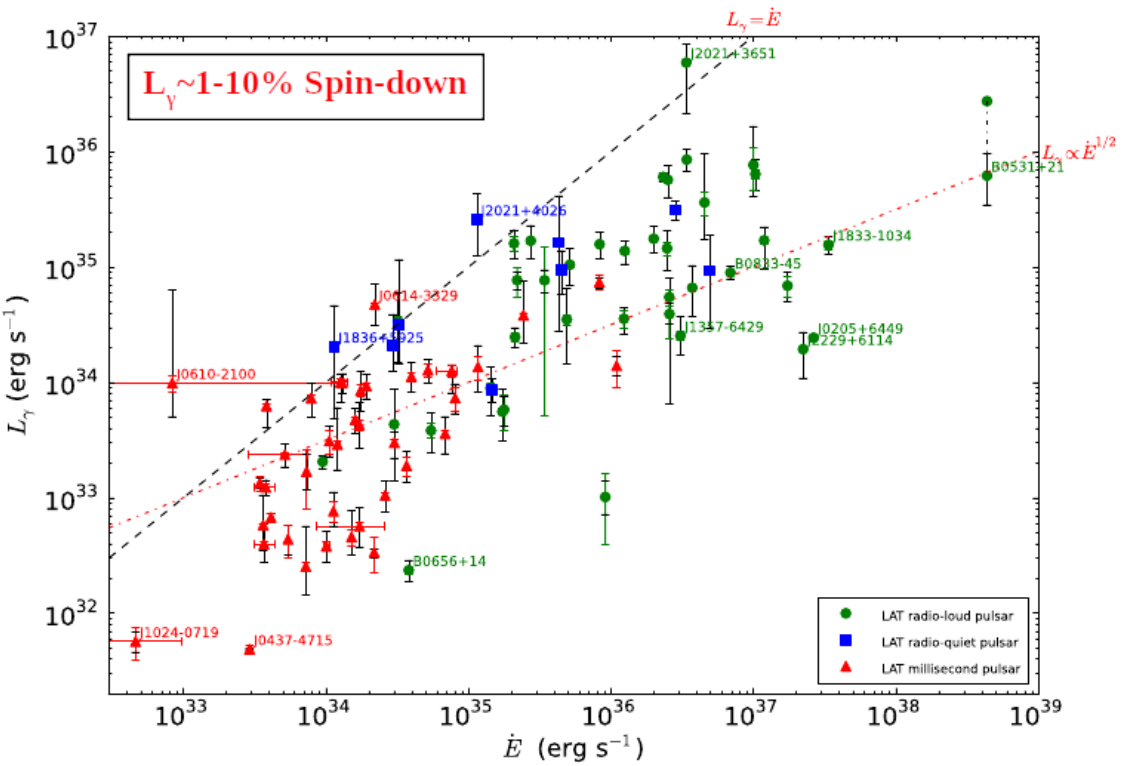

Figure 6.1: Gamma-ray luminosity, L_γ, as a function of the pulsar spindown, $\dot{E}$, from the second *Fermi*-LAT pulsar catalog. Figure taken and adapted from Abdo et al. (2013).

in the nineties (Nolan et al. 1996) to 117 in the second Fermi-LAT catalog in 2013 (Abdo et al. 2013), becoming the largest number of identified sources in the Galaxy, and this number continues to increase with more exposure time and better data-analysis techniques. As of April 16, 2020, this number has more than doubled since 2013 with 253 pulsars[1]. The relevant observational features can be summarized as follow:

- Gamma-ray pulsars are all rotation-powered (as opposed to magnetars where the main source of energy is of magnetic origin). They can be divided into two well-separated populations in the $P - \dot{P}$ diagram: (i) old, low-field ($B_\star \sim 10^9$G) millisecond pulsars whose rotation period was spun up by accretion, (ii) young, high-field ($B_\star \sim 10^{12}$G) isolated pulsars whose rotation period is of order $P \sim 100$ms.

- The gamma-ray luminosity above 100 MeV represents about $1 - 10\%$ of the total energy budget, i.e., the pulsar spindown (Figure 6.1). We can therefore assert, in a model independent way, that pulsars are extremely efficient particle accelerators. This number also gives a lower limit to the amount of dissipation within the magnetosphere.

[1] https://confluence.slac.stanford.edu/display/GLAMCOG/Public+List+of+LAT-Detected+Gamma-Ray+Pulsars

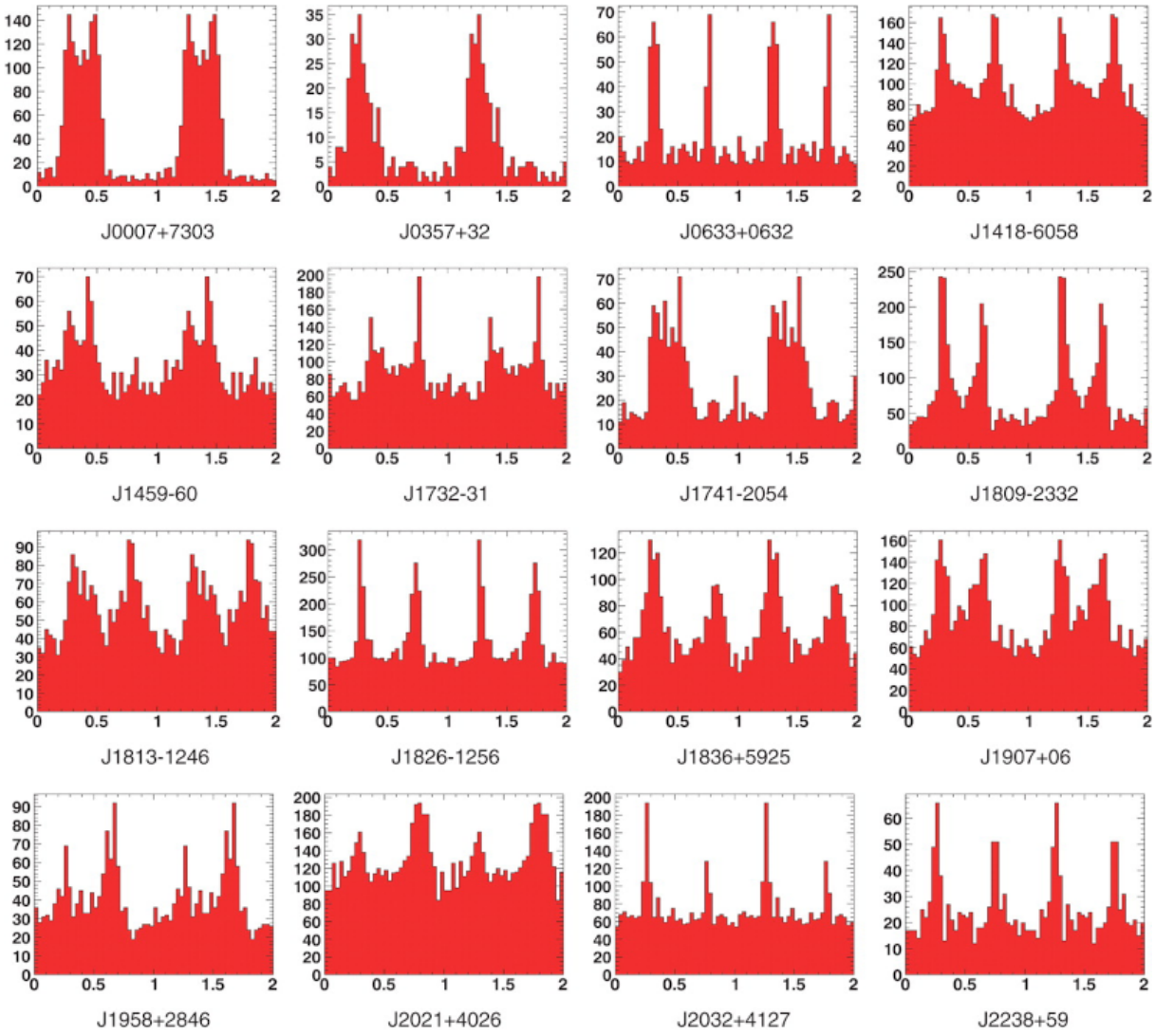

Figure 6.2: Sample of 16 pulsar gamma-ray pulse profiles reported by the *Fermi*-LAT collaboration. Two rotation periods are shown per pulsar. Figure taken from Abdo et al. (2009).

- The phase-averaged gamma-ray spectrum is well-modelled by a hard power-law at low energies followed by an exponential cut off at a few GeV.

- The pulse profile presents in most cases (with a $\sim 75\%$ probability) two well-separated peaks per rotation period, sometimes with significant emission in between them that is often referred to as the "bridge emission" (Figure 6.2). The peaks are not necessarily symmetric, but they are often separated by about 0.5 in phase, suggesting that the emission pattern is composed of two oppositely directed beams. This is very different than in radio where most pulsars present a single pulse per period, which is consistent with a single beam pointing away from the polar cap (with the notable exception of the Crab pulsar and millisecond pulsars).

- Gamma-ray pulses are usually not aligned with the radio pulses, suggesting that two distinct regions of the magnetosphere are involved in the emission

mechanisms (here again with the notable exception of the Crab pulsar and millisecond pulsars).

- The detection of $>$ GeV photons, and even TeV photons in the Crab and Vela pulsars (Ansoldi et al. 2016, Arache Djannati-Ataï 2019 private communications), rules out a polar-cap origin for the pulsed emission because these photons would be absorbed by the strong magnetic field near the star. Thus, the outer-parts of the magnetosphere are favored.

- Statistically and for a given sensitivity, more pulsars are detected in gamma rays than in radio (except for millisecond pulsars where the radio emission is systematically observed), suggesting that the gamma-ray beam is wider than the radio beam.

All of these robust features give precious clues on the origin of the pulsed emission. The shape of pulses is usually interpreted as the result of geometrical effects. In principle, this information should suffice to constrain the loci of the emitting regions, but in practice lightcurve fitting is often insufficient to disentangle between models (degeneracy of solutions). Current lightcurve modelling in the context of, e.g., the outer-gap (Cheng et al. 1986; Romani & Yadigaroglu 1995), the slot gap (Arons 1983; Muslimov & Harding 2003) or the two-pole caustics models (Dyks & Rudak 2003), are based on a vacuum inclined dipolar field. In these models, the emitting zones are put by hand. Today, we know that the vacuum dipole is not a correct model for the magnetosphere. Bai & Spitkovsky (2010a) made one step further using the force-free fields to model pulsar light curves (see also Kalapotharakos et al. 2012a; Li et al. 2012). But here again, the emitting zones must be prescribed since force-free MHD simulations cannot capture particle acceleration, and therefore the origin of the high-energy pulsed emission remained still highly uncertain. The next logical step to make further progress is to use a self-consistent approach that PIC simulations can offer.

6.2 3D setup and radiation

6.2.1 Initial fields

To reach this goal, I transformed `Zeltron` into a full 3D spherical grid, i.e., by including the azimuthal direction, ϕ. The initial setup is the same as for the 2D axisymmetric model: a rotating dipolar field anchored onto the surface of the star with a high plasma supply from the surface of the star. The initial magnetic field is given by the usual dipole formula,

$$\mathbf{B}(t) = \frac{3\left(\mathbf{e_r}\cdot\boldsymbol{\mu}\right)\mathbf{e_r} - \boldsymbol{\mu}}{r^3}, \tag{6.1}$$

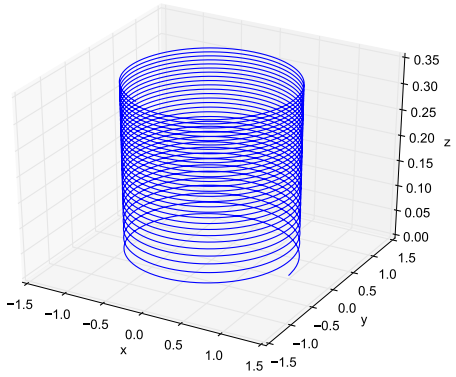

Figure 6.3: 3D electron trajectory moving along a circular magnetic field line contained within the xy-plane, with a curvature-drift motion along the z-direction.

or more explicitly as

$$B_{\rm r} = \frac{2\mu}{r^3}\left[\sin\chi\sin\theta\cos\left(\Omega t-\phi\right)+\cos\chi\cos\theta\right] \tag{6.2}$$

$$B_{\theta} = \frac{\mu}{r^3}\left[-\sin\chi\cos\theta\cos\left(\Omega t-\phi\right)+\cos\chi\sin\theta\right] \tag{6.3}$$

$$B_{\phi} = -\frac{\mu}{r^3}\sin\chi\sin\left(\Omega t-\phi\right), \tag{6.4}$$

where χ is the magnetic obliquity angle, $\chi = \arccos(\boldsymbol{\Omega}\cdot\boldsymbol{\mu}/\Omega\mu)$. The corotation electric field is enforced at the inner boundary to set the field lines into a solid rotation.

6.2.2 Synchrotron and curvature cooling

To obtain meaningful results in terms of radiative output, radiative cooling must be turned on. In `Zeltron` , cooling is self-consistently captured via the radiation reaction force first introduced in Chapter 2. As a reminder, the radiation reaction force is composed of two terms, a non-relativistic term and a relativistic term (Eq. 2.32). The relativistic term, which scales as γ^2, is clearly dominant in this context where $\gamma \gg 1$. This being said, I realized back then that the non-relativistic term was necessary to capture the correct curvature radiation cooling rate, even in the ultra-relativistic regime.

To see this, we consider the test case of a single particle trajectory initially moving along a circular magnetic field line in the xy-plane, such that $\mathbf{v}\times\mathbf{B} = \mathbf{0}$ and with no electric field, $\mathbf{E} = \mathbf{0}$. This configuration is known to lead to a curvature-drift motion of the particle perpendicular to the magnetic loop, i.e., along the z-direction (Figure 6.3). The curvature-drift velocity normalized by the speed of light is given by the ratio of the particle Larmor radius over the radius of curvature

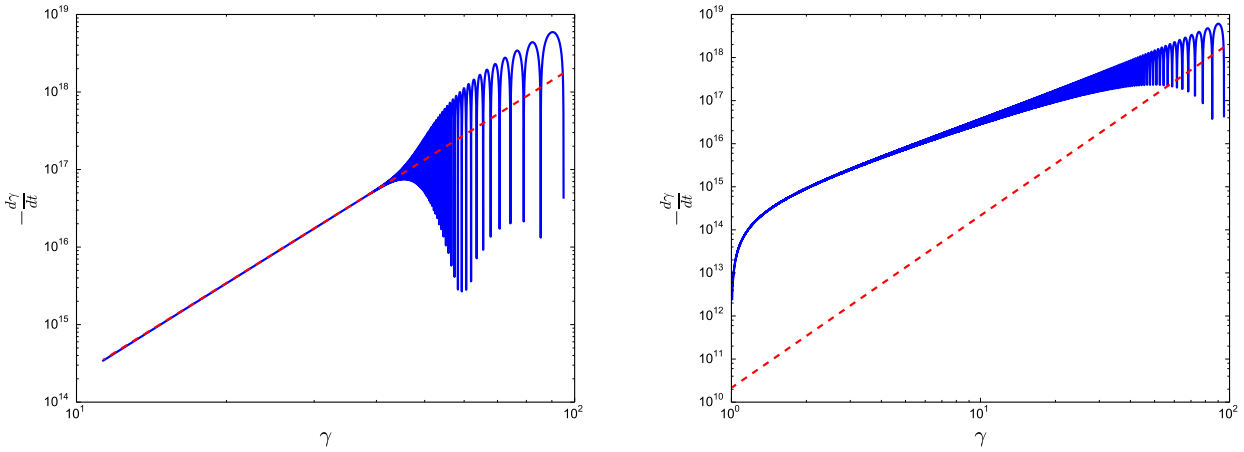

Figure 6.4: Power losses as function of γ for an initial $\gamma_0 = 95$ with (left) and without (right) the non-relativistic term in the radiation reaction force, g^{NR}. The red dashed line is the analytical $P_{\mathrm{curv}} \propto \gamma^4$ curvature losses law (Eq. 6.10).

of the magnetic field line,

$$\beta_{\mathrm{cd}} = \frac{\gamma m_{\mathrm{e}} c^2}{e B_0 R_{\mathrm{c}}} = \frac{R_{\mathrm{L}}}{R_{\mathrm{c}}}. \tag{6.5}$$

From this expression, we can see that the curvature motion has a meaning as long as the particle Larmor radius is small in comparison with the radius of curvature, i.e., $\beta_{\mathrm{cd}} < 1$. In pulsars, we have $R_{\mathrm{L}} \ll R_{\mathrm{c}}$ so that the curvature-drift motion is non-relativistic, $\beta_{\mathrm{cd}} \ll 1$. Therefore, along the z-direction the non-relativistic term of the radiation reaction force should dominate. Indeed, the z-component of the radiation reaction force is

$$g_{\mathrm{z}}^{\mathrm{NR}} = \frac{2}{3} r_{\mathrm{e}}^2 \left[(\mathbf{E} + \boldsymbol{\beta} \times \mathbf{B}) \times \mathbf{B} + (\boldsymbol{\beta} \cdot \mathbf{E}) \, \mathbf{E} \right] \cdot \mathbf{e}_{\mathrm{z}} = -\frac{2}{3} r_{\mathrm{e}}^2 \beta_{\mathrm{cd}} B_0^2, \tag{6.6}$$

for the non-relativistic term, and

$$g_{\mathrm{z}}^{\mathrm{UR}} = -\frac{2}{3} r_{\mathrm{e}}^2 \gamma^2 \left[(\mathbf{E} + \boldsymbol{\beta} \times \mathbf{B})^2 - (\boldsymbol{\beta} \cdot \mathbf{E})^2 \right] \boldsymbol{\beta} \cdot \mathbf{e}_{\mathrm{z}} = -\frac{2}{3} r_{\mathrm{e}}^2 \gamma^2 \beta_{\mathrm{cd}}^3 B_0^2, \tag{6.7}$$

for the relativistic term. The ratio of the two yields

$$\frac{g_{\mathrm{z}}^{\mathrm{NR}}}{g_{\mathrm{z}}^{\mathrm{UR}}} = \frac{1}{\gamma^2 \beta_{\mathrm{cd}}^2}. \tag{6.8}$$

The non-relativistic term dominates if

$$\gamma < \sqrt{\frac{R_{\mathrm{c}}}{R_0}} = 7.6 \times 10^4 R_{\mathrm{c},8}^{1/2} B_{0,5}^{1/2}, \tag{6.9}$$

where $R_0 = m_{\mathrm{e}} c^2 / e B_0$, $R_{\mathrm{c},8} = R_{\mathrm{c}} / 10^8 \mathrm{cm}$, and $B_{0,5} = B_0 / 10^5 \mathrm{G}$. Thus, for typical conditions at the light cylinder of gamma-ray pulsars, the non-relativistic term is

dominant even in the ultra-relativistic limit, $\gamma \gg 1$. If this term is not included, the velocity equilibrium will be incorrect and therefore the ultra-relativistic term will be in turn incorrect. Without the non-relativistic term, the cooling rate is inconsistent with the expected curvature radiation losses (Figure 6.4), $P_{\rm curv}$, which can be derived as

$$P_{\rm curv} = -\mathbf{g}\cdot\mathbf{v} = \frac{2}{3} r_{\rm e}^2 c B_0^2 \beta_{\rm cd}^2 \left(1+\gamma^2\beta^2\right) = \frac{2}{3} e^2 c \frac{\gamma^4}{R_{\rm c}^2}. \tag{6.10}$$

Note that the non-relativistic term can be neglected in the pure synchrotron regime. To summarize, including the full expression of the radiation reaction force captures both synchrotron and curvature cooling.

The presence of strong cooling in the magnetosphere sets a new energy scale in the system: the radiation-reaction-limited particle energy, $\gamma_{\rm rad}$, which can be estimated at the light cylinder as (see Chapter 1)

$$\gamma_{\rm rad}^{\rm LC} \sim \sqrt{\frac{3eR_{\rm LC}^3}{2r_{\rm e}^2 B_\star R_\star^3}} \approx 9.5\times10^4 B_{\star,12}^{-1/2} R_{\star,6}^{-3/2} R_{\rm LC,8}^{3/2}. \tag{6.11}$$

In simulations, the magnetic field strength is lower than realistic values by orders of magnitude due to numerical limitations, and therefore radiative cooling should be negligible in simulations if nothing is done. In practice, we rescale $\gamma_{\rm rad}$ to much lower energies by artificially magnifying the effect of radiative losses by a numerical factor $\kappa_{\rm rad} \gg 1$, so that $\gamma_{\rm rad}^{\rm LC}$ is of the same order as the plasma magnetization at the light cylinder, $\sigma_{\rm LC} \sim 100$ in simulations, i.e., as in nature.

6.2.3 Synchrotron and curvature spectrum

Within the framework of classical electrodynamics, the radiation power spectrum emitted by a single charged particle is given by the classical synchrotron formula (Blumenthal & Gould 1970),

$$\frac{dE}{dtd\nu} = \frac{\sqrt{3}e^3\tilde{B}_\perp}{m_{\rm e}c^2}\left(\frac{\nu}{\nu_{\rm c}}\right)\int_{\nu/\nu_{\rm c}}^{+\infty} K_{5/3}(x)dx, \tag{6.12}$$

where $K_{5/3}$ is the modified Bessel function of 5/3 order, ν is the radiation frequency, $\tilde{B}_\perp$ is the effective perpendicular magnetic field, and

$$\nu_{\rm c} = \frac{3e\tilde{B}_\perp\gamma^2}{4\pi m_{\rm e}c} \tag{6.13}$$

is the critical frequency. In the usual synchrotron formula where there is no external electric field, we simply have $\tilde{B}_\perp = B\sin\alpha$, where α is the angle between the particle velocity and the magnetic field vectors. In an arbitrary situation, the

effective perpendicular magnetic field can be derived as follows. The equation of motion of a single particle is

$$\frac{d\gamma m_{\rm e}\mathbf{v}}{dt} = q\left(\mathbf{E}+\boldsymbol{\beta}\times\mathbf{B}\right) \tag{6.14}$$

$$\frac{d\gamma m_{\rm e}c^2}{dt}\frac{\boldsymbol{\beta}}{c}+\gamma m_{\rm e}c\frac{d\boldsymbol{\beta}}{dt} = q\left(\mathbf{E}+\boldsymbol{\beta}\times\mathbf{B}\right). \tag{6.15}$$

Noticing that

$$\frac{d\gamma m_{\rm e}c^2}{dt} = q\mathbf{E}\cdot\mathbf{v}, \tag{6.16}$$

yields

$$\frac{d\boldsymbol{\beta}}{dt} = \frac{q}{\gamma m_{\rm e}c}\left[\mathbf{E}+\boldsymbol{\beta}\times\mathbf{B}-\left(\boldsymbol{\beta}\cdot\mathbf{E}\right)\boldsymbol{\beta}\right]. \tag{6.17}$$

In the usual synchrotron regime (no cooling, no electric field), we would only have

$$\frac{d\boldsymbol{\beta}}{dt} = \frac{q\left(\boldsymbol{\beta}\times\mathbf{B}\right)}{\gamma m_{\rm e}c}, \tag{6.18}$$

and therefore, we interpret

$$\tilde{\mathbf{B}}_{\perp} = \mathbf{E}+\boldsymbol{\beta}\times\mathbf{B}-\left(\boldsymbol{\beta}\cdot\mathbf{E}\right)\boldsymbol{\beta}, \tag{6.19}$$

as the effective perpendicular magnetic field in the general case. In the pure curvature radiation regime, the radius of curvature is fully determined by the fields as (Kelner et al. 2015)

$$R_{\rm c} = \frac{\gamma m_{\rm e}c^2}{e\tilde{B}_{\perp}}. \tag{6.20}$$

This result is particularly well-suited for numerical purposes because the radiation power, whether this is synchrotron or curvature radiation, is solely determined by local quantities (the fields felt at the particle position), therefore there is no need to reconstruct the curvature of field lines from the global field topology as this is usually done.

6.2.4 Reconstruction of light curves

We reconstruct the emission pattern projected on a screen located at $r = r_{\rm max}$ for any distant observers looking at an arbitrary viewing angle α, defined with respect to the star rotation axis, and phase ω defined with respect to the fixed (xyz)-coordinate system as shown in figure 6.5. The unit vector along the line of sight is

$$\mathbf{e}_{\rm obs} = \left(\sin\alpha\cos\omega,\ \ \sin\alpha\sin\omega,\ \ \cos\alpha\right)_{\rm x,y,z}. \tag{6.21}$$

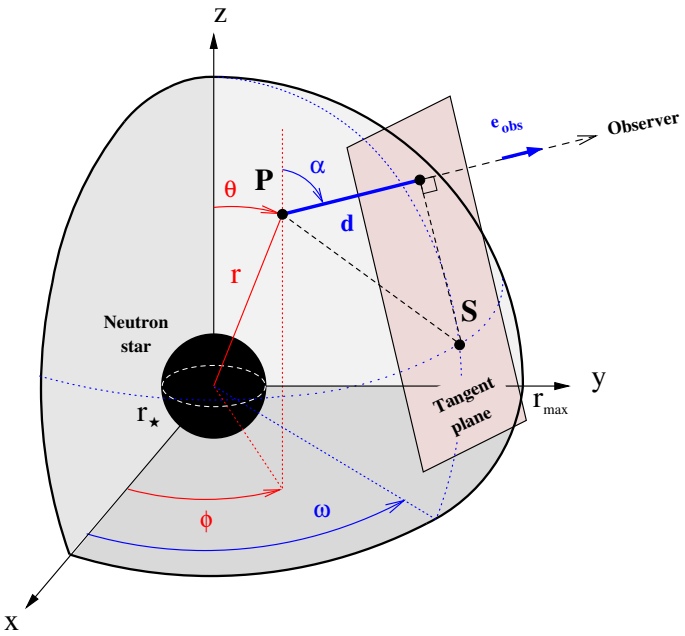

Figure 6.5: Relevant geometrical quantities referred in the text to reconstruct light curves.

A photon emitted at the point $P(r, \theta)$ along the observer's line of sight will arrive with a time delay, t_d, due to its finite time of flight to reach the screen S. This time delay is given by

$$t_\mathrm{d} = \frac{\mathbf{PS} \cdot \mathbf{e}_\mathrm{obs}}{c}, \tag{6.22}$$

where

$$\mathbf{PS} \cdot \mathbf{e}_\mathrm{obs} = r_\mathrm{max} - r \left[\sin\alpha \sin\theta \cos\left(\omega - \phi\right) + \cos\alpha \cos\theta\right]. \tag{6.23}$$

Folded onto the pulsar rotation phase, $\Phi_\mathrm{p} \in [0, 1]$, gives

$$\Phi_\mathrm{p} = \frac{1}{2\pi} \mathrm{Modulo}\left[\omega - \Omega t_\mathrm{d}, 2\pi\right], \tag{6.24}$$

where the origin of phases, $\Phi_\mathrm{p} = 0$, is defined by the plane containing $\boldsymbol{\mu}$ and $\boldsymbol{\Omega}$.

We assume that photons go along straight lines and that they are not absorbed along their path to the observer (optically thin), except if they are eclipsed by the star. Thus, photons do not need to be evolved by the code which saves on computing time. Instead, we sample the radiative output of the simulation regularly by producing a "macrophoton" per macroparticle focused along the direction of the emitting particle due to the strong relativistic beaming for $\gamma \gg 1$. A macrophoton represents a large collection of physical photons of different energies that compose the spectrum given in Eq. (6.12). Knowing the initial positions and directions are sufficient to reproduce the full emission pattern on the sky, or simply referred to as "skymap" in the following.

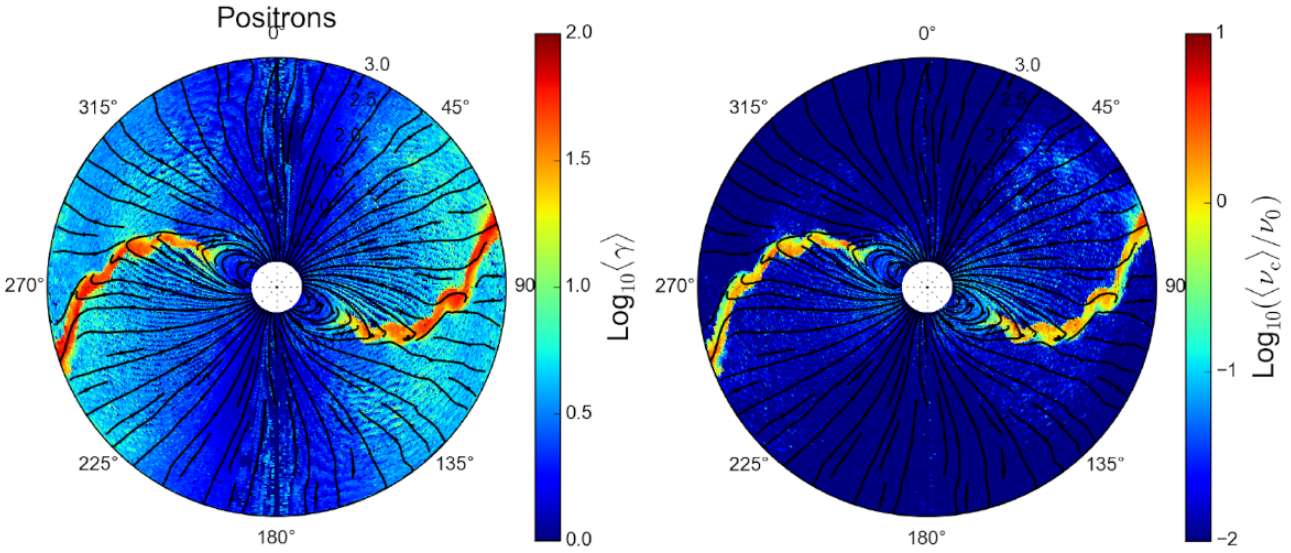

Figure 6.6: Mean particle Lorentz factor (left) and photon frequency (right) for a pulsar obliquity $\chi = 30^{\mathrm{o}}$. Frequencies are normalized to $\nu_0 = 3eB_\star/4\pi m_\mathrm{e}c$.

6.3 Inclined magnetospheres and synthetic light curves

Similarly to the 2D axisymmetric model, the magnetosphere quickly settles into a quasi-steady, quasi-force-free state after a few spin periods. The magnetosphere presents all of the expected features: a corotating magnetosphere inside the light cylinder and an undulating current sheet beyond, geometrically contained within a spherical wedge between $\theta = \pi/2 - \chi$ and $\theta = \pi/2 + \chi$. As for the aligned rotator, the current sheet is the main site of particle acceleration (see Figure 6.6, left panel). Here again, the energy gained by the particles is set by the upstream plasma magnetization at the light cylinder, $\gamma \sim \sigma_\mathrm{LC} \approx 50$. As a result of this, the equatorial current sheet is also the main source of high-energy synchrotron emission (see Figure 6.6, right panel). The asymmetry between both species remains in the oblique solution, with precipitating high-energy electrons and high-energy positrons being pushed outwards (Figure 6.7), but this asymmetry decreases with increasing obliquity angle and disappears entirely for the orthogonal rotator by symmetry.

Figure 6.8 (left) is a 3D rendering of the total high-energy radiation flux, defined above the fiducial synchrotron frequency $\nu_0 = 3eB_\star/4\pi m_\mathrm{e}c$, shining at all phases irrespective of the observer's viewing angle. It is clearly visible from this figure that the emission originates exclusively from outside the light cylinder, in contrast to classical models. The nature of the emission is synchrotron radiation produced by the particles trapped within the sheet and following Speiser orbits. The emission is spatially extended but the flux peaks at the base of the sheet, near the light cylinder where particles are most efficiently accelerated and where the fields are strongest.

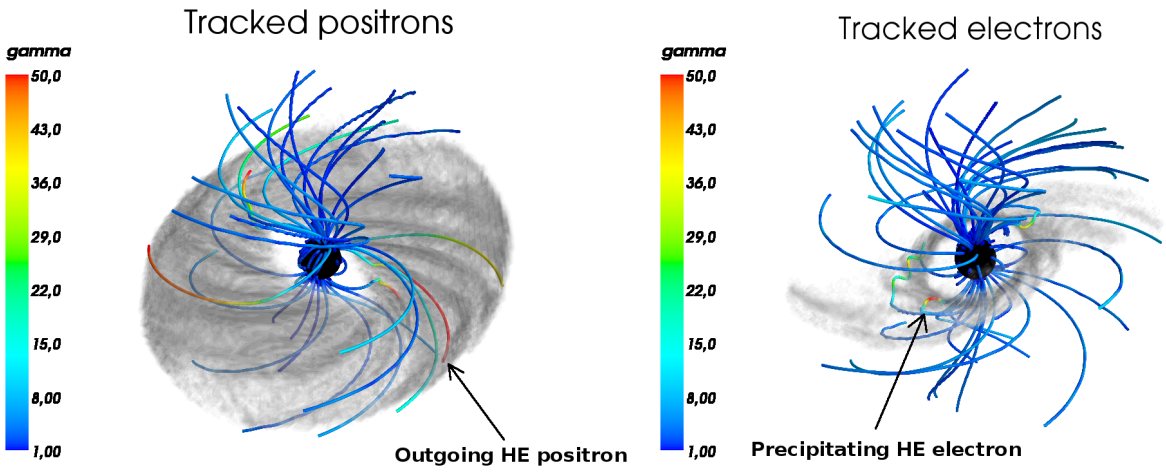

Figure 6.7: Typical high-energy positron (left) and electron (right) trajectories accelerated in the equatorial current sheet via relativistic reconnection. Trajectories are shown in the corotating frame so that the current sheet appears as static in this frame. The grey regions show where the high-energy radiation flux (integrated over all angles) originates in the simulation (Figure 6.8).

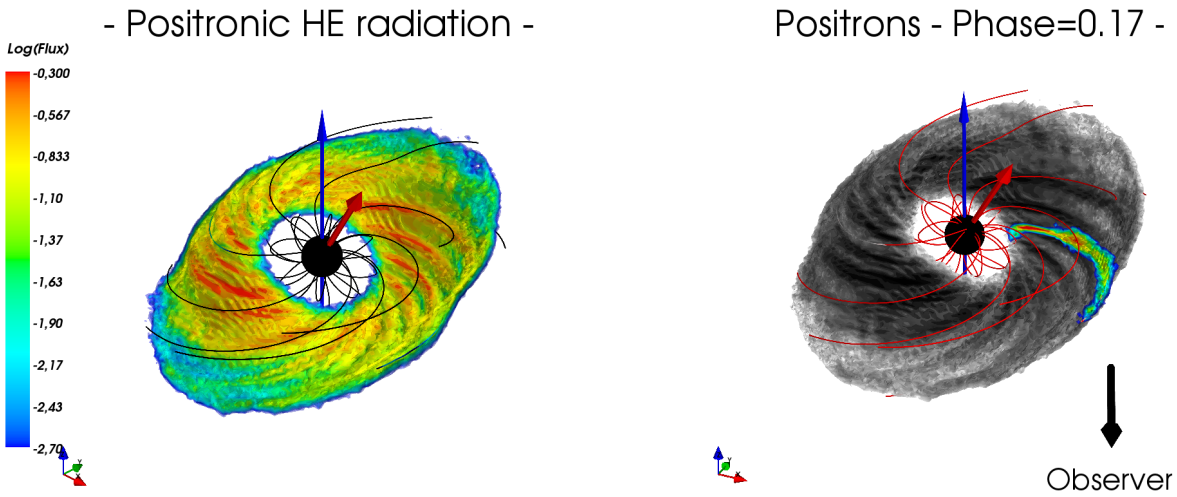

Figure 6.8: Total high-energy radiation flux for $\chi = 30^{o}$ (left panel) as opposed to the flux received by an observer looking along the direction shown by the black arrow (right panel, region in color).

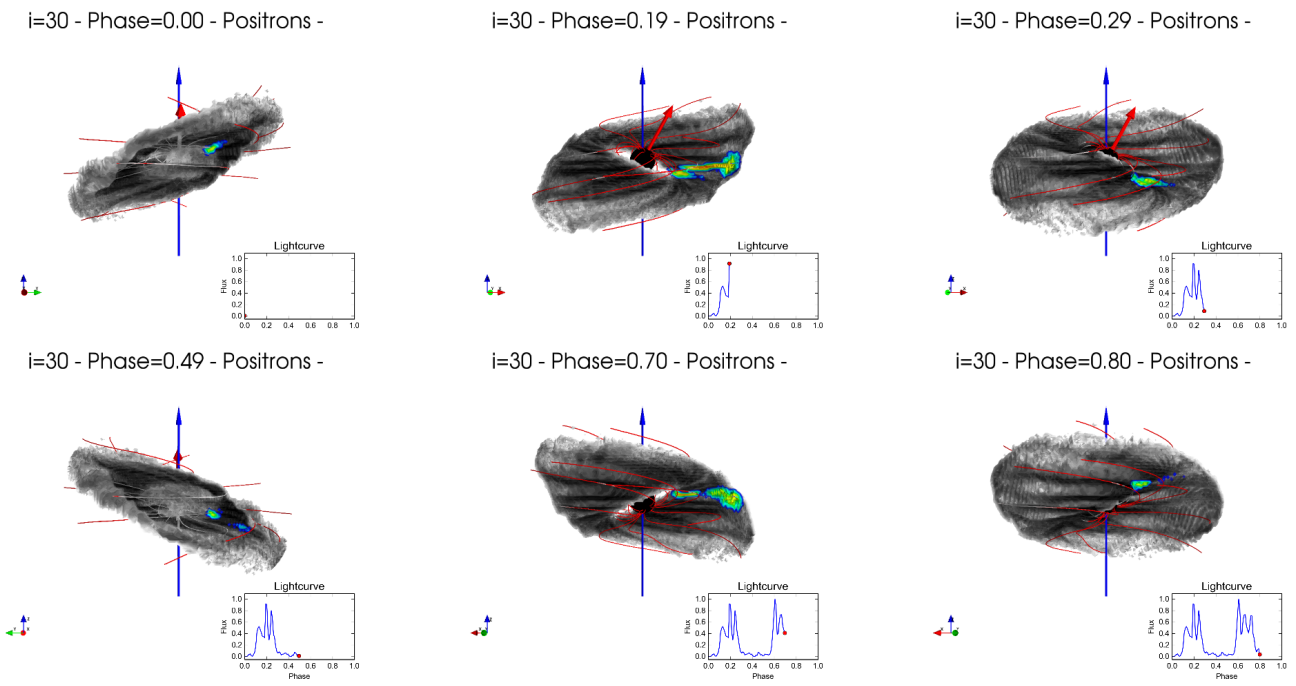

Figure 6.9: Evolution of the caustic of emission as a function of the pulsar phase for an observer looking along the equatorial plane ($\alpha = 90^{\rm o}$), and formation of the light curve (inset curve) for $\chi = 30^{\rm o}$.

Due to relativistic beaming and retardation effects, a distant observer sees photons emitted from a narrow strip of the sheet, as shown in Figure 6.8 (right panel). At a given phase, the observer receives all the photons emitted by the particles moving (nearly radially) towards the observer, which is the accumulation of photons emitted at different times and locations but arriving in phase at the observer. This phenomenon is known as the "caustic effect". Figure 6.9 shows how the caustic pattern changes as the pulsar performs a full spin. It also shows how much flux is received by the observer as a function of pulsar phase, i.e., how the light curve forms. The caustic effect leads to the formation of bright pulses of synchrotron radiation each time the observer's line of sight crosses the current layer. In other words, the light curve is shaped by the geometry of the equatorial current sheet. In most cases, it happens twice per period, but it can also happen only once at small viewing angles. Our simulations provide a robust and natural explanation to the observed features of *Fermi* pulsar light cuves.

Figure 6.10 shows the full skymap of emission for $\chi = 45^{\rm o}$. From this figure, we can reconstruct a synthetic light curve for any observer (line of constant α) as depicted in the right panel. For an observer looking along the equatorial plane, both pulses of emission are nearly identical and separated by 0.5 in phase. The symmetry breaks at smaller viewing angles, so that the more general solution is two peaks of different amplitudes, but their separation is not smaller than 0.4. This is very different from semi-analytical models which assumes a constant emissivity with latitude. We predict that the emitted power is concentrated within the equatorial

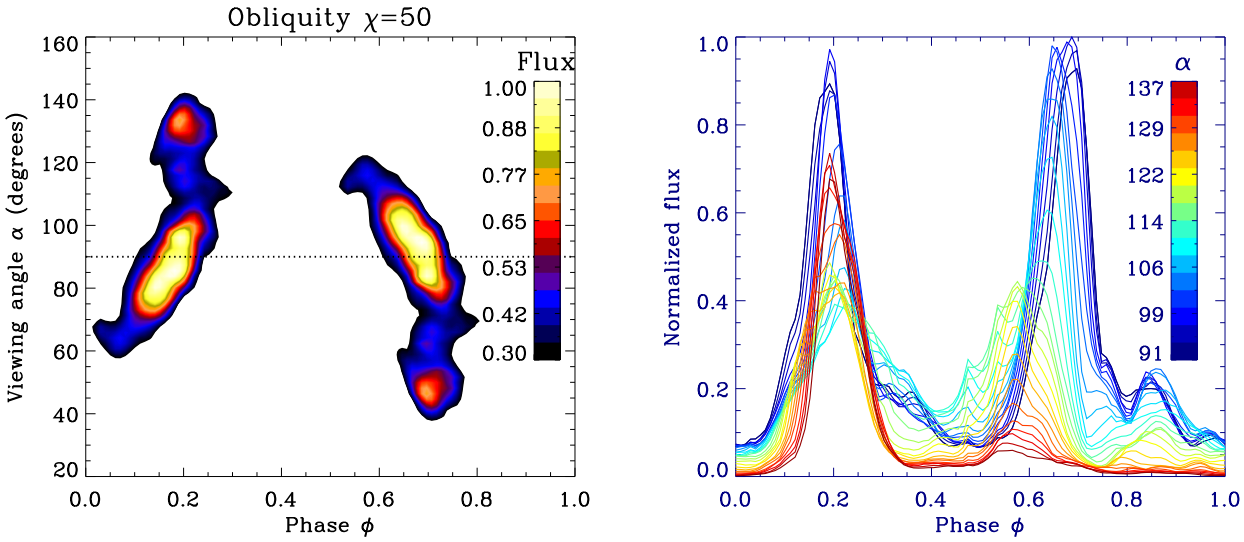

Figure 6.10: Left: High-energy synchrotron emission pattern projected on the sky for an obliquity angle $\chi = 45^{o}$. Right: Resulting synthetic light curves as a function of the viewing angles. Figure taken from Cerutti (2018).

regions where the Poynting power is the highest, even for the orthogonal rotator where the current sheet is present at all latitudes. The gamma-ray beam generally covers a wide solid angle on the sky, of order 1 steradian. This result fits well with the scenario of a broad gamma-ray beam misaligned with a thinner radio beam. Assuming a polar-cap origin for the radio emission yields a radio pulse near phase $\Phi_{\rm P} = 0$, meaning that it is always shifted $\gtrsim 0.2$ in phase from the gamma-ray pulse. The radiative efficiency is also very high. With a typical dissipation rate comprised between $10-20\%$ within $3R_{\rm LC}$, the high-energy synchrotron power carries between 2% (orthogonal rotator) and up to 9% (aligned rotator) of the total spindown power. These numbers are consistent with the observed levels ($1-10\%$, Sect. 6.1).

While the comparison with gamma-ray observations has remained rather qualitative so far, it is already possible to perform lightcurve fitting thanks to the library of synthetic skymaps performed for all magnetic obliquities. With the help of Aloïs de Valon during his Master 1 internship in 2017, we aimed at comparing simulated light curves with the second *Fermi*-LAT pulsar catalog (Abdo et al. 2013) using a simple χ-squared fitting method. The results of his analysis suggest that (i) millisecond pulsars are on average more aligned than young pulsars, (ii) there is a hint of an alignment of the magnetic axis on a $10^5 - 10^6$ yrs timescale, which is consistent with what is reported in radio (Young et al. 2010), and with the theoretical prediction proposed in Philippov et al. (2014), and (iii) the magnetic axis is nearly randomly distributed for very young pulsars, suggesting that there may be no preferential orientation at birth.

Although very promising and interesting, we are not fully confident that these results are robust given the large uncertainties in the exact shape of the theoretical light curves. These uncertainties are largely due to the intrinsic variability within

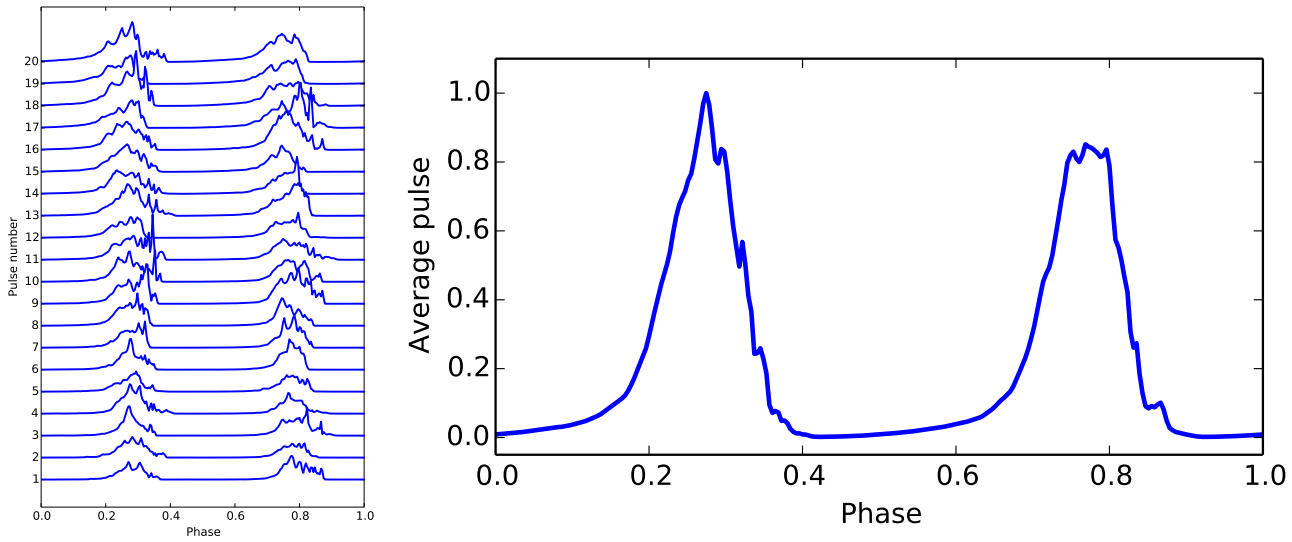

Figure 6.11: Left: Synchrotron lightcurve reconstructed after each pulsar rotation period. Right: Average lightcurve after stacking all individual lightcurves from the left panel. Figure taken from Cerutti & Philippov (2017).

a lightcurve associated with the tearing and the kink modes developing in the current layer. These plasma instabilities produces secondary peaks and troughs in the lightcurve, which may well be physical although most likely exaggerated in simulations due to the small separation between scales. In constrast, *Fermi* lightcurves are folded over months of exposure to collect enough photons, meaning that the reported lightcurves represent a time average pulse profile over a very large number of rotation period. The way to go to make further progress on this would be to integrate 3D simulations for several rotation periods, at least 10, and make a time average to smooth them out before making a direct comparison with the *Fermi* catalog. Figure 6.11 illustrates the intra-pulse variability induced by the formation of plasmoids in the current layer, and it shows how lightcurve stacking helps at recovering a smooth average pulse profile. This has been achieved with 2D PIC simulations of an orthogonal rotator in the equatorial plane (more details in Sect. 6.5 below).

Our findings were confirmed by two other studies, by Philippov & Spitkovsky (2018) and Kalapotharakos et al. (2018) using different PIC codes and different prescriptions for the plasma supply.

6.4 Polarization

Another diagnostic that can readily be simulated from first principles is polarization. This diagnostic is very promising at disentangling between models because it is very sensitive to the magnetic field topology where synchrotron (or curvature) photons are being produced. Unfortunately, it is not yet possible to measure it in the gamma-ray band (however, see Giomi et al. 2017), but future missions like

HARPO aim at filling this gap (Gros et al. 2018). Polarization is observed in the radio band for a long time, it is generally consistent with a "S"-shape pattern which is the signature of an emitting zone located at the polar cap of the star (Radhakrishnan & Cooke 1969). As far as the incoherent emission is concerned, like the synchrotron radiation process, it can be detected today in the optical band. Unfortunately, pulsars are very dim in this band and therefore polarization can be measured for a few targets only.

The best polarimetric measurement available today is from the Crab pulsar with phase-resolved data in the optical and UV bands (Smith et al. 1988; Graham-Smith et al. 1996; Słowikowska et al. 2009). The data show an abrupt swing of the polarization angle correlated with each pulse of emission. This result cannot be reproduced in the framework of classical magnetospheric models (polar cap, outer gap, slot gap). However, it does make a lot of sense if each pulse of light is produced when the line of sight crosses the current sheet, because this is a location where the magnetic field naturally changes its polarity and thus, where the polarization angle should swing by 180° (Pétri & Kirk 2005). In some sense, the data were speaking for themselves for all this time. Another important element to notice is that the optical pulse profile is nearly identical to the gamma-ray profile in the Crab, suggesting that they have a common origin, and therefore that we may use the optical data as a proxy for the gamma-ray polarization properties.

In 2016, I hired Jérémy Mortier for his Master 1 summer project to model the expected phase-resolved polarization signal directly from the 3D PIC simulation data. Synchrotron radiation emitted by a single particle is highly polarized. The degree of linear polarization reaches about 75%. For an ensemble of particles with a broad energy and angular distribution, the degree of polarization is usual much smaller. The circular component is suppressed for ultrarelativistic particles (Ginzburg & Syrovatskii 1965), it will not be discussed in this section. To compute the degree of linear polarization, Jérémy began by reconstructing the Stokes parameters, I, Q, and U, by summing over the contribution from all the particles pointing towards the observer at a given pulsar phase, $N_{\rm obs}$,

$$I = \sum_{i=1}^{N_{\rm obs}} w_i F(\xi_i) \tag{6.25}$$

$$Q = \sum_{i=1}^{N_{\rm obs}} w_i G(\xi_i) \cos(2{\rm PA_i}) \tag{6.26}$$

$$U = \sum_{i=1}^{N_{\rm obs}} w_i G(\xi_i) \sin(2{\rm PA_i}), \tag{6.27}$$

where $F(\xi) = \xi \int_\xi^{+\infty} K_{5/3}(\xi')d\xi'$ and $G(\xi) = \xi K_{2/3}(\xi)$ are the usual synchrotron functions, and w is the particle weight. PA is the polarization angle defined between the rotation axis and the effective perpendicular magnetic field direction, $\tilde{\mathbf{B}}_\perp$

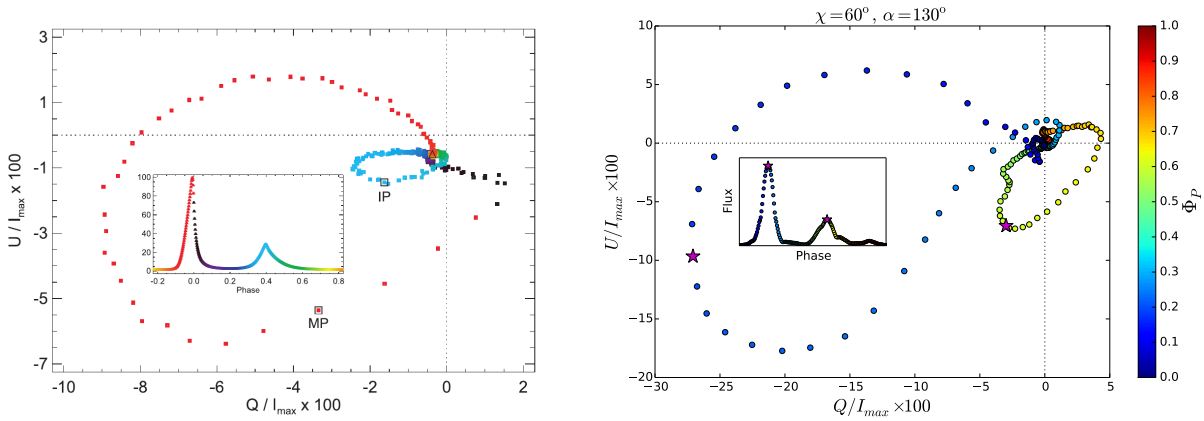

Figure 6.12: Vector diagram measured in the optical (left, Słowikowska et al. 2009) and vector diagram simulated from the PIC model (right panel, Cerutti et al. 2016a). Inset curves show the pulse profile.

(Eq. 6.19), projected onto the plane of the sky. The degree of linear polarization from this ensemble of particles is then given by

$$\Pi = \frac{\sqrt{Q^2 + U^2}}{I}, \tag{6.28}$$

and the angle of polarization is given by

$$\tan 2\mathrm{PA} = \frac{U}{Q}. \tag{6.29}$$

Jérémy generated a synthetic library of vector diagrams, $U(Q)$, for any viewing angle α and magnetic obliquity angle χ. The vector diagram is an effective way to visualize swings of the polarization angle. We found that wherever there is a pulse of emission, there is a full loop in the vector diagram, i.e., PA swings by 180°. In the general case where lightcurves have two pulses, there are two loops in the vector diagram meaning that the direction of the magnetic field rotates by 180° after the first crossing of the layer, followed by another rotation by 180° after the second crossing of the layer, which brings us back to the initial magnetic polarity. The size and the orientation of the loops change as a function of the viewing and obliquity angles. The observed pattern in the Crab pulsar is a small loop nested inside a bigger loop, both pointing in the $(Q < 0, U < 0)$ quadrant (Figure 6.12, left panel). We found that there is a unique set of parameters which can explain this pattern, it corresponds to a viewing angle $\alpha \sim 130°$ and a magnetic obliquity $\chi \sim 60°$ (Figure 6.12, right panel). This is a new and independent way to constrain the Crab pulsar geometrical parameters. This result is also consistent with the usual estimate based on the X-ray morphology of the nebula (Weisskopf et al. 2012).

We predict a high degree of polarization in the gamma-ray band, similar to what is reported in optical. Figure 6.13 shows how Π varies with χ, and more importantly, it shows a significant difference between on-pulse and off-pulse polarization. On-pulse emission is always weaker than the off-pulse emission by a factor

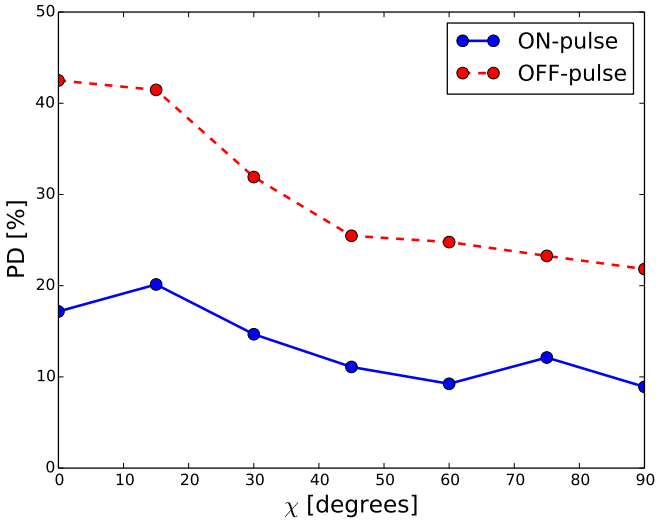

Figure 6.13: Predicted linear degree of polarization in the gamma-ray band on- and off-pulse.

~ 2 (on: $\Pi \sim 10-20\%$, off: $\Pi \sim 20-40\%$). Depolarization in the pulse is the result of the caustic effect (Dyks et al. 2004; Cerutti et al. 2016b), i.e., because of the superposition of photons emitted at different locations where the orientation of the field is different. From $1-2R_{\rm LC}$ where most of the synchrotron emission comes from, the orientation of the field changes rapidly: from a poloidal- to a toroidal-dominated magnetic structure. This anticorrelation between flux and degree of polarization is also observed in the Crab pulsar.

The study of polarization is a very powerful diagnostic, which combined with pulse profile modeling could really make a difference at disentangling between models and constrains pulsar parameters. The high degree of polarisation predicted in the gamma-ray band makes pulsars one of the best targets for future polarimetric missions.

6.5 Dissipation of the striped wind

6.5.1 Context and motivations

In this last section, I report on my latest study which aims at studying the large-scale dynamics of pulsar winds, with an emphasis on dissipation of the striped wind structure and particle acceleration. A long standing problem in pulsar wind theory is the fate of the equatorial current sheet: does it survive or not on its way to the nebula? So far, this issue has led to contradictory conclusions. With the hope to solve the "sigma-problem"[2], Coroniti (1990) proposed that the layer thickness

[2]The puzzle is to understand why the plasma in the nebula is weakly magnetized while the pulsar wind itself is strongly magnetized. Porth et al. (2013) showed that the nebula is most likely magnetized, meaning that there is in fact no sigma-problem.

should increase with radius so that the striped wind should disappear once the layer thickness becomes comparable to the distance between two consecutive stripes, i.e., the striped wind half wavelength, $\pi R_{\rm LC}$. More formally, the above condition translates into the following condition:

$$\Delta \equiv \frac{\delta}{\pi R_{\rm LC}} = 1, \tag{6.30}$$

where δ is the layer thickness, and Δ is the filling factor of the current layer. Using a simple reconnection scenario, Coroniti (1990) predicted that the striped wind should fully dissipate far upstream the pulsar wind termination radius. Lyubarsky & Kirk (2001) and later Kirk & Skjæraasen (2003) argued that the release of magnetic energy should lead to a net work applied on the wind, leading to an effective acceleration of the wind and a decrease of the dissipation rate due to relativistic time dilation effects. They came to the conclusion that pulsar winds should not have enough time to dissipate, unless the current layer is filled with an unusually high plasma supply.

These early scenarios are based on simplistic models of magnetic reconnection, and to some extent on a simple model of pulsar magnetospheres and winds. I felt it was the good moment to revisit this issue in light of what we have learnt over the last 5 years on relativistic reconnection and pulsar magnetospheres. My objective was to reconcile dissipation at small scales with a realistic model of reconnection and pulsar winds within the same global PIC model. PIC simulations described above focused on the closest parts to the star: the magnetosphere and the base of the wind up to a few light cylinder radii. Thus, the radial extent is too limited to draw solid conclusions on the fate of the wind at large scales. To this end, I obtained a 27 million CPU-hours time allocation on the Irene supercomputer at TGCC in CEA via PRACE in 2018 to perform 3D PIC simulations from the stellar surface up to 50 light cylinders away. I summarize below what represented a strenuous work, perhaps the most challenging project I have undertaken so far, which has just come to an end in the summer 2020. This work is also the logical followup of a similar attempt limited to 2D simulations in the equatorial plane of an orthogonal rotator (Cerutti & Philippov 2017).

6.5.2 Results

For this study, I chose a split-monopole configuration for the fields (Michel 1973b; Bogovalov 1999) because it is a good model of the striped wind structure. The region inside the light cylinder where the field should significantly depart from the monopolar structure is of little interest for this study, and for this reason the light cylinder is brought as close as possible to the stellar surface, $R_{\rm LC} = 3R_\star$. Three inclinations are considered: $\chi = 30^{\rm o}$, $60^{\rm o}$ and $85^{\rm o}$. A dense neutral pair plasma is injected from the stellar surface at all times so that the magnetosphere is close to the force-free regime. Figure 6.14 shows density isosurfaces of the final state of the

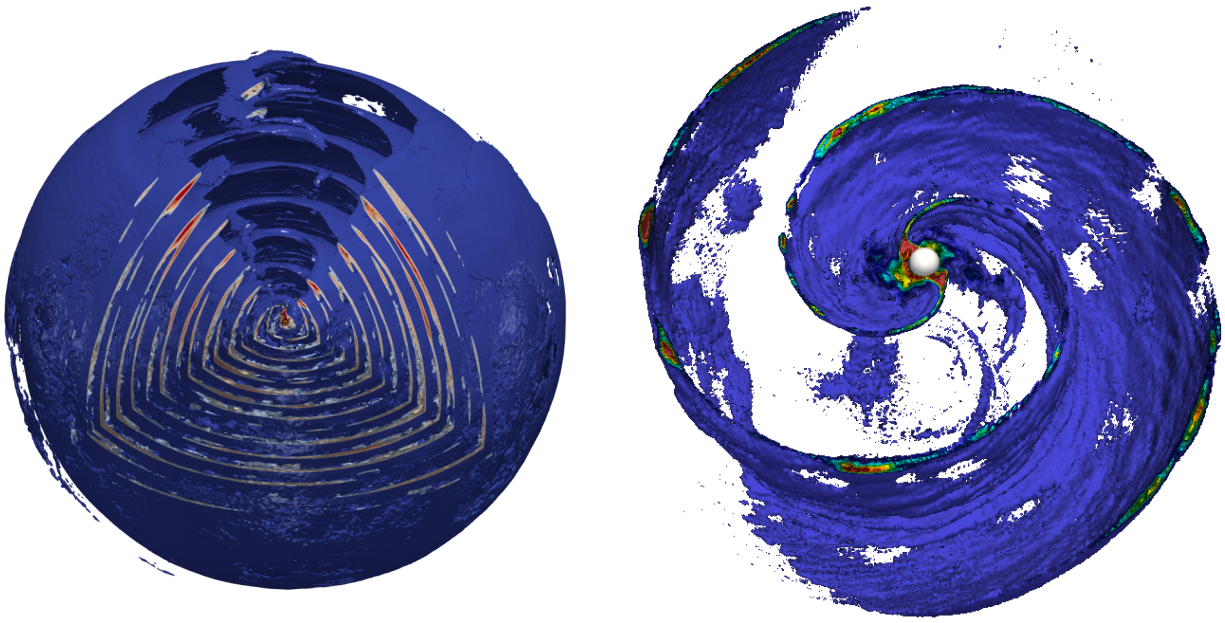

Figure 6.14: Density isosurfaces of a pulsar wind with $\chi = 60^{\circ}$. Left: Global view of the simulation box, $r_{\rm max} = 50R_{\rm LC}$. A quarter of the upper hemisphere has been removed to highlight the internal structure of the wind (Cerutti et al. 2020). Right: Zoomed-in view on the inner regions, only the lower hemisphere is shown for clarity.

simulation, reached after about 10 spin periods. The overall structure is consistent with the split-monopole prediction (Bogovalov 1999): an undulating current layer geometrically confined within $\pi/2 - \chi < \theta < \pi/2 + \chi$. At higher latitudes, the wind is smooth and consistent with a single monopole solution (Michel 1973b). The current layer is highly unstable to kink modes, and more importantly to the relativistic tearing mode. The layer breaks up into a dynamical chain of magnetic flux ropes forming near the light cylinder and merging to form bigger structures, well visible on the zoomed-in view in Figure 6.14 (right panel). These structures are reminiscent of 3D studies of plane-parallel reconnection (Chapter 3). This dynamical behavior proceeds up to $\sim 10R_{\rm LC}$ beyond which the expansion of the wind freezes substructures in the layer.

Figure 6.15 shows that dissipation of the Poynting flux proceeds at all radii, without any sign of saturation, and reaches about 50% at $50R_{\rm LC}$. This power is channeled to particle kinetic energy flux which continuously increases with radius. The spectrum of particles leaving the box can be schematically decomposed into two components:

(i) A narrow, low-energy component in the polar regions, outside the stripes, whose energy-scale is set by the wind bulk Lorentz factor, Γ. The increase in the particle energy is associated with the bulk acceleration of the wind via ideal MHD processes.

(ii) A broad hard power-law tail in the striped wind, with a low-energy break

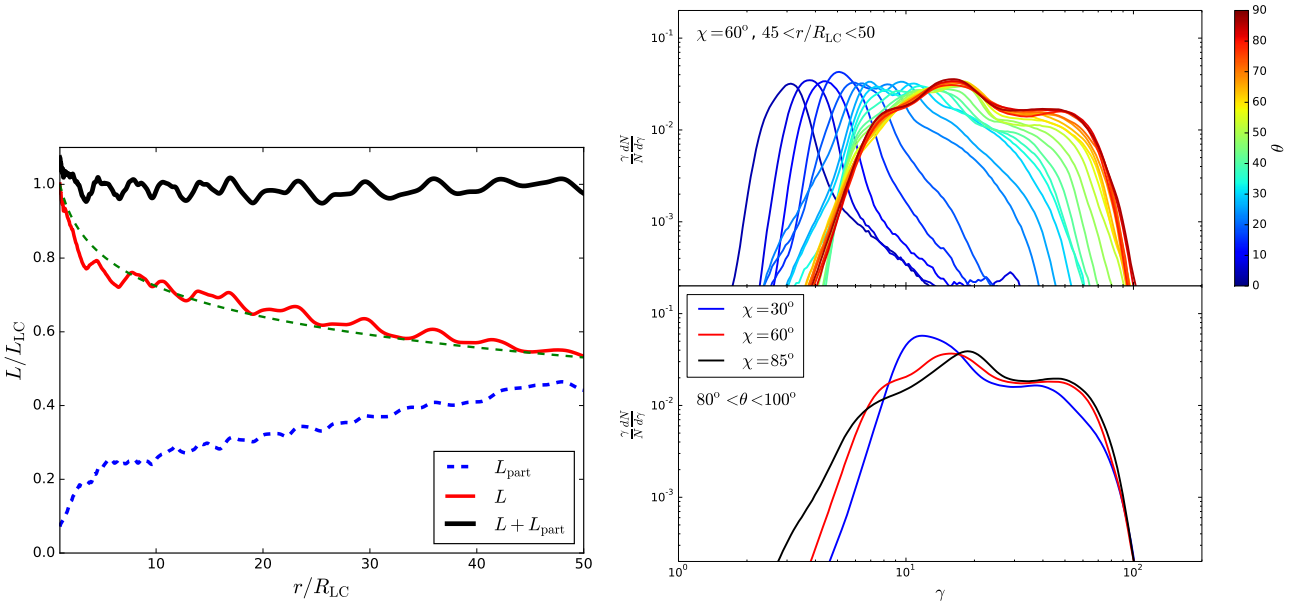

Figure 6.15: Left: Radial evolution of the Poynting and particle kinetic energy flux for $\chi = 60^o$. The green dashed curve is the analytical toy model with $\beta_{\rm rec} \approx 0.12$. Right: Outgoing particle spectrum at $r = 50R_{\rm LC}$ as a function of latitude (top) and for all three magnetic inclination (bottom). Figures adapted from Cerutti et al. (2020).

set by the bulk Lorentz factor of the wind Γ, and a high-energy break set by the magnetization parameter at the light cylinder $\sigma_{\rm LC}$. The hard power-law index is consistent with efficient particle acceleration via relativistic reconnection in the high-σ regime, i.e., $dN/d\gamma \propto \gamma^{-1}$. Thus, the spectrum is the result of non-thermal particle acceleration in the wind co-moving frame.

In the inner regions, the wind Lorentz factor grows nearly linearly with radius as expected (Eq. 4.26). Past the fast magnetosonic point, located in the simulations at $r \sim 4R_{\rm LC}$, it saturates to about $\gamma_\infty \approx 10$, while dissipation continues to operate further away. This is evidence that dissipation does not lead to a significant acceleration of the wind. Instead, the energy is dissipated in the form of hot particles confined within magnetic islands. This is a very different picture than the one drawn by Lyubarsky & Kirk (2001) and Kirk & Skjæraasen (2003).

6.5.3 A toy model for dissipation

To extrapolate the results to realistic scales, I proposed a simple 1D spherical model inspired from simulations. In the steady state, dissipation of the Poynting flux is governed by Joule's term. In its integral form, the Poynting flux theorem yields

$$L(r) - L_0 = -\int_{R_{\rm LC}}^{r}\int_0^{\pi}\int_0^{2\pi} (\mathbf{J}\cdot\mathbf{E})\, r^2 \sin\theta dr d\theta d\phi. \tag{6.31}$$

To a very good accuracy, simulations show that $\mathbf{J}\cdot\mathbf{E}\approx J_\theta E_\theta$. The current being localized within X-points, we can interpret the electric field aligned with the current as the reconnection electric field, usually parametrized as (Lyubarskii 1996; Uzdensky & Spitkovsky 2014)

$$E_{\rm rec}=\beta_{\rm rec}B_\phi^{\rm up}, \tag{6.32}$$

where $\beta_{\rm rec}$ is the dimensionless reconnection rate, and $B_\phi^{\rm up}$ is the local magnetic field strength above the current layer. To a very good accuracy, simulations indicate that the latter is very close to the ideal Michel field solution, meaning that the layer is fed with fresh unreconnected field, so that

$$B_\phi^{\rm up}\approx\frac{R}{R_{\rm LC}}B_\star\left(\frac{r_\star}{r}\right)^2. \tag{6.33}$$

The relation between the current and the field is given by Ampère's law, as (Cerutti & Philippov 2017)

$$\frac{4\pi}{c}J_\theta\delta=2B_\phi^{\rm up}. \tag{6.34}$$

Putting everything together, and assuming for the ϕ-integral that Joule's term is non-zero only in the sheet of angular size $\Delta\phi\sim\delta/r$, we obtain the remarkably simple result

$$\frac{L(r)}{L_0}=1-\beta_{\rm rec}\ln\left(\frac{r}{R_{\rm LC}}\right), \tag{6.35}$$

where a constant numerical factor of order unity has been integrated into $\beta_{\rm rec}$ to simplify the expression. This model is a good fit to the radial evolution of the Poynting flux for a reconnection rate $\beta_{\rm rec}\approx 0.12$, which is consistent with plane-parallel studies of reconnection.

6.5.4 Implications

PIC simulations of the striped wind suggest that reconnection proceeds at a similar rate at all radii. It is independant of the layer thickness and solely governed by the reconnection rate as long as the magnetosphere is in the force-free regime, i.e., if there are no vacuum gaps which is appropriate for describing pair producing pulsars, the regime of interest. In the ultrarelativistic regime ($\sigma\gg 1$), reconnection studies show that this rate weakly depends on the system size, layer thickness or plasma magnetization (Werner et al. 2018), as reported here. This result leads to the rather extraordinary conclusion that all pair producing pulsars should dissipate at approximatively the same rate. Using Eq. (6.35), there is a universal dissipation radius given by

$$R_{\rm diss}=R_{\rm LC}\exp\left(\beta_{\rm rec}^{-1}\right)\sim 10^2-10^4R_{\rm LC}, \tag{6.36}$$

for $\beta_{\rm rec}=0.1-0.2$, meaning that the striped wind should be fully dissipated well before entering the nebula in isolated systems where $R_{\rm nebula}/R_{\rm LC}\sim 10^9\gg R_{\rm diss}$.

This work also suggests that the wind bulk Lorentz factor is much less relativistic than previously thought. In the classical models (Rees & Gunn 1974; Wilson & Rees 1978; Kennel & Coroniti 1984), the wind is perfectly cold, monoenergetic with $\Gamma \sim 10^4 - 10^6$. We find instead that the wind is composed of hot pairs with a broad energy spectrum confined within magnetic islands, themselves moving relativistically along with the wind bulk Lorentz factor approximately given by,

$$\Gamma_\infty \sim \mu_{\rm M}^{1/3} \lesssim 100, \tag{6.37}$$

where $\mu_{\rm M} \equiv B^2/4\pi n m_{\rm e} c^2$ is Michel magnetization parameter. Last, we find that dissipation leads to non-thermal particle acceleration in the striped wind. The predicted particle distribution is a broad power law limited by $\gamma_{\rm min} \sim \Gamma_\infty \sim \mu_{\rm M}^{1/3}$ at low energies, and limited by $\mu_{\rm M}$ at high energies, with a spectral index close to $dN/d\gamma \propto \gamma^{-1}$. Scaled to the Crab pulsar parameters with $\mu_{\rm M} \sim 10^5$ gives $50 \lesssim \gamma \lesssim 10^5$. Injected at the shock front, these energetic pairs could well be at the origin of the mysterious radio emission in the Crab Nebula (Meyer et al. 2010).

Part III

Black-hole magnetospheres

This last part focuses on my recent efforts to develop a fully kinetic model of black hole magnetospheres, motivated by a particularly exciting observational context that I describe in the first chapter (Chapter 7). To this end, general relativistic effects must be implemented in `Zeltron` . This work began in the Spring 2017 with Jérémy Mortier Master 2 thesis project aimed at developing the Maxwell solver in curved spacetime. Sasha Philippov and Kyle Parfrey then joined this effort in the Fall 2017 and thanks to their strong commitment, a first version of the code in 2D was completed by the end of 2017. In parallel to this work, Amir Levinson, professor at the University of Tel Aviv and expert in the field of black hole electrodynamics, joined IPAG for 5 months as a University Grenoble Alpes' visiting professor to work with me on a 1D PIC model combined with a Monte-Carlo model for the radiative transfer, based on a 1D spherical version of `Zeltron` . Thanks to these new implementations that I describe in Chapter 8, `Zeltron` became the first general relativistic radiative PIC code (GRRPIC) in the world, opening up new perspectives.

In the last chapter, I will describe the first applications of the code focused on the case studies of a Kerr black hole immersed in a uniform or a monopolar magnetic field configuration. These studies lead to two publications in the prestigious Physical Review Letters journal (Parfrey et al. 2019; Crinquand et al. 2020), the former even made the cover of the journal and led to a significant coverage by scientific magazines[3]. Today, the study of black-hole magnetospheres has become my main research project, and it will continue to be at the center of my activity for the next 5 years at least, thanks to the ERC-funded project SPAWN, which will be described in more details in Part IV.

[3] APS Viewpoint, Nature, La Recherche

Chapter 7

Context and the need for a kinetic description

This chapter is adapted from the narrative part of the SPAWN ERC proposal.

7.1 Context and motivations

Black holes are often regarded as the simplest astrophysical objects because they are fully characterized by their mass, their spin and electric charge. Whether they are supermassive or of stellar-mass, black holes are involved in some of the most energetic astrophysical phenomena in the Universe such as active galactic nuclei (AGN), microquasars and gamma-ray bursts. Their activity often results in the presence of a disk gas and dust as well as a relativistic plasma jet. This phenomenon of accretion-ejection is accompanied by an efficient acceleration of particles which translates into a powerful non-thermal radiation at all wavelengths, predominantly in the radio, X-ray and gamma-ray bands. How and where are these particles accelerated near black holes is still a mystery.

Today, this issue is strongly motivated by the release in April 2019 of the first image of the shadow of the supermassive black hole M87* by the Event Horizon Telescope (EHT, Event Horizon Telescope Collaboration 2019a). This image represents the imprint on the sky of the black hole event horizon itself (Figure 7.1, left panel). The surrounding radiation is most likely of synchrotron origin emitted by relativistic electrons immersed in a strong magnetic field carried by the plasma orbiting the black hole, bringing direct evidence for efficient particle acceleration near black holes. The relativistic jet of M87 itself has been imaged for years with increasing angular resolution down to a few Schwarzschild radii (Blandford et al. 2019) (Figure 7.1, right panel). Hence, there is a tantalizing connection between horizon-scale processes and the formation of relativistic jets, although it is still unclear how the image of the jet connects with the image of the shadow. The supermassive black hole SgrA* at the Galactic Center has not been imaged yet by the EHT collaboration (the source is too variable). Nonetheless, the Gravity

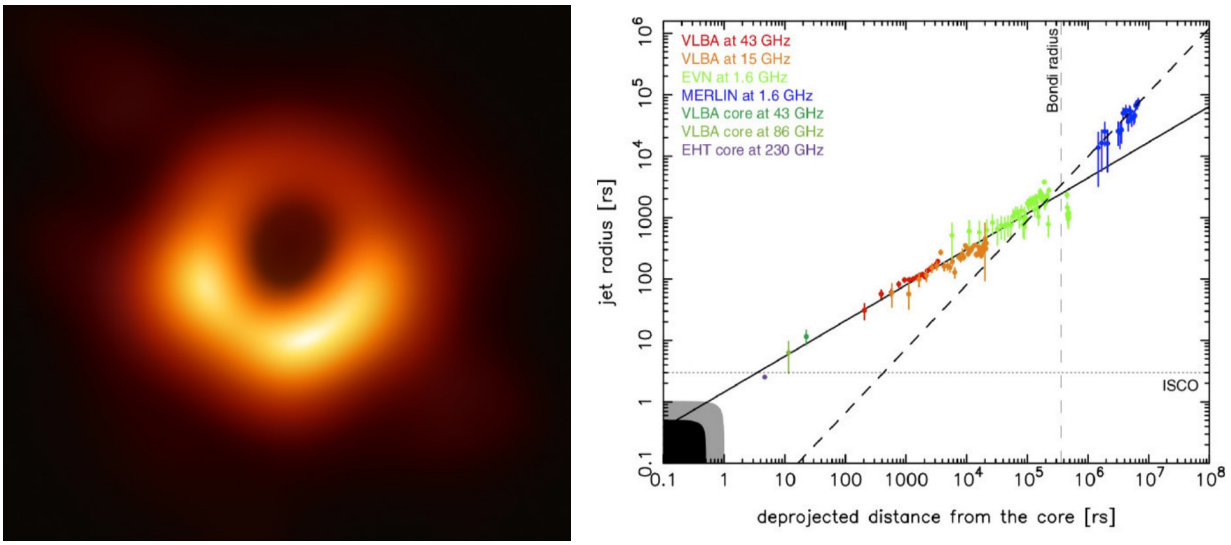

Figure 7.1: Left: Shadow of the M87⋆ black hole (Event Horizon Telescope Collaboration 2019a). Right: M87 relativistic jet width as a function of the distance to the black hole, figure taken from Blandford et al. (2019).

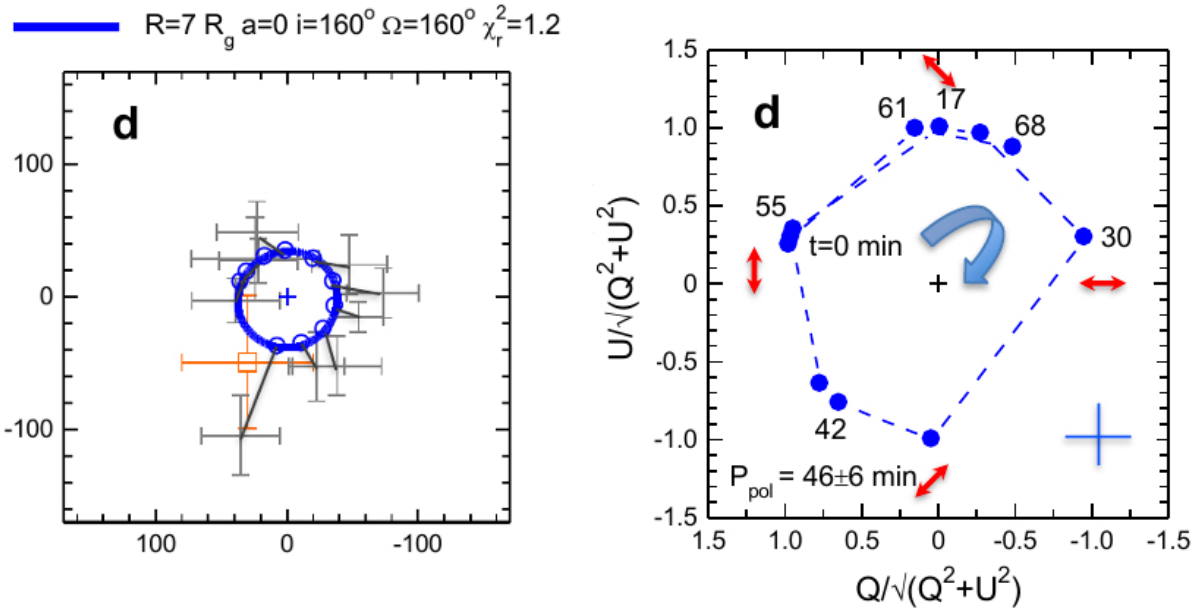

Figure 7.2: Left: Gravity observation of a "hotspot" circling around the Galactic supermassive black hole SgrA⋆, and the best-fit orbital solution of radius $r = 7$ gravitational radii (blue circle). Right: Orbital modulation of polarization. Plots taken from Gravity Collaboration (2018).

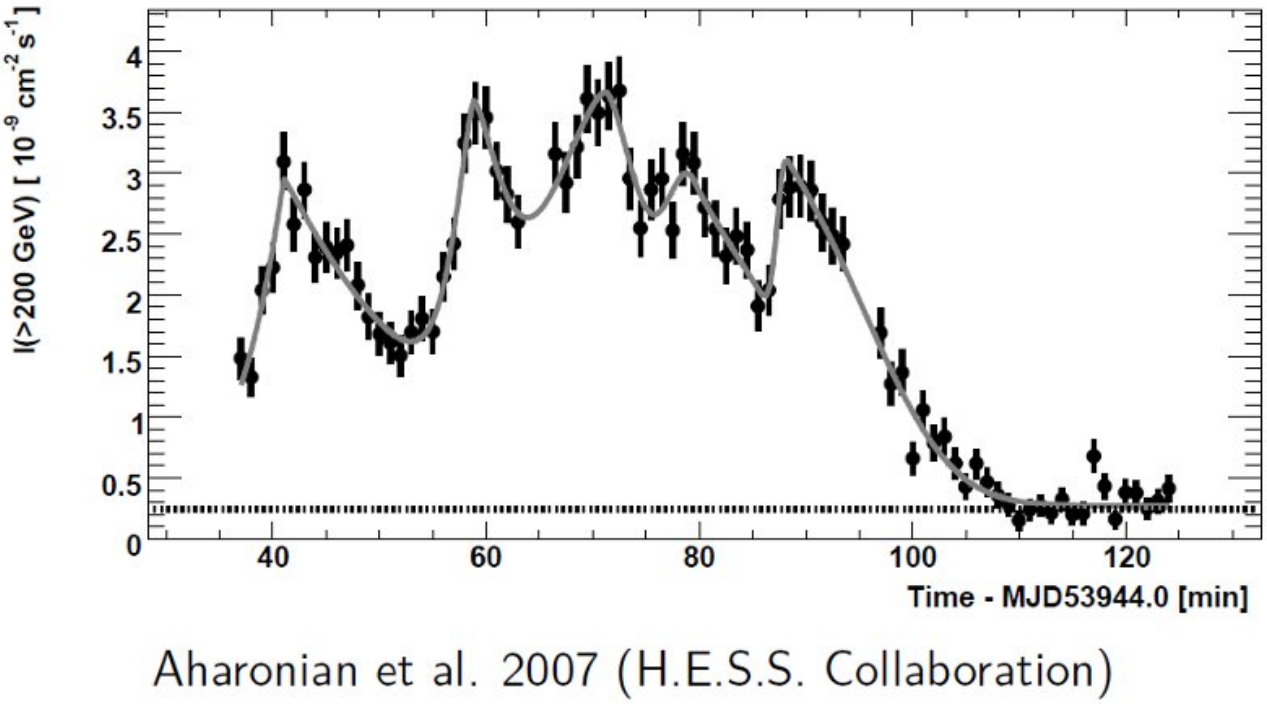

Figure 7.3: Sub-horizon scale gamma-ray variability above 200 GeV reported during an exceptional falre detected by HESS from the blazar PKS 2155 – 304 (Aharonian et al. 2007).

collaboration observing in the IR band with the VLTI has recently reported the detection of a hotspot lying at the inner-most stable orbit during IR flares, also of synchrotron origin (Gravity Collaboration 2018) (Figure 7.2, left panel). In addition, they argue that polarization measurements strongly support that the hole is immersed in a large-scale poloidal magnetic field (Figure 7.2, right panel). This discovery suggests that a global episode of magnetic reconnection is triggered near the black hole, very much like a magnetic storm within the Earth magnetosphere.

On the other extreme of the electromagnetic spectrum, ultra-rapid gamma-ray flares detected in several AGN indicate efficient particle acceleration on timescales sometimes even shorter than the horizon-light-crossing time (e.g., Aharonian et al. 2007; Albert et al. 2007; Aleksić et al. 2014, Figure 7.3). To come back to the case of M87, Gamma-ray observations combined with VLBA radio imaging show that the short gamma-ray flares are correlated with a significant radio brightening of the core (Acciari et al. 2009), bringing additional evidence that there is a tight connection between particle acceleration and jet formation in the close vicinity of black holes. This broad array of horizon-scale observations allows us, for the first time, to probe physics in curved spacetime. To this end, it is of prime importance to have an accurate model of the plasma in the closest environment of black holes, simply referred to as the "magnetosphere" in the following, to decipher these observations. This region is external to the hole and is characterized by complex general relativistic electrodynamics where electron-positron pair creation, particle acceleration and non-thermal radiation take place (Figure 7.4). In contrast to their

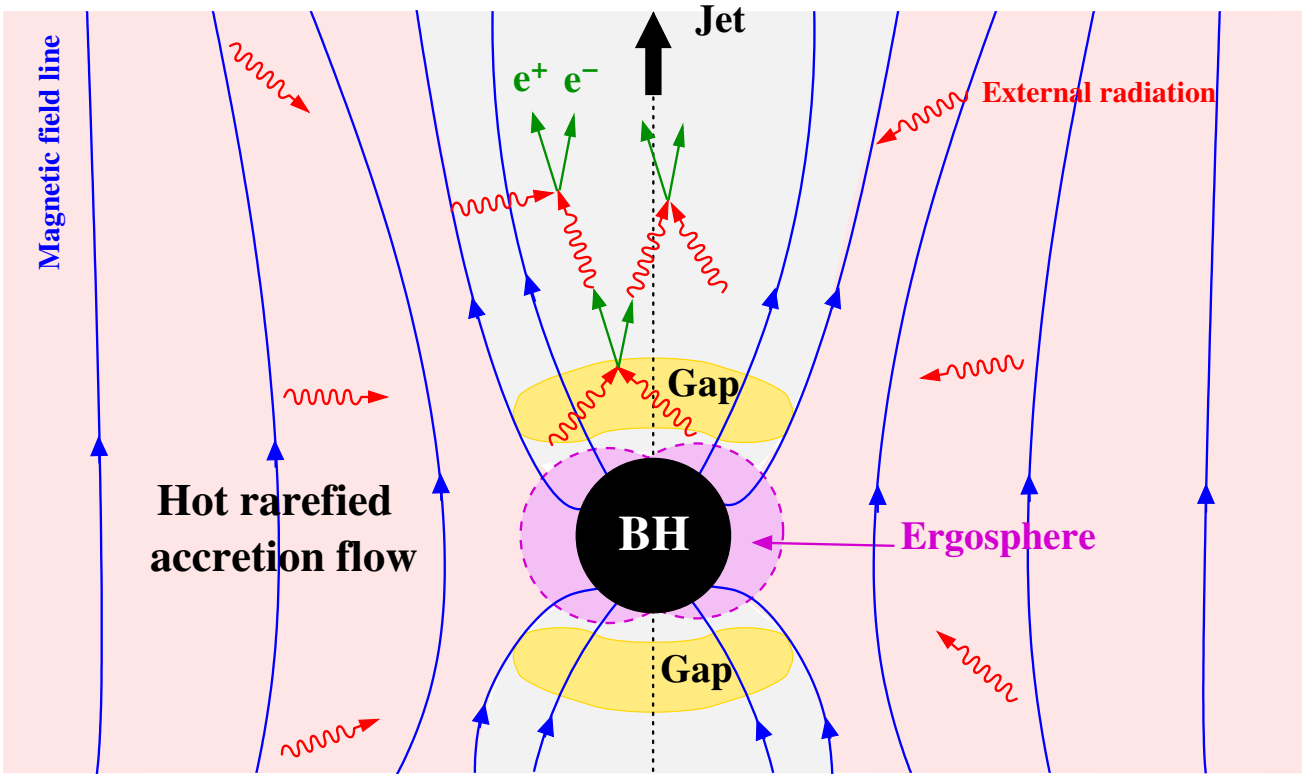

Figure 7.4: This diagram sketches the magnetosphere of a rotating black hole embedded in a hot under-dense plasma and threaded by external magnetic field lines. Field lines passing through the "ergosphere" (magenta regions) are forced into rotation and an electrostatic gap forms at the hole polar caps (yellow regions). Photon-photon annihilation injects electron-positron pairs in the gap regions and leads to the discharge of the polar cap associated with particle acceleration and the emission of high-energy radiation. This process results in the formation of an outflow at the base of the jet.

closest analog that are pulsar magnetospheres, black holes cannot hold strong magnetic field nor inject charges because they do not possess a solid material surface. Thus, a black-hole magnetosphere can exist only in the presence of an external source of plasma and magnetic field. It is commonly accepted that the source is the accretion flow whose properties depend on the environment.

Theoretically, particle acceleration and jet formation can be both understood in the context of a rapidly rotating black hole (or Kerr black hole) embedded in a low-density plasma and with a large-scale magnetic field. The rotation of the black hole drags spacetime within a few gravitational radii (the Lense-Thirring effect). This general relativistic effect forces the magnetic field lines to rotate and hence induces a strong electric field at the black-hole poles. Particles can then be electrostatically accelerated in a similar fashion as in a pulsar polar-cap gap (Chapter 4, Figure 7.4). The energy reservoir is the black hole spin that is electromagnetically extracted in the form of a Poynting-flux-dominated jet via the Blandford-Znajek mechanism (Blandford & Znajek 1977). To test this scenario, an accurate description of black hole electrodynamics is required.

7.2 State-of-the-art and the need to go beyond the magnetohydrodynamic approach

Solving for the structure of the magnetosphere is a challenging problem. It can be solved analytically only for a few cases and under ideal conditions, as for instance for a monopolar, i.e., purely radial magnetic field as in the Blandford-Znajek solution. For more realistic configurations, equations must be solved numerically. Current state-of-the-art simulations have been performed within the framework of general relativistic magnetohydrodynamics (GRMHD). These simulations can capture the overall structure of the magnetosphere, currents and fields for a given geometry (Koide et al. 2002; Komissarov 2005; McKinney 2006a), but no constraints about particle acceleration and non-thermal radiation can be inferred. This is an intrinsic limitation of the method because the dynamics of individual particles is not taken into account. Particle momenta are averaged out and therefore any information about the particle energy spectrum is lost.

At best, recent radiative GRMHD simulations with ray-tracing can be done and generate synthetic maps as it was done extensively in support of the EHT image of M87* (Event Horizon Telescope Collaboration 2019b; Porth et al. 2019), but this is applicable to the thermal radiation only. Even then, however, the electron temperature as well as the energy partition between electrons (which radiate) and ions (which carry the momentum) must be prescribed. These fundamental parameters are still poorly constrained and motivate strong theoretical and modeling efforts (Kawazura et al. 2019). It depends essentially on how collisionless magnetized plasmas dissipate their energy on the microscopic scales which cannot be captured by an MHD model. The current situation is even more critical if one realizes that the plasma loading within the innermost parts of the jet produced in GRMHD simulations is solely controlled by the minimum density floor required for numerical stability reasons, and not by physics. Instead, the jet may be loaded with relativistic electron-positron pairs created by the annihilation of photons within low-density, nearly vacuum regions (gaps) within the magnetosphere (Figure 7.4) which is by no means describable by a fluid approach.

Therefore, the MHD approach is not able to generate reliable observables which in turn does not allow one to connect the model to observations. There is an urgent need to revisit black hole magnetospheres in light of new and more adequate numerical methods to uncover where and how particle acceleration and radiation take place around black holes. GRPIC simulations come as a natural response to this call for help, which motivated me to dive into the development of `Zeltron` in curved spacetime.

Chapter 8

Numerical developments in Zeltron: 3+1 implementation

This chapter focuses on the numerical developments done in `Zeltron` to capture electrodynamics, particle motion and radiative transfer in curved space time for an arbitrary metric. The more specific case of the Kerr metric will be discussed in the next chapter when dealing with applications to black hole magnetospheres. In this chapter and for the rest of this memoir, we will use the $(-,+,+,+)$ signature for the metric, use Greek indices for the full 4D tensors components and Latin indices for the spatial components. Except in the radiative transfer section (Sect. 8.4), we will further assume that $c = G = M = 1$, where M is the mass of the black hole, and G is the gravitational constant. Last, we will consider stationnary metrics only.

8.1 The 3+1 description of general relativity

Solving equations in the context of general relativity implies that one must manipulate 4-dimensional objects. The spirit of the "3+1 formalism" is to slice the full spacetime by purely space-like 3-dimensional hypersurfaces, or referred to as the "absolute space", parametrized by a universal "absolute" time (Thorne et al. 1986; Gourgoulhon 2007). This decomposition serves essentially two purposes for us here: (i) it allows to rewrite all equations into a familiar flat-spacetime way and therefore gives an easier physical intuition, and (ii) it is well-suited for numerical methods where there is a single time parameter and time step everywhere in the simulation and a rigid numerical grid. Thus, this approach allows one to preserve the overall architecture of a code initially designed in flat spacetime like `Zeltron` . This method is commonly used by the numerical relativity community to solve Einstein and GRMHD equations.

If x^i are the spatial coordinate in the fixed 3D-space characterized by the spatial metric γ_{ij}, and t is the time coordinate, it is convenient to write the spacetime

interval in the ADM form (Arnowitt et al. 1962),

$$ds^2 = -\alpha^2 dt^2 + \gamma_{ij}\left(dx^i + \beta^i dt\right)\left(dx^j + \beta^j dt\right) \tag{8.1}$$
$$ds^2 = \left(\beta^2 - \alpha^2\right) dt^2 + 2\beta_i dx^i dt + \gamma_{ij} dx^i dx^j, \tag{8.2}$$

so that the full 4D-metric, $g_{\mu\nu}$, can be written as

$$g_{\mu\nu} = \begin{pmatrix} \beta^2 - \alpha^2 & \beta_j \\ \beta_i & \gamma_{ij} \end{pmatrix}. \tag{8.3}$$

Thus, there is a direct correspondance between the 3-metric and the spatial part of the 4-metric, $\gamma_{ij} = g_{ij}$. The inverse metric, $g^{\mu\nu}$, is obtained with the usual identity relation $g_{\mu\nu}g^{\nu\sigma} = \delta^\sigma_\mu$, such that

$$g^{\mu\nu} = \begin{pmatrix} -\frac{1}{\alpha^2} & \frac{\beta^j}{\alpha^2} \\ \frac{\beta^i}{\alpha^2} & \gamma^{ij} - \frac{\beta^i\beta^j}{\alpha^2} \end{pmatrix}, \tag{8.4}$$

and therefore $\gamma^{ij} \neq g^{ij}$. The determinant of the spatial metric is $\gamma \equiv \det(\gamma_{ij})$ (we will use a different notation for the Lorentz factor in the following).

The parameter α is known as the "lapse function". Physically, this quantity relates the coordinate time t to the proper time τ measured locally by "fiducial observers" (FIDO) at rest with respect to the absolute 3D-space

$$d\tau = \alpha dt. \tag{8.5}$$

It can also be understood as the gravitational redshift experienced by the FIDO. The 4-velocity vector of these FIDO is given by

$$n_\mu = (-\alpha, 0, 0, 0). \tag{8.6}$$

The "shift vector", β^i, represents the velocity of the spatial grid, meaning that in the general case where $\beta^i \neq 0$ the coordinate grid is moving with respect to the FIDO. This can be seen by looking at the coordinate velocity component of the FIDO,

$$n^\mu = g^{\mu\nu}n_\nu = \frac{1}{\alpha}\left(1, -\beta^i\right). \tag{8.7}$$

All of the expressions given in this section are general, we will see in the next chapter the specific case of the Kerr metric expressed in a spherical Kerr-Schild coordinate system.

8.2 Maxwell solver in curved spacetime

8.2.1 Maxwell's equation in 3+1

Within the "3+1" framework and following Komissarov (2004), Maxwell's equations can be rewritten into a familiar flat spacetime form as

$$\boldsymbol{\nabla}\cdot\mathbf{D} = 4\pi\rho, \tag{8.8}$$

$$\frac{1}{\sqrt{\gamma}}\frac{\partial}{\partial t}(\sqrt{\gamma}\mathbf{D}) = \boldsymbol{\nabla}\times\mathbf{H} - 4\pi\mathbf{J}, \tag{8.9}$$

$$\boldsymbol{\nabla}\cdot\mathbf{B} = 0, \tag{8.10}$$

$$\frac{1}{\sqrt{\gamma}}\frac{\partial}{\partial t}(\sqrt{\gamma}\mathbf{B}) = -\boldsymbol{\nabla}\times\mathbf{E}. \tag{8.11}$$

For a stationary metric $\partial\sqrt{\gamma}/\partial t = 0$, we end up with even simpler expressions

$$\boldsymbol{\nabla}\cdot\mathbf{D} = 4\pi\rho \tag{8.12}$$

$$\frac{\partial\mathbf{D}}{\partial t} = \boldsymbol{\nabla}\times\mathbf{H} - 4\pi\mathbf{J} \tag{8.13}$$

$$\boldsymbol{\nabla}\cdot\mathbf{B} = 0 \tag{8.14}$$

$$\frac{\partial\mathbf{B}}{\partial t} = -\boldsymbol{\nabla}\times\mathbf{E}. \tag{8.15}$$

One immediately sees that instead of two fields in flat spacetime, we now have four fields $\mathbf{E}$, $\mathbf{D}$, $\mathbf{B}$ and $\mathbf{H}$. $\mathbf{D}$ and $\mathbf{B}$ are the electric and magnetic fields measured by the FIDO, while the $\mathbf{E}$ and $\mathbf{H}$ are auxiliary fields related to the former fields via

$$\mathbf{E} = \alpha\mathbf{D} + \boldsymbol{\beta}\times\mathbf{B}, \tag{8.16}$$

$$\mathbf{H} = \alpha\mathbf{B} - \boldsymbol{\beta}\times\mathbf{D}. \tag{8.17}$$

$\mathbf{E}$ and $\mathbf{H}$ can be interpreted as the fields seen from the grid, where α and $\boldsymbol{\beta}$ give the transformation of the FIDO measured fields due to the motion of the grid. In the flat spacetime limit where $\alpha = 1, \beta^i = 0$, one can easily check that $\mathbf{E} = \mathbf{D}$ and $\mathbf{H} = \mathbf{B}$ as it should. Maxwell's equations written in the 3+1 form recall those written for an electromagnetic active medium as opposed to their expression in vacuum, but here this role is played by the curvature of spacetime.

The current density appearing in Eq. (8.13) is coordinate based. It is related to current measured by the FIDO, $\mathbf{j}$, as follows

$$\mathbf{J} = \alpha\mathbf{j} - \rho\boldsymbol{\beta}, \tag{8.18}$$

where the second term is due to the motion of the grid with respect to the FIDO, and ρ is the FIDO-measured charge density.

8.2.2 Numerical implementation

The form of the time-dependent Maxwell equations being formally identical to flat spacetime, the main architecture of the Maxwell solver, which involves the second-order accurate Yee algorithm, can be preserved (see Chapter 2). The field components are staggered in space and in time: **E**, **D** and **J** are defined along the cell edges at full time steps, while **B**, **H** are defined at the cell faces at half time steps. The code manipulates all 6 components for each field (3 covariant and 3 contravariant), i.e., 24 components.

The curl of a vector **A** written in components is defined as

$$(\boldsymbol{\nabla}\times\mathbf{A})^i = \frac{1}{\sqrt{\gamma}}\epsilon^{ijk}\partial_j A_k, \tag{8.19}$$

where ϵ^{ijk} is the Levi-Civita symbol. Eqs. (8.13), (8.15) therefore become

$$\partial_t D^i = \frac{1}{\sqrt{\gamma}}\epsilon^{ijk}\partial_j H_k - 4\pi J^i, \tag{8.20}$$

$$\partial_t B^i = -\frac{1}{\sqrt{\gamma}}\epsilon^{ijk}\partial_j E_k, \tag{8.21}$$

and Eqs. (8.16)-(8.17) become

$$E_i = \alpha D_i + \sqrt{\gamma}\epsilon_{ijk}\beta^j B^k, \tag{8.22}$$

$$H_i = \alpha B_i - \sqrt{\gamma}\epsilon_{ijk}\beta^j D^k. \tag{8.23}$$

This apparent simplicity hides important numerical subtleties, which are inherent to the Yee lattice and the coupling between components living in different places via the fields **E** and **H**.

To see this, and for illustrative purposes only, we shall consider only the radial component of Eq. (8.21) and assume axisymmetry for simplicity ($\partial_\phi = 0$). On the Yee lattice, this equation can be written in a finite-difference and time-centered way as

$$\frac{{B^r}_{ir,i\theta+1/2}^{n+1/2} - {B^r}_{ir,i\theta+1/2}^{n-1/2}}{\Delta t} = -\frac{1}{\sqrt{\gamma}\Delta\theta}\left(E_{\phi\,ir,i\theta+1}^{\;n} - E_{\phi\,ir,i\theta}^{\;n}\right), \tag{8.24}$$

where $(ir, i\theta)$ are the cell indices, and n is the coordinate time index. To solve this equation, we need

$$E_{\phi_{ir,i\theta}} = \alpha D_{\phi_{ir,i\theta}} + \sqrt{\gamma}\left(\beta^r {B^\theta}_{ir,i\theta} - \beta^\theta {B^r}_{ir,i\theta}\right). \tag{8.25}$$

In this equation, we are calling B^θ and B^r which are not located in $(ir, i\theta)$. To preserve second-order accuracy, we need to make sure all quantities are centered in space and in time. In this specific example, we chose for the following solution (shown for B^θ only for conciseness)

$${B^\theta}_{ir,i\theta} = \frac{\left(\sqrt{\gamma}B^\theta\right)_{ir+1/2,i\theta} + \left(\sqrt{\gamma}B^\theta\right)_{ir-1/2,i\theta}}{\sqrt{\gamma}_{ir+1/2,i\theta} + \sqrt{\gamma}_{ir-1/2,i\theta}}. \tag{8.26}$$

The $\sqrt{\gamma}$ weighting is here in order to do a fair weighting between the two contributions. Another complication is that the E_i components involve the covariant components D_i that must be computed from D^i, which is the component evolved by the code, using

$$D_i = \gamma_{ij} D^j. \tag{8.27}$$

This apparently harmless operation leads in fact to the same issue as the one raised above: it calls for other components defined in different places on the Yee lattice. Thus, here again all components must be carefully centered in space in a similar way as B^θ above, otherwise the second-order accuracy is lost.

In summary, the Yee solver can be preserved in the full general relativistic extension, but the mixing between different field components significantly complicates the original algorithm. Spatial and time centering should be done with extreme care.

8.2.3 Poisson solver

Like in the flat spacetime version of `Zeltron` , we chose a charge and current deposition technique that does not satisfy charge conservation to machine roundoff precision (volume weighting technique, see Chapter 2), and therefore a divergence cleaning must be applied. We did not change the numerical method either, Poisson equation is solved using the iterative 5-point stencil Gauss-Seidel method. In 3+1, Poisson equation is written as

$$\nabla^2 \delta\phi = -\left(4\pi\rho - \boldsymbol{\nabla}\cdot\mathbf{D}\right), \tag{8.28}$$

or in components as

$$\frac{1}{\sqrt{\gamma}}\partial_i\left(\sqrt{\gamma}\gamma^{ij}\partial_j\delta\phi\right) = -\left(4\pi\rho - \frac{1}{\sqrt{\gamma}}\partial_i\left(\sqrt{\gamma}D^i\right)\right). \tag{8.29}$$

8.3 Particle pusher

8.3.1 Equation of motion in 3+1

In the 3+1 formalism, the equations of motion in the presence of electromagnetic fields are given by (Parfrey et al. 2019)

$$\frac{dx^i}{dt} = v^i = \alpha\frac{\gamma^{ij}u_j}{\Gamma} - \beta^i, \tag{8.30}$$

$$\frac{du_i}{dt} = -\Gamma\partial_i\alpha + u_j\partial_i\beta^j - \frac{\alpha}{2\Gamma}\partial_i\left(\gamma^{jk}\right)u_j u_k + \alpha\frac{q}{m}\left(D_i + \sqrt{\gamma}\epsilon_{ijk}\frac{\gamma^{jl}u_l}{\Gamma}B^k\right), \tag{8.31}$$

where v^i are the particle coordinate 3-velocity components, u_i the particle 4-velocity components, and $\Gamma = \sqrt{1+\gamma^{ij}u_i u_j}$ is the particle Lorentz factor as measured by the FIDO. The last term in Eq. (8.31) represents the Lorentz force, the

other terms are metric-induced forces. The term $\partial_i \alpha$ can be interpreted as the classical gravitational acceleration felt by the FIDO.

8.3.2 Tetrads and Boris push

Here again, our philosophy was to preserve as much as possible the architecture of the flat spacetime version, and the advantageous features of the Boris pusher, as far as the equation of motion is concerned. However, because of the non-linear term $\propto \partial_i \left(\gamma^{jk}\right) u_j u_k$ in Eq. (8.31), the Boris push cannot be directly applied. The solver that we designed split the equation of motion into two components (Strang splitting): the first one includes all the metric-induced terms, and the second includes the Lorentz force. The first step is to perform a Lorentz boost into a locally flat spacetime of the FIDO where the metric-induced terms vanish, so that the usual Boris push can be applied. To this end, we make use of the tetrad formalism to transform all physical quantities in and out of this frame (Takahashi 2007). As for the metric-induced terms, we use an iterative implicit midpoint algorithm. This part of the code has been mostly Kyle Parfrey's and Sasha Philippov's work.

8.4 Monte-Carlo implementation of radiative transfer

To model radiative transfer in a self-consistent way, photons must be included in the code as a separate population of discrete particles, like charged particles. Interactions between photons and charged particles are modeled using a Monte-Carlo approach, i.e., based on probabilities of interaction. This probabilistic approach is perfectly-suited to PIC simulations. Our method relies on the use of cumulative distribution functions to generate all the desired distributions. To speed up the computation of radiative transfer, we searched for approximate but accurate analytical expressions that we give below. I then compare the results to known solutions.

In the following, we will consider inverse Compton scattering and γ-γ pair production, which are thought to be the main processes of interest for producing high-energy gamma-ray emission and for generating pairs in black hole magnetospheres. Calculations are derived in flat spacetime, so that all physical quantities should be understood as measured by the FIDO in the context of general relativity. The speed of light c reappears in this section as this is more familiar in the field of radiative transfer, and the particle Lorentz factor will be written again as γ also to match the usual notations in the field. The energy of gamma-ray photons is ϵ_1 and the energy of the target soft radiation is ϵ_0, both in units of $m_e c^2$.

8.4.1 Inverse Compton

In this section, we consider a single electron upscattering a soft photon arriving with a pitch angle to the particle's direction of motion θ_0, and angle ϕ_0 in the perpendicular plane. The photon is scattered with the angles θ_1 and ϕ_1. The scattering rate per photon energy per solid angle in the electron's rest frame (marked with primes) is

$$\frac{dN}{dt' d\epsilon_1' d\Omega_1'} = \int_{\epsilon'} \int_{\Omega'} \delta\left(\epsilon' - \epsilon_0'\right) \delta\left(\Omega' - \Omega_0'\right) c \frac{d\sigma}{d\epsilon_1' d\Omega_1'} d\epsilon' d\Omega', \tag{8.32}$$

where

$$\frac{d\sigma}{d\epsilon_1' d\Omega_1'} = \frac{r_e^2}{2} \left(\frac{\epsilon_1'}{\epsilon_0'}\right)^2 \left(\frac{\epsilon_1'}{\epsilon_0'} + \frac{\epsilon_0'}{\epsilon_1'} - \sin^2\Theta'\right) \delta\left(\epsilon_1' - \frac{\epsilon_0'}{1 + \epsilon_0'\left(1 - \cos\Theta'\right)}\right). \tag{8.33}$$

The total scattered photon energy distribution is given by

$$\frac{dN}{dt' d\epsilon_1'} \propto \int_{\Omega_1'} \frac{d\sigma}{d\epsilon_1' d\Omega_1'} d\Omega_1'. \tag{8.34}$$

Rearranging the delta function as

$$\delta\left(\epsilon_1' - \frac{\epsilon_0'}{1 + \epsilon_0'\left(1 - \cos\Theta'\right)}\right) = \frac{1}{\epsilon_1'^2} \delta\left(\cos\Theta' - 1 - \frac{1}{\epsilon_0'} + \frac{1}{\epsilon_1'}\right), \tag{8.35}$$

gives

$$\frac{dN}{dt' d\epsilon_1'} \propto \frac{1}{\epsilon_0'^2} \left[\frac{\epsilon_1'}{\epsilon_0'} + \frac{\epsilon_0'}{\epsilon_1'} + \left(\frac{1}{\epsilon_0'} - \frac{1}{\epsilon_1'}\right)^2 + 2\left(\frac{1}{\epsilon_0'} - \frac{1}{\epsilon_1'}\right)\right]. \tag{8.36}$$

The scattered photon energy's range is limited by the natural bounds of the cosine

$$-1 \leq \cos\Theta' \leq 1, \tag{8.37}$$

so that

$$\frac{1}{1 + 2\epsilon_0'} \leq \left(\frac{\epsilon_1'}{\epsilon_0'}\right) \leq 1. \tag{8.38}$$

If one defines $x = \epsilon_1'/\epsilon_0'$, we have

$$\frac{dN}{dt' d\epsilon_1'} \propto f(x) = x + \frac{1}{x} + \frac{1}{{\epsilon_0'}^2}\left(1 - \frac{2}{x} + \frac{1}{x^2}\right) + \frac{2}{\epsilon_0'}\left(1 - \frac{1}{x}\right). \tag{8.39}$$

Please note that constant multiplicative factors are dropped because we will normalize the final cumulative distribution to 1. A primitive of f is

$$F(x) = -\frac{1}{x{\epsilon_0'}^2} + x\left(\frac{1}{{\epsilon_0'}^2} + \frac{2}{\epsilon_0'}\right) + \frac{x^2}{2} + \left(1 - \frac{2}{\epsilon_0'} - \frac{2}{{\epsilon_0'}^2}\right)\ln x. \tag{8.40}$$

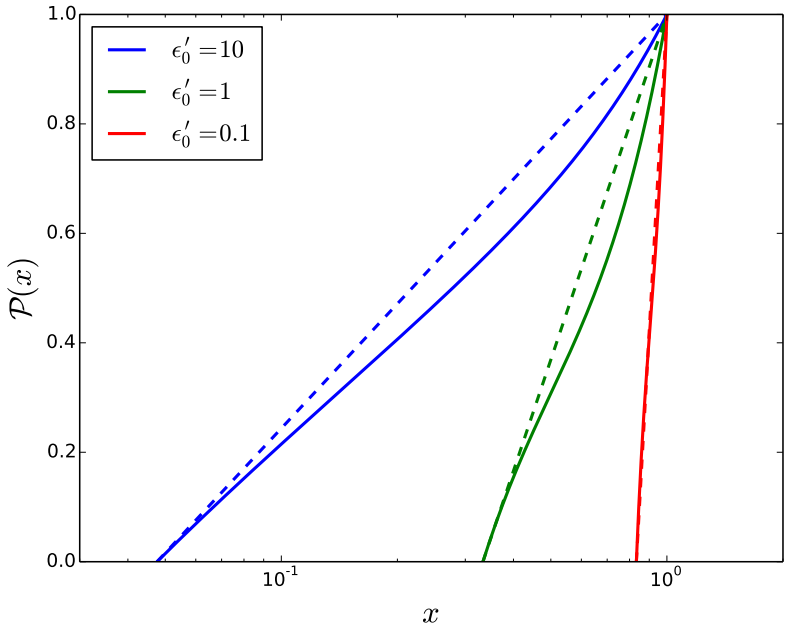

Figure 8.1: Exact (solid lines) and approximate (dashed line, Eq. 8.41) cumulative distribution functions, $\mathcal{P}(x)$, for $\epsilon'_0 = 0.1,\ 1,\ 10$.

This formula is exact and valid in all regimes (i.e., Thomson and Klein-Nishina). However, the form of this equation is not practical because it is not analytically invertible. In the limit where $x \ll 1$, $f \approx 1/x$. We will see later that this approximation is rather good even if $x \sim 1$ (in any case x is always less than 1 due to the kinematics). In this case, a primitive is simply $F(x) = \ln x$, and therefore the normalized cumulative distribution is

$$\mathcal{P}(x) = \frac{\int_{1/1+2\epsilon'_0}^{\epsilon'_1/\epsilon'_0} f(x)\,dx}{\int_{1/1+2\epsilon'_0}^{1} f(x)\,dx} = 1 + \frac{\ln x}{\ln(1+2\epsilon'_0)}. \tag{8.41}$$

This function is shown in Figure 8.1 along with the exact formula for comparison. To invert this distribution, we choose a random number uniformly distributed between 0 and 1, $\mathcal{R}$, that will probe the values of $\mathcal{P}$ (see also Chapter 3). Therefore, the scattered photon energy in the electron's rest frame is

$$\boxed{\epsilon'_1 = \epsilon'_0 \exp\left[-(1-\mathcal{R})\ln(1+2\epsilon'_0)\right]}. \tag{8.42}$$

In Figure 8.2 (left panel) shows the reconstructed scattering energy distribution obtained with a sample of 100,000 target photons for various values of ϵ'_0.

The second step is to compute the scattering angle Θ'. It is related to the photon angles via

$$\cos\Theta' = \mu'_1\mu'_0 + \sqrt{1-\mu'^2_1}\sqrt{1-\mu'^2_0}\cos(\phi_1 - \phi_0), \tag{8.43}$$

where $\mu'_{0,1} = \cos\theta'_{0,1}$. Rigorously speaking, one should first pick the angle ϕ_1 as a random number uniformly distributed between 0 and 2π and then deduce μ'_1 from

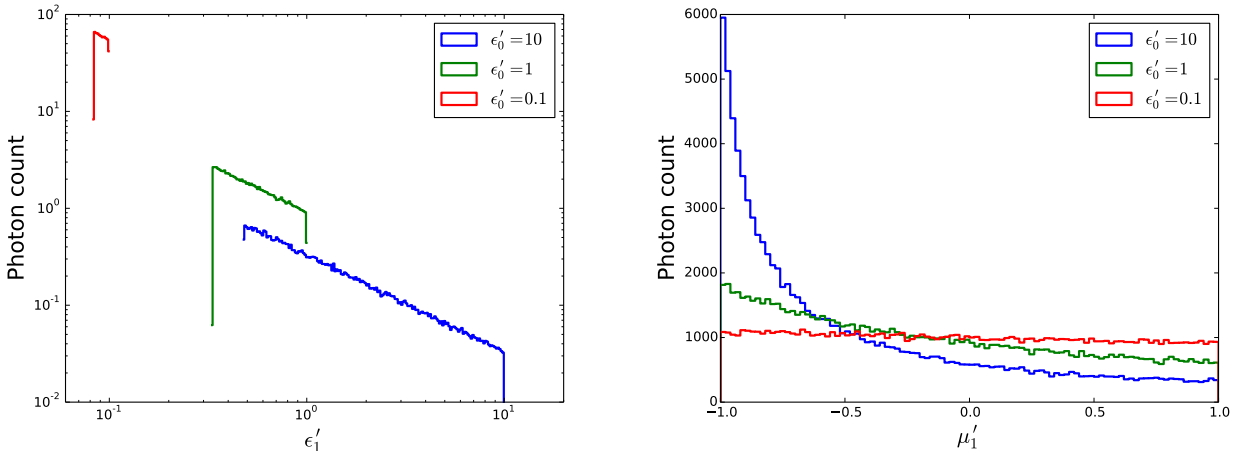

Figure 8.2: Scattered photon energy (left) and angular (right) distributions in the electron's frame reconstructed from a sample of 100,000 target photons for $\gamma = 100$ and $\epsilon'_0 = 0.1,\ 1,\ 10$.

the scattered photon angular distribution knowing its energy. In practice this is not necessary because the electrons we are considering will always be ultrarelativistic, if not, inverse Compton scattering would thus be irrelevant. Hence, if $\gamma \gg 1$, the incoming radiation is beamed within a cone of aperture angle $1/\gamma \ll 1$ in the electron's frame (this is the usual "head-on collision approximation"), and therefore a very good approximation is to set $\mu'_0 \approx -1$ so that

$$\cos\Theta' \approx -\mu'_1. \tag{8.44}$$

Since $\cos\Theta'$ is given by Eq. (8.35), we have

$$\boxed{\mu'_1 = \frac{1}{\epsilon'_1} - \frac{1}{\epsilon'_0} - 1}. \tag{8.45}$$

Note that the angle ϕ_1 is not needed anymore. Figure 8.2 (right panel) shows the recovered angular distribution obtained with a sample of 100,000 target photons for various values of ϵ'_0.

Once we know ϵ'_1 and μ'_1, we can then reconstruct the scattered photon energy in the FIDO frame using the usual relativistic Doppler shift transformation,

$$\boxed{\epsilon_1 = \gamma\,(1 + \beta\mu'_1)\,\epsilon'_1}. \tag{8.46}$$

Conservation of energy gives us the energy of the electron after the scattering

$$\boxed{\gamma \leftarrow \gamma + \epsilon_0 - \epsilon_1}. \tag{8.47}$$

In the end, only four simple analytical expressions are needed in the code, those that are encapsulated in boxes.

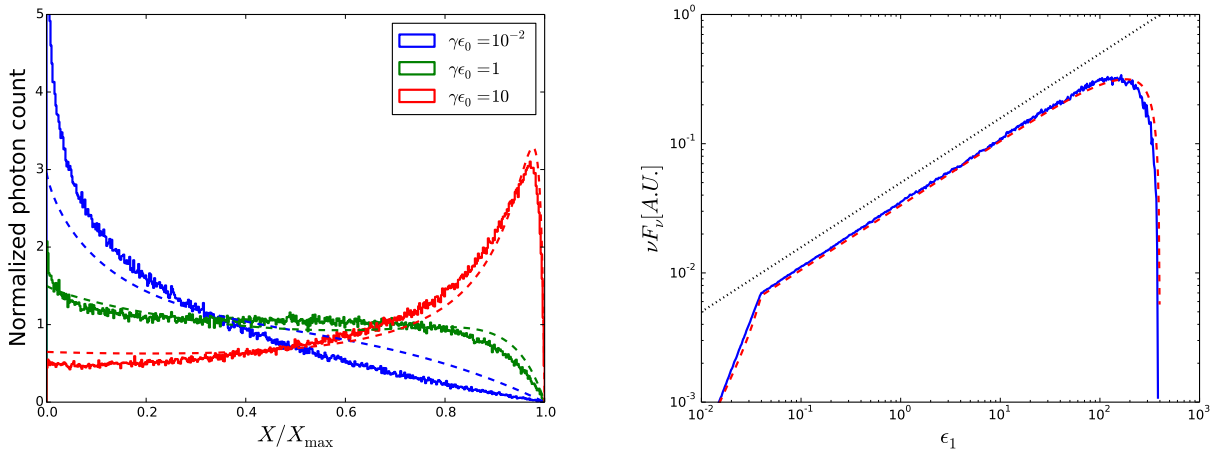

Figure 8.3: Left: Scattered photon spectra in the lab's frame reconstructed from a sample of 400,000 target photons isotropically distributed for $\gamma = 100$ and $\gamma\epsilon_0 = 0.01,\ 1,\ 10$ (solid lines). Jones kernel is overplotted for comparison (dotted lines). Right: Spectral energy distribution of the scattered photons on 100,000 electrons distributed with a power-law of index $p = 2$, with $\gamma_{\min} = 10^2$ and $\gamma_{\max} = 10^4$, and 100 target photons per electron, with an energy $\epsilon_0 = 10^{-6}$ (blue solid line). Comparison with the numerically integrated solution of the Thomson kernel (red dashed line) and the asymptotic power-law solution (red dotted line).

Test 1: Isotropic target photons

Jones (1968) derived an analytical expression for the scattered photon spectrum from a single electron in an isotropic and monoenergetic distribution of soft photons. His solution is both valid in the Thomson and in the Klein-Nishina regimes, and it is therefore ideal to compare with our solution. Jones' kernel is proportional to the following function

$$f_{\rm Jones}\left(q\right) = 2q\ln q + \left(1+2q\right)\left(1-q\right) + \frac{1}{2}\frac{\left(\Gamma_{\epsilon_0} q\right)^2}{1+\Gamma_{\epsilon_0} q}\left(1-q\right), \tag{8.48}$$

where

$$\Gamma_{\epsilon_0} = 4\epsilon_0\gamma, \tag{8.49}$$

$$q = \frac{\epsilon_1}{\Gamma_{\epsilon_0}\left(\gamma-\epsilon_1\right)}. \tag{8.50}$$

Kinematics gives the following energy range

$$\epsilon_0 \leq \epsilon_1 \leq \gamma\frac{\Gamma_{\epsilon_0}}{1+\Gamma_{\epsilon_0}}. \tag{8.51}$$

Defining $X = \epsilon_1/4\gamma^2\epsilon_0$, it gives

$$\frac{1}{4\gamma^2} \leq X \leq \frac{1}{1+4\gamma\epsilon_0}. \tag{8.52}$$

For direct comparison, we generate a sample of 400,000 soft photons isotropically distributed. To do so, we first generate a random number uniformly distributed between -1 and 1 to pick a value for μ_0 and we compute the target photon energy in the electron's frame

$$\epsilon_0' = \gamma\,(1 - \beta\mu_0)\,\epsilon_0. \tag{8.53}$$

Using Eqs. (8.42, 8.45, 8.46), we can reconstruct the resulting scattered photon spectrum in the lab frame. Results are shown in Figure 8.3 (left panel) in the Thomson and in the Klein-Nishina regimes. Overall, the agreement is good in all regimes.

Test 2: Electrons with a power-law distribution

Another simple and visual test, is to compute the scattered photon spectrum for a single target photon energy, ϵ_0, and a power-law energy distribution for the electrons,

$$\frac{dN}{d\gamma} \propto \gamma^{-p},\ \gamma_{\rm min} \leq \gamma \leq \gamma_{\rm max}. \tag{8.54}$$

In the Thomson regime and assuming that $\gamma_{\rm min} \ll \gamma \ll \gamma_{\rm max}$, the photon spectrum is a power-law

$$\frac{dN}{dtd\epsilon_1} \propto \epsilon_1^{-\left(\frac{p+1}{2}\right)}. \tag{8.55}$$

Our test compares the distribution reconstructed from a sample of 100,000 electrons for which we have drawn 100 target photons per electron, with the numerically integrated Thomson kernel spectrum and the expected analytical power-law solution (see Figure 8.3, right panel). The agreement is nearly perfect. Note that the distribution recovered from the Monte-Carlo is also valid in the Klein-Nishina regime.

8.4.2 γ-γ pair production

We follow here the same strategy as for the inverse Compton scattering. We consider a single gamma-ray photon annihilating with a soft photon arriving with a pitch angle θ_0 and azimuth angle ϕ_0 with respect to the gamma-ray photon direction of propagation. The interaction leads to the destruction of the photons and the creation of an electron-positron pair, $\gamma + \gamma \rightarrow e^+ + e^-$. We assume that the gamma-ray photon energy is much larger than the low-energy photon, $\epsilon_1 \gg \epsilon_0$.

We begin by first defining the relativistic invariant

$$s = \frac{\epsilon_0\epsilon_1}{2}\,(1 - \cos\theta_0)\,. \tag{8.56}$$

The threshold for pair production is

$$s = m_{\rm e}^2 c^4 = 1. \tag{8.57}$$

The Lorentz factor and 3-velocity of the created pair in the center-of-mass frame are

$$\gamma' = \sqrt{s}, \tag{8.58}$$

$$\beta' = \sqrt{1 - \frac{1}{s}}. \tag{8.59}$$

In the limit where $\epsilon_1 \gg \epsilon_0$, the Lorentz factor and 3-velocity of the center-of-mass frame are given by

$$\gamma_{\rm CM} \approx \frac{\epsilon_1}{2\sqrt{s}}, \tag{8.60}$$

$$\beta_{\rm CM} \approx 1 - \frac{2s}{\epsilon_1^2}. \tag{8.61}$$

The angular distribution of the electron (positron) produced in the center-of-mass frame is given by the differential cross section as (Bonometto & Rees 1971)

$$\frac{d\sigma_{\gamma\gamma}}{d\mu_1'} = \frac{\pi r_{\rm e}^2}{2}\beta'\left(1-\beta'^2\right)\left(\frac{1-\left(\beta'\mu_1'\right)^4 + 2\left(1-\beta'^2\right)\left[\beta'^2 - \left(\beta'\mu_1'\right)^2\right]}{\left(1-\left(\beta'\mu_1'\right)^2\right)^2}\right), \tag{8.62}$$

where $\mu_1' = \cos\theta_1'$, θ_1' is the angle between the velocity of the pair produced with respect to the gamma-ray direction in the center-of-mass frame. After a few rearrangements, this distribution can be rewritten in the following and more convenient form ($x = \mu_1'$)

$$\frac{d\sigma_{\gamma\gamma}}{d\mu_1'} \propto f\left(x\right) = 1 + \frac{2\beta'^2}{1-\beta'^2x^2} - \frac{2\beta'^4\left(1-x^2\right)^2}{\left(1-\beta'^2x^2\right)^2}. \tag{8.63}$$

Assuming that $\beta' \ll 1$ where the cross section is maximum, we can safely neglect the last term, i.e.,

$$f\left(x\right) \approx 1 + \frac{2\beta'^2}{1-\beta'^2x^2}. \tag{8.64}$$

After performing a partial fraction decomposition, we obtain the following primitive

$$F\left(x\right) = x + 2\beta'\tanh^{-1}\left(\beta'x\right). \tag{8.65}$$

Unfortunately, this expression is still not suitable for our purpose since it cannot be analytically inverted. A solution is to remove the contribution of x and keep only the second term. The reason it is safe to do so is that for $x \sim 0$ where it most contributes, the second term expands as $\propto \beta'^2 x$ and therefore the main features of F are conserved. We will see later on that this is indeed a very good approximation, and therefore a good primitive of f is

$$F\left(x\right) \approx 2\beta'\tanh^{-1}\left(\beta'x\right). \tag{8.66}$$

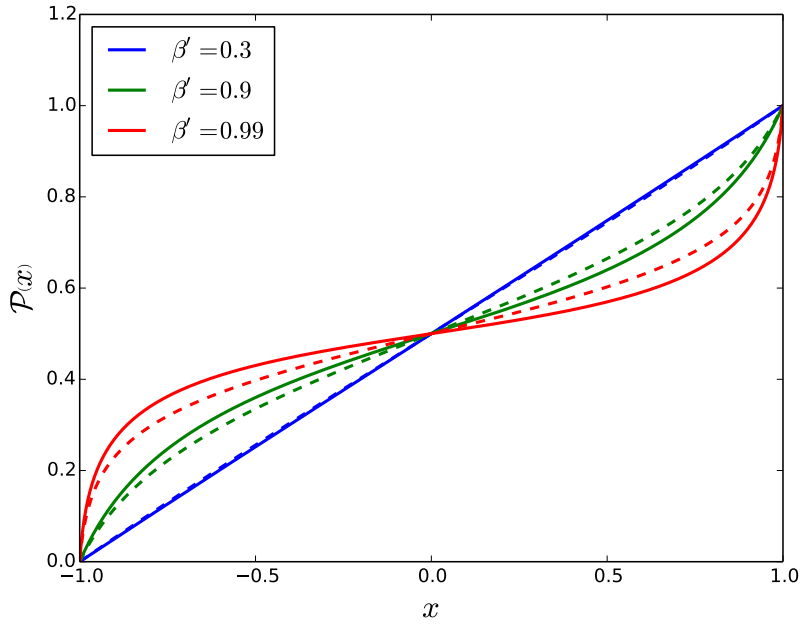

Figure 8.4: Exact (solid lines) and approximate (dashed line, Eq. 8.68) cumulative distribution functions, $\mathcal{P}(x)$, for $\beta' = 0.3,\ 0.9,\ 0.99$.

Then, the cumulative distribution function is

$$\mathcal{P}(x) = \frac{\int_{-1}^{x} f(x)dx}{\int_{-1}^{+1} f(x)dx} = \frac{F(x) - F(-1)}{F(1) - F(-1)} \tag{8.67}$$

$$\mathcal{P}(x) = \frac{1}{2}\left[\frac{\tanh^{-1}(\beta' x)}{\tanh^{-1}\beta'} + 1\right]. \tag{8.68}$$

This solution is compared with the exact, numerically integrated cumulative distribution in Figure 8.4 for several values of β'. One sees that the match is nearly perfect for small β' as expected from our expansion, but surprisingly our solution is also a good fit for $\beta' \approx 1$.

To invert the distribution, we choose a random number uniformly distributed between 0 and 1, $\mathcal{R}$, that will probe the value of $\mathcal{P}$. Therefore, the cosine of the electron (positron) angle with respect to the gamma-ray direction in the center-of-mass frame is

$$\mu_1' = \frac{1}{\beta'}\tanh\left[(2\mathcal{R} - 1)\tanh^{-1}\beta'\right], \tag{8.69}$$

or

$$\boxed{\mu_1' = \frac{1}{\beta'}\tanh\left[(2\mathcal{R} - 1)\ln\left(\gamma'(1 + \beta')\right)\right]}. \tag{8.70}$$

Figure 8.5 (left panel) presents the results of a test where the electron (positron) angular distribution is reconstructed from a sample of 100,000 electrons using Eq. (8.70). The distributions approach well the exact solutions (dashed lines, Eq. 8.63) for all values of β'.

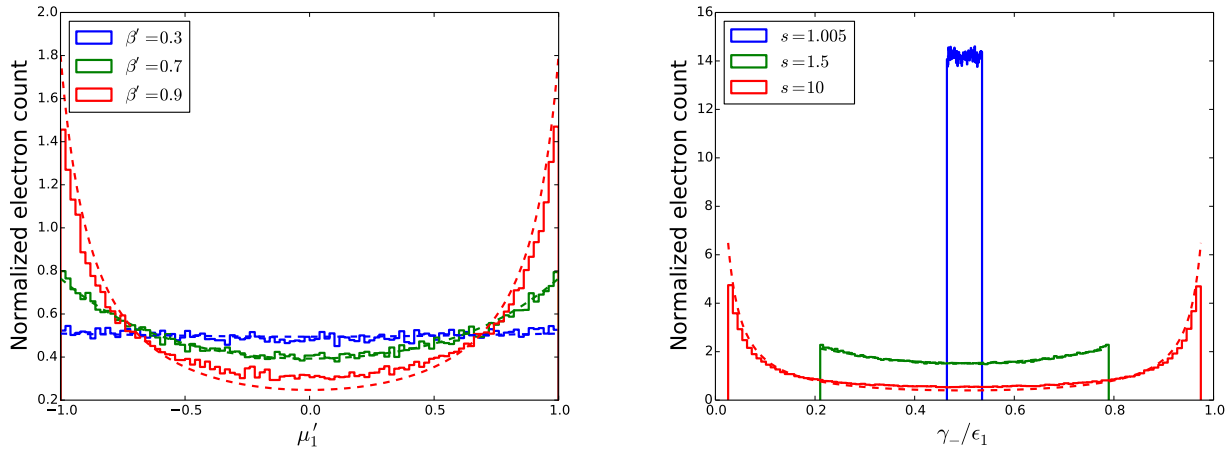

Figure 8.5: Left: Reconstructed electron (positron) angular distribution in the center-of-mass frame (solid histograms) using a sample of 100,000 electrons and Eq. (8.70), and comparison with the exact distribution (dashed lines) for $\beta' = 0.3, 0.7, 0.9$. Right: Reconstructed electron (positron) energy distribution in the lab frame (solid histograms) using a sample of 500,000 electrons and Eq. (8.71), and comparison with the exact distribution (dashed lines) for $s = 1.005, 1.5, 10$.

All quantities are now known in the center-of-mass frame. Therefore, the last step is to perform a Lorentz boost to recover the energy of the created pair in the lab (FIDO) frame, such that

$$\boxed{\gamma_- = \gamma_{\rm CM}\left(\sqrt{s} + \beta_{\rm CM}\sqrt{s-1}\mu_1'\right)}. \tag{8.71}$$

We arbitrarily chose to pick first the electron energy but given the symmetry of the energy distribution (see below), this choice does not artificially create any asymmetry between both species. Conservation of energy gives the positron energy as

$$\boxed{\gamma_+ = \epsilon_1 + \epsilon_0 - \gamma_-}. \tag{8.72}$$

Comparison with the exact solution

The final test is to compare the electron energy distribution with the exact spectrum in the lab frame (see my PhD thesis, Chapter 6, Eq. 44.239, or the appendix in Cerutti et al. 2009). Using a sample of 500,000 electrons with $\epsilon_0 = 10^{-2}$ and $\mu_0 = 0$, we reconstruct the energy distribution for several values of ϵ_1, i.e., close and far to threshold (see Figure 8.5, right panel). Here again, the agreement between the exact solution and the reconstructed distribution is very good in all regimes, and we now feel confident that our approximate formulae can be safely used in `Zeltron` . For pair production, only three analytical expressions are needed in the code (equations encapsulated in boxes).

Chapter 9

2D axisymmetric model

This last chapter focuses on the first applications of the code to black hole magnetospheres, in the framework of the Kerr metric. We begin with a brief overview of the main features of this metric in Sect. 9.1. We then turn our attention to the ideal case of a Kerr black hole immersed into a uniform magnetic field aligned with the black-hole spin axis. We proceed in two stages: (i) first, we explore the vacuum regime and compare our numerical solution to the analytical Wald (1974) solution (Sect. 9.2), and (ii) in a second stage, we explore the plasma-filled, quasi-force-free regime using an ad-hoc pair creation prescription (Sect. 9.4). We close this chapter with simulations including self-consistent pair creation in both 1D and 2D (Sect. 9.5).

9.1 The Kerr metric

Spacetime around a stationary rotating black hole is described by the Kerr metric (Kerr 1963). Using spherical Kerr-Schild coordinates, the Kerr metric is given by (Komissarov 2004)

$$g_{\mu\nu} = \begin{pmatrix} z-1 & z & 0 & -za\sin^2\theta \\ z & 1+z & 0 & -a\sin^2\theta\,(1+z) \\ 0 & 0 & \rho^2 & 0 \\ -za\sin^2\theta & -a\sin^2\theta\,(1+z) & 0 & \Sigma\sin^2\theta/\rho^2 \end{pmatrix}, \tag{9.1}$$

where

$$\rho^2 = r^2 + a^2\cos^2\theta, \tag{9.2}$$

$$z = \frac{2r}{\rho^2}, \tag{9.3}$$

$$\Sigma = \left(r^2+a^2\right)^2 - a^2\Delta\sin^2\theta, \tag{9.4}$$

$$\Delta = r^2 + a^2 - 2r. \tag{9.5}$$

The lapse function and the shift-vector in Kerr-Schild coordinates are

$$\alpha = \frac{1}{\sqrt{1+z}}, \tag{9.6}$$

$$\beta^i = \left(\frac{z}{1+z}, 0, 0\right), \tag{9.7}$$

meaning that the grid is moving towards the black hole. This motion of the grid removes the well-known coordinate singularity at the event horizon present in the more widely used Boyer-Lindquist coordinates. This is a very convenient feature for numerical purposes, hence the choice of the Kerr-Schild coordinates. This choice comes at the cost of a non-diagonal form of the spatial metric in these coordinates, as opposed to Boyer-Lindquist. The a parameter is the dimensionless spin of the black hole, ranging from $a = 0$ for a Schwarzschild hole, to (asymptotically) $a = 1$ for a maximally rotating hole.

A Kerr black hole has several critical surfaces of interest here, shown in Figure 9.1:

(i) The event horizon is a spherical surface of radius, $r_{\rm H}$, given by the condition $\Delta = 0$. The largest of the two roots gives

$$r_{\rm H} = 1 + \sqrt{1 - a^2}, \tag{9.8}$$

where $r_{\rm H}$ should be understood in units of the gravitational radius $r_{\rm g} = GM/c^2$. It varies from $r_{\rm H} = 2$ for $a = 0$, down to $r_{\rm H} = 1$ for $a = 1$. Inside this surface, an observer cannot be stationary with respect to infinity, it is necessarily dragged inward.

(ii) The ergosphere is the volume enclosed inside the critical surface defined by $g_{tt} = 0$. The largest of the two roots gives

$$r_{\rm erg} = 1 + \sqrt{1 - a^2 \cos^2\theta}. \tag{9.9}$$

This surface is not spherical (except if $a = 0$), it varies from $r_{\rm erg} = r_{\rm H}$ at the poles to $r_{\rm erg} = 2 \geq r_{\rm H}$. Inside the ergosphere, an observer cannot be stationary with respect to a distant observer, it is necessarily dragged by the rotation of spacetime. Unlike inside the event horizon, an object is still capable of moving in or out of the ergosphere.

(iii) Light surfaces are the analog of the light cylinder in pulsars. They mark the limit where rigid corotation is possible. In black-hole magnetospheres, there are two of such surfaces: the inner one and the outer one. To obtain these surfaces, one should consider a particle at a fixed radius r and fixed latitude θ, moving around the black hole at a fixed angular velocity $\Omega = d\phi/dt$. Then, the relativistic interval simplifies into (Komissarov 2004)

$$\frac{ds^2}{dt^2} = f = g_{tt} + 2g_{t\phi}\Omega + g_{\phi\phi}\Omega^2. \tag{9.10}$$

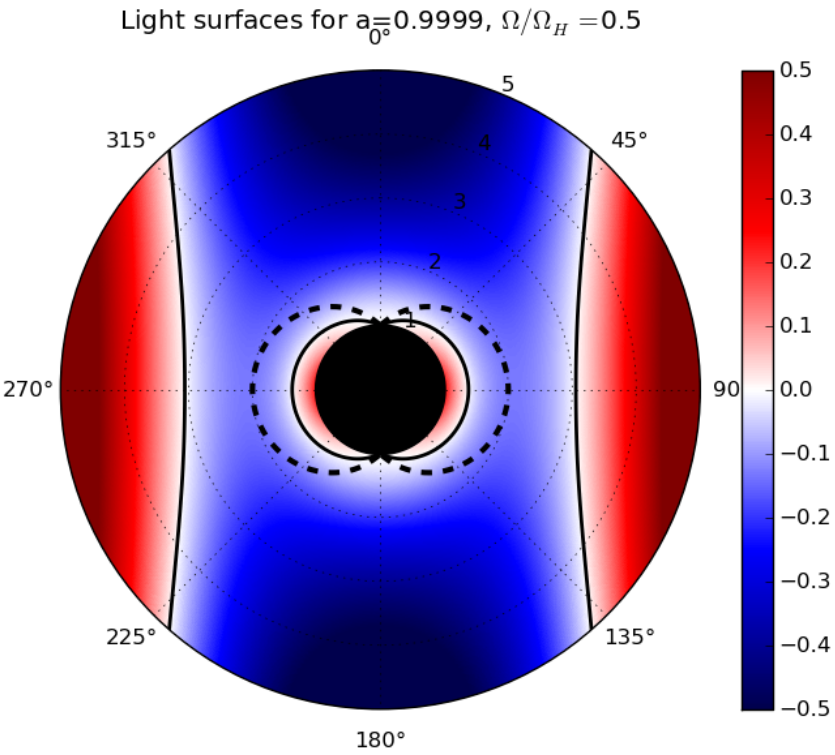

Figure 9.1: Map of the light-surface function f (Eq. 9.10) for a black-hole spin $a = 0.9999$ and an angular velocity $\Omega = \Omega_{\rm H}/2$. Light surfaces are shown as black solid lines where $f = 0$. In the blue region ($f < 0$) corotation is possible, while in the red region (f>1) corotation become superluminal. The outer-boundary of the ergosphere is shown by the black dashed line (Eq. 9.9), and the black disk is the volume enclosed inside the event horizon (Eq. 9.8).

If $f < 0$, then the rotation is time-like, i.e., subluminal and solid rotation is possible. If $f > 0$, it becomes space-like, i.e., superluminal and solid rotation is impossible. Hence, light surfaces are given by the condition $f = 0$. In the following, Ω will refer to the angular velocity of the magnetic field lines, which will be compared with the angular velocity of the hole defined as $\Omega_{\rm H} = a/2r_{\rm H}$. The inner light surface is located inside the ergosphere, but outside the event horizon. The outer light surface is always outside the ergosphere. Figure 9.1 shows the light surfaces in the case of a maximally rotating hole for $\Omega = \Omega_{\rm H}/2$. Subluminal rotation is possible only in between the two light surfaces.

9.2 Uniform field: Vacuum solution

The first test we performed with the code was to recover the solution of a Kerr black hole immersed into a uniform magnetic field aligned with the rotation axis of the hole and without plasma. Assuming that the energy density in the field is small so that it does not significantly change the Kerr metric (i.e., a test field),

Wald (1974) derived an exact solution to this problem. Using the fact that the solution must be stationary and axisymmetric, and converge to the flat space time solution at infinity, he obtained a unique solution given by

$$A^\mu = \frac{B_0}{2}\left(m^\mu + 2ak^\mu\right), \tag{9.11}$$

where B_0 is the flat spacetime magnetic field strength, and

$$m^\mu = \partial_\phi = (0,0,0,1), \tag{9.12}$$

and

$$k^\mu = \partial_t = (1,0,0,0), \tag{9.13}$$

are the Killing vectors along the ϕ- and the time coordinates respectively, which translate the stationarity and the axisymmetry of the solution. The components are given by

$$\begin{aligned} A^t &= aB_0 && (9.14)\\ A^r &= 0 && (9.15)\\ A^\theta &= 0 && (9.16)\\ A^\phi &= \frac{B_0}{2}, && (9.17) \end{aligned}$$

or in the more useful covariant form,

$$\begin{aligned} A_t &= \frac{B_0}{2}\left(g_{t\phi} + 2ag_{tt}\right) && (9.18)\\ A_r &= \frac{B_0}{2}\left(g_{r\phi} + 2ag_{rt}\right) && (9.19)\\ A_\theta &= 0 && (9.20)\\ A_\phi &= \frac{B_0}{2}\left(g_{\phi\phi} + 2ag_{t\phi}\right). && (9.21) \end{aligned}$$

From the vector potential, the **B** and **E** fields can be reconstructed using the usual formulae

$$\begin{aligned} B^i &= \frac{1}{\sqrt{\gamma}}\epsilon^{ijk}\partial_j A_k, && (9.22)\\ E_i &= -\partial_i A_t - \partial_t A_i. && (9.23) \end{aligned}$$

To test Wald prediction, we immersed the black hole into a uniform field valid for a Schwarzschild black hole and let the system evolve. After a (long) transient, the numerical solution indeed converges towards the Wald configuration. Figure 9.2 shows the result obtained by `Zeltron` at time $t = 102r_{\rm g}/c$ for a black-hole spin $a = 0.999$. The solution is characterized by the expulsion of the magnetic field lines away from the horizon. This phenomenon is often called the "Meissner effect"

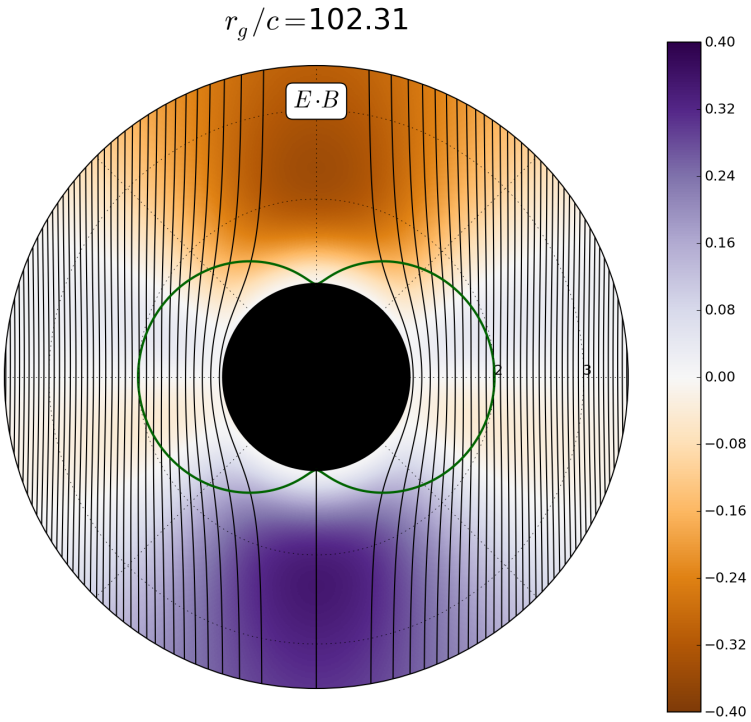

Figure 9.2: Wald configuration simulated with `Zeltron` for $a = 0.999$. Black solid contours show magnetic field lines (they are isocontours of the potential vector A_ϕ). In color is the magnitude of the electric field parallel to the magnetic field, $\mathbf{D}\cdot\mathbf{B}/B_0^2$. The green solid line shows the maximal radial extent of the ergosphere.

in analogy with the perfect diamagnetic behavior of a superconducting material. Using Eq. (9.21), we can easily show that the magnetic flux of Wald solution though one hemisphere at the horizon[1] (say the upper one) is given by (King et al. 1975)

$$\Psi_{\rm BH} = \int_0^{\pi/2}\int_0^{2\pi}\sqrt{\gamma}B^r d\theta d\phi = 2\pi A_\phi(r_{\rm H},\pi/2), \tag{9.24}$$

$$\Psi_{\rm BH} = \pi r_{\rm H}^2 B_0\left(1-\frac{a^4}{r_{\rm H}^4}\right). \tag{9.25}$$

Thus, we can see that for a maximally rotating black hole, as the one simulated here ($a\to 1$), $\Psi_{\rm BH}\to 0$.

9.3 The plasma supply problem

Wald solution has another feature that is of even greater importance for our purpose here. The rotation of the hole induces a strong unscreened electric field parallel to the magnetic field, $D_\parallel = \mathbf{D}\cdot\mathbf{B}/B_0 \lesssim B_0$ (color-coded in Figure 9.2), near the hole. The electric field is distributed according to a quadrupolar-like angular distribution with maxima at the poles, meaning that a charge injected there will

[1] Of course, the flux through the whole horizon is zero in virtue of $\boldsymbol{\nabla}\cdot\mathbf{B}=0$.

be quickly accelerated to high energies and possibly leading to pair creation and plasma screening, akin to what happens in pulsar magnetospheres (Chapter 4). Therefore, it is natural to expect that the vacuum solution is not a good model for active black holes surrounded by plasma.

Like in pulsars, the issue of plasma supply in black-hole magnetospheres is a long standing problem. However, in some respects, the problem is even more open that in the case of pulsars, because there is no primary beam of charges extracted from the surface that we can rely on to initiate a cascade. As we will see in the following, the main difficulty is to load open field lines passing through the horizon, i.e., the relativistic jet, which are disconnected from the rest of the magnetosphere. Even in the presence of an accretion disk, plasma feeding from the disk to the jet cannot be realized unless one invokes non-ideal effects to allow the particles to go across field lines. This means that the plasma must be created in-situ.

One of the most promising scenario involves γ-γ annihilation into electron-positron pairs, where the source of gamma rays originates from the innermost parts of the accretion flow. If the density of gamma rays provided by the accretion flow (or any other external source) is sufficient to screen the vacuum electric field, then a quasi force-free magnetosphere is established. In the next section (Sect. 9.4), we will assume that pair production is vigorous throughout the magnetosphere using an ad-hoc prescription for plasma injection. However, if the density of external gamma rays is too low to screen the field, then charges experience a large fraction of the vacuum potential drop and initiate a pair cascade leading again to (partial) plasma screening. In Sect. 9.5, the full radiative transfer will be considered and the transition from the vacuum to the force-free regimes will be investigated.

9.4 Uniform field: Plasma-filled solution

9.4.1 Setup and magnetospheric features

The next logical step after the vacuum Wald configuration was to simulate a plasma field configuration, assuming the same asymptotically uniform magnetic field structure. We initialize the simulation with the exact Wald fields given in Eq. (9.11), but with no charges. Then, pairs are injected everywhere in the box at every timestep, and at a rate proportional to the local value of the parallel electric field in the cell, similar in spirit to Belyaev (2015) in the context of pulsar magnetospheres. The injected pair density as measured by FIDO, $\delta n_{\rm inj}$, is then parameterized by

$$\delta n_{\rm inj} = \frac{1}{8\pi e}\frac{|\mathbf{D}\cdot\mathbf{B}|}{B}, \text{ if } |\mathbf{D}\cdot\mathbf{B}|/\mathrm{B}^2 > \epsilon_{\mathbf{D}\cdot\mathbf{B}}, \tag{9.26}$$

$$\delta n_{\rm inj} = 0, \text{ otherwise}, \tag{9.27}$$

where $\epsilon_{\mathbf{D}\cdot\mathbf{B}} < 1$ is a fixed injection threshold, whose role is to control the strength of pair production. We performed two realizations: a 'high-plasma supply' simulation with $\epsilon_{\mathbf{D}\cdot\mathbf{B}} = 10^{-3}$, and a 'low-plasma supply' simulation with $\epsilon_{\mathbf{D}\cdot\mathbf{B}} = 10^{-2}$.

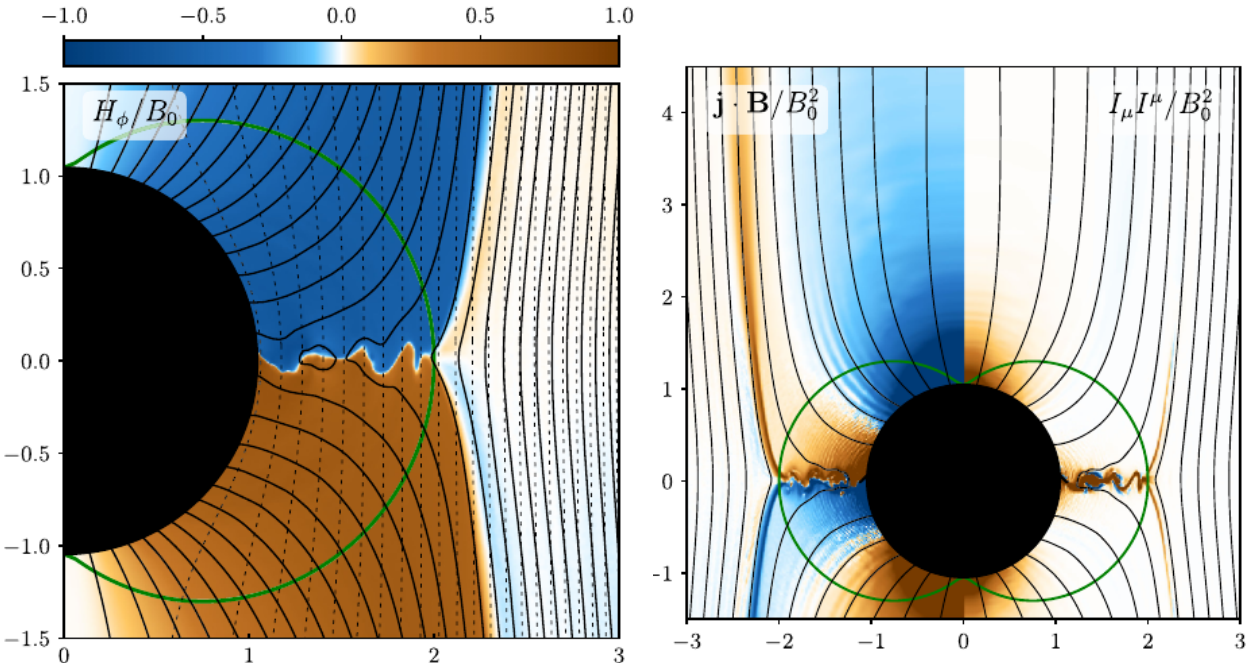

Figure 9.3: Left: Magnetic structure of a plasma filled magnetosphere for an asymptotically uniform magnetic field. Right: Electric current structure. Figure taken from Parfrey et al. (2019).

The inner boundary lies inside the horizon at $r_{\rm min} = 0.985 r_{\rm H}$ (thanks to Kerr-Schild coordinates), while the outer boundary is located at $r_{\rm max} = 8 r_{\rm g}$. The grid is equally spaced in $\log r$ and $\cos\theta$ and contains 1280×1280 cells. The plasma scales are fixed by the magnetic field strength which cannot be arbitrarily large due to numerical limitations. In dimensionless units, the fiducial magnetic field strength is

$$\tilde{B}_0 = \frac{e B_0 r_{\rm g}}{m_{\rm e} c^2} = \frac{r_{\rm g}}{r_{\rm L}}, \tag{9.28}$$

i.e., it gives the ratio between the horizon scale and the fiducial particle Larmor scale, or in other words the ratio between the fiducial macroscopic and microscopic scales. In this work, it is fixed at $\tilde{B}_0 = 10^3$ ($r_{\rm L} = 10^{-3} r_{\rm g}$), that is the maximum scale separation we can afford with $\sim 10^3$ grid cells. Then, the fiducial Goldreich-Julian plasma density is given by $n_0 = \Omega_{\rm H} B_0 / 2\pi e c$ and plasma magnetization $\sigma_0 = B_0^2 / 4\pi n_0 m_{\rm e} c^2 = 2000$, using a black-hole spin $a = 0.999$.

The first lesson we have learned from black-hole simulations is that a steady state regime is established after a much longer dynamical time than in pulsars. While a few pulsar rotation periods is usually sufficient to reach a steady state solution, at least $\gtrsim 40 r_{\rm g}/c$ is needed for black-hole magnetospheres. Figure 9.3 (left panel) shows a snapshot of the magnetic structure reached at time $t = 40 r_{\rm g}/c$. The result is very close to the force-free solution (Komissarov 2004, 2005). It is composed of a series of field lines passing through the ergosphere dragged and twisted by the rotation of space time, with a significant fraction passing through the horizon in sharp contrast to the vacuum solution. We call this region the 'jet'. These field lines are also characterized by a strong toroidal component due to field

line winding (see H_ϕ color-coded in Figure 9.3).

A current sheet forms within the ergosphere along the equatorial plane, which sustains the reversal in the magnetic field orientation. Passed the outer edge of the ergosphere, the current splits into two vertical layers along the magnetic separatrices, which separate field lines passing through the ergosphere and in rotation with the hole, and static field lines outside (Figure 9.3, right panel). These current layers are the analog of the separatrix current layers located inside the light cylinder in pulsars, located at the interface between open and closed field lines. The current then closes through the polar cap of the hole via the jet, the analog of polar-cap open field lines in pulsars. This is the establishment of these strong currents that dramatically changes the structure of the magnetosphere, from a perfectly expelled magnetic field configuration in vacuum to an approximately split-monopole configuration near the horizon (Komissarov & McKinney 2007). It is also interesting to note that the current density is space-like everywhere, meaning that both species must carry the current, and therefore that pair production is necessary to reach this state. Like in all other situations we have encountered in this memoir, the equatorial current layer is here again unstable to kink and tearing modes, which in return facilitate fast magnetic reconnection. Islands form and merge before they are eventually swallowed by the black hole.

9.4.2 Energy extraction: Blandford-Znajek versus Penrose process

The toroidal field in the jet carries electromagnetic power away from the hole in the form of a Poynting-flux-dominated outflow as predicted by Blandford & Znajek (1977). This is the first ab-initio demonstration that this mechanism is viable. The free energy is the black-hole spin which is electromagnetically extracted at infinity by the plasma jet. The Poynting flux through a spherical surface as measured from infinity is

$$L_{\rm EM}^{\infty} = \iint T_t^{\rm r} \alpha \sqrt{\gamma} d\theta d\phi = \iint S^r \sqrt{\gamma} d\theta d\phi, \tag{9.29}$$

where $T^{\mu\nu}$ is the energy-momentum tensor, and

$$S^i = \frac{1}{4\pi} \frac{1}{\sqrt{\gamma}} \epsilon^{ijk} E_j H_k, \tag{9.30}$$

is the Poynting vector measured at infinity. Thus,

$$L_{\rm EM}^{\infty} = \frac{1}{2} \int_0^{\pi} \left(E_\theta H_\phi - E_\phi H_\theta \right) d\theta. \tag{9.31}$$

In Boyer-Lindquist coordinates, Blandford & Znajek (1977) showed that

$$T_t^{\rm r} \alpha \sqrt{\gamma} = \frac{1}{4\pi} \Omega \left(\Omega_{\rm H} - \Omega \right) \left(\partial_\theta A_\phi \right)^2 \frac{r^2 + a^2}{\rho^2} \sin\theta, \tag{9.32}$$

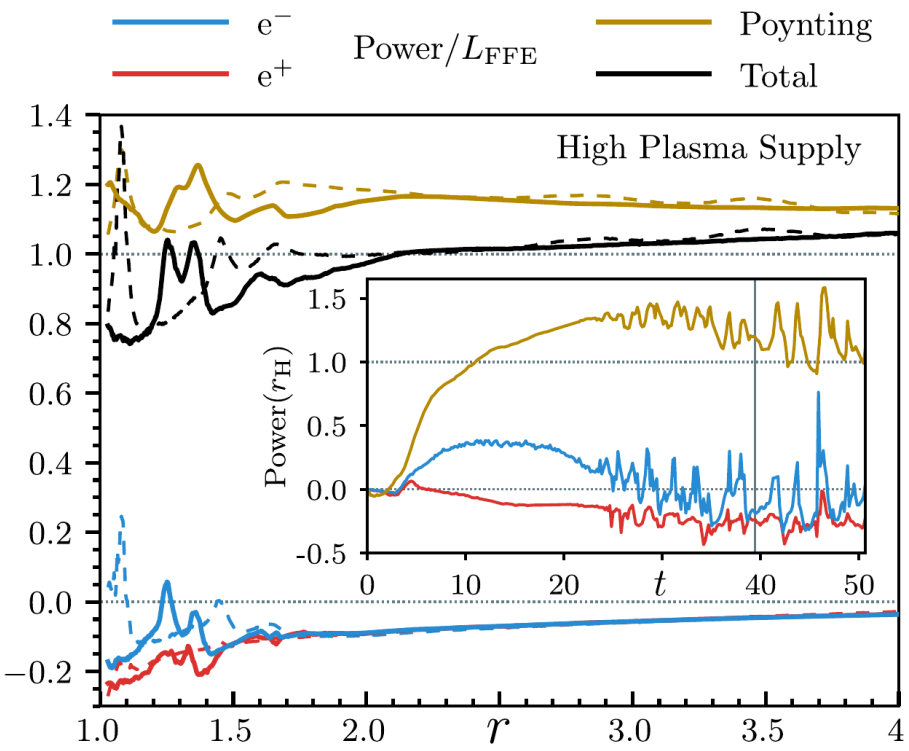

Figure 9.4: Radial profile of the electromagnetic and particle kinetic energy flux through a spherical surface of radius r. Inset: Time evolution of the extracted power measured at the black-hole event horizon. Powers are normalized to the ideal force-free value.

and that therefore energy extraction is maximum if the field-line angular velocity equals half the angular velocity of the horizon, $\Omega = \Omega_{\rm H}/2$. The measure of $\Omega = -E_\theta/\sqrt{\gamma}B^{\rm r}$ in the simulation indicates that $\Omega \approx \Omega_{\rm H}/2$ is a natural outcome of these plasma-filled solutions. Figure 9.4 shows the radial and temporal profiles of the Poynting flux. It is normalized to the power measured in a force-free MHD simulation performed by Kyle with his code `PHAEDRA` (Parfrey et al. 2012). The same amount is extracted in the PIC simulation, meaning that a quasi force-free state has indeed been successfully reached.

The electromagnetic component represents the majority of the energy flux extracted at infinity, but this is not all. To our great surprise, the plasma contained in magnetic islands are plunging towards the hole with a net negative energy at infinity, defined as

$$e_\infty = -u_t. \tag{9.33}$$

The ingestion of negative energy particles by the black hole effectively extracts energy to infinity and slows down the hole. This mechanism was imagined by Penrose (1969); Penrose & Floyd (1971). In its original form, Penrose imagined an object entering and splitting in the ergosphere into two fragments, one entering the hole with an apparent negative energy seen from infinity while the other leaves the ergosphere with a net energy gain. In this operation, the second body has taken away some of the rotational energy from the hole. In simulations, we can measure

the total energy flux carried away by the particles as

$$L_{\rm kin}^{\infty} = \iint e_{\infty} v^r n \sqrt{\gamma} d\theta d\phi. \tag{9.34}$$

Figure 9.4 shows that the Penrose process can be temporarily as important as the Blandford-Znajek process at the black hole horizon when a large magnetic island dives into the hole.

Another key new result from these kinetic simulations is evidence for particle acceleration in the ergospheric current sheet. The particle spectrum extends all the way to the maximum potential drop, $\Gamma_{\rm max} \sim a\tilde{B}_0 \approx 10^3$.

9.5 Pair producting solution

While this first global model is a key milestone in our understanding of black hole electrodynamics, it is not yet fully consistent because of the use of an ad-hoc prescription for pair creation. In this section, I present our first attempts to model the dynamics of the magnetosphere with full radiative transfer for a fixed, isotropic and homogeneous external radiation field. Only inverse Compton scattering and γ–γ annihilation will be considered in the following.

9.5.1 Setup and scales

Simulations are initialized with a single monopolar magnetic field configuration. At this stage, this configuration is preferred to the "more realistic" split-monopole configuration, in order to capture the dynamics of the polar-cap discharge without any interference from the reconnecting equatorial current sheet. In the low-spin limit[2], the field is given by

$$A_\phi = B_0 \left(1 - \cos\theta\right), \tag{9.35}$$

so that

$$B^r = \frac{B_0 \sin\theta}{\sqrt{\gamma}}. \tag{9.36}$$

The hole is initially immersed into an isotropic cloud of mono-energetic gamma rays, of dimensionless energy ϵ_1. The latter is chosen above the threshold for pair production, $\epsilon_1 \sim \epsilon_0^{-1}$ where ϵ_0 is the dimensionless background photon energy, so that they can trigger pair creation in the simulation. The density of the target radiation field is n_0, so that the fiducial optical depth of the medium is

$$\tau_0 = n_0 \sigma_{\rm T} r_{\rm g}. \tag{9.37}$$

Choosing τ_0, $\tilde{B}_0$ and ϵ_0 is the complete set of parameters of the problem under the assumption made here. In particular, they set all the relevant energy scales of the problem:

[2]The exact expression for the vacuum monopole solution is given in the Appendix in Crinquand et al. (2020).

- The maximum (vacuum) particle energy $\Gamma_{\rm max} \sim aeB_0 r_{\rm g}/m_{\rm e}c^2 = a\tilde{B}_0$.
- The energy scale of created pairs is $\Gamma_{\rm pp} \sim \epsilon_0^{-1}$, because the γ–γ cross section peaks near the threshold for pair production.
- The Klein-Nishina break energy scale $\Gamma_{\rm KN} \sim \epsilon_0^{-1} \sim \Gamma_{\rm pp}$.
- The radiation-reaction-limited energy scale, $\Gamma_{\rm rad}$, given by the balance between acceleration and inverse Compton cooling,

$$eB_0 = \mathcal{P}_{\rm ic}/c, \tag{9.38}$$

where $\mathcal{P}_{\rm ic}$ is the inverse Compton cooling power. In the Klein-Nishina regime, which is of main interest here since $\Gamma_{\rm KN} \sim \Gamma_{\rm pp}$, losses are given by (Blumenthal & Gould 1970)

$$\mathcal{P}_{\rm ic} \approx \frac{3}{8}\sigma_{\rm T} \int \frac{n}{\epsilon} \left(\ln 4\epsilon\Gamma - \frac{11}{6} \right) d\epsilon. \tag{9.39}$$

For a monoenergetic photon field, $n = n_0 \delta(\epsilon - \epsilon_0)$, we have

$$\mathcal{P}_{\rm ic} \approx \frac{3}{8}\frac{\tau_0}{\epsilon_0} \left(\ln 4\epsilon_0\Gamma - \frac{11}{6} \right). \tag{9.40}$$

Thus,

$$\Gamma_{\rm rad} = \frac{1}{4\epsilon_0} \exp\left(\frac{8B_0\epsilon_0}{3\tau_0} + \frac{11}{6} \right). \tag{9.41}$$

In the following, we will consider the following hierarchy of scales:

$$1 \ll \Gamma_{\rm pp} \ll \Gamma_{\rm max} \ll \Gamma_{\rm rad}. \tag{9.42}$$

9.5.2 1D model

In collaboration with Amir Levinson, we tackled this problem in 1D in the co-rotating frame and along a single field line inclined at an angle $\theta_0 = 30^{\rm o}$ from the black-hole spin axis. As a matter of fact, I began this work before the global model presented in the previous section. Equations in 1D are much simpler to solve, in particular the equation of motion because we assumed a truly 1D motion of the particles, i.e., inwards or outwards along the field line. Another advantage of this approach is that we can afford a much larger, more realistic separation of scales. In this work, we chose $a = 0.9$, $\Gamma_{\rm pp} \sim \epsilon_0 = 10^8$, $\Gamma_{\rm max} \sim \tilde{B}_0 \approx 10^{14}$. These parameters are close to those inferred in the core of the M87 AGN.

The domain is composed of $65,536$ cells and is ranging from $r_{\rm min} = r_{\rm H}$ to $r_{\rm max} = 4r_{\rm g}$. We studied the effect of the optical depth on the development of the cascade, $\tau_0 = 1,\ 5,\ 10$. We observed that for $\tau_0 < 5$, the cascade cannot be

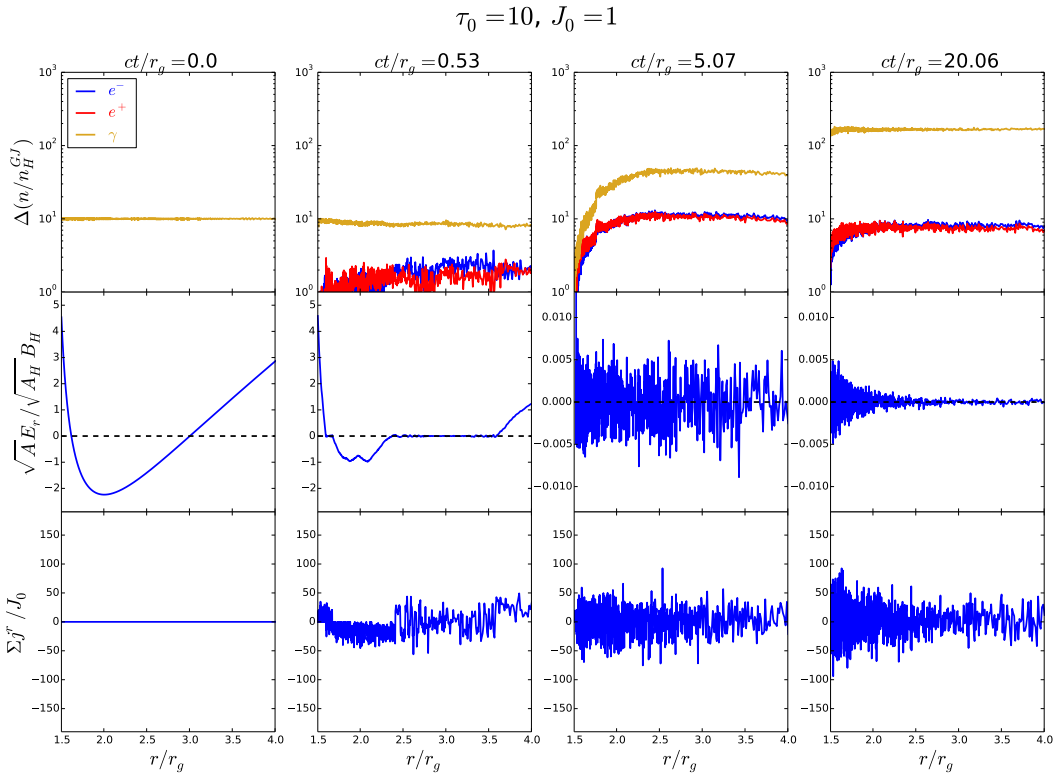

Figure 9.5: Time evolution (from left to right) of the plasma and photon densities (top), electric field (middle) and current densities (bottom) in the 1D black-hole gap for $\tau_0 = 10$.

self-sustained after the initial transient burst of pairs and the magnetosphere is cleared out of plasma after $t \sim 10 r_g/c$. At higher optical depth, pair creation is sufficiently efficient to screen the large initial gap and the solution seems stable over the duration of the simulation. The flow is composed of a multi-Goldreich-Julian pair plasma ($\kappa \sim 5$ for $\tau_0 = 10$). Figure 9.5 shows the overall time evolution of the solution, from the initial vacuum state to the force-free regime.

From this run, we infer the gamma-ray power emerging from the black-hole gap to be of order $10^{-4} - 10^{-5}$ of the Blandford-Znajek power. This power is of the same order, although a bit smaller than the observed quiescent TeV gamma-ray flux (Aharonian et al. 2006; Albert et al. 2008), assuming that the jet power is provided by the Blandford-Znajek mechanism. A puzzle remained though after these first numerical experiments: the final state of the simulation appears to be very stable, with no sign of intrinsic variability contrary to what one would expect from a spark gap. We realized later that this is partially due to the too short integration time of the simulation (Kisaka et al. 2020). As we discuss next, the other fundamental element is the multi-dimensional aspect and the presence of the light surfaces, which are absent in this 1D model.

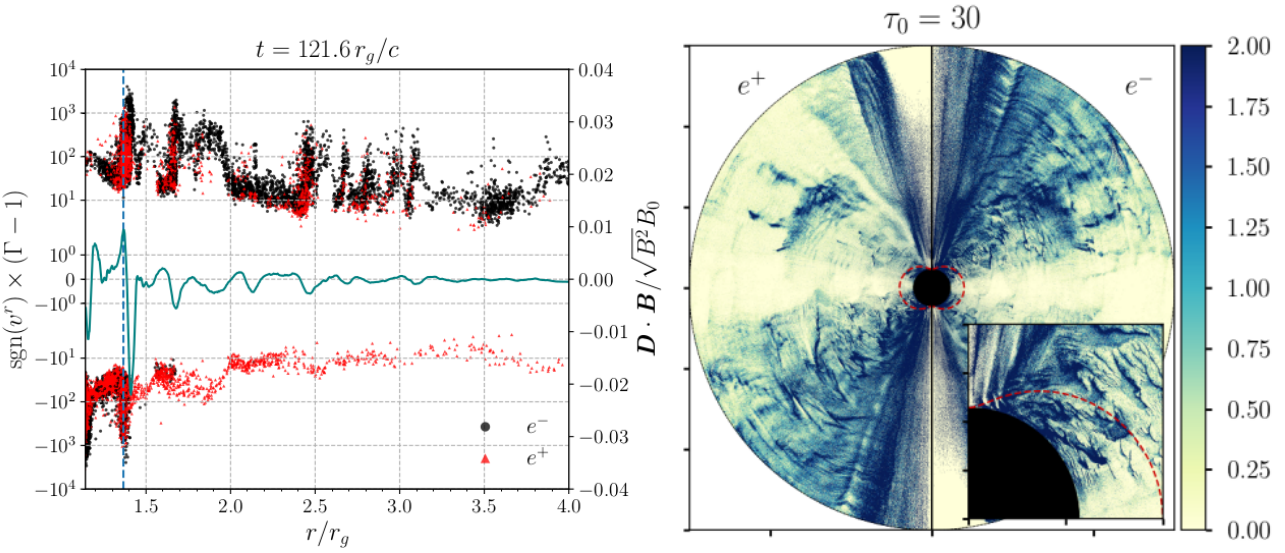

Figure 9.6: Left: Unscreened electric field (blue solid line) and phase-space diagram for pairs (black and red dots) along the $\theta = 45^{\circ}$ direction. Right: Plasma density map in the high optical depth regime, $\tau_0 = 30$. Figures taken from Crinquand et al. (2020).

9.5.3 2D model

The extension of the pair producing solutions to full 2D axisymmetric simulations was performed by my student Benjamin Crinquand during the first year of his PhD thesis. The 2D grid is uniform in θ and in $\log r$. It ranges from $r_{\rm min} = 0.9 r_{\rm H}$ to $r_{\rm max} = 15 r_{\rm g}$ and $\theta \in [0, \pi]$, and contains 2000×1152 cells. The black-hole spin is again very high, $a = 0.99$. This choice is not motivated by observations since there is no robust or well-constrained measures yet. Instead, our purpose here is to have the largest spatial extent of the ergosphere to maximize all related physical effects. The magnetic field strength is set to $\tilde{B}_0 = 5 \times 10^5$ and $\epsilon_0 = 5 \times 10^{-3}$, so that $\Gamma_{\rm max}/\Gamma_{\rm pp} = a \tilde{B}_0 \epsilon_0 \approx 2500 \gg 1$.

After the initial transient burst of pair creation, a steady state is established within 50-100$r_{\rm g}/c$ which consists of a flow of pairs carrying the negative (positive) poloidal current in the upper (lower) hemisphere where $\boldsymbol{\Omega} \cdot \mathbf{B} > 0$ ($\boldsymbol{\Omega} \cdot \mathbf{B} < 0$). At low optical depth ($\tau_0 \lesssim 10$), a large steady gap forms near the horizon. Particle are accelerated close to the vacuum potential drop, pushing the particles deep into the Klein-Nishina regime ($\Gamma_{\rm max} \gg \Gamma_{\rm KN}$). This leads to a drop in the inverse Compton cross section and therefore pair production occurs outside the gap. The dynamic of the gap and pair production are thus decoupled. The size of the gap shrinks with increasing optical depth, from macroscopic scales to sub-horizon, although not microscopic, scales governed by the inverse Compton mean free path, $\sim r_{\rm g}/\tau_0 \approx 0.06 r_{\rm g}$ for $\tau_0 = 30$. In the high optical depth regime, pair production and the evolution of the gap are tightly connected leading to quasi-periodic screening/re-opening of the gap and the generation of discrete bursts of pairs. This intermittency is well visible in Figure 9.6 (left panel), which shows the

radial evolution of the parallel electric field and the phase-space diagram of pairs.

In the poloidal plane, thin shells of pairs form near the horizon (Figure 9.6, right panel). These shells propage inwards or outwards depending on where pair production occurs, meaning that a critical surface where the flow velocity vanishes must exist in the magnetosphere. This surface is often called the "stagnation surface". While the existence of this surface is predicted by most models, its precise location is still a matter of debate in the community (e.g., Broderick & Tchekhovskoy 2015; Chen & Yuan 2020). A detailed analysis shows that such a surface indeed exists and that this role is unambiguously played by the inner light surface. This is where the gap forms, other critical surfaces such as the null- or the magnetohydrodynamic stagnation surfaces are irrelevant for the discharge. We believe that this important result should be robust against any magnetic configuration since the field structure always approches a split monopole near the horizon in the force-free regime (Komissarov & McKinney 2007).

Another robust feature of the work is the self-consistent modeling of the activation of the Blandford-Znajek process. The Blandford-Znajek prediction is (Blandford & Znajek 1977),

$$L_{\rm BZ} = \iint T_t^{\rm r} \alpha \sqrt{\gamma} d\theta d\phi. \tag{9.43}$$

For a monopole, $\partial_\theta A_\phi = B_0 \sin\theta$, Eq. (9.32) becomes

$$L_{\rm BZ} = \frac{1}{2} B_0^2 \int_0^\pi \Omega \left(\Omega_{\rm H} - \Omega\right) \frac{r^2 + a^2}{\rho^2} \sin^3\theta d\theta. \tag{9.44}$$

Estimated at the horizon, and assuming $\Omega = \Omega_{\rm H}/2$, and using a second-order low-spin expansion gives

$$L_{\rm BZ} = \frac{B_0^2 \Omega_{\rm H}^2}{6}. \tag{9.45}$$

Numerically, we indeed found that $L_{\rm EM}^{\infty} \approx L_{\rm BZ}$ at the horizon. This result is valid for all optical depth explored in this work at the horizon. A sizeable amount is dissipated to accelerate particles which is eventually radiated away in the form of optically thin gamma-ray emission. For $\tau_0 = 30$, the radiative efficiency represents about 3% of the total Blandford-Znajek power, making the spark-gap scenario promising for explaining fast gamma-ray flares in AGN. More work is needed to fully caracterize the expected radiative signatures, this is one of the important direction of research we will develop next in the context of the ERC project, which is described in more details in the following.

Part IV

Perspectives

The results on the kinetic modeling of black-hole magnetospheres is opening up a wide array of exciting future investigations. Thanks to the ERC-funded project SPAWN, we will be able to fully deploy our new and unique numerical capabilities in the context of black-hole astrophysics in the next 5 years and beyond. The time is now ripe to explore in more details plasma generation, particle acceleration and non-thermal radiation near black holes. The objectives of this project are summarized by the following key scientific questions:

- What is the basic structure of a black hole magnetosphere?
- How and where are particles accelerated in the magnetosphere?
- How and where is the plasma generated around black holes?
- What are the expected observational signatures of particle acceleration near black holes?

We will address these fundamental questions in light of the most recent and future observations of SgrA* and M87* by Gravity and the EHT, ultra-rapid GeV-TeV gamma-ray flares in the *Fermi* and CTA era, as well as active black holes in binary systems and their implications in electromagnetic counterparts of gravitational waves events in the era of advanced LIGO-VIRGO, and more generally of multi-messenger astronomy. The SPAWN project will explore 4 main axes of research, which are described below and graphically summarized in Figure 9.7. The description of each axis is taken and adapted from the narrative part (B2) of the ERC proposal.

9.6 Pair production and jet loading. Application to EHT observations & ultra-rapid AGN gamma-ray flares

The most immediate objective is to connect our simulations with observations. To this end, one important aspect to develop further is the initial magnetic configuration. While it was important to begin with a monopolar configuration as reported in Crinquand et al. (2020), it is time to consider more realistic configurations and in particular to evaluate the role of reconnection in the ergospheric current sheet in the pair production process. As we have shown in this previous study, pair creation is intermittent and it is natural to expect that bursts of pairs are accompanied by high-energy gamma rays, which may well be at the origin of gamma-ray flares routinely observed in the gamma-ray domain. Other radiative processes (i.e., other than inverse Compton and gamma-gamma pair production) such as synchrotron and curvature photons will also be integrated into the code to probe the low-energy part of the emission spectrum.

Therefore, the main objective of this project will be to compute the radiative signatures from the discharge and reconnection in the magnetosphere. More

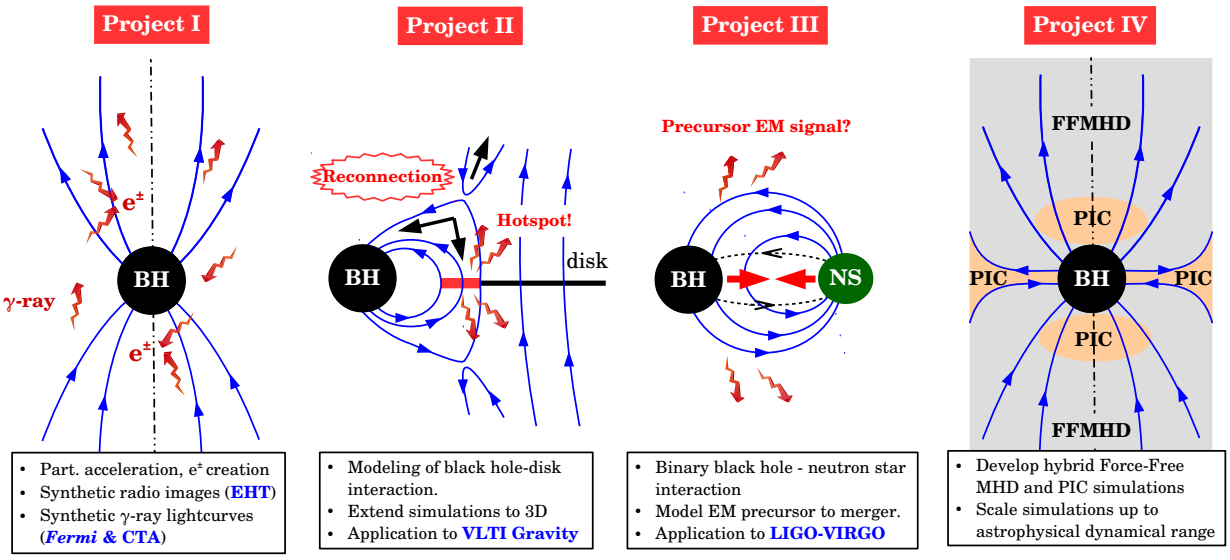

Figure 9.7: Graphical summary of all projects and their objectives.

specifically, gamma-ray lightcurves will be reconstructed as seen by an observer at infinity. The `Zeltron` code also has the capability to compute polarization signatures of the emission for any observer's viewing angle (see Sect. 6.4), this feature must be adapted in full general relativity. These synthetic observables will be compared with the properties of flaring AGN observed in the GeV domain with the *Fermi*-LAT and in the TeV domain today with HESS, MAGIC and VERITAS, and tomorrow with CTA. Flares are often associated with changes in the polarization properties of the radio emission, which can also be directly compared with our simulations.

The last key objective will be to reconstruct synthetic synchrotron images as seen by an observer at infinity, and to compare them with EHT images of the black hole shadow and jet of M87⋆. This work is Benjamin's main project for the last year of his PhD. With these diagnostics at hand, we will be able to test the magnetospheric contribution to the image, which is currently out of reach of the standard GRMHD models.

9.7 Black-hole-disk interaction. Application to Gravity observations of SgrA⋆

Active black holes are surrounded by a hot accretion flow. The accretion disk plays two important roles for keeping the black hole active: (i) it is a reservoir of a large supply of plasma, and (ii) it can maintain and even generate a large-scale magnetic field that is brought in towards the black hole by accretion. The black hole can then be magnetically connected to the disk, in an analog way to the more familiar configuration of a young star-disk interaction. The field lines

connecting the horizon to the inner parts of the accretion disk are expected to be highly twisted by the differential rotation between the Keplerian disk velocity profile and the rotation of the hole.

Previous studies have shown that the region of the disk that remains magnetically connected to the hole is confined within the inner-most regions, i.e., close to the inner stable circular orbit (ISCO) (Uzdensky 2005). The magnetic linkage between the disk and the hole can be momentarily disrupted by reconnection episodes within the boundary layer (separatrix) between the closed field lines connected to the hole and the open field lines of the disk. Such events could result in efficient bursts of energetic particles flowing along newly reconnected field lines. This mechanism could be compared with the canonical model of solar flares in which a magnetic arch of plasma reconnects leading on one side to the ejection of hot plasma in the interplanetary medium, and to the bombardment of the solar surface by energetic particles and leading to hotspots at the base of the magnetic footprints. In the black hole case, part of the flow of particles is swallowed by the hole while the other part bombards the innermost regions of the accretion flow, resulting in a localized hot spot at the ISCO (as depicted in Fig. 9.7, panel Project II).

The recent ground-breaking discovery of a hot spot orbiting at the ISCO of SgrA* by Gravity (Gravity Collaboration 2018) brings a very compelling case for exploring this scenario more closely. Polarization measurements also supports the idea of a large-scale poloidal field being present in the system. The goal of this project will be to model the time evolution of the black-hole-disk magnetic linkage and capture the cycle of magnetic reconnection events, first using 2D axisymmetric GRPIC simulations. The numerical setup will be similar to the one introduced by Uzdensky (2005); Yuan et al. (2019), i.e., the dynamics of the disk will not be self-consistently modeled but instead it will be set as a fixed perfectly conducting, infinitely thin disk rotating at the Keplerian velocity and truncated at the ISCO. The flux of energetic particles bombarding the disk will be used as a proxy to model the expected thermal emission. Lightcurves as well as polarization of the emission will be reconstructed from the simulations and directly compared with Gravity observations. Our objective will also be to predict the duty cycle of the observed flares by integrating the simulations on long time scales.

The last stage of this project will be to extend the setup to full 3D, i.e., by adding the azimuthal direction. Indeed, it is very unlikely that the problem will remain perfectly axisymmetric. We expect that plasma instabilities such as the king modes will break the axisymmetry, and therefore result in a single or multiple hotspots on the disk rather than a perfect ring.

9.8 Binary black hole-neutron star interaction. Application to LIGO-VIRGO

As argued above, the presence of an external magnetic field treading the black-hole horizon, and therefore the presence of a plasma holding the field in place is needed to extract the black-hole rotational energy and to accelerate particles. Shortly after the discovery of the first gravitational wave signals associated with binary black-hole mergers (Abbott et al. 2016), one of the crucial astrophysical question was whether such a system could result in an electromagnetic counterpart, both before and after the merger. Up to now, the answer is negative which suggests that the system has cleared the plasma out of its closest environment over its evolution.

The situation is very much different in the case of a black-hole-neutron star binary system, yet to be discovered by LIGO-VIRGO (although the event S190814bv detected in August 2019 is a good candidate). In this case, the neutron star provides the strong external field to seed particle acceleration and pair creation around the black hole, in a similar fashion as described in Sect. 9.5. The neutron star does not even need to be electrodynamically active in the sense of plasma generation and pair creation within its own magnetosphere as long as the black hole companion is rotating. It is therefore possible to expect a strong non-thermal electromagnetic signal during the inspiral phase from such a system. The flux should become brighter as both stars get closer together since the field strength on the black hole horizon will increase as one over the distance cubed, if one assumes a dipolar field for the neutron star.

Our objective will be to predict what the expected electromagnetic signal should be in the inspiral phase, by modeling a black hole magnetosphere embedded in an external dipolar field. The presence of the neutron star will first be felt as an outer boundary conditions for the fields evolving in time (approaching the hole). The second step will be to include the neutron star self-consistent within the box. Both stars will be approaching each other at a velocity consistent with the energy losses due to the emission of gravitational waves (not modeled here, but prescribed). Various parameters for the neutron star will be explored, high/low surface field, rotating/non-rotating, and for several black hole masses. Predicting the expected signatures throughout the electromagnetic spectrum prior the merger and the forthcoming gamma-ray burst will be key to localize such events in the sky in synergy with LIGO-VIRGO detections, and also to identify some of the multiple transients that will be seen on a daily basis with future grounded-based sky surveys such as the LSST in optical, SKA in radio, and CTA in the gamma-ray band.

9.9 The need to scale simulations up: Hybrid PIC-force-free simulations

A major limitation of the PIC approach is the unrealistically small separation of scales that can be simulated because the code must resolve both the microscopic scales (particle Larmor radius) and the macroscopic, system-size scales (horizon scale), i.e., the $\tilde{B}_0$ parameter introduced in Eq. (9.28). It is then a fair question to ask whether our numerical experiments are astrophysically relevant. The goal of this last project will be to explore new numerical methods to scale our simulations up to a realistic dynamical range. After all, when one looks at our first PIC simulation of the black hole magnetosphere (Fig. 9.3), the solution is extremely close to the force-free MHD (FFMHD) solution almost everywhere except in small non-ideal regions, namely the equatorial current sheet and close to the polar caps of the hole, where dissipation, particle acceleration and pair production occur. Hence, a large amount of computing power is "wasted" in simulating FFMHD regions with the full PIC machinery.

What I propose instead is to combine the PIC approach with the FFMHD formalism, which does not need particles, in the same code. FFMHD is also much cheaper than regular MHD simulations because the equation of motion to solve is simply given by the force-free condition,

$$F_{\mu\nu}J^{\nu} = 0. \tag{9.46}$$

The goal will be to implement a switch in the code that will choose whether particles are needed or not in a given region, and therefore confine the full PIC power where it is really needed. In more practical terms, the simulation will first begin in the ideal force-free regime everywhere. What is usually done in FFMHD codes is that any component of the electric field parallel to the B field is removed at every time step to ensure that the force-free condition, $\mathbf{D}\cdot\mathbf{B} = 0$, does not break down and the code with it. The electric field is also renormalized if $D^2 > B^2$ (Spitkovsky 2006; Parfrey et al. 2012). Instead, our goal will be to define a threshold of minimum $\mathbf{D}\cdot\mathbf{B}$ allowed before switching to the kinetic description. As the simulation goes, the code will find the non-ideal locations in a dynamical way, where the PIC approach is most needed.

The objective will be to revisit the simulations performed in at least Projects I and II with this new approach using much larger numerical box to validate whether these results can be extrapolated to larger, more relevant astrophysical scales. This project will also allow us to perform more realistic predictions for the particle and photon energy spectra. Astrophysical applications of this code can also be extended, but not limited to pulsar magnetospheres.

9.10 Project impact

This ambitious project relies almost entirely on the newest version of the `Zeltron` code, which includes all general relativistic corrections. This is currently the only PIC code in the world that has this capability and therefore we are determined to maintain and fructify our leadership to explore the urgent question of particle acceleration near black holes. The SPAWN project will also pave the road towards an ab-initio modeling of relativistic binary systems and their potential electromagnetic counterparts to gravitational waves events. This project will bring a strong theoretical support to current and future major instruments such as Gravity in infrared, *Fermi* and the Cherenkov Telescope Array in gamma rays, the Event Horizon Telescope in radio, where Europe is strongly involved. The last project is more exploratory and is meant to prepare for the next generation of astrophysical numerical code: multi-approaches for multi-scale, multi-physics, and therefore more realistic simulations.

Part V

Curriculum Vitae & list of publications

9.11 Curriculum Vitae

9.11.1 Personal information

Family name, First name: CERUTTI, Benoît
ORCID Number: http://orcid.org/0000-0001-6295-596X
Date of birth: 26 April 1984
Nationality: French
URL for web site: http://ipag.osug.fr/~ceruttbe/

9.11.2 Education

2010: PhD in astrophysics at the Laboratoire d'Astrophysique de Grenoble (LAOG), Université de Grenoble, France. Supervisor: Guillaume Dubus.

2007: Master in particle physics and astroparticles, Physics Department, Université Joseph Fourier, France.

2007: Master in physical engineering, Grenoble Institute of Technology (ENSPG), France.

9.11.3 Current and previous positions

2015-Today: Chargé de Recherche at CNRS (CRCN). Institut de Planétologie et d'Astrophysique de Grenoble, CNRS/Université Grenoble Alpes, France.

2013-2015: Lyman P. Spitzer Jr Postdoctoral Fellow, Department of Astrophysical Sciences, Princeton University, USA. Collaborators: Prof. A. Spitkovsky & A. Philippov.

2010-2013: Postdoctoral Fellow, Physics Department, University of Colorado at Boulder, USA. Collaborators: Prof. D. A. Uzdensky, Prof. M. C. Begelman & Dr. G. Werner.

9.11.4 Awards & fellowships

2020: CNRS bronze medal.
2019: ERC Consolidator grantee.
2018: PRACE allocation 17th call grantee.
2018: France-Berkeley Fund grantee.
2013: Lyman Spitzer Jr. Fellowship.

9.11.5 Supervision of graduate students and Postdoctoral fellows

2020-: ERC-SPAWN postoc Ileyk El Mellah.

2020-2023: Co-supervision of Ibrahim Ceyhun Andaç co-tutelle PhD thesis, joint between the Université Grenoble Alpes and Istanbul Technical University, French government scholarship, "Ab-initio modeling of pulsar-disk interaction: applications to transitional millisecond pulsars and fallback disks".

2018-2021: Co-supervision of Benjamin Crinquand PhD thesis, ENS fellowship, "Ab-initio modeling of a rotating black hole magnetosphere."

4 Master thesis projects: Jérémy Mortier (M1: 2016, M2: 2017), Aloïs de Valon (M1: 2017), B. Crinquand (M2: 2018). 1 License project: Sarkis Rastikian (L2: 2009).

9.11.6 Teaching activities

2015-2020: Invited lecturer at the PhD schools: Cargèse 2016 , Les Houches 2017 & 2019, and Astrosim 2017 & 2020.

2010: Plasma Physics class, two lectures of 75 minutes each, University of Colorado.

2007-2010: Graduate Teaching Assistant (Moniteur) in introductory electromagnetism for undergraduate students ($\sim$ 50 students, 64 hrs per year), Université Joseph Fourier, France.

9.11.7 Outreach activities

2007-Today: Regular host of public night observations at IPAG (2-3 nights per year), group of 20 attendees per night.

2012: General public talk "Latest news from the high-energy Universe" at the Alliance Française de Denver.

2009: General public conference "Gamma-ray astronomy and the violent Universe", 100 Hours of Astronomy.

9.11.8 Organisation of scientific meetings

2019: Chair of the organizing committee of Les Houches school in plasma physics, Les Houches, France. Attendance: 46 PhD & Master students and postdocs, 24 invited lecturers.

2015: Member of the organizing committee of the PCTS workshop "Accelerating Cosmic-Ray Comprehension", Princeton University, USA. About 50 international participants.

9.11.9 Institutional responsibilities

2017-Today: Organizer of the weekly Astrophysics colloquium, IPAG, Université Grenoble Alpes, France ($\sim$ 30 colloquia per year, $\sim$50 attendees).

2014: Co-organizer of the weekly Astrophysics colloquium, Princeton University, USA ($\sim$ 100 attendees).

2011-2013: Organizer of the weekly plasma physics seminars, CIPS, University of Colorado, USA ($\sim$ 15 attendees).

2009-2010: Organizer of the public observation nights program, Grenoble Observatory, France (7 nights per year and 20 participants per night).

9.11.10 Reviewing activities

2010-: Referee for A&A, MNRAS, ApJ, Journal of Plasma Physics, PRL, Nature, about 5 per year.
2018-: Review panel member of the French national supercomputer facility (GENCI, CT4 committee: Astrophysics & Geophysics).
2017-: Examiner PhD thesis committee: G. Brambilla (University of Milan, 2017), G. Voisin (LUTH-Observatoire de Paris, 2017), C. Guépin (IAP-Observatoire de Paris, 2019).
2020: External referee and panel member for a lecturer position (maître de conférences) at Paris-Sorbonne Université.
2014-: Review panel member for the NASA's Astrophysics Theory Program (ATP).
2018-: Reviewer for the NASA Theoretical and Computational Astrophysics Networks Program (TCAN).
2017-: Reviewer for PRACE.
2017-: Reviewer for the DIM ACAV (research fund for astrophysics laboratories in Paris).
2014-: Reviewer for the Polish National Science Centre.
2018-: Reviewer for the FONDECYT regular grant (Chile).

9.12 List of talks

9.12.1 Conferences

- **Invited talk** at the online mini-conference "Frontiers of Magnetic Reconnection Research in Heliophysical, Astrophysical, and Laboratory Plasmas", APS-DPP annual meeting 2020, Nov. 2020, USA.

- **Invited talk** at the "Workshop on Relativistic Plasma Astrophysics", May 2020, Purdue University, USA. Postponed to 2021.

- **Invited talk** at the PHAROS conference 2020 "The multi-messenger physics and astrophysics of neutron stars", April 2020, Patras, Greece - Canceled due to the Covid-19 pandemic.

- **Invited talk** at workshop "Simulating the evolution and emission of relativistic outflows", November 2019, Meudon, France.

- **Contributed talk** at the "IRAM-France day", Jan. 2019, Paris, France.

- **Invited talk** at the 46th European Physical Society Conference on Plasma Physics (EPS 2019), July 2019, Milan, Italy.

- **Invited talk** at the High Energy Phenomena in Relativistic Outflows (HEPRO VII) conference, July 2019, Barcelona, Spain.

- **Lecturer** at Les Houches school of Physics, May 2019, Les Houches, France.

- **Invited talk** at the Astrosim workshop: "Highlights and prospects for numerical astrophysics in France", October 2018, Lyon, France.

- **Invited talk** at the PNHE workshop: "Journées théories" , October 2018, Paris, France.

- **Invited talk** at the "Workshop on Relativistic Plasma Astrophysics", May 2018, Purdue University, USA.

- **Invited talk** at the PHAROS Cost action workshop "Neutron stars: towards a global view", March 2018, Rome, Italy.

- **Invited talk** at the AGILE Symposium "A decade of AGILE: Results, challenges and prospects of gamma-ray astrophysics", December 2017, Rome, Italy.

- **Invited talk** at the Nordita workshop "Exascale thinking of particle energization problems", August 2017, Stockholm, Swenden.

- **Invited lecturer** at Astrosim: École numérique pour l'astrophysique, June 2017, Lyon, France.
- **Invited lecturer** at Les Houches school of Physics, May 2017, Les Houches, France.
- **Invited talk** at the "TPC MeV polarimetry" workshop, April 2017, Palaiseau, France.
- **Invited talk** at the conference on "Cosmic Ray Origin – beyond the standard models", September 2016, San Vito di Cadore, Italy.
- **Invited talk** at the workshop on "Beyond a PeV", September 2016, Paris, France.
- **Invited talk** at the workshop on "Modelling Nebulae", June 2016, Sant Cugat, Spain.
- **Invited lecturer** at the Cargèse school 2016 "Astrophysical jets", May 2016, Cargèse, France. 3 hrs lecture for about 50 graduate students.
- **Contributed talk** at the "Texas Symposium 2015", Dec. 2015, Geneva, Switzerland.
- **Invited talk** at the French meeting on "Particle acceleration processes", Dec. 2015, Grenoble, France.
- **Invited talk** at the "Relativistic Laboratory Astrophysics" workshop, Nov. 2015, Harnack-Haus, Berlin, Germany.
- **Invited talk** at the ISSI workshop on "Jets and Winds in Pulsar Wind Nebulae, Gamma-ray Bursts and Blazars: Physics of Extreme Energy Release", Nov. 2015, Bern, Switzerland.
- **Contributed talk** at the conference "Magnetic fields from the sun to black holes, in memory of Jean Heyvaerts", Nov. 2014, Paris, France.
- **Invited talk** at the "High Energy processes around compact objects", June 2014, Florence, Italy.
- **Invited talk** at the "Workshop on Relativistic Plasma Astrophysics", May 2014, Purdue University, USA.
- **Invited talk** at the ISSI workshop on "The Strongest Magnetic Fields in the Universe", Feb. 2014, Bern, Switzerland.
- **Invited talk** at the 55th Annual Meeting of the APS Division of Plasma Physics, Nov. 2013, Denver, USA.

- **Contributed talk** at the "Max-Planck/Princeton Center for Plasma Physics meeting", Oct. 2013, Princeton, USA.
- **Contributed talk** at the international workshop "From Black Holes to Cosmic Rays : when plasmas go wild", Oct. 2013, Les Houches, France.
- **Invited talk** at the "Variable Galactic gamma-ray sources" workshop, Apr. 2013, Barcelona, Spain.
- **Contributed talk** at the 2012 JSI workshop "Nature's particle accelerators", Oct. 2012, Annapolis, USA.
- **Invited talk** at the French meeting on "Particle acceleration processes", Sept. 2012, Paris, France.
- **Contributed talk** at the "French workshop on magnetic reconnection", Sept. 2012, Paris, France.
- **Contributed talk** at the "5th International Symposium on High-Energy Gamma-Ray Astronomy", July 2012, Heidelberg, Germany.
- **Invited talk** at the "The Flaring Crab: Surprise and Impact", July 2012, Frascati, Italy.
- **Invited talk** at the international workshop on "Particles and Radiation from Cosmic Accelerators CA2012", Feb. 2012, Chiba University, Japan.
- **Contributed talk** at the "219th AAS Meeting", Jan. 2012, Austin, USA.
- **Invited talk** at the "Texas Symposium 2010", Dec. 2010, Heidelberg, Germany.
- **Invited talk** at the "Variable Galactic gamma-ray sources" workshop, Nov. 2010, Heidelberg, Germany.
- **Contributed talk** at the French Society of Astronomy meeting, June 2010, Marseille, France.
- **Contributed talk** at the ICREA Workshop on "The High-Energy Emission from Pulsars and their Systems", Apr. 2010, Sant Cugat, Spain.
- **Contributed talk** at "The 2009 Fermi Symposium", Nov. 2009, Washington D.C., USA.
- **Invited talk** at "The GeV-TeV sky" workshop, Sept. 2009, Palaiseau, France.
- **Contributed talk** at the French Society of Astronomy meeting, July 2009, Besançon, France.

- **Contributed talk** at "High-energy phenomena in massive stars", Feb. 2009, Jaén, Spain.
- **Contributed talk** at "Simbol-X Second International Symposium", Dec. 2008, Paris, France.
- **Contributed talk** at the French Society of Astronomy meeting, July 2008, Paris, France.
- **Contributed talk** at the French Society of Astronomy meeting, July 2007, Grenoble, France.

9.12.2 Seminars

- **Online Astrophysics Colloquium**, University of Amsterdam, November 2020, Amsterdam, Netherlands.
- **Online Astrophysics Colloquium**, Radboud University, November 2020, Nejmegen, Netherlands.
- **DAMTP astrophysics seminar**, DAMTP, February 2020, Cambridge, England.
- **CAMK Colloquium**, CAMK, June 2019, Warsaw, Poland.
- **Astrophysics Colloquium**, IAP, Jan. 2018, Paris, France.
- **Colloquium at Columbia University**, Department of Astronomy, Nov. 2017, New-York City, USA.
- **Seminar at CEA/DAM/DIF**, Sept. 2017, Bruyères-Le-Châtel, France.
- **Astronomy and Astrophysics Seminar**, Tel Aviv University, June 2017, Tel Aviv, Israel.
- **Astrophysics and Cosmology Seminar**, Ben Gurion University of the Negev, June 2017, Beer-Sheva, Israel.
- **Astrophysics seminar**, The Racah Institute de Physics, June 2017, Jerusalem, Israel.
- **LUTh seminar**, Dec. 2016, Meudon, France.
- **AHE seminar at APC**, Apr. 2016, Paris, France.
- **Saclay SAp Seminar**, Feb. 2016, Saclay, France.
- **CASA/JILA Astrophysics Lunch Seminar**, Jan. 2015, Boulder, USA.

- **Thunch talk**, Princeton University, Dec. 2014, Princeton, USA.
- **CITA seminar**, CITA, Sept. 2014, Toronto, Canada.
- **Astroplasmas Seminar**, Princeton University, Sept. 2014, Princeton, USA.
- **Seminar at DESY**, DESY Zeuthen, Feb. 2014, Zeuthen, Germany.
- **CIPS Seminar**, University of Colorado, Nov. 2013, Boulder, USA.
- **Séminaire IRAP**, Institut de recherche en astrophysique et planétologie, Oct. 2013, Toulouse, France.
- **Astroplasmas Seminar**, Princeton University, July 2013, Princeton, USA.
- **Séminaire LUPM**, Laboratoire Univers et Particules de Montpellier, March 2013, Montpellier, France.
- **CIPS Seminar**, University of Colorado, Feb. 2013, Boulder, USA.
- **Séminaire IPAG**, Institut de Planétologie et d'Astrophysique de Grenoble, Sept. 2012, Grenoble, France.
- **KIPAC Tea Talk**, Stanford University, Aug. 2012, Palo Alto, USA.
- **Séminaire GReCO**, Institut d'Astrophysique de Paris, March 2012, Paris, France.
- **KIPAC Tea Talk**, Stanford University, Dec. 2011, Palo Alto, USA.
- **CIPS Seminar**, University of Colorado, Oct. 2011, Boulder, USA.
- **CASA/JILA Astrophysics Lunch Seminar**, University of Colorado, May 2011, Boulder, USA.
- ***Fermi* lunch Talk**, KIPAC, Stanford University, March 2011, Menlo Park, USA.
- **Astronomical Observatory**, Jagiellonian University, Nov. 2010, Kraków, Poland.
- **CIPS Seminar**, University of Colorado, Oct. 2010, Boulder, USA.

9.13 List of publications

9.13.1 Refereed journals articles

33. **Cerutti, B.**, Philippov, A., and Dubus, G., "Dissipation of the striped pulsar wind and non-thermal particle acceleration: 3D PIC simulations", Astronomy and Astrophysics in press (2020).

32. **Cerutti, B.**, and Giacinti, G., "A global model of particle acceleration at pulsar wind termination shocks", Astronomy and Astrophysics in press (2020).

31. Crinquand, B., **Cerutti, B.**, Philippov, A., Parfrey, K., and Dubus, G., "Multi-dimensional simulations of ergospheric pair discharges around black holes", Phys. Rev. Lett. 124, 145101 (2020).

30. Guépin, C., **Cerutti, B.**, and Kotera, K., "Proton acceleration in pulsar magnetospheres", Astronomy and Astrophysics 635, A138 (2020).

29. Philippov, A., Uzdensky, D. A., Spitkovsky, A., and **Cerutti, B.**, "Pulsar Radio Emission Mechanism: Radio Nanoshots as a Low Frequency Afterglow of Relativistic Magnetic Reconnection", The Astrophysical Journal Letters 876, L6 (2019).

28. Crinquand, B., **Cerutti, B.**, and Dubus, G., "Kinetic modeling of the electromagnetic precursor from an axisymmetric binary pulsar coalescence", Astronomy and Astrophysics 622, A161 (2019).

27. Parfrey, K., Philippov, A., and **Cerutti, B.**, "First-Principles Plasma Simulations of Black-Hole Jet Launching", Phys. Rev. Lett. 122, 035101 (2019).

26. Levinson, A., and **Cerutti, B.**, "Particle-in-cell simulations of pair discharges in a starved magnetosphere of a Kerr black hole", Astronomy and Astrophysics 616, A184 (2018).

25. Werner, G. R., Uzdensky, D. A., Begelman, M. C., **Cerutti, B.**, and Nalewajko, K., "Nonthermal particle acceleration in collisionless relativistic electron-proton reconnection", MNRAS 473, 4840 (2018).

24. **Cerutti, B.**, and Philippov, A., "Dissipation of the striped pulsar wind", Astronomy and Astrophysics 607, A134 (2017).

23. **Cerutti, B.**, Mortier, J., and Philippov, A., "Polarized synchrotron emission from the equatorial current sheet in gamma-ray pulsars", MNRAS 463, L89 (2016).

22. **Cerutti, B.**, Philippov, A., and Spitkovsky, A., "Modeling high-energy pulsar lightcurves from first principles", *MNRAS*, **457**, 2401 (2016). (arXiv:1511.01785)

21. Werner, G. R., Uzdensky, D. A., **Cerutti, B.**, Nalewajko, K., and Begelman, M. C., "The extent of power-law energy spectra in collisionless relativistic magnetic reconnection in pair plasmas", *The Astrophysical Journal Letters*, **816**, L8 (2016). (arXiv:1409.8262)

20. Philippov, A., **Cerutti, B.**, Tchekhovskoy, A., and Spitkovsky, A., "Ab-initio pulsar magnetosphere: the role of general relativity", *The Astrophysical Journal Letters*, **815**, L19 (2015). (arXiv:1510.01734)

19. Nalewajko, K., Uzdensky, D. A., **Cerutti, B.**, Werner, G. R., and Begelman, M. C.,"On the distribution of particle acceleration sites in plasmoid-dominated relativistic magnetic reconnection", *The Astrophysical Journal*, **815**, 101 (2015). (arXiv:1508.02392)

18. Philippov, A., Spitkovsky, A., and **Cerutti, B.**, "Ab-initio pulsar magnetosphere: three-dimensional particle-in-cell simulations of oblique pulsars", *The Astrophysical Journal Letters*, **801**, L19 (2015). (arXiv:1412.0673)

17. **Cerutti, B.**, Philippov, A., Parfrey, K., and Spitkovsky, A., "Particle acceleration in axisymmetric pulsar current sheets", *MNRAS*, **448**, 606 (2015). (arXiv:1410.3757)

16. **Cerutti, B.**, Werner, G. R., Uzdensky, D. A., and Begelman, M. C., "Gamma-ray flares in the Crab Nebula: A case of relativistic reconnection?", *Invited paper in the annual Special Issue of Physics of Plasmas*, **21**, 056501 (2014). (arXiv:1401.3016)

15. **Cerutti, B.**, Werner, G. R., Uzdensky, D. A., and Begelman, M. C., "Three-dimensional relativistic pair plasma reconnection with radiative feedback in the Crab Nebula ", *The Astrophysical Journal*, **782**, 104 (2014). (arXiv:1311.2605)

14. Dubus, G., and **Cerutti, B.**, "What caused the GeV flare of PSR B1259-63?", *Astronomy and Astrophysics* **557**, A127 (2013). (arXiv:1308.4531)

13. **Cerutti, B.**, Werner, G. R., Uzdensky, D. A., and Begelman, M. C., "Simulations of Particle Acceleration beyond the Classical Synchrotron Burnoff Limit in Magnetic Reconnection: An Explanation of the Crab Flares", *The Astrophysical Journal* **770**, 147 (2013). (arXiv:1302.6247)

12. Nalewajko, K., Begelman, M. C., **Cerutti, B.**, Uzdensky, D. A., and Sikora, M., "Energetic constraints on a rapid gamma-ray flare in PKS 1222+216", *MNRAS*

425, 2519-2529 (2012). (arXiv:1202.2123)

11. **Cerutti, B.**, Werner, G. R., Uzdensky, D. A., and Begelman, M. C., "Beaming and rapid variability of high-energy radiation from relativistic pair plasma reconnection", *The Astrophysical Journal Letters* **754**, L33 (2012). (arXiv:1205.3210)

10. Zdziarski, A. A., Sikora, M., Dubus, G., Yuan, F., **Cerutti, B.**, and Ogorzalek, A., "The gamma-ray emitting region of the jet in Cyg X-3", *MNRAS* **421**, 2956-2968 (2012). (arXiv:1111.0878)

9. **Cerutti, B.**, Uzdensky, D. A., and Begelman, M. C., "Extreme particle acceleration in magnetic reconnection layers: Application to the gamma-ray flares in the Crab Nebula", *The Astrophysical Journal* **746**, 148 (2012). (arXiv:1110.0557)

8. Uzdensky, D. A., **Cerutti, B.**, and Begelman, M. C., "Reconnection-powered Linear Accelerator and Gamma-Ray Flares in the Crab Nebula", *The Astrophysical Journal Letters* **737**, L40 (2011). (arXiv:1105.0942)

7. **Cerutti, B.**, Dubus, G., Malzac, J., Szostek, A., Belmont, R., Zdziarski, A. A., and Henri, G.,"Absorption of high-energy gamma rays in Cygnus X-3", *Astronomy and Astrophysics* **529**, A120 (2011). (arXiv:1103.3875)

6. **Cerutti, B.**, Malzac, J., Dubus, G., and Henri, G.,"Modeling the three-dimensional pair cascade in binaries. Application to LS 5039", *Astronomy and Astrophysics* **519**, A81 (2010). (arXiv:1006.2683)

5. Dubus, G., **Cerutti, B.**, and Henri, G.,"Relativistic Doppler-boosted emission in gamma-ray binaries", *Astronomy and Astrophysics* **516**, A18 (2010). (arXiv:1004.0511)

4. Dubus, G., **Cerutti, B.**, and Henri, G.,"The relativistic jet of Cygnus X-3 in gamma rays", *MNRAS Letters* **404**, L55-L59 (2010). (arXiv:1002.3888)

3. **Cerutti, B.**, Dubus, G., and Henri, G.,"One-dimensional pair cascade emission in gamma-ray binaries. An upper-limit to cascade emission at superior conjunction in LS 5039", *Astronomy and Astrophysics* **507**, 1217-1224 (2009). (arXiv:0909.5587)

2. **Cerutti, B.**, Dubus, G., and Henri, G.,"Spectral signature of a free pulsar wind in the gamma-ray binaries LS 5039 and LSI $+61^{\circ}303$", *Astronomy and Astrophysics* **488**, 37-46 (2008). (arXiv:0807.1226)

1. Dubus, G., **Cerutti, B.**, and Henri, G., "The modulation of the gamma-ray emission from the binary LS 5039", *Astronomy and Astrophysics* **477**, 691-700 (2008). (arXiv:0710.0968)

9.13.2 Book chapters

4. Sironi L., and **Cerutti, B.**, "Particle Acceleration in Pulsar Wind Nebulae: PIC Modelling", Chapitre du livre intitulé "Modelling Nebulae" édité par D. Torres pour Springer (2017). (arXiv:1705.10815)

3. **Cerutti, B.**, and Beloborodov, A., "Electrodynamics of pulsar magnetospheres", Space Science Reviews, Chapitre du livre intitulé "Jets and Winds in Pulsar Wind Nebulae and Gamma-ray Bursts" (2017). (arXiv:1611.04331)

2. Kargaltsev, O., **Cerutti, B.**, Lyubarsky, Y., and Striani, E., "Pulsar-Wind Nebulae: Recent Progress in Observations and Theory", *Invited review paper for Space Science Reviews* (2015). (arXiv:1507.03662)

1. Kagan, D., Sironi, L., **Cerutti, B.**, and Giannios, D., "Relativistic magnetic reconnection in pair plasmas and its astrophysical applications", *Invited review paper accepted for publication in Space Science Reviews* (2015). (arXiv:1412.2451)

9.13.3 Conference proceedings

14. **Cerutti, B.**, "Present status of particle acceleration in relativistic outflows", Proceedings of Science, (2019).

13. **Cerutti, B.**, "Gamma-ray pulsars: What have we learned from ab-initio kinetic simulations?", Rendiconti Lincei, (2019). (arXiv:1811.09215)

12. **Cerutti, B.**, "Particle acceleration and radiation in pulsars: New insights from kinetic simulations", Nuclear and Particle Physics Proceedings 297, 85-90 (2018).

11. **Cerutti, B.**, Werner, G. R., Uzdensky, D. A., and Begelman, M. C., "Rapid High-Energy Emission Variability in Relativistic Pair Plasma Reconnection", Submitted to AIP Conference Proceedings, *5th International Symposium on High-Energy Gamma-Ray Astronomy*, Edited by F. Aharonian, W. Hofmann, & F. Rieger, (2013).

10. **Cerutti, B.**, and Dubus, G.,"On the origin of the GeV and TeV emission in gamma-ray binaries", Proceedings of Science, 25$^{\text{th}}$Texas Symposium on *Relativistic Astrophysics*, Edited by F. M. Rieger, C. van Eldik, & W. Hofmann, (2010).

9. Dubus, G., and **Cerutti, B.**,"Massive stars at (very) high energies: gamma-ray binaries", Cambridge University Press, IAU Symposium 272 on *Active OB stars: structure, evolution, mass loss and critical limits*, Edited by C. Neiner, G. Wade, G. Meynet & G. Peters, (2010).

8. Cerutti, B., Dubus, G., and Henri, G.,"High-energy radiation from the relativistic jet of Cygnus X-3", Proceedings of the *Annual meeting of the French Society of Astronomy and Astrophysics*, Edited by S. Boissier, M. Heydari-Malayeri, R. Samadi & D. Valls-Gabaud, (2010).

7. Cerutti, B., Dubus, G., and Henri, G.,"Relativistic motion and beamed radiation in gamma-ray binaries", Astrophysics and Space Science Proceedings, *The High-Energy Emission from Pulsars and their Systems*, Edited by N. Rea & D. F. Torres, (2010).

6. Cerutti, B., Dubus, G., and Henri, G.,"Anisotropic pair cascading in gamma-ray binaries", ASP Conference Series, *High energy phenomena in massive stars*, Edited by J. Martí, P. L. Luque-Escamilla & J. A. Combi **422**, 41-48 (2010).

5. Cerutti, B., Dubus, G., and Henri, G.,"Modeling the high-energy radiation in gamma-ray binaries", Proceedings of the 2009 *Fermi* Symposium, eConf Proceedings C091122 (2009).

4. Cerutti, B., Dubus, G., and Henri, G.,"Pair cascading in gamma-ray binaries", Proceedings of the *Annual meeting of the French Society of Astronomy and Astrophysics*, Edited by M. Heydari-Malayeri, C. Reylé, & R. Samadi, 139-142 (2009).

3. Cerutti, B., Dubus, G., Henri, G., Hill, A. B., and Szostek, A.,"What can Simbol-X do for gamma-ray binaries", AIP Conference Proceedings of the *Second International Simbol-X Symposium*, Edited by J. Rodriguez & P. Ferrando, 263-266 (2009).

2. Cerutti, B., Dubus, G., and Henri, G.,"Probing pulsar winds with gamma-ray binaries", Proceedings of the *Annual meeting of the French Society of Astronomy and Astrophysics*, Edited by C. Charbonnel, F. Combes, & R. Samadi, 187-190 (2008).

1. Cerutti, B., Dubus, G., and Henri, G.,"Anisotropic inverse Compton scattering in gamma-ray binaries", Proceedings of the *Annual meeting of the French Society of Astronomy and Astrophysics*, Edited by J. Bouvier, A. Chalabaev, & C. Charbonnel, 158-161 (2007).

Bibliography

Abbott, B. P., Abbott, R., Abbott, T. D., et al. 2016, Phys. Rev. Lett., 116, 061102

Abbott, B. P., Abbott, R., Abbott, T. D., et al. 2017a, Phys. Rev. Lett., 119, 161101

Abbott, B. P., Abbott, R., Abbott, T. D., et al. 2017b, Astrophysical Journal, Letters, 848, L12

Abdo, A. A., Ackermann, M., Ajello, M., et al. 2011, Science, 331, 739

Abdo, A. A., Ackermann, M., Ajello, M., et al. 2009, Science, 325, 840

Abdo, A. A., Ackermann, M., Ajello, M., et al. 2010a, Astrophysical Journal, 708, 1254

Abdo, A. A., Ackermann, M., Ajello, M., et al. 2010b, Astrophysical Journal, Supplement, 187, 460

Abdo, A. A., Ajello, M., Allafort, A., et al. 2013, Astrophysical Journal, Supplement, 208, 17

Acciari, V. A., Aliu, E., Arlen, T., et al. 2009, Science, 325, 444

Adriani, O., Barbarino, G. C., Bazilevskaya, G. A., et al. 2009, Nature, 458, 607

Aharonian, F., Akhperjanian, A. G., Bazer-Bachi, A. R., et al. 2007, Astrophysical Journal, Letters, 664, L71

Aharonian, F., Akhperjanian, A. G., Bazer-Bachi, A. R., et al. 2006, Science, 314, 1424

Albert, J., Aliu, E., Anderhub, H., et al. 2008, Astrophysical Journal, Letters, 685, L23

Albert, J., Aliu, E., Anderhub, H., et al. 2007, Astrophysical Journal, 669, 862

Aleksić, J., Ansoldi, S., Antonelli, L. A., et al. 2014, Science, 346, 1080

Aliu, E., Archambault, S., Aune, T., et al. 2014, Astrophysical Journal, Letters, 781, L11

Ansoldi, S., Antonelli, L. A., Antoranz, P., et al. 2016, Astron. & Astrophys., 585, A133

Arnowitt, R. L., Deser, S., & Misner, C. W. 1962, Canonical analysis of general relativity, 127

Arons, J. 1979, Space Sci. Rev., 24, 437

Arons, J. 1983, Astrophysical Journal, 266, 215

Arons, J. 2009, in Astrophysics and Space Science Library, Vol. 357, Astrophysics and Space Science Library, ed. W. Becker, 373

Arons, J. 2012, Space Sci. Rev., 173, 341

Atoyan, A. M. & Aharonian, F. A. 1996, Mon. Not. of the Royal Astron. Soc., 278, 525

Baade, W. & Zwicky, F. 1934, Proceedings of the National Academy of Science, 20, 259

Bai, X.-N. & Spitkovsky, A. 2010a, Astrophysical Journal, 715, 1282

Bai, X.-N. & Spitkovsky, A. 2010b, Astrophysical Journal, 715, 1270

Balbo, M., Walter, R., Ferrigno, C., & Bordas, P. 2011, Astron. & Astrophys., 527, L4

Bednarek, W. & Idec, W. 2011, Mon. Not. of the Royal Astron. Soc., 414, 2229

Begelman, M. C. 1998, Astrophysical Journal, 493, 291

Belyaev, M. A. 2015, Mon. Not. of the Royal Astron. Soc., 449, 2759

Berenger, J.-P. 1994, Journal of Computational Physics, 114, 185

Berenger, J.-P. 1996, Journal of Computational Physics, 127, 363

Beskin, V. S., Chernov, S. V., Gwinn, C. R., & Tchekhovskoy, A. A. 2015, Space Sci. Rev., 191, 207

Birdsall, C. K. & Langdon, A. B. 1991, Plasma Physics via Computer Simulation

Blackman, E. G. & Field, G. B. 1994, Phys. Rev. Lett., 72, 494

Blandford, R., Meier, D., & Readhead, A. 2019, Annual Review of Astron and Astrophys, 57, 467

Blandford, R. D. 2002, in Lighthouses of the Universe: The Most Luminous Celestial Objects and Their Use for Cosmology, ed. M. Gilfanov, R. Sunyeav, & E. Churazov, 381

Blandford, R. D. & Znajek, R. L. 1977, Mon. Not. of the Royal Astron. Soc., 179, 433

Blumenthal, G. R. & Gould, R. J. 1970, Reviews of Modern Physics, 42, 237

Bogovalov, S. V. 1999, Astron. & Astrophys., 349, 1017

Bonazzola, S., Mottez, F., & Heyvaerts, J. 2015, Astron. & Astrophys., 573, A51

Bonometto, S. & Rees, M. J. 1971, Mon. Not. of the Royal Astron. Soc., 152, 21

Broderick, A. E. & Tchekhovskoy, A. 2015, Astrophysical Journal, 809, 97

Buckley, R. 1977, Mon. Not. of the Royal Astron. Soc., 180, 125

Buehler, R., Scargle, J. D., Blandford, R. D., et al. 2012, Astrophysical Journal, 749, 26

Bühler, R. & Blandford, R. 2014, Reports on Progress in Physics, 77, 066901

Bykov, A. M., Pavlov, G. G., Artemyev, A. V., & Uvarov, Y. A. 2012, Mon. Not. of the Royal Astron. Soc., 421, L67

Capdessus, R., d'Humières, E., & Tikhonchuk, V. T. 2012, Phys. Rev. E, 86, 036401

Cerutti, B. 2018, arXiv e-prints, arXiv:1811.09215

Cerutti, B. 2019, in High Energy Phenomena in Relativistic Outflows VII, 12

Cerutti, B. & Beloborodov, A. M. 2017, Space Sci. Rev., 207, 111

Cerutti, B., Dubus, G., & Henri, G. 2009, Astron. & Astrophys., 507, 1217

Cerutti, B. & Giacinti, G. 2020, arXiv e-prints, arXiv:2008.07253

Cerutti, B., Mortier, J., & Philippov, A. A. 2016a, Mon. Not. of the Royal Astron. Soc., 463, L89

Cerutti, B., Philippov, A., & Dubus, G. 2020, arXiv e-prints, arXiv:2008.11462

Cerutti, B., Philippov, A., Parfrey, K., & Spitkovsky, A. 2015, Mon. Not. of the Royal Astron. Soc., 448, 606

Cerutti, B. & Philippov, A. A. 2017, Astron. & Astrophys., 607, A134

Cerutti, B., Philippov, A. A., & Spitkovsky, A. 2016b, Mon. Not. of the Royal Astron. Soc., 457, 2401

Cerutti, B., Uzdensky, D. A., & Begelman, M. C. 2012a, Astrophysical Journal, 746, 148

Cerutti, B., Werner, G. R., Uzdensky, D. A., & Begelman, M. C. 2012b, Astrophysical Journal, Letters, 754, L33

Cerutti, B., Werner, G. R., Uzdensky, D. A., & Begelman, M. C. 2013, Astrophysical Journal, 770, 147

Cerutti, B., Werner, G. R., Uzdensky, D. A., & Begelman, M. C. 2014a, Physics of Plasmas, 21, 056501

Cerutti, B., Werner, G. R., Uzdensky, D. A., & Begelman, M. C. 2014b, Astrophysical Journal, 782, 104

Chen, A. Y. & Beloborodov, A. M. 2014, Astrophysical Journal, Letters, 795, L22

Chen, A. Y., Cruz, F., & Spitkovsky, A. 2020, Astrophysical Journal, 889, 69

Chen, A. Y. & Yuan, Y. 2020, Astrophysical Journal, 895, 121

Cheng, C. Z. & Knorr, G. 1976, Journal of Computational Physics, 22, 330

Cheng, K. S., Ho, C., & Ruderman, M. 1986, Astrophysical Journal, 300, 500

Clausen-Brown, E. & Lyutikov, M. 2012, Mon. Not. of the Royal Astron. Soc., 426, 1374

Contopoulos, I. 2007, Astron. & Astrophys., 472, 219

Contopoulos, I. & Kazanas, D. 2002, Astrophysical Journal, 566, 336

Contopoulos, I., Kazanas, D., & Fendt, C. 1999, Astrophysical Journal, 511, 351

Coroniti, F. V. 1990, Astrophysical Journal, 349, 538

Crinquand, B., Cerutti, B., & Dubus, G. 2019, Astron. & Astrophys., 622, A161

Crinquand, B., Cerutti, B., Philippov, A. e., Parfrey, K., & Dubus, G. 2020, Phys. Rev. Lett., 124, 145101

Daugherty, J. K. & Harding, A. K. 1982, Astrophysical Journal, 252, 337

Davis, L. 1947, Physical Review, 72, 632

de Jager, O. C. & Harding, A. K. 1992, Astrophysical Journal, 396, 161

de Jager, O. C., Harding, A. K., Michelson, P. F., et al. 1996, Astrophysical Journal, 457, 253

Deutsch, A. J. 1955, Annales d'Astrophysique, 18, 1

Drenkhahn, G. & Spruit, H. C. 2002, Astron. & Astrophys., 391, 1141

Durant, M., Kargaltsev, O., Pavlov, G. G., Kropotina, J., & Levenfish, K. 2013, Astrophysical Journal, 763, 72

Dyks, J., Harding, A. K., & Rudak, B. 2004, Astrophysical Journal, 606, 1125

Dyks, J. & Rudak, B. 2003, Astrophysical Journal, 598, 1201

Elkina, N. V. & Büchner, J. 2006, Journal of Computational Physics, 213, 862

Erber, T. 1966, Reviews of Modern Physics, 38, 626

Esirkepov, T. Z. 2001, Computer Physics Communications, 135, 144

Event Horizon Telescope Collaboration. 2019a, Astrophysical Journal, Letters, 875, L1

Event Horizon Telescope Collaboration. 2019b, Astrophysical Journal, Letters, 875, L5

Fang, K., Kotera, K., & Olinto, A. V. 2012, Astrophysical Journal, 750, 118

Galeev, A. A., Rosner, R., & Vaiana, G. S. 1979, Astrophysical Journal, 229, 318

Giannios, D., Uzdensky, D. A., & Begelman, M. C. 2009, Mon. Not. of the Royal Astron. Soc., 395, L29

Ginzburg, V. L. & Syrovatskii, S. I. 1965, Annual Review of Astron and Astrophys, 3, 297

Giomi, M., Bühler, R., Sgrò, C., Longo, F., & Atwood, W. B. 2017, in American Institute of Physics Conference Series, Vol. 1792, 6th International Symposium on High Energy Gamma-Ray Astronomy, 070022

Gold, T. 1968, Nature, 218, 731

Goldreich, P. & Julian, W. H. 1969, Astrophysical Journal, 157, 869

Goodman, J. & Uzdensky, D. 2008, Astrophysical Journal, 688, 555

Goodwin, S. P., Mestel, J., Mestel, L., & Wright, G. A. E. 2004, Mon. Not. of the Royal Astron. Soc., 349, 213

Gourgoulhon, E. 2007, arXiv e-prints, gr

Graham-Smith, F., Dolan, J. F., Boyd, P. T., et al. 1996, Mon. Not. of the Royal Astron. Soc., 282, 1354

Gravity Collaboration. 2018, Astron. & Astrophys., 618, L10

Greenwood, A. D., Cartwright, K. L., Luginsland , J. W., & Baca, E. A. 2004, Journal of Computational Physics, 201, 665

Grenier, I. A. & Harding, A. K. 2015, Comptes Rendus Physique, 16, 641

Gros, P., Amano, S., Attié, D., et al. 2018, Astroparticle Physics, 97, 10

Gruzinov, A. 2005, Physical Review Letters, 94, 021101

Guépin, C., Cerutti, B., & Kotera, K. 2020, Astron. & Astrophys., 635, A138

Guilbert, P. W., Fabian, A. C., & Rees, M. J. 1983, Mon. Not. of the Royal Astron. Soc., 205, 593

Guo, F., Li, H., Daughton, W., & Liu, Y.-H. 2014, Phys. Rev. Lett., 113, 155005

H. E. S. S. Collaboration, Abramowski, A., Aharonian, F., et al. 2014, Astron. & Astrophys., 562, L4

Hansen, B. M. S. & Lyutikov, M. 2001, Mon. Not. of the Royal Astron. Soc., 322, 695

Harding, A. K. & Lai, D. 2006, Reports on Progress in Physics, 69, 2631

Hester, J. J. 2008, Annual Review of Astron and Astrophys, 46, 127

Hester, J. J., Scowen, P. A., Sankrit, R., et al. 1995, Astrophysical Journal, 448, 240

Hewish, A., Bell, S. J., Pilkington, J. D. H., Scott, P. F., & Collins, R. A. 1968, Nature, 217, 709

Hibschman, J. A. & Arons, J. 2001a, Astrophysical Journal, 554, 624

Hibschman, J. A. & Arons, J. 2001b, Astrophysical Journal, 560, 871

Higuera, A. V. & Cary, J. R. 2017, Physics of Plasmas, 24, 052104

Hones, Jr., E. W. & Bergeson, J. E. 1965, J. Geophys. Res., 70, 4951

Hoyle, F., Narlikar, J. V., & Wheeler, J. A. 1964, Nature, 203, 914

Huang, X., Yuan, Q., & Fan, Y.-Z. 2020, arXiv e-prints, arXiv:2003.02865

Jaroschek, C. H. & Hoshino, M. 2009, Physical Review Letters, 103, 075002

Jones, F. C. 1968, Physical Review, 167, 1159

Kagan, D., Sironi, L., Cerutti, B., & Giannios, D. 2015, Space Sci. Rev., 191, 545

Kalapotharakos, C., Brambilla, G., Timokhin, A., Harding, A. K., & Kazanas, D. 2018, Astrophysical Journal, 857, 44

Kalapotharakos, C. & Contopoulos, I. 2009, Astron. & Astrophys., 496, 495

Kalapotharakos, C., Harding, A. K., Kazanas, D., & Contopoulos, I. 2012a, Astrophysical Journal, Letters, 754, L1

Kalapotharakos, C., Kazanas, D., Harding, A., & Contopoulos, I. 2012b, Astrophysical Journal, 749, 2

Kargaltsev, O., Cerutti, B., Lyubarsky, Y., & Striani, E. 2015, Space Sci. Rev., 191, 391

Kawazura, Y., Barnes, M., & Schekochihin, A. A. 2019, Proceedings of the National Academy of Science, 116, 771

Kelner, S. R., Prosekin, A. Y., & Aharonian, F. A. 2015, Astronomical Journal, 149, 33

Kennel, C. F. & Coroniti, F. V. 1984, Astrophysical Journal, 283, 694

Kerr, R. P. 1963, Phys. Rev. Lett., 11, 237

King, A. R., Lasota, J. P., & Kundt, W. 1975, Phys. Rev. D, 12, 3037

Kirk, J. G. 2004, Phys. Rev. Lett., 92, 181101

Kirk, J. G., Lyubarsky, Y., & Petri, J. 2009, Astrophysics and Space Science Library, Vol. 357, The Theory of Pulsar Winds and Nebulae, ed. W. Becker, 421

Kirk, J. G. & Skjæraasen, O. 2003, Astrophysical Journal, 591, 366

Kisaka, S., Levinson, A., & Toma, K. 2020, arXiv e-prints, arXiv:2007.02838

Koide, S., Shibata, K., Kudoh, T., & Meier, D. L. 2002, Science, 295, 1688

Komissarov, S. S. 2004, Mon. Not. of the Royal Astron. Soc., 350, 427

Komissarov, S. S. 2005, Mon. Not. of the Royal Astron. Soc., 359, 801

Komissarov, S. S. 2006, Mon. Not. of the Royal Astron. Soc., 367, 19

Komissarov, S. S. 2013, Mon. Not. of the Royal Astron. Soc., 428, 2459

Komissarov, S. S. & Lyubarsky, Y. E. 2003, Mon. Not. of the Royal Astron. Soc., 344, L93

Komissarov, S. S. & Lyutikov, M. 2011, Mon. Not. of the Royal Astron. Soc., 414, 2017

Komissarov, S. S. & McKinney, J. C. 2007, Mon. Not. of the Royal Astron. Soc., 377, L49

Krause-Polstorff, J. & Michel, F. C. 1985a, Mon. Not. of the Royal Astron. Soc., 213, 43P

Krause-Polstorff, J. & Michel, F. C. 1985b, Astron. & Astrophys., 144, 72

Lai, D. 2012, Astrophysical Journal, Letters, 757, L3

Landau, L. D. & Lifshitz, E. M. 1971, The classical theory of fields, ed. Landau, L. D. & Lifshitz, E. M.

Larrabee, D. A., Lovelace, R. V. E., & Romanova, M. M. 2003, Astrophysical Journal, 586, 72

Li, J., Spitkovsky, A., & Tchekhovskoy, A. 2012, Astrophysical Journal, 746, 60

Lobanov, A. P., Horns, D., & Muxlow, T. W. B. 2011, Astron. & Astrophys., 533, A10

Lyubarskii, Y. E. 1996, Astron. & Astrophys., 311, 172

Lyubarsky, Y. & Kirk, J. G. 2001, Astrophysical Journal, 547, 437

Lyubarsky, Y. E. 2003, Mon. Not. of the Royal Astron. Soc., 345, 153

Lyubarsky, Y. E. 2005, Mon. Not. of the Royal Astron. Soc., 358, 113

Lyubarsky, Y. E. 2012, Mon. Not. of the Royal Astron. Soc., 427, 1497

Lyutikov, M., Balsara, D., & Matthews, C. 2012, Mon. Not. of the Royal Astron. Soc., 422, 3118

Lyutikov, M., Sironi, L., Komissarov, S. S., & Porth, O. 2017a, Journal of Plasma Physics, 83, 635830601

Lyutikov, M., Sironi, L., Komissarov, S. S., & Porth, O. 2017b, Journal of Plasma Physics, 83, 635830602

Lyutikov, M. & Uzdensky, D. 2003, Astrophysical Journal, 589, 893

Marder, B. 1987, Journal of Computational Physics, 68, 48

Mayer, M., Buehler, R., Hays, E., et al. 2013, Astrophysical Journal, Letters, 775, L37

McDonald, J. & Shearer, A. 2009, Astrophysical Journal, 690, 13

McKinney, J. C. 2006a, Mon. Not. of the Royal Astron. Soc., 368, 1561

McKinney, J. C. 2006b, Mon. Not. of the Royal Astron. Soc., 368, L30

Medvedev, M. V. 2000, Astrophysical Journal, 540, 704

Mehlhaff, J. M., Werner, G. R., Uzdensky, D. A., & Begelman, M. C. 2020, arXiv e-prints, arXiv:2002.07243

Meyer, M., Horns, D., & Zechlin, H. S. 2010, Astron. & Astrophys., 523, A2

Michel, F. C. 1973a, Astrophysical Journal, 180, 207

Michel, F. C. 1973b, Astrophysical Journal, Letters, 180, L133

Michel, F. C. 2004, Advances in Space Research, 33, 542

Michel, F. C. & Li, H. 1999, Phys. Rep., 318, 227

Mignone, A., Striani, E., Tavani, M., & Ferrari, A. 2013, Mon. Not. of the Royal Astron. Soc., 436, 1102

Most, E. R. & Philippov, A. A. 2020, Astrophysical Journal, Letters, 893, L6

Munz, C.-D., Omnes, P., Schneider, R., Sonnendrücker, E., & Voß, U. 2000, Journal of Computational Physics, 161, 484

Muslimov, A. G. & Harding, A. K. 2003, Astrophysical Journal, 588, 430

Nalewajko, K. 2018, Mon. Not. of the Royal Astron. Soc., 481, 4342

Nalewajko, K., Uzdensky, D. A., Cerutti, B., Werner, G. R., & Begelman, M. C. 2015, Astrophysical Journal, 815, 101

Neukirch, T. 1993, Astron. & Astrophys., 274, 319

Nodes, C., Birk, G. T., Lesch, H., & Schopper, R. 2003, Physics of Plasmas, 10, 835

Nolan, P. L., Fierro, J. M., Lin, Y. C., et al. 1996, Astronomy and Astrophysics, Supplement, 120, 61

Ostriker, J. P. & Gunn, J. E. 1969, Astrophysical Journal, 157, 1395

Pacini, F. 1967, Nature, 216, 567

Pacini, F. 1968, Nature, 219, 145

Parfrey, K., Beloborodov, A. M., & Hui, L. 2012, Mon. Not. of the Royal Astron. Soc., 423, 1416

Parfrey, K., Philippov, A., & Cerutti, B. 2019, Phys. Rev. Lett., 122, 035101

Parker, E. N. 1957, J. Geophys. Res., 62, 509

Pavlov, G. G., Teter, M. A., Kargaltsev, O., & Sanwal, D. 2003, Astrophysical Journal, 591, 1157

Penrose, R. 1969, Nuovo Cimento Rivista Serie, 1, 252

Penrose, R. & Floyd, R. M. 1971, Nature Physical Science, 229, 177

Pétri, J. 2007, Astron. & Astrophys., 469, 843

Pétri, J. 2012, Mon. Not. of the Royal Astron. Soc., 424, 605

Pétri, J. 2015, Mon. Not. of the Royal Astron. Soc., 450, 714

Pétri, J. 2016, Journal of Plasma Physics, 82, 635820502

Pétri, J., Heyvaerts, J., & Bonazzola, S. 2002a, Astron. & Astrophys., 387, 520

Pétri, J., Heyvaerts, J., & Bonazzola, S. 2002b, Astron. & Astrophys., 384, 414

Pétri, J. & Kirk, J. G. 2005, Astrophysical Journal, Letters, 627, L37

Pétri, J. & Kirk, J. G. 2007, Plasma Physics and Controlled Fusion, 49, 1885

Pétri, J. & Lyubarsky, Y. 2007, Astron. & Astrophys., 473, 683

Petropoulou, M. & Sironi, L. 2018, Mon. Not. of the Royal Astron. Soc., 481, 5687

Petschek, H. E. 1964, NASA Special Publication, 50, 425

Philippov, A., Tchekhovskoy, A., & Li, J. G. 2014, Mon. Not. of the Royal Astron. Soc., 441, 1879

Philippov, A., Timokhin, A., & Spitkovsky, A. 2020, Phys. Rev. Lett., 124, 245101

Philippov, A. A., Cerutti, B., Tchekhovskoy, A., & Spitkovsky, A. 2015a, Astrophysical Journal, Letters, 815, L19

Philippov, A. A. & Spitkovsky, A. 2014, Astrophysical Journal, Letters, 785, L33

Philippov, A. A. & Spitkovsky, A. 2018, Astrophysical Journal, 855, 94

Philippov, A. A., Spitkovsky, A., & Cerutti, B. 2015b, Astrophysical Journal, Letters, 801, L19

Piro, A. L. 2012, Astrophysical Journal, 755, 80

Plotnikov, I., Grassi, A., & Grech, M. 2018, Mon. Not. of the Royal Astron. Soc., 477, 5238

Porth, O., Chatterjee, K., Narayan, R., et al. 2019, Astrophysical Journal, Supplement, 243, 26

Porth, O., Komissarov, S. S., & Keppens, R. 2013, Mon. Not. of the Royal Astron. Soc., 431, L48

Porth, O., Komissarov, S. S., & Keppens, R. 2014, Mon. Not. of the Royal Astron. Soc., 438, 278

Qin, H., Zhang, S., Xiao, J., et al. 2013, Physics of Plasmas, 20, 084503

Radhakrishnan, V. & Cooke, D. J. 1969, Astrophys. Lett., 3, 225

Rees, M. J. & Gunn, J. E. 1974, Mon. Not. of the Royal Astron. Soc., 167, 1

Ripperda, B., Bacchini, F., Teunissen, J., et al. 2018, Astrophysical Journal, Supplement, 235, 21

Romani, R. W. & Yadigaroglu, I.-A. 1995, Astrophysical Journal, 438, 314

Romanova, M. M. & Lovelace, R. V. E. 1992, Astron. & Astrophys., 262, 26

Ruderman, M. A. & Sutherland, P. G. 1975, Astrophysical Journal, 196, 51

Rudy, A., Horns, D., DeLuca, A., et al. 2015, Astrophysical Journal, 811, 24

Scharlemann, E. T. & Wagoner, R. V. 1973, Astrophysical Journal, 182, 951

Schopper, R., Birk, G. T., & Lesch, H. 1999, Physics of Plasmas, 6, 4318

Schopper, R., Lesch, H., & Birk, G. T. 1998, Astron. & Astrophys., 335, 26

Shibata, S. 1989, Astrophysics and Space Science, 161, 187

Sironi, L. & Cerutti, B. 2017, Astrophysics and Space Science Library, Vol. 446, Particle Acceleration in Pulsar Wind Nebulae: PIC Modelling, ed. D. F. Torres, 247

Sironi, L., Giannios, D., & Petropoulou, M. 2016, Mon. Not. of the Royal Astron. Soc., 462, 48

Sironi, L. & Spitkovsky, A. 2009, Astrophysical Journal, Letters, 707, L92

Sironi, L. & Spitkovsky, A. 2011, Astrophysical Journal, 741, 39

Sironi, L. & Spitkovsky, A. 2014, Astrophysical Journal, Letters, 783, L21

Sironi, L., Spitkovsky, A., & Arons, J. 2013, Astrophysical Journal, 771, 54

Słowikowska, A., Kanbach, G., Kramer, M., & Stefanescu, A. 2009, Mon. Not. of the Royal Astron. Soc., 397, 103

Smith, F. G., Jones, D. H. P., Dick, J. S. B., & Pike, C. D. 1988, Mon. Not. of the Royal Astron. Soc., 233, 305

Smith, I. A., Michel, F. C., & Thacker, P. D. 2001, Mon. Not. of the Royal Astron. Soc., 322, 209

Sokolov, I. V., Naumova, N. M., Nees, J. A., Mourou, G. A., & Yanovsky, V. P. 2009, Physics of Plasmas, 16, 093115

Speiser, T. W. 1965, J. Geophys. Res., 70, 4219

Spitkovsky, A. 2006, Astrophysical Journal, Letters, 648, L51

Spitkovsky, A. 2008, Astrophysical Journal, Letters, 682, L5

Spitkovsky, A. & Arons, J. 2002, in Astronomical Society of the Pacific Conference Series, Vol. 271, Neutron Stars in Supernova Remnants, ed. P. O. Slane & B. M. Gaensler, 81

Striani, E., Tavani, M., Vittorini, V., et al. 2013, Astrophysical Journal, 765, 52

Sturrock, P. A. 1971, Astrophysical Journal, 164, 529

Sweet, P. A. 1958, in IAU Symposium, Vol. 6, Electromagnetic Phenomena in Cosmical Physics, ed. B. Lehnert, 123–+

Swisdak, M. 2013, Physics of Plasmas, 20, 062110

Takahashi, R. 2007, Mon. Not. of the Royal Astron. Soc., 382, 567

Tamburini, M., Pegoraro, F., Di Piazza, A., Keitel, C. H., & Macchi, A. 2010, New Journal of Physics, 12, 123005

Tavani, M., Bulgarelli, A., Vittorini, V., et al. 2011, Science, 331, 736

Tchekhovskoy, A., Philippov, A., & Spitkovsky, A. 2016, Mon. Not. of the Royal Astron. Soc., 457, 3384

Tchekhovskoy, A., Spitkovsky, A., & Li, J. G. 2013, Mon. Not. of the Royal Astron. Soc., 435, L1

Teraki, Y. & Takahara, F. 2013, Astrophysical Journal, 763, 131

Thielheim, K. O. & Wolfsteller, H. 1994, Astrophysical Journal, 431, 718

Thorne, K. S., Price, R. H., & MacDonald, D. A. 1986, Black holes: The membrane paradigm

Timokhin, A. N. 2006, Mon. Not. of the Royal Astron. Soc., 368, 1055

Timokhin, A. N. & Arons, J. 2013, Mon. Not. of the Royal Astron. Soc., 429, 20

Uzdensky, D. A. 2005, Astrophysical Journal, 620, 889

Uzdensky, D. A., Cerutti, B., & Begelman, M. C. 2011, Astrophysical Journal, Letters, 737, L40

Uzdensky, D. A. & Kulsrud, R. M. 2000, Physics of Plasmas, 7, 4018

Uzdensky, D. A., Loureiro, N. F., & Schekochihin, A. A. 2010, Phys. Rev. Lett., 105, 235002

Uzdensky, D. A. & Spitkovsky, A. 2014, Astrophysical Journal, 780, 3

Vay, J.-L. 2008, Physics of Plasmas, 15, 056701

Vietri, M. 1996, Astrophysical Journal, Letters, 471, L95

Villasenor, J. & Buneman, O. 1992, Computer Physics Communications, 69, 306

Wada, T. & Shibata, S. 2011, Mon. Not. of the Royal Astron. Soc., 418, 612

Wald, R. M. 1974, Phys. Rev. D, 10, 1680

Weisskopf, M. 2011, in Extreme and Variable High Energy Sky (Extremesky 2011), 2

Weisskopf, M. C., Elsner, R. F., Kolodziejczak, J. J., O'Dell, S. L., & Tennant, A. F. 2012, Astrophysical Journal, 746, 41

Weisskopf, M. C., Tennant, A. F., Arons, J., et al. 2013, Astrophysical Journal, 765, 56

Werner, G. R. & Uzdensky, D. A. 2017, Astrophysical Journal, Letters, 843, L27

Werner, G. R., Uzdensky, D. A., Begelman, M. C., Cerutti, B., & Nalewajko, K. 2018, Mon. Not. of the Royal Astron. Soc., 473, 4840

Werner, G. R., Uzdensky, D. A., Cerutti, B., Nalewajko, K., & Begelman, M. C. 2016, Astrophysical Journal, Letters, 816, L8

Wilson, D. B. & Rees, M. J. 1978, Mon. Not. of the Royal Astron. Soc., 185, 297

Yamada, M., Kulsrud, R., & Ji, H. 2010, Reviews of Modern Physics, 82, 603

Yee, K. 1966, IEEE Transactions on Antennas and Propagation, 14, 302

Young, M. D. T., Chan, L. S., Burman, R. R., & Blair, D. G. 2010, Mon. Not. of the Royal Astron. Soc., 402, 1317

Yuan, Q., Yin, P.-F., Wu, X.-F., et al. 2011, Astrophysical Journal, Letters, 730, L15

Yuan, Y., Blandford, R. D., & Wilkins, D. R. 2019, Mon. Not. of the Royal Astron. Soc., 484, 4920

Zelenyi, L. M. & Krasnoselskikh, V. V. 1979, Soviet Ast., 23, 460

Zenitani, S. & Hoshino, M. 2001, Astrophysical Journal, Letters, 562, L63

Zenitani, S. & Hoshino, M. 2007, Astrophysical Journal, 670, 702

Zenitani, S. & Hoshino, M. 2008, Astrophysical Journal, 677, 530

Zhdankin, V., Werner, G. R., Uzdensky, D. A., & Begelman, M. C. 2017, Phys. Rev. Lett., 118, 055103

Zweibel, E. G. & Yamada, M. 2009, Annual Review of Astron and Astrophys, 47, 291